The Deportment of Manganese of the Gamsberg East Orebody, South Africa

Archibald Mokete Moses

24460029

GLG 890

March 2015

Submitted in fulfilment for the requirements of the Master of Science,
Department of Geology

Faculty of Natural and Agricultural Sciences
University of Pretoria

Department of Geology and University of Pretoria Plagiarism Declaration Form

The Department of Geology places great emphasis upon integrity and ethical conduct in the preparation of all written work submitted for academic evaluation.

While academic staff teaches you about systems of referring and how to avoid plagiarism, you too have a responsibility in this regard. If you are at any stage uncertain as to what is required, you should speak to your lecturer before any written work is submitted.

You are guilty of plagiarism if you copy something from a book, article or website without acknowledging the source and pass it off as your own. In effect you are stealing something that belongs to someone else. This is not only the case when you copy work word-by-word (verbatim), but also when you submit someone else's work in a slightly altered form (paraphrase) or use a line of argument without acknowledging it. You are not allowed to use another student's past written work. You are also not allowed to let anybody copy your work with the intention of passing if off as his/her work.

Students who commit plagiarism will lose all credits obtained in the plagiarised work. The matter may also be referred to the Disciplinary Committee (Students) for a ruling. Plagiarism is regarded as a serious contravention of the University's rules and can lead to expulsion from the University.

The declaration which follows must be appended to all written work submitted while you are a student of the Department of Geology. No written work will be accepted unless the declaration has been completed and attached.

I (full names): Archibald Mokete Moses

Student number: 24460029

MSc thesis title: *The deportment of manganese of the Gamsberg East Orebody, South Africa.*

Declaration

1. I understand what plagiarism is and am aware of the University's policy in this regard.

2. I declare that I would submit documents and presentations (e.g. essay, report, project, assignment, dissertation, thesis etc.) that are my own original work. Where other people's work has been used (either from a printed source, internet or any other source), this has been properly acknowledged and referenced in accordance with departmental requirements.

3. I have not used another student's past written work to hand in as my own.

4. I have not allowed, and will not allow, anyone to copy my work with the intention of passing it off as his or her own work.

Signature: ________________ **Date:**____________ **Place:**____________

Original data remains company property and confidential, therefore will be available upon request from Black Mountain Mining PTY Ltd. Geology Department, Aggeneys, Northern Cape Province.

Signature: ___________________ **Date:**_____________ **Place:**_____________

Abstract

The Gamsberg East orebody is the least studied orebody of the Gamsberg zinc (Zn) deposit. The Gamsberg Zn deposit is a largest undeveloped “Broken Hill-type” deposit, which is well known for relatively low zinc grade as well as manganese (Mn) being a problem and penalty element. The occurrence of manganese within the sphalerite crystal lattice is one of the reasons for the lack of mining development over the past three decades. The recent metallurgical test works of the Gamsberg East ore showed that alabandite floats faster than sphalerite and this adds to the Mn penalty factor. Alabandite (MnS) was first reported as trace concentrations, but it was most recently found in anomalous concentrations in the Gamsberg East orebody. Up to 16 %wt alabandite occurs within the pelitic schist of the Gams Formation, and concentrations below 2 %wt occur within the top half of meta-pelite ore. The occurrence of alabandite is also associated with thicker or well developed portions of the ore horizon, which is also associated with manganese enrichment. The model of formation for alabandite is similar to that of sphalerite and Fe-sulphides during metal-sulphide formation in the Gamsberg Zn deposit. Alabandite is therefore pre-metamorphic and its formation is controlled by change in redox water conditions from chemogenic to detrital facies, sulphur fugacity, change in pH and hydrothermal fluids with temperature less than 300 °C, rich in manganese and iron but poor in zinc. Manganese is also hosted in silicate and oxide minerals, such as by pyrophanite, jacobsite, franklinite, amphiboles, micas, pyroxenes/pyroxenoids, and garnets.

Table of contents

Page No.

Appendices

Appendix 1: A geological map of the Gamsberg Zn deposit and detailed lithostratigraphy
Appendix 2: 1. A structural geology interpreted map of the Gamsberg Zn deposit derived from geophysical survey reports and a map presented in Odling (1987). 2. Surface interpolated surface thickness variation
Appendix 3: Samples information data
Appendix 4: Hand specimen photos and descriptions
Appendix 5a: Microphotographs of thin sections
Appendix 5b: Microphotographs of polished mounts
Appendix 5c: Back-scaterred images
Appendix 6a: ICP data
Appendix 6b: XRF data
Appendix 7: XRD data
Appendix 8: EDS data
Appendix 9a: Alabandite mineral chemistry data
Appendix 9b: Sphalerite mineral chemistry data
Appendix 9c: Silicate mineral chemistry data
Appendix 9d: Oxide mineral chemistry data

Tables

Page no.

Figures

Acknowledgements

I would like to thank Anglo American Exploration Division and the Gamsberg Project team for granting and sponsoring my MSc studies. Without them this study wouldn't have even taken-off. I would like to thank Gerald Boting, Braen Migogo from Vedanta Resources in Aggeneys for taking over the sponsorship and offering me employment at Black Mountain Mining. My regards also goes to the various geology departments at Aggeneys for their continued support and input.

Over the years I received immense support from my family and friends, especially my brother Thabo Moses. To my geologist friends, I would like to thank you for all the discussion and the geo-poetry sessions we had. All the ideas were never lost and are somehow fused within the thesis. To my wife, Khensani thanks a lot for your spiritual and emotional support through trying times.

Last but not least, my warm regards to Prof. Roland Merkle (supervisor) and the University of Pretoria, for the opportunity and guidance throughout the years.

Chapter 1: Introduction

Section 1: Introduction to the manganese problem of the Gamsberg zinc deposit

The Gamsberg zinc (Zn) deposit is well known for manganese (Mn) being a challenge and penalty element and this is one reason for the lack of mining development since its discovery (Rozendaal, 1986; Rozendaal, 2008; Goodfellow and Lydon, 2007; Schouwstra et al., 2010; McClung and Viljoen, 2011). An investigation carried out in 1972, subsequent to the discovery of the economic base metal ore horizon, revealed that the Gamsberg orebody displays a significant bulk-rock Mn concentration, as well as Mn-bearing sphalerite [ZnS], and that manganese has detrimental effects in ore beneficiation processes (Voet et al., 2000).

Over the past three and a half decades, extensive geo-metallurgical research has been carried out to deal with Mn issues for downstream Zn production. Different aspects have been investigated, including improving the quality of the Zn concentrate, ozone oxidation (electrowinning process) and refinery processing by Mintek DC arc technology for the production of Zn metal (Ahlrichs, 1975; Roos, 1997).

An investigation by Ahlrichs (1975) revealed that aeration prior to flotation improved the sphalerite recoveries, and therefore the quality of zinc concentrates, regarding the Mn concentrations. In this investigation it also was discovered that the presence of alabandite [MnS] contributed to the high Mn concentrations – of above 3% Mn – of the Gamsberg zinc concentrate. Mineralogical analysis showed that alabandite shares mineralogical characteristics with sphalerite, and up to 15.5 %wt alabandite was present in one of the Gamsberg ore samples (Ahlrichs, 1975; Schouwstra et al., 2010; McClung and Viljoen, 2011). According to Ahlrichs (1975), alabandite also shares flotation characteristics with pyrrhotite, and this similarity is of advantage as alabandite is depressed along with pyrrhotite and therefore manganese concentrations decrease to 8.8% Mn from 11.2% Mn.

In 1992, Gold Fields of South Africa Ltd. investigated ozone oxidation for Zn production of the Gamsberg ore (Van Leeuwen and Ponelis, 1992). Ozone oxidation, as one of the oxidative precipitation techniques of the electrowinning process, has a capability to oxidise manganese to insoluble MnO_2 (Van Leeuwen and Ponelis, 1992; Zhang and Cheng, 2007). A report by Van Leeuwen and Ponelis (1992) said that ozone consumption of 0.6 kg per kg of manganese would be required to produce 18 300 kg of MnO_2 on a daily basis. This report presented a high capital cost for only removing manganese, to which ozone generation, storage and transportation also would add costs.

A study by Zhang and Cheng (2007) showed that, in the electrowinning processing of zinc ores, Mn has both positive and negative effects. Manganese concentrations of less than 5 g/L (5 000 ppm or 0.5 %wt) can minimise the corrosion rate of the anodes and reduce the contamination of cathodic Zn with lead (Pb), while a concentration of more than 5 g/L of Mn in the flotation circuit results in the build-up of a Mn layer on the anodes, which then causes limited carrying capacity of the metal ions, therefore reducing the yield capacity of Zn. According to Zhang and Cheng (2007), a number of different strong oxidants are available to deal with Mn concentration above 0.5 %wt.

Mintek DC arc technology has an advantage to cope with any manganese concentrations of the Gamsberg concentrate and produce a clean Zn product, but due to negative environmental and health concerns and high energy consumption, its application was dismissed, despite the considerable cost advantage compared to electrolyte processing (Roos, 1997).

Processing of the Gamsberg zinc concentrate by pressure leach, solution purification, electrowinning processing, melting and casting have remained the favourable choice for Zn production of the Gamsberg ores (Reid and Harley, 2009).

For a while, Mn issues seemed to be under control, but in 2010 the results of metallurgical test works carried out by Anglo Research Laboratory indicated that the presence of alabandite within the ore negatively affected the flotation response of the sphalerite (Schouwstra et al., 2010). It was not the first time the presence of alabandite was related to Mn issues during ore processing, but this time alabandite was found to have a better recovery than sphalerite when $CuSO_4$ (copper sulphate) was used as a reagent to activate sphalerite during flotation (Schouwstra et al., 2010). In 2010, it was not the first time the presence of alabandite within the Gamsberg Zn deposit was discussed, but it was described as an accessory sulphide mineral within the Gamsberg ore as early as 1972 (Ahlrichs, 1975; Rozendaal, 1986; Schouwstra et al., 2010). Despite the occurrence of alabandite in the Gamsberg Zn deposit, alabandite has received little research attention, hence little information is available on its distribution, paragenesis and mode of occurrence, and its effects on the metallurgical processing of zinc ore from the Gamsberg ore (Ahlrichs, 1975; Rozendaal, 1986, Schouwstra et al., 2010; McClung and Viljoen, 2011).

Apart from the challenges related to the Mn deportment, a number of other factors have delayed the development of the Gamsberg Zn deposit to the exploitation stage, despite several pre-feasibility studies having been undertaken in the past decades. These factors include issues related to the low zinc grade of the Gamsberg Zn deposit compared to ore grades globally, the removal of Mn from the zinc concentrate, long-term low zinc prices, a shift in priorities during the emergence of Skorpion Zinc Mine in Namibia, the change of mining bill legislature in 2000, and the economic recession in 2009/2010, which had a negative effect on the overall commodity prices (Voet et al., 2000; Prinsloo, 2010). It was during this economic slump that Vedanta Resources Plc acquired the zinc assets from Anglo American Plc (Prinsloo, 2010). By 2015 Vedanta Resources had commence developing a 4MPTA open pit operation in the Gamsberg Zn deposit.

Section 2: Aims and objectives

The challenges related to Mn within the Gamsberg Zn deposit initiated the interest to investigate the deportment of Mn of the Gamsberg East orebody. These challenges that prompted this investigation are;

- the relatively high manganese content within the ore
- the complex mineralogy of the ore and presence of alabandite
- the manganese issues related to metallurgical processing of the zinc ore
- the overall structural complexities of the Gamsberg Zn deposit

The Gamsberg East orebody is one of the four areas of mineralisation in the Gamsberg Zn deposit: Gamsberg North orebody, Gamsberg West orebody and Gamsberg South orebody (see section 3 of Chapter 1). The Gamsberg East orebody presents a good opportunity for such an investigation, as it is the least explored and therefore has been subjected to little research in general.

Investigate the distribution of Mn of the Gamsberg East Orebody. In this study, the aim will be achieved through understanding the probable genetic controls for the mode of formation of alabandite and other Mn-bearing minerals. The following holistic approach is undertaken to;

- study of mineralogy and petrography in order to:
    - identify Mn bearing minerals and mineral assemblages
    - understand relationships of Mn-minerals particular coexisting alabandite-spahlerite and Mn-bearing silicates
    - understand the distribution of elements within Mn-bearing minerals and between coexisting Mn-bearing minerals
- understand the geochemistry of the ore horizon through:
    - Characterization of rock types
    - 3D modelling of manganese distribution
- determine present structural and metamorphic influences that played a role in the present-day characteristic of the orebody.

The investigation will contribute towards an understanding of the mineralogical evolution in the Gamsberg East orebody, especially the manganese-bearing minerals. In addition geometallurgical understanding will assist in improving zinc recoveries and managing the managanese penalty factor for future mining of the Gamsberg East orebody.

Section 3: Study area and historical background

1.3.1 Geographical location of the Gamsberg Zn deposit

The Gamsberg Zn deposit is geographically located at 29˚15´7˝ S and 18˚58´52˝ E, within the Gamsberg Mountain. The Gamsberg Mountain lies 20 km east of Aggeneys town and about 250 km west of Upington in the Northern Cape province, South Africa (Figure 1). Aggeneys town is well known for the exploitation of Pb, Cu and Zn deposits by Black Mountain Mining PTY Ltd.

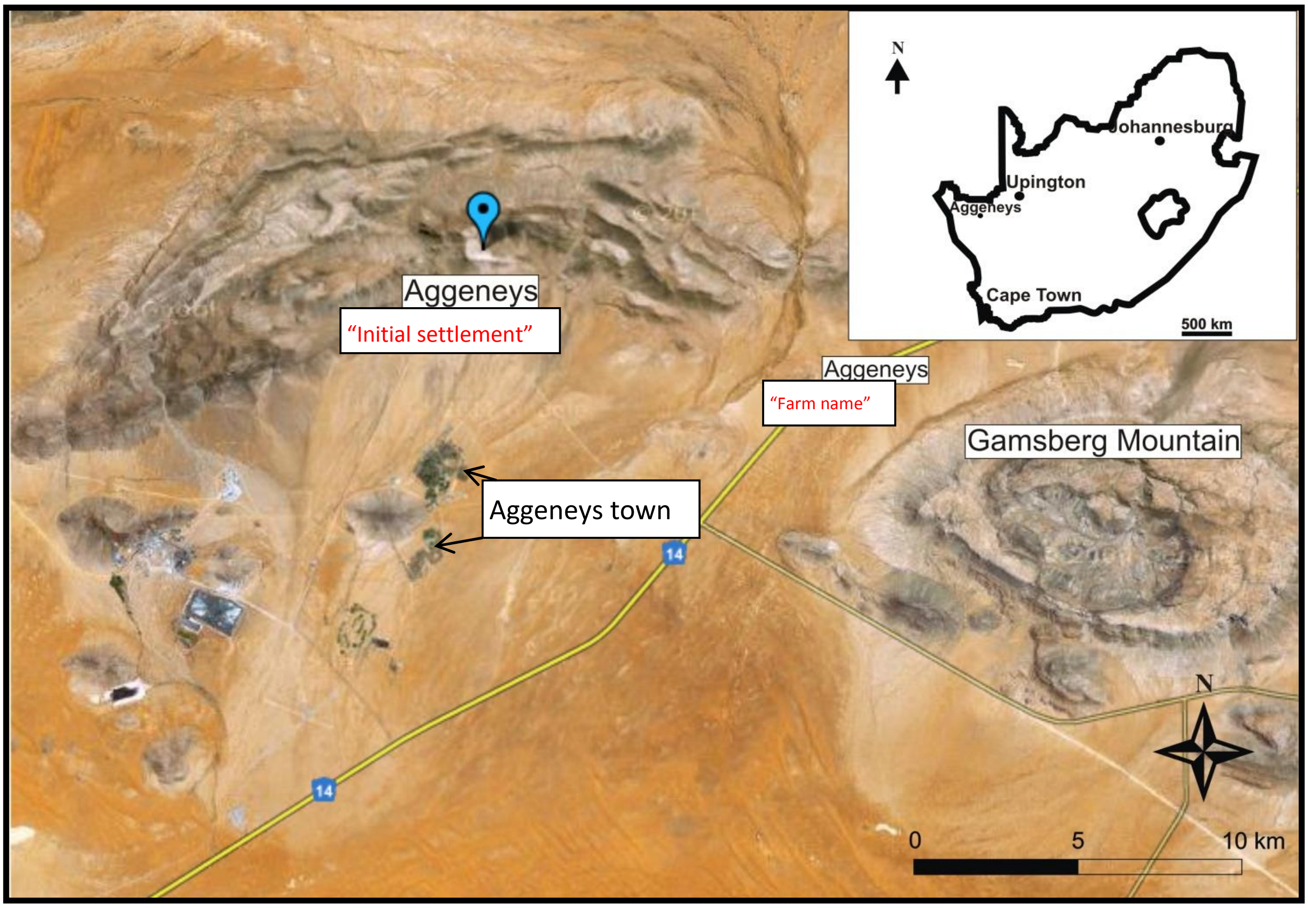

Figure 1. Location of the Gamsberg Mountain east of Aggeneys town, with the N14 highway passing between Aggeneys town and Gamsberg Mountain, in the Northern Cape province, South Africa *(Courtesy of Black Mountain Mining).*

1.3.2 Physiographic features of the Gamsberg Mountain

The Gamsberg Mountain is a steep-sided and flat-topped inselberg that rises to 250 m above the general level of the Bushmanland plain (Rozendaal, 1986). The mountain has a maximum length of 7.2 km in the east-west direction and a maximum width of 4.6 km (Rozendaal, 1986; Voet et al., 2000). The central basin is kidney shaped, and it is 3.8 km by 1.6 km in extent. The floor is nearly horizontal and lies 60 to 70 m below the mountain rim. The top of the mountain represents an erosional relic of the former extensive peneplain (Voet et al., 2000). The prominent inselberg and ranges of hills in and around the Aggeneys area characterise the arid landscape of the area (Rozendaal, 1986).

The Gamsberg Mountain is located within a semi-arid region, with an average annual rainfall of ±112 mm and daytime temperatures ranging between 15˚C and 38˚C. The largest part of the Gamsberg Mountain is defined by the Succulent Karoo Ecosystem Programme (SKEP) as a biodiversity hotspot and ecologically sensitive area because it hosts several endemic species of succulent plants, termed “white quartz patch succulents” (see Figure 2 for examples) (Gamsberg Project Manual, 2010). The Gamsberg Mountain is also home to a variety of fauna, including a southern frog. The terrain to the east of the Gamsberg Mountain is relatively flat, but rough with quartz ridges and boulders throughout (Gamsberg Project Manual, 2010).

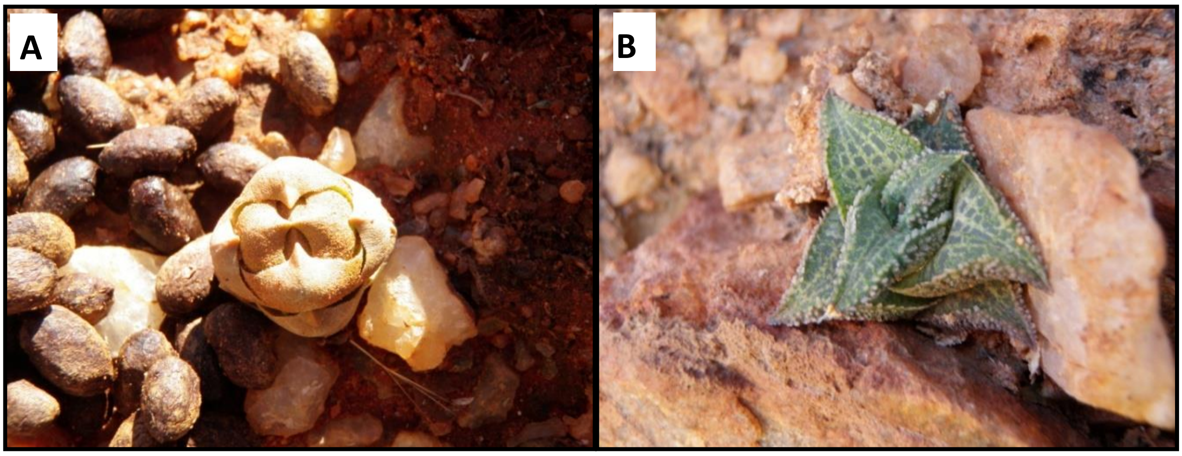

Figure 2. Some of the succulents occurring within the eastern part of the Gamsberg Zn deposit (A): Crassulacolumnaris and (B): Haworthiaverosa.

1.3.3 A brief history of the Gamsberg Zn deposit

In 1954, R. G. Niemoller, a farmer and prospector of manganiferous iron ore, magnetite, barite and sillimanite, discovered the Gamsberg deposit (Rozendaal, 1986). His discovery initiated interest in the deposit and the later discovery of barite and then Zn deposits (Rozendaal, 1986; Reid et al., 1987). The mining of barite commenced by Zimro long before the zinc potential was recognised (Rozendaal, 1986). Only in 1972 did exploration of the base metal mineralisation begin and, since then, about 115 000 m of drilling has been completed by three companies: Newmont/Okiep Copper Company (OCC; 1972 to 1979), Goldfields of South Africa (GFSA; 1992 to 1993) and Anglo American (AAED; 2001 to 2009) (Reid et al., 1986; Rozendaal, 1986; Gamsberg Project Manual, 2010).

Four main areas of mineralisation are recognised within the Gamsberg Zn deposit: Gamsberg North, Gamsberg West, Gamsberg South and Gamsberg East (Figure 3) (Stalder and Rozendaal, 2005a, 2005b, 2005c; Rozendaal, 2008). The Gamsberg North, West and South orebodies were the first to be explored – in 1972 for base metal sulphides, and the Gamsberg East orebody was only discovered in 2005 (Rozendaal, 1986; 2008). The Gamsberg East orebody is well known for the mining of a bedded barite deposit, and its base metal deposit is the least explored of the four (Rozendaal, 1986; Stalder and Rozendaal, 2005a; 2005b; 2005c; McClung et al., 2007; Rozendaal, 2008; Gamsberg Project Manual, 2010). Figure 3 shows the exposed base metal sulphides-hosting rocks of the Gamsberg Zn deposit and drillhole positions of different mining and exploration concession holders since its discovery.

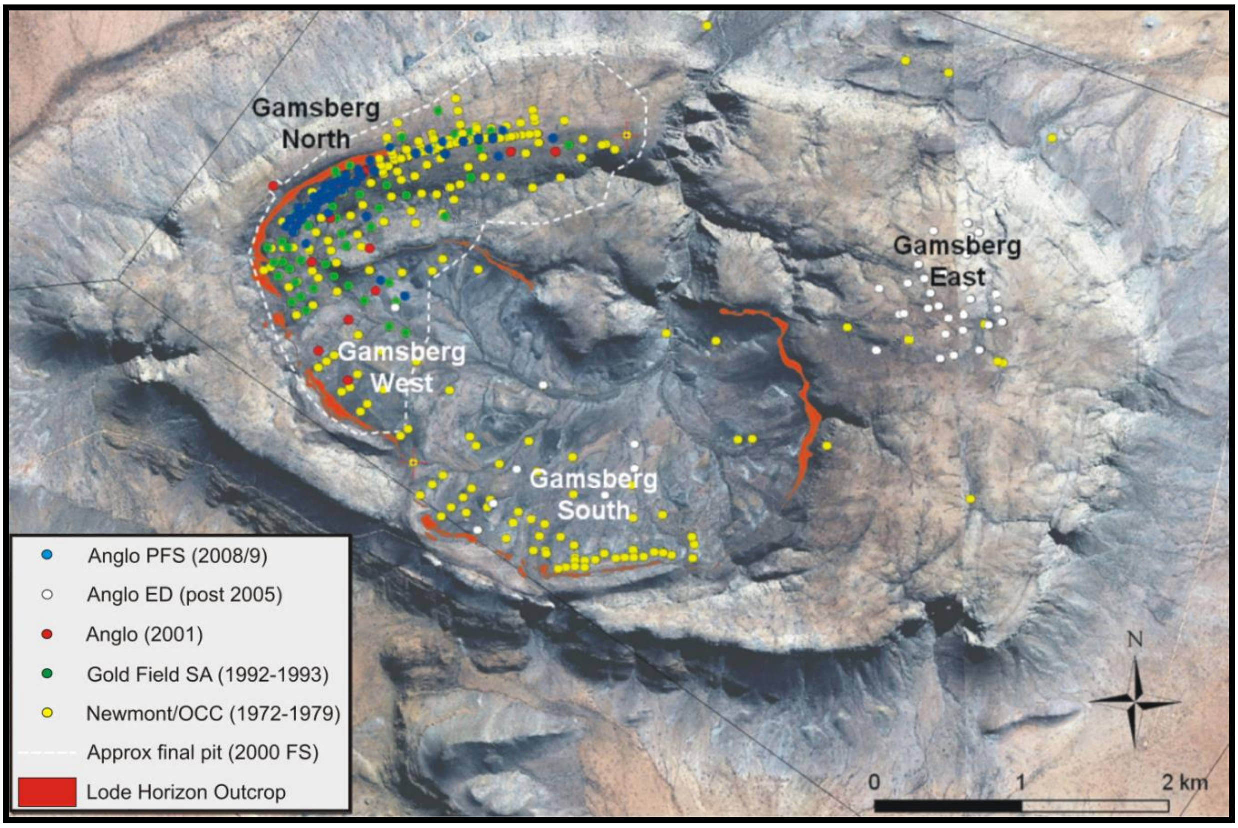

Figure 3. Satellite image of the Gamsberg Mountain showing positions of ore bodies drilled by various concession holders (modified from the Gamsberg Project Manual, 2010).

Chapter 2: Geological background of the study area

Section 1: The geology of the Aggeneys-Gamsberg metallogenic district

The Aggeneys-Gamsberg metallogenic district (Figure 4) comprises the Swartberg (Black Mountain), Broken Hill and Big Syncline deposits (all three termed the Aggeneys deposits), as well as the Gamsberg Zn deposit further to the east (Rozendaal 1986; Ryan et al., 1986; Stalder and Rozendaal, 2002). The Gamsberg Zn deposit is distinctly different from the rest of the Aggeneys deposits due to the high concentration of Zn and Mn, the economic occurrence of bedded barite associated with sulphide formation, and the size of the deposit, whereas the Aggeneys deposits are relatively smaller, enriched in Pb and Cu, and have low Zn and barite concentrations (Ryan et al., 1986; McClung et al, 2007; Cornell et al., 2009). The district exhibits east-west metal zonation, with the Gamsberg Zn deposit enriched in Zn, Pb, and Ba, whereas the Swartberg is enriched with Pb, Zn, Cu, Ag and minor Ba (McClung et al., 2007).

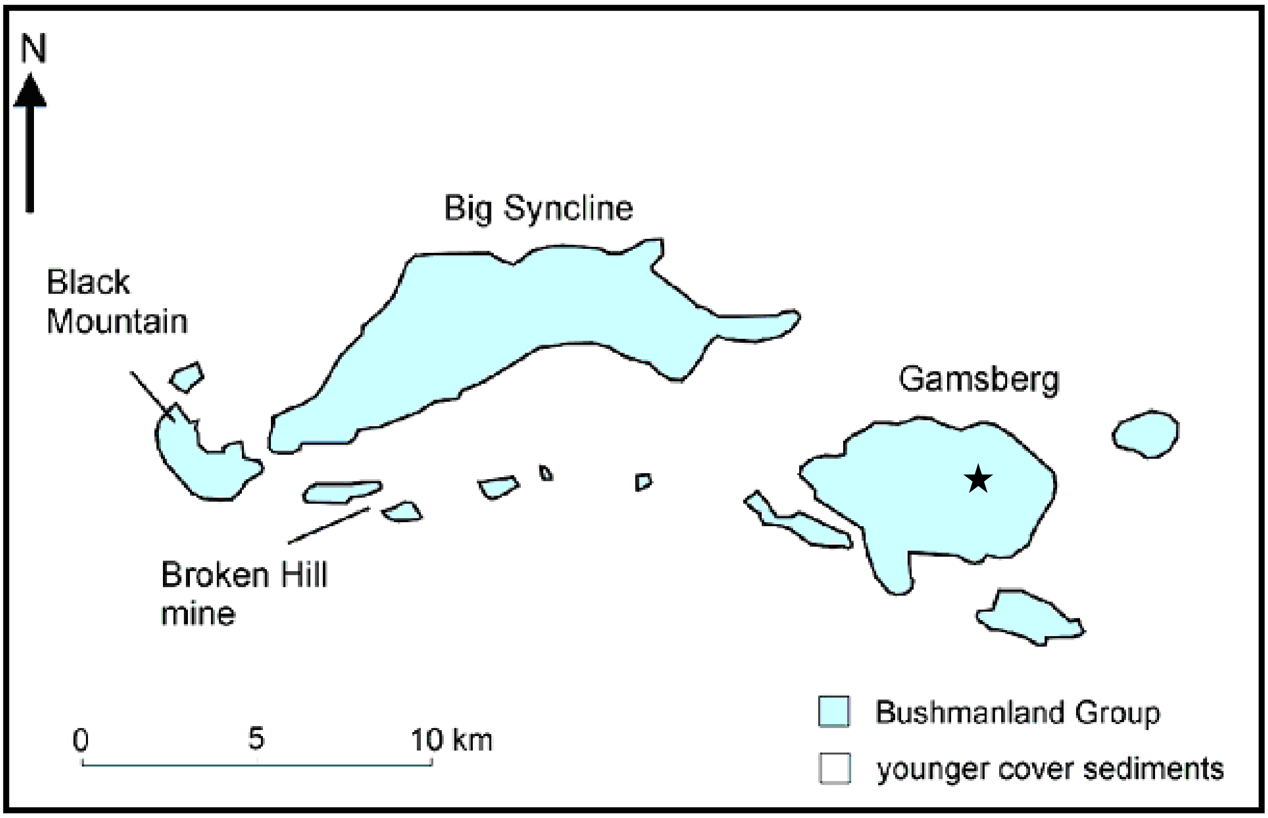

Figure 4. Location and geology map of Aggeneys-Gamsberg deposits. A star denotes the study area (from Stalder and Rozendaal, 2005).

The Aggeneys-Gamsberg deposits host about 439 Mt of base metal sulphides at an average grade of 3.6% Zn, 1.43% Pb, 0.21% Cu and 21 g/t Ag, as well as 6 Mt of barite (Reid and Harley, 2009; McClung and Viljoen, 2011). The Gamsberg Zn deposit alone hosts about 265 Mt of base metal sulphides, and all the economic barite (McClung et al., 2007; McClung and Viljoen, 2011).

The Aggeneys-Gamsberg deposits are associated with the “Broken Hill-type” (BHT) deposits, characterised by base metal mineralisation of economic interest, occurring within early Mesoproterozoic poly-deformed and medium- to high-grade metamorphosed terranes (Walters, 1996; Stalder and Rozendaal, 2002; 2004; 2005a; 2005b; 2005c; Goodfellow and Lydon, 2007). The “Broken Hill-type” deposits are a subtype of SEDEX (Sedimentary-Exhalative) deposits, forming by exhalative ore-forming processes. Goodfellow and Lydon (2007) comprehensively defined SEDEX deposits as sediment-hosted sulphides, predominantly of Zn, Pb, and Ag, which typically take the form of tabular bodies interbedded with iron sulphides and basinal sedimentary rocks deposited on the seafloor. The “Broken Hill-type” deposits are generally thought to have formed in restricted basins with massive sulphide facies and iron formation facies grading into oxide facies and barite-magnetite beds (Stalder and Rozendaal 2005a; 2005b; 2005c; Goodfellow and Lydon 2007; McClung et al., 2007; Rozendaal 2008; Cornell et al., 2009).

The Aggeneys-Gamsberg deposits formed in one or more rift-related third-order basins into which metallic brines were discharged by conduits (feeder faults) (McClung, 2006). The source of the metal remains a subject of interest, with the western-most deposits (Swartberg deposit) regarded as proximal to the metallic source (McClung, 2006). Distal facies, such as interpreted for the Gamsberg Zn deposit, include laminated pyrite and pyrrhotite, manganese-bearing minerals, calcium carbonates, iron oxides, barite and phosphates (Goodfellow and Lydon, 2007).

Over the past few decades, researchers of the Aggeneys-Gamsberg deposits have proposed different genetic models. Rozendaal and Stumpfl (1984) classified the Gamsberg Zn deposit as a volcano-sedimentary sequence of Proterozoic age. Rozendaal (1986) proposed two models for the genesis of the Gamsberg Zn deposit: a sedimentary environment related to a distal island arc or, alternatively, a Red Sea intercontinental environment. Ryan et al. (1986) considered the Aggeneys-Gamsberg deposits as stratabound exhalative sedimentary deposits with close genetic affinities to the Broken Hill deposit of Australia. Recently, more and more publications on the Aggeneys-Gamsberg deposits agree with the BHT model and favour a synsedimentary origin model for the formation of the base metal ore deposits (Stalder and Rozendaal, 2002; Stalder and Rozendaal, 2004; 2005a; 2005b; 2005c; Goodfellow and Lydon, 2007; McClung et al., 2007; Rozendaal, 2008).

Isotopic evidence from a study by Gertloff (2004) has revealed that the mineralisation of the Aggeneys-Gamsberg deposits formed in a closed system – a sub-seafloor environment, rather than along the seawater-sediment interface, and therefore did not form from hot metalliferous brines mixing with a sulphate-rich seawater-derived fluid, as previously thought. The lack of Cu within the Gamsberg Zn deposits suggests that the ore-forming fluid temperatures were below 300 ˚C (Goodfellow and Lydon, 2007).

The genesis of the base metal ores continues to be a subject of debate, and metamorphic and structural distortions add to the complexity of the evolution of the “Broken Hill-type” deposits.

Section 2: Regional geology

2.2.1 The Namaqua-Natal Belt and its subdivisions

The Gamsberg Zn deposit is located in the Namaqua-Natal Mobile Belt of South Africa (Rozendaal, 1986; Bailie and Reid, 2005; Eglington, 2006; McClung et al., 2007; Cornell et al., 2009). The Namaqua-Natal Mobile Belt comprises complexly folded and faulted Mesoproterozoic metasediments and metavolcanics that have been subjected to polyphase deformation and medium- to high-grade metamorphism (Rozendaal, 1986; Bailie and Reid, 2005; Stalder and Rozendaal, 2005; McClung et al., 2007). The belt is well known for its contribution to the reconstruction of greater networks of Mesoproterozoic belts, and for defining the configuration of Rodinia, the Neo- to Mesoproterozoic supercontinent (Eglington and Armstrong, 2003; Bailie et al., 2007a).

The Namaqua-Natal Mobile Belt is continuous along the southern margin of the Kaapvaal Craton and is partially covered by Phanerozoic material (Karoo Supergroup and younger), as evidenced by seismic studies (Thomas et al., 1994; Eglington, 2006; Dewey et al., 2006; Eglington and Armstrong, 2003). In the eastern part of South Africa, the belt outcrop is termed the Natal Province, and the western outcrop is termed the Namaqua Metamorphic Complex (NMC) (Cornell et al., 1996; Dewey et al., 2006; Eglington and Armstrong, 2003). Figure 5 shows the position of the Namaqua-Natal Belt relative to the Kaapvaal Craton and Cape Fold Belt. It also shows the subdivisions of the western part of the NMC.

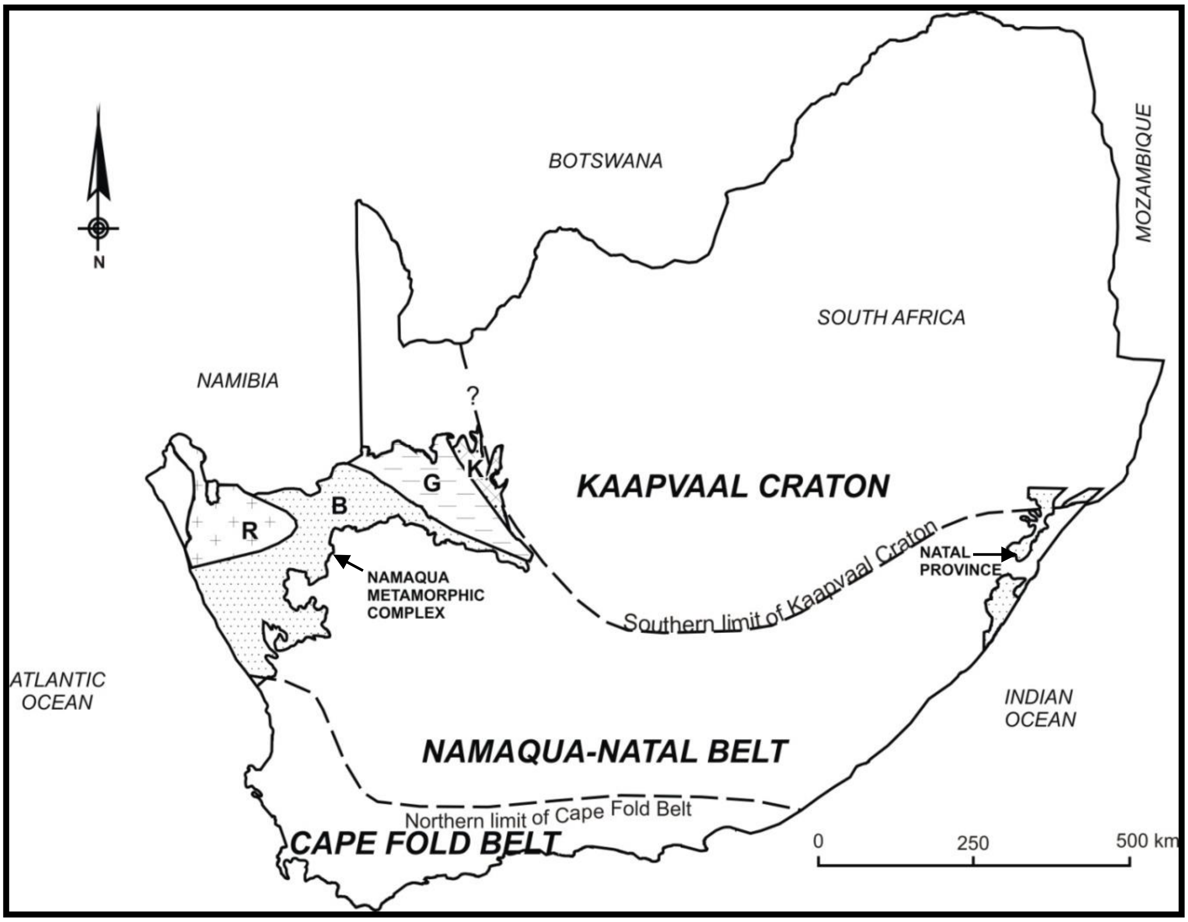

Figure 5: Regional extent of the Namaqua-Natal Belt relative to the Kaapvaal Craton and Cape Fold Belt. The map shows the positions of the outcrops of the Namaqua Metamorphic Complex and Natal Province. **R**: Richtersveld sub-province, **K:** Kheis sub-province, **B:** Bushmanland sub-province, and **G:** Gordonia sub-province (modified from Eglington and Armstrong, 2003).

The Namaqua Metamorphic Complex is a crescent-shaped belt with several transcurrent faults crosscutting the complex, allowing subdivision into four tectono-stratigraphic terranes, namely the Richtersveld, Bushmanland, Gordonia and Kheis sub-provinces (see Figure 5) (Moore et al., 1990; Eglington and Armstrong, 2003; Dewey et al., 2006; McClung, 2006).

The Richtersveld sub-province, located in the northwest part of the NMC, is characterised by greenschist metamorphic rocks (Dewey et al., 2006). These rocks comprise a Palaeoproterozoic suite of mafic to felsic lavas, ignimbrites and other volcanic rocks, interbedded with various sedimentary rocks that were contemporaneously intruded by calc-alkaline, I-type granitoids in a continental volcanic arc (Dewey et al., 2006; McClung, 2006; Bailie et al., 2007; Cornell et al., 2010).

The Gordonia sub-province is subdivided into two parts, the eastern Areachap and the western Kakamas Terranes (Dewey et al., 2006; McClung, 2006). The Areachap Terrane hosts a juvenile, bimodal volcanic arc, and sedimentary rocks of Mesoproterozoic age (McClung, 2006). The Kakamas Terrane consists of thin packages of quartzites and calc-silicate rocks intruded by syn- to post-Namaquan orogeny granitic rocks (McClung, 2006).

The Kheis sub-province forms the eastern margin of the NMC and borders the Kaapvaal Craton (Dewey et al., 2006). It is a thin-skinned fold-and-thrust belt comprising quartzites, phyllites and metabasalts (Eglington, 2006; McClung, 2006).

The Bushmanland sub-province is subdivided into the Aggeneys Terrane (equivalent to the Bushmanland Terrane or the Bushmanland Group), Okiep Terrane and Garies Terrane (see Figure 6) (Eglington, 2006). Dewey et al. (2006) also subdivided the Bushmanland sub-province into the Bushmanland Terrane (equivalent to the Aggeneys Terrane and Bushmanland Group) and the Namaqualand Terrane (equivalent to the Okiep and Garies Terranes). The Bushmanland sub-province hosts variably thick metavolcanic and metasedimentary successions of psammo-pelitic schists and gneisses, quartzite and calc-silicate rocks, which are intruded by a number of syn- to post-collisional granites of Namaquan age (McClung, 2006). According to the South African Committee for Stratigraphy (SACS), the Bushmanland Group comprises volcano-sedimentary sequences and hosts the giant base-metal Aggeneys-Gamsberg deposits (Reid et al., 1997; Stalder and Rozendaal, 2005). Figures 6 and 7 show geological maps and the subdivision of the Bushmanland sub-province.

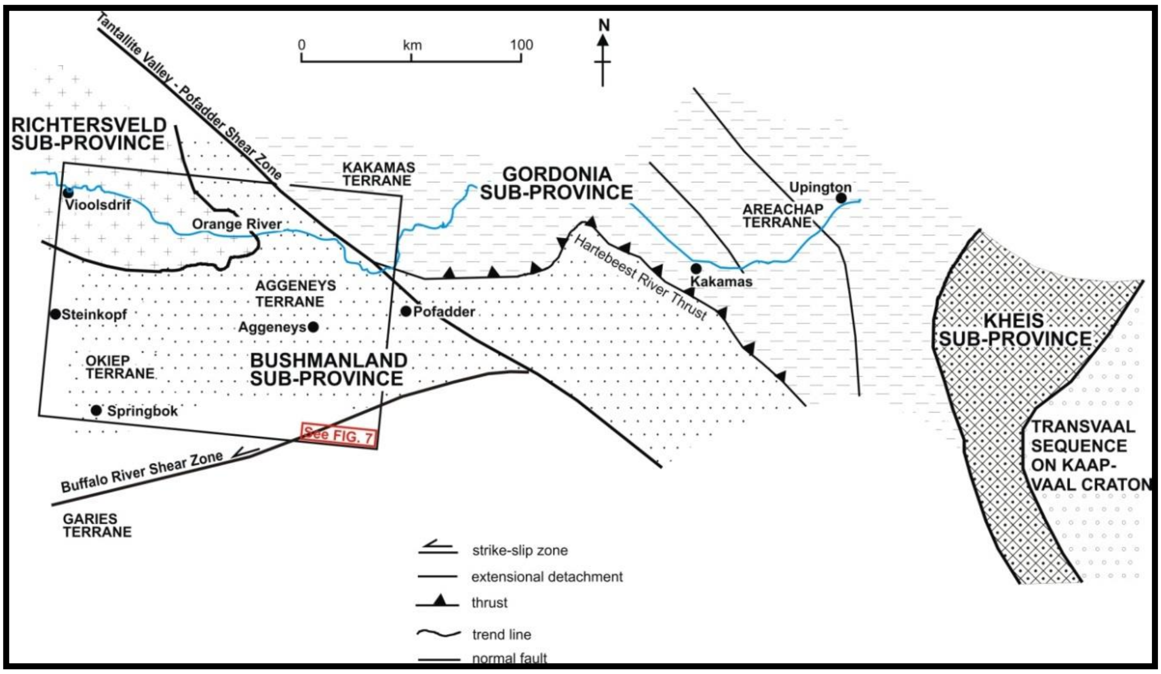

Figure 6. Geological map of western South Africa showing the position of the Namaqua Metamorphic Complex and its subdivisions and the insert of Figure 7 (after Dewey et al., 2006).

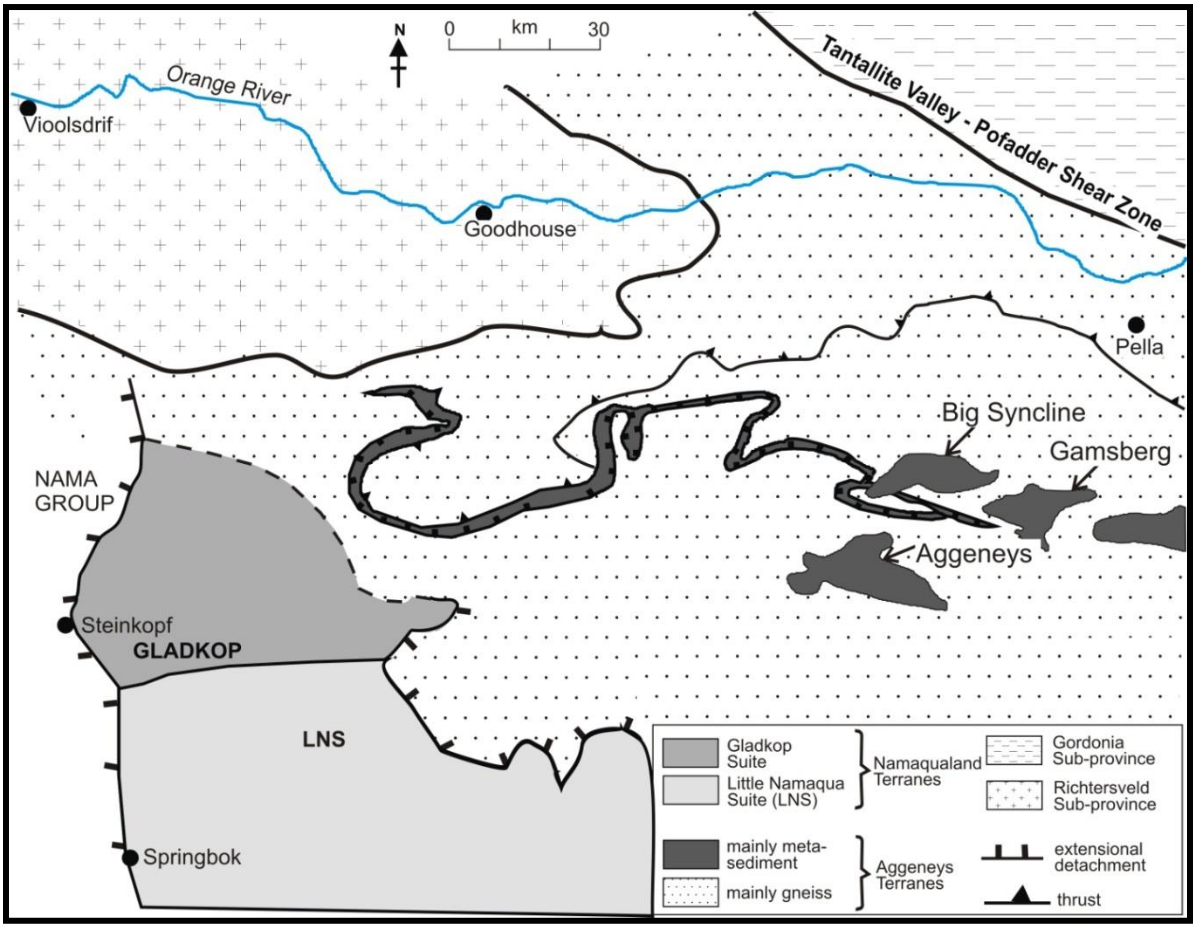

Figure 7. *(Insert in Figure 6)* Geological map of the Bushmanland Group, which includes the Namaqualand Terranes and Aggeneys Terranes (after Dewey et al., 2006).

The nature of the basement of the NMC, especially that of the Bushmanland sub-province, remains a subject of debate (Moore et al., 1990; McClung, 2006). According to Moore et al. (1990), three heterogeneous “basements” of the NMC are geographically distributed across the Richtersveld, Gordonia, and Bushmanland sub-provinces. The basement of the Richtersveld sub-province is dominated by 2.0 Ga extrusive andesite, calc-silicate rocks, and metavolcanic sequences of the Orange River Group and the 1.9 Ga Vioolsdrif Igneous Suite (Moore et al., 1990). The basement of the Gordonia sub-province is characterised by medium- to high-grade metamorphic garnet-sillimanite-cordierite bearing gneisses of unknown ages (Moore et al., 1990; McClung, 2006). The basement of the Bushmanland sub-province comprises the controversial Achab gneiss (see 2.2.2), the Gladkop Suite observed in the Steinkopf area, and the Lammershoek gneisses of the Okiep Copper District (Moore et al., 1990).

2.2.2 The stratigraphy of the Bushmanland Group

The Bushmanland Group has undergone extensive tectonic duplication and stacking due to thrusting and deformation, resulting in a highly complex package and the proposal of various stratigraphic interpretations (Ryan et al., 1986; Bailie et al., 2007a). Figure 8 compares stratigraphic interpretations of the Bushmanland Group by different authors. The average thickness of the Bushmanland Group is approximately 1 000 m (Rozendaal, 1986; Stalder and Rozendaal 2004; 2005c; Bailie et al., 2007a; McClung et al., 2007). The supracrustal rocks of the Bushmanland Group are often synformal and structurally overturned and folded into basal gneisses (Ryan et al., 1986). These infold or “schist belts” generally form ranges of hills (see Figure 7) whereas the basal gneisses usually weather negatively and underlie the sand-filled valleys (Ryan et al., 1986).

The stratigraphic sequence of the Bushmanland Group consists of basal augen gneiss, overlain by pink gneiss, followed by a series of metasedimentary rock units and capped by conglomerate, amphibolite and leucocratic gneiss (Rozendaal, 1986; Ryan et al., 1986; Stalder and Rozendaal, 2005c; McClung et al., 2007). The Bushmanland Group metasedimentary rocks were originally extensive in distribution but have been extremely eroded and are well preserved only in the Aggeneys and Gamsberg area (Ryan et al., 1986).

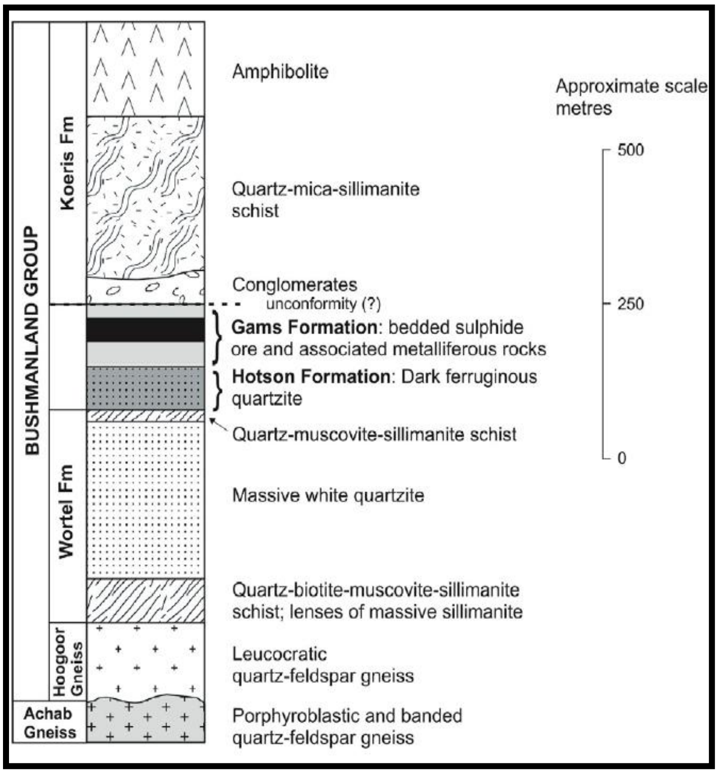

Figure 9. Schematic section of the Bushmanland Group stratigraphy in and around the Aggeneys-Gamsberg area (Stalder and Rozendaal, 2005).

The Achab gneiss in the Aggeneys-Gamsberg area is made up of leucocratic poikiloblastic microperthite augen, elongated parallel to the foliation and set in a matrix of quartz, microcline, plagioclase and biotite (Ryan et al., 1986). This is interpreted as a basement of the Aggeneys-Gamsberg area, but views are divided on the Bushmanland basement (Cornell et al., 2009). The Achab Gneiss “basement” may represent an exotic terrane partially subducted under the Richtersveld terrane between 1800 and 1750 Ma, therefore resulting in intrusive leucogranitic bodies emplaced into the Richtersveld terrane (Moore et al., 1990). These represent an early tectonic event that did not affect the Bushmanland Group (Moore et al., 1990).

The Hoogoor Gneiss is a suite of pink, leucocratic granitic gneiss (Reid et al., 1986; Cornell et al., 2009), interpreted by some authors, e.g. Ryan et al. (1986), as meta-rhyolite extruded prior to the deposition of Bushmanland supracrustal rocks (Rozendaal, 1986; Stalder and Rozendaal, 2005). This suite is estimated to have a maximum thickness of 200 m (Ryan et al., 1986). The Hoogoor Gneiss has a heterogeneous texture and often weathers to a pink-brown colour and displays granitic exfoliation (Ryan et al., 1986). Another view is that the Hoogoor Gneiss is a sub-aerially deposited acid volcanic tephra (Moore et al., 1990). Cornell et al. (2009), on the other hand, have interpreted the Hoogoor Gneiss to have intruded just before the deposition of Bushmanland “cap”, the Koeris Formation (see Figure 9). A sharp contact is usually observed with the Namies Schist, but thin and discontinuous lenses of schist, quartzite and amphibolite occur within the pink gneiss (Ryan et al., 1986).

The Wortel Formation consists of two units, namely the Namies schist and the Pella quartzite (Rozendaal, 1986). The Namies schist is an upward-coarsening succession of aluminous schist composed of quartz, muscovite, K-feldspar, sillimanite, biotite and sulphide minerals (Ryan et al., 1986; McClung et. al., 2007). It is a thick sequence of highly foliated, brown (weathered) to grey-green (fresh) psammo-pelitic schist of approximately 75 to 100 m thick, and it forms a conformable contact with the overlying Pella quartzite (Rozendaal, 1986; Ryan et al., 1986; Lacassie et al., 2007).

The Pella quartzite is a succession of massive white quartzite, dark quartzite and interbedded lenses of aluminous schist (Rozendaal, 1986; Lacassie et al., 2007). It averages 50 m in thickness in the Aggeneys Mountains and varies from 5 m to 900 m thick across the Bushmanland Terrane (Ryan et al., 1986). Thicknesses in excess of 100 m are likely a result of duplication due to folding (Ryan et al., 1986). The white quartzite is milky white to grey, massive with a glassy texture, and completely recrystallized (Ryan et al., 1986; Rozendaal, 1986). The pelitic schist at the top of the Wortel Formation is irregular and discontinuous, and consists of quartz, muscovite, biotite, sillimanite, magnetite and garnet (Ryan et al., 1986). The Wortel Subgroup is interpreted as metamorphosed shallow-water black shale and quartz arenite (Stalder and Rozendaal, 2005c).

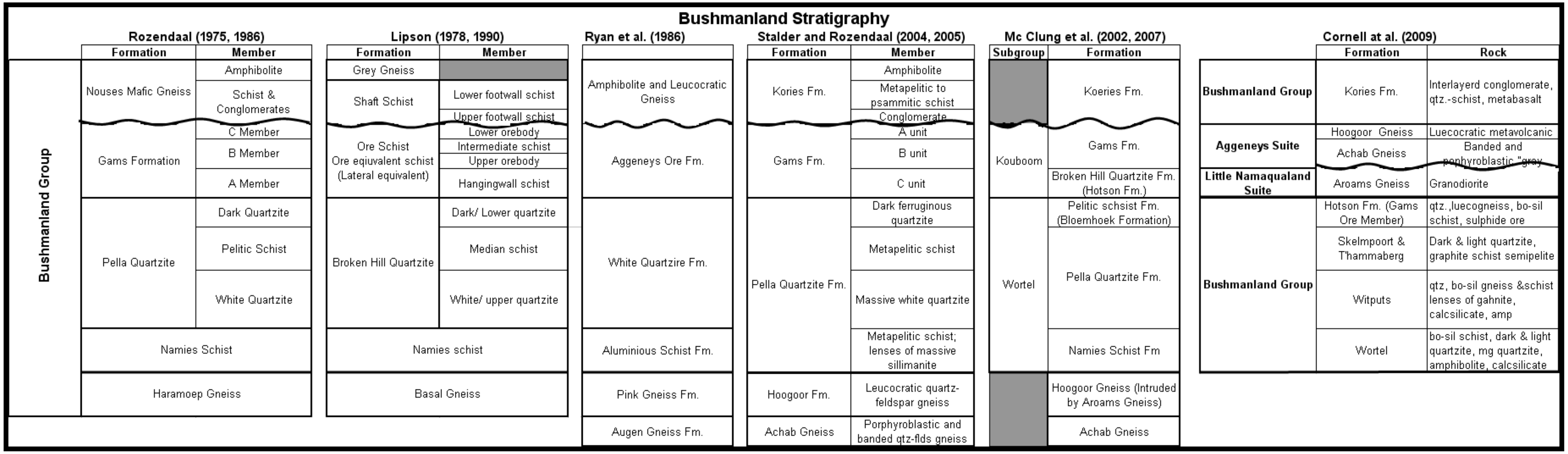

Bushmanland Stratigraphy

Rozendaal (1975, 1986)

	Formation	Member
Bushmanland Group	Nouses Mafic Gneiss	Amphibolite
		Schist & Conglomerates
	Gams Formation	C Member
		B Member
		A Member
	Pella Quartzite	Dark Quartzite
		Pelitic Schist
		White Quartzite
	Namies Schist	
	Haramoep Gneiss	

Lipson (1978, 1990)

Formation	Member
Grey Gneiss	▨
Shaft Schist	Lower footwall schist
	Upper footwall schist
Ore Schist Ore eqiuvalent schist (Lateral equivalent)	Lower orebody
	Intermediate schist
	Upper orebody
	Hangingwall schist
Broken Hill Quartzite	Dark/ Lower quartzite
	Median schist
	White/ upper quartzite
Namies schist	
Basal Gneiss	

Ryan et al. (1986)

Amphibolite and Leucocratic Gneiss
Aggeneys Ore Fm.
White Quartzire Fm.
Aluminious Schist Fm.
Pink Gneiss Fm.
Augen Gneiss Fm.

Stalder and Rozendaal (2004, 2005)

Formation	Member
Kories Fm.	Amphibolite
	Metapelitic to psammitic schist
	Conglomerate
Gams Fm.	A unit
	B unit
	C unit
Pella Quartzite Fm.	Dark ferruginous quartzite
	Metapelitic schist
	Massive white quartzite
	Metapelitic schist; lenses of massive sillimanite
Hoogoor Fm.	Leucocratic quartz-feldspar gneiss
Achab Gneiss	Porphyroblastic and banded qtz-flds gneiss

Mc Clung et al. (2002, 2007)

Subgroup	Formation
▨	Koeries Fm.
Kouboom	Gams Fm.
	Broken Hill Quartzite Fm. (Hotson Fm.)
Wortel	Pelitic schsist Fm. (Bloemhoek Formation)
	Pella Quartzite Fm.
	Namies Schist Fm
▨	Hoogoor Gneiss (Intruded by Aroams Gneiss)
▨	Achab Gneiss

Cornell at al. (2009)

	Formation	Rock
Bushmanland Group	Kories Fm.	Interlayerd conglomerate, qtz.-schist, metabasalt
Aggeneys Suite	Hoogoor Gneiss	Luecocratic metavolcanic
	Achab Gneiss	Banded and pophyroblastic "gray
Little Namaqualand Suite	Aroams Gneiss	Granodiorite
Bushmanland Group	Hotson Fm. (Gams Ore Member)	qtz.,luecogneiss, bo-sil schist, sulphide ore
	Skelmpoort & T'hammaberg	Dark & light quartzite, graphite schist semipelite
	Witputs	qtz, bo-sil gneiss &schist lenses of gahnite, calcsilicate, amp
	Wortel	bo-sil schist, dark & light quartzite, mg quartzite, amphibolite, calcsilicate

Figure 8. Stratigraphic sequence comparisons of the Bushmanland Group by various authors (Ryan et al., 1986; Stalder and Rozendaal, 2005; Bailie et al., 2006; McClung et al., 2006; Cornell et al., 2009).

The Wortel Subgroup is unconformably overlain by the Kouboom Subgroup, which comprises the Hotson and the Gams Formations (Stalder and Rozendaal, 2005c; McClung et al., 2007). The Hotson Formation consists of a package of dark-coloured quartzites, whereas the Gams Formation consists of aluminous schists and chemogenic sedimentary rocks (Rozendaal, 1986; Stalder and Rozendaal, 2005c; McClung et al., 2007). The Gams Formation is equivalent to the Aggeneys Ore Formation (Ryan et al., 1986).

The Gams Formation is the ore-bearing horizon in the Aggeneys-Gamsberg area and consists of a sequence of metalliferous metasedimentary rocks (Rozendaal and Stumpfl, 1984; Rozendaal, 1986; Stalder and Rozendaal, 2005; McClung et al., 2007). It hosts interbedded metapelite up to 100 m thick and is associated with the occurrence of barite deposits (Stalder and Rozendaal, 2005; McClung et al., 2007). In the Gamsberg Zn deposit, base-metal and Fe sulphides are mostly confined to quartz-sillimanite-muscovite-graphite and quartz-garnet-magnetite-amphibole rocks (Stalder and Rozendaal, 2005c). The current investigation is focused on the Gams Formation and it therefore will be discussed in detail in Chapter 3.

The Koeris Formation unconformably overlies the Gams Formation and is the topmost and most well-preserved sequence (Rozendaal, 1986; Stalder and Rozendaal, 2005). The Koeris Formation consists of a succession of psammitic schist of 400 to 500 m thick, interlayered with meta-conglomerates, ortho-amphibolite and quartz-feldspar-muscovite gneiss (Stalder and Rozendaal, 2002; Lacassie et al., 2007; McClung et al., 2007). The Koeris Formation represents the termination of the depositional cycle, with the upper amphibolite unit representing the minimum age of the Bushmanland Group rocks (Stalder and Rozendaal, 2005b; Cornell et al., 2009).

Section 3: The age, deformation and metamorphism of the Bushmanland Group

2.3.1 The age of the Bushmanland Group

The depositional age of the Bushmanland Group is constrained between 2.0 and 1.65 Ga (Moore et al., 1990; Stalder and Rozendaal, 2005; McClung, 2006; Bailie et al., 2007a; 2007b). According to Moore et al. (1990), the basement of the Bushmanland Group was reworked by the collision or crustal accretion that took place between 2.0 and 1.65 Ga, which affected only the basement and not the supracrustal sequence. SHRIMP U-Pb single zircon ages from detrital zircons in heavy mineral layers in a quartzite at Aggeneys presented ages of 2.0 to 1.8 Ga (Bailie et al., 2007a; 2007b). The Sm-Nd isochron ages of 1649 ± 90 Ma obtained from the Koeris Formation (amphibolite) are thought to represent a good estimate for the minimum age of the Bushmanland Group (Bailie et al., 2007a). The age of the Achab gneiss was determined from single zircon SHRIMP U-Pb to be 2.0 Ga, which represents the maximum ages, and this gneiss is therefore interpreted as the basement of the Bushmanland Group (Ryan et al., 1986; Watkeys, 1986; Moore et al., 1990; Reid et al., 1997; Stalder and Rozendaal, 2005c; Cornell and Pettersson, 2007; Bailie et al., 2007a; 2007b).

Cornell et al. (2009) reported the Achab Gneiss to be even younger than the Bushmanland supracrustal rocks, with an age of 1.16 Ga. This report further proposes that the base metal deposits are not older than 1 650 Ma, but younger than 1 285 ± 14 Ma. The ore horizon is interpreted as being older than 1 198 ± 10 Ma and 1 154 ± 18 Ma, derived from detrital zircons found in the unconformably overlying Koeris Formation and almost certainly older than the 1 130 ± 35 Ma age of the Koeris Formation metabasalts. Cornell et al. (2009) argue that the older Bushmanland Group, including the sedimentary-exhalative Cu-Pb-Zn-Ag ore, was formed in a stable continental basin prior to the Okiepian collision event at 1 200 Ma. Thereafter, the younger group represented by the Koeris Formation formed after the collision at about 1 130 Ma.

The ages of the Bushmanland Group are obscured by the deformation and the unclear structural contact relationship between the gneisses and metasedimentary rocks (Bailie et al., 2007a). Many authors (Moore et al., 1990; Stalder and Rozendaal, 2005c; McClung, 2006; Bailie et al., 2007a; 2007b) still prefer the minimum ages of the Koeris Formation (1 650 Ma), and the issue of the maximum ages and the basement of the Bushmanland Group remains a subject of controversy.

2.3.2 The deformation and metamorphism of the Bushmanland Group

The Bushmanland Group, as part of the Namaqua-Natal Mobile Belt, is a poly-deformed and metamorphosed region (Rozendaal, 1986; Ryan et al., 1986; Rozendaal and Stalder, 2005a; 2005b; 2005c; McClung et al., 2007). The structural complexity, multiple deformation and high-grade metamorphism have resulted in a complicated tectonic model for the Bushmanland Group, especially in the Aggeneys-Gamsberg ore district (Bailie et al., 2007a; 2007b). Two tectono-magmatic events, the Kibaran event (1 220 to 1 170 Ma) and the Namaquan event (1 060 to 1 030 Ma) are responsible for the architecture of the Bushmanland Group (Moore et al., 1990; Robb et al., 1999; McClung et al., 2007).

Ryan et al. (1986) have presented a complete image of the deformation events of the Bushmanland Group using multiple folding as structural evidence. F_1 deformation is characterised by isoclinal folds with sharp tapering hinge zones. F_2 deformation folds are isoclinal and display rounded hinge zones. F_3 deformation is considered to be responsible for the large-scale, open, asymmetric, synformal and antiformal structures and, most importantly, it is recognised for the preservation of the supracrustal rocks of the Bushmanland Group. F_4 deformation is represented by north-northwest-trending monoclinal folds with steep limbs dipping to the east. F_4 deformation is responsible for deforming all pre-existing structures and its influence is mostly evident in the fold closure area of F_2 and F_3.

According to Rozendaal and Stalder (2002; 2005c) metamorphic conditions have been constrained by the presence of cordierite, sillimanite, K-feldspar, quartz and muscovite in the metapelites, with P-T conditions reaching 2.8 to 4.5 kbar at 630 to 670˚C. Textural evidence indicates that peak metamorphic conditions were contemporaneous with and outlasted the second deformation event, but D_2 was terminated before the onset of the third deformation event (Rozendaal and Stalder, 2005c). The formation of epidote at the expense of amphibole, the development of chlorite along existing foliation planes and newly recrystallised quartz in the late shear fabric are all due to the effects of retrograde metamorphism (Rozendaal and Stalder, 2005c). Both F_1 and M_1 where over-printed by the succeeding deformation and metamorphic events (Ryan et al., 1986).

Section 4: Local geology of the Gamsberg Zn deposit

2.4.1 The geology and stratigraphy of the Gamsberg Zn deposit

The geological understanding and stratigraphy of the Gamsberg Zn deposit has been developed over a period of 40 years since its discovery in the 1970s, with great contributions from work carried out in and around Aggeneys.

The Gamsberg Zn deposit, as part of the Mesoproterozoic Namaqua-Natal Mobile Belt, comprises multi-phase deformed and medium- to high-grade metamorphosed rocks (Rozendaal, 2008). The deposit is formed in a basin that was differentiated into reduced basin facies and oxygenated shelf facies (Stumpfl, 1979; Stalder and Rozendaal, 2004). The basin environment reflects a rapid change in the original depositional environment of sedimentation, and interplay of periods of clastic, carbonate and silica deposition, with pulses supplying ore solutions (Stumpfl, 1979; Stalder and Rozendaal, 2004). The base metal mineralisation is stratabound, pre-metamorphic, and hosted by a supracrustal sequence of quartzo-feldspathic gneisses, quartzite, and pelitic, psammitic and calc-silicate schists, and orthoamphibolite (McClung, 2007; Rozendaal, 2008).

Appendix 1a provides the detailed geology and stratigraphy of the Gamsberg Zn deposit. The map and stratigraphy were compiled by the Anglo American Exploration Division, but derived from various publications such as Joubert (1986); Rozendaal (1986); Colliston et al. (1989); Moore et al. (1990); McClung et al. (2007); and the South African Committee for Stratigraphy (SACS, 1980). The stratigraphy of the Gamsberg Zn deposit is no different from the stratigraphy of the Bushmanland Group, presented in section 2 of Chapter 2.

The Gamsberg Zn deposit's metasedimentary rocks are well preserved in the core of a large sheath-fold structure (Stalder and Rozendaal, 2005c; Rozendaal, 2008). Figure 10 is a simplified geological map of the Gamsberg Zn deposit and shows the East-West and North-South cross-sections of the Gamsberg Mountain. It also shows the interpolated sheath fold position and the "overturned limb" in the Gamsberg East orebody. The layers in the Gamsberg deposit dip towards the east at increasingly steep angles and eventually exceed 90˚, resulting in a moderately eastwards dipping layer in the east of the Gamsberg Zn deposit.

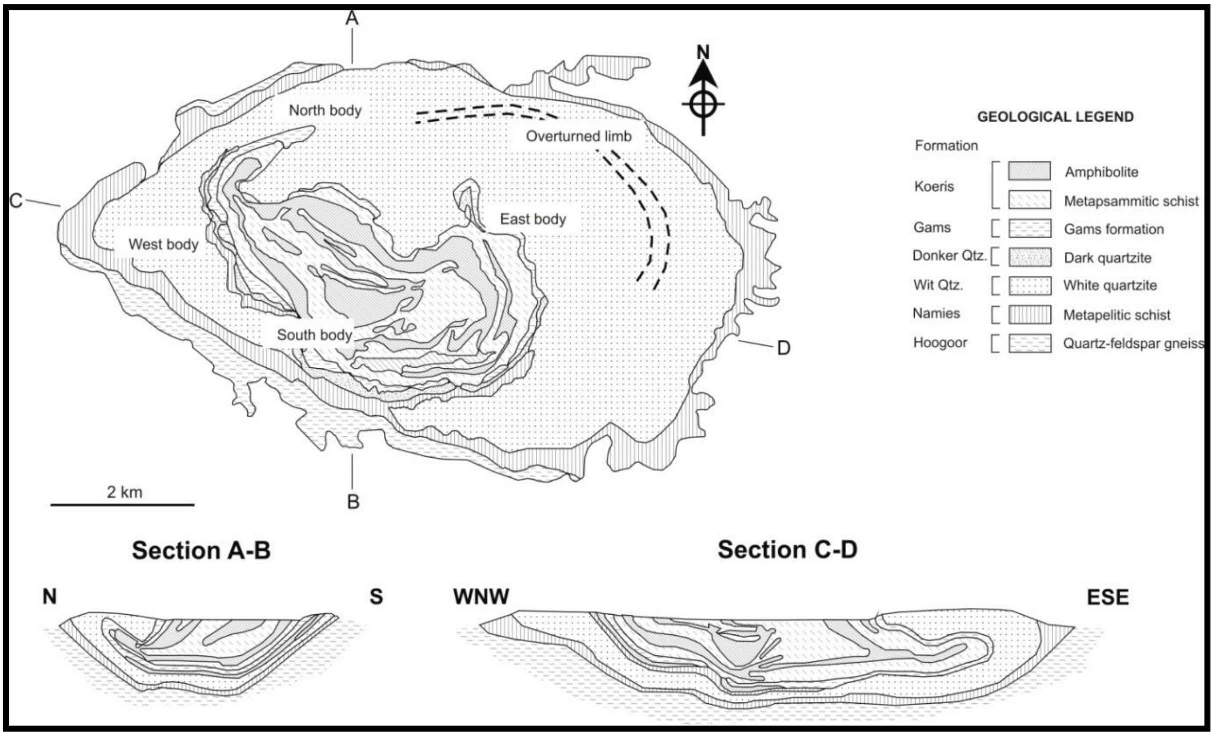

Figure 10. The general geological map showing different orebodies, the position of the overturned limb and N-S (A-B) and WNW-ESE (C-D) cross-sections of the Gamsberg Zn deposit (from Rozendaal, 2008; Schouwstra et al., 2010).

The structural evolution of the Gamsberg basin explains the current morphology and the preservation of mineralisation in a large sheath-fold structure of the Gamsberg Mountain (Voet et al., 2000). Sheath folds have extremely curvilinear hinge geometries, which result from the rotation of fold hinges, initiated in a direction orthogonal to shearing (Alsopa and Holdsworth, 1999). The sheath fold in the Gamsberg Zn deposit is developed mainly within the meta-sedimentary rocks under plastic conditions, consequently preserving the orebody. Weathering resistance of the white quartzite resulted in the current inselberg shape (Voet et al., 2000). As part of the stratigraphy of the Gamsberg Zn deposit, the Gamsberg East orebody is interpreted as structurally overturned, compared to the Gamsberg North orebody, as the ore horizon is located at the top of the large sheath fold (Rozendaal, 2008).

The use of the sheath folding for structural interpretation of the Gamsberg Zn deposit has recently been accepted, but the original idea is still used by some authors (Rozendaal, 1978; Rozendaal and Stalder, 2004; 2005a). For sheath folding, F_1 and F_2 folding are interpreted to have occurred simultaneously, forming a large sheath fold in the Gamsberg basin, and they were later folded by F_3 folding (Rozendaal and Stalder, 2004; 2005a).

The original interpretation by Rozendaal (1978) coincides with the regional structural interpretation of the Bushmanland Terrane (Voet et al., 2000). Figure 11 illustrates that the “Gamsberg Basin” is affected by at least three phases of deformation events, resulting in the apparently circular shape of the Gamsberg inselberg (Voet et al., 2000). F_1 forms a synformal shape with maximum stress in the north-south direction. F_2 folding is synformally superimposed on F_1, verging in an east-west direction. The nose of the F_2 sheath fold lies at a depth greater than 1 000 m beneath the White Quartzite Formation in the Gamsberg East orebody. F_3 folding is an open synform superimposed on the bowl shape of the “Gamsberg Basin”. The Gamsberg North orebody is structurally recognised by the well-exposed, ***m***-shaped folding, and indicative of F_3 folding (Voet et al., 2000).

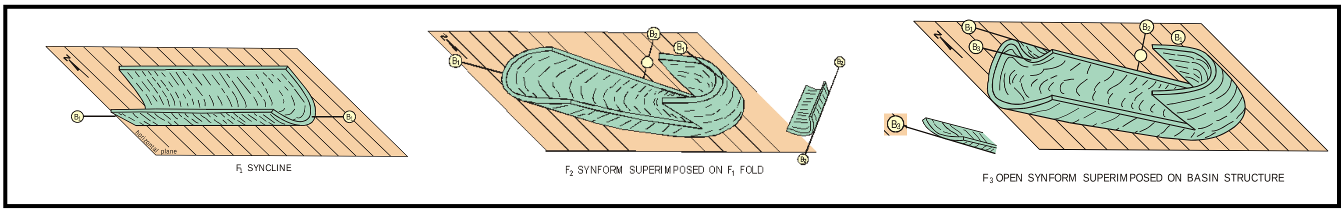

Figure 11: Structural evolution of the Gamsberg Basin (Voet et al., 2000).

Appendix 2 presents a detailed structural map and the interpretation of the Gamsberg Basin from geophysical surveys. A structural map published by N. E. Odling (1987) provides structural information of the interior of the basin, a thrust fault along the Gamsberg East orebody’s margin, projected fold axial planes, and NE-trending faults. A number of geophysical surveys were carried out on the

Gamsberg Mountain between 2005 and 2010 to provide and support structural interpretation at greater depths. These surveys include the Transient Electromagnetic (TEM), Airborne Electromagnetic (EM), Airborne Magnetic (AM), and SQUID surveys (Anglo American Plc, 2006a; 2006b).

2.4.2 The Gams Formation of the Gamsberg Zn deposit

The Gams Formation is the ore-bearing horizon of the Gamsberg Zn deposit (Rozendaal, 1978; 1986). It consists of about 100 m of metalliferous metasedimentary rocks, associated with the occurrence of barite deposits and base metal sulphides (Rozendaal and Stumpfl, 1986; Rozendaal, 1986; 2008; Rozendaal and Stalder 2005; McClung et al., 2007). The current resource estimation, in 2010, of the Gamsberg East orebody is about 60 Mt at an average grade of 8% Zn above 4% Zn cut-off grade, or alternatively 30 Mt at a higher average grade of 10% Zn above a 7% Zn cut-off grade (Reid and Harley, 2009).

The Gams Formation overlies a regionally developed sequence of aluminous schists and quartzite, which are interpreted as metamorphosed shallow-water black shale and quartz arenite respectively (Stalder and Rozendaal, 2005). The base-metal and Fe sulphides are mostly confined to quartz-sillimanite-muscovite-graphite and quartz-garnet-amphibole rocks (Stalder and Rozendaal, 2005b). The stratigraphic units of the Gams Formation are defined as a pelitic-chemogenic rock sequence, where a sedimentary exhalative genetic model has been invoked to account for the association of sulphide mineralisation (Rozendaal, 1986; Stalder and Rozendaal, 2004; 2005b; 2005c; Rozendaal, 2008).

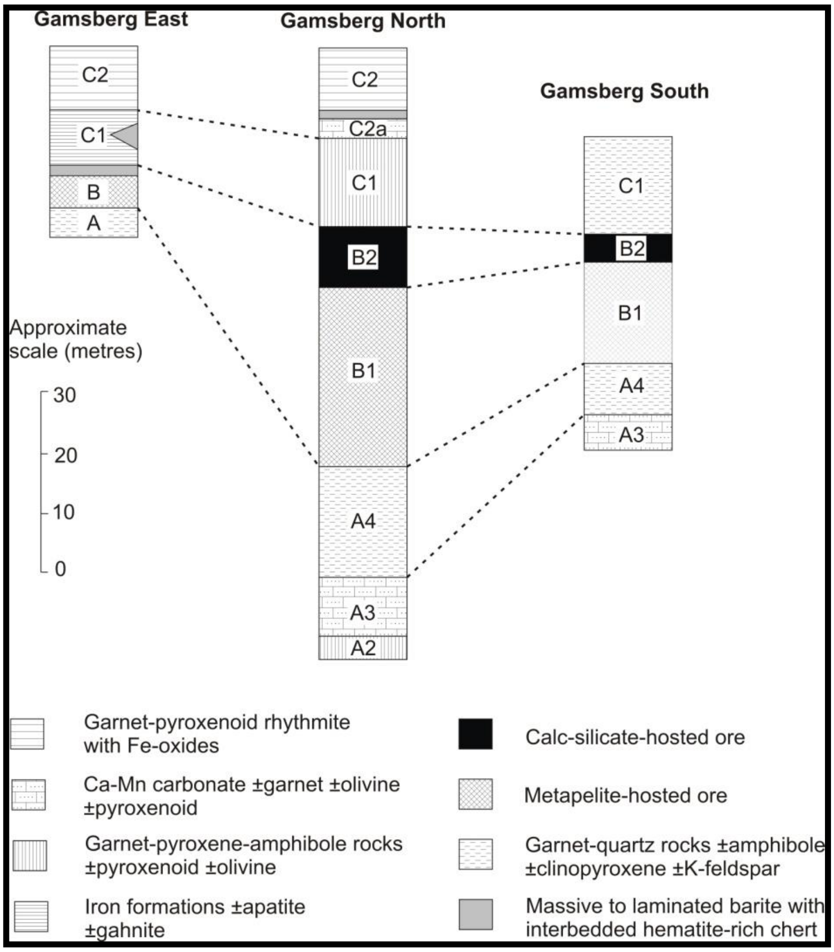

Figure 12. The lithostratigraphy correlation of Gams Formation units across the Gamsberg Zn deposit (modified from Stalder and Rozendaal, 2002, and Rozendaal, 2008).

Figure 12 presents the stratigraphic correlations between the well-studied and outcropping Gamsberg North orebody, and the Gamsberg South and Gamsberg East orebodies. This correlation is based on structural and petrographical evidence (Rozendaal, 2008).

The Gams Formation is divided into three members or units, from older to younger (A, B and C units), based on variations in the mineralogical and chemical composition of the lithologies (Rozendaal, 1986; Rozendaal and Stalder 2005b; Rozendaal, 2008; McClung and Viljoen, 2011). The A unit is an upward-coarsening unit comprising Fe-Mn silicates, impure marbles and quartz-garnet rocks (Stalder and Rozendaal, 2004; 2005b; Rozendaal, 2008; McClung and Viljoen, 2011). The B unit hosts the economic base-metal sulphide mineralisation and is subdivided into the lower graphite-rich metapelite schist, pelitic ore, and garnet-magnetite ore units (Stalder and Rozendaal, 2002; 2005a; 2005b; Rozendaal, 2008; Schouwstra et al., 2010). The C unit is upward-coarsening and overlies the ore horizon (McClung and Viljoen, 2011). It consists of Fe-Mn silicate and silicate-carbonate facies metasediments and an upper unit of garnet-pyroxenoid ± quartz rocks (Stalder and Rozendaal, 2005b; 2005c; McClung and Viljoen, 2011).

The Gamsberg Zn deposit has been affected by upper amphibolite metamorphic facies, and ductile and brittle deformation have resulted in textural changes and the remobilisation of the sulphide ore constituents (Stalder and Rozendaal, 2005a; 2005b; McClung and Viljoen, 2011). Such textural changes are observed throughout the Gamsberg Zn deposit and include grain-size increase, annealing of crystalline sulphide masses, formation of repeated compositional banding, aggregation of sulphide minerals into discordant areas of low strain, and presence of deformation textures like twinning, bend cleavage planes, undulose extinction and brecciation (McClung and Viljoen, 2011). These textures are typical of the “Broken Hill-type” deposit (McClung and Viljoen, 2011).

Chapter 3: Literature Review of the Gams Formation of the Gamsberg East orebody

Section 1: The Gams Formation in the Gamsberg East orebody

Rozendaal (2008) investigated the stratigraphy and the mineralogy of seven drillhole intersections of the Gamsberg East orebody. The investigations revealed that some units of the Gams Formation are absent within the Gamsberg East orebody (Rozendaal, 2008). The absence of these units resulted from tectonic complexities that have led to structural discontinuities, therefore complicating the spatial distribution of the units, particularly towards the east, proximal to the fold closure (Rozendaal, 2008). Textural features of the orebody and of a contact between the Gams Formation and hanging-wall and foot-wall schist indicate extensive tectonism and brecciation due to differences in rock competency (Rozendaal, 2008). Laterally, the thickness of the Gams Formation increases towards the east, as indicated by a significant increase in the thickness of the entire Gams Formation and a better definition of the basal A unit (Stalder and Rozendaal, 2005). The thickness variation may have resulted from the ductile behaviour during deformation, or from primary thickening due to basin deepening and/or due to non-development or lateral facies change (Stalder and Rozendaal, 2002; Rozendaal, 2008). Figure 13 shows a cross-section of the Gamsberg East orebody, indicating lateral variation and interpolation of the orebody.

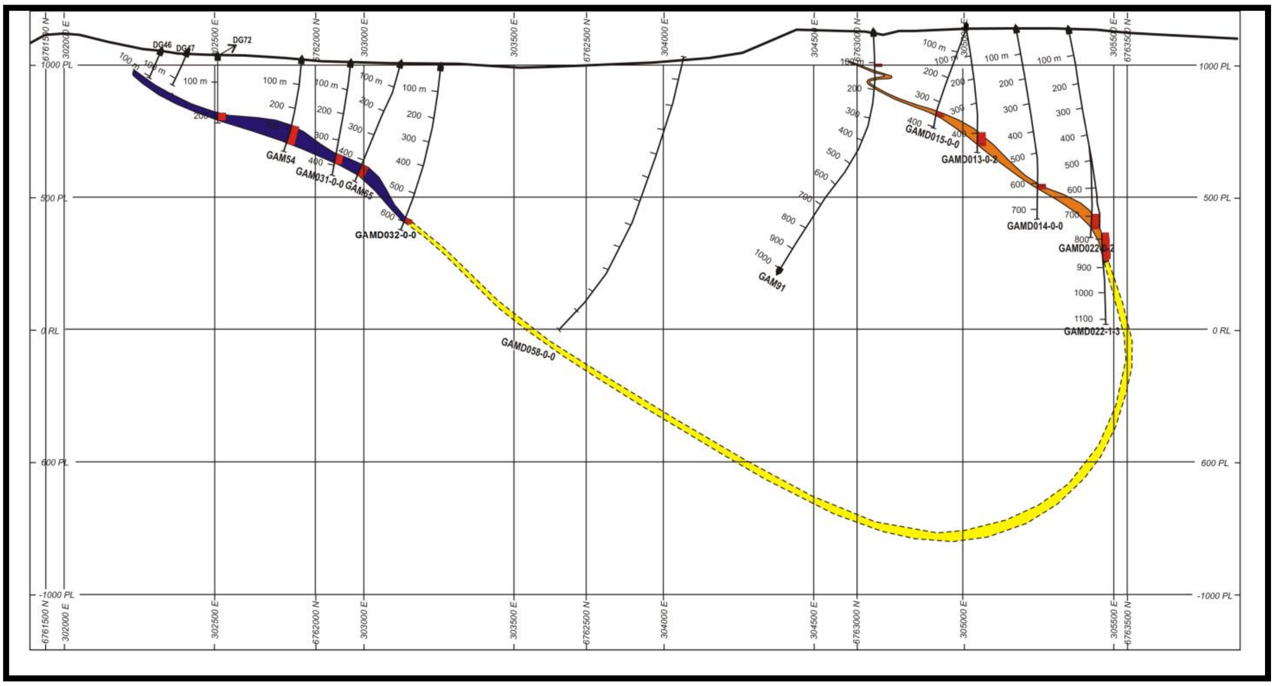

Figure 13. The northeast-southwest cross-section showing the lithological correlation and interpolation of the Gams Formation of the Gamsberg East orebody (courtesy of the Gamsberg Project Manual, 2010).

The sequence of the Gams Formation in the Gamsberg East orebody is inverse compared to the well-studied Gamsberg North orebody (Rozendaal, 2008). Unlike the North orebody, the East orebody is characterised by the top A unit overlying the B unit, and the C unit being at the base (Rozendaal, 2008). Table 1 provides a summary of the stratigraphy of the Gams Formation in the East orebody.

Table 1. The stratigraphy of the Gams Formation of the Gamsberg East orebody developed from seven drillholes investigated by Rozendaal (2008).

Unit	Assemblages	Lithology code
A2	Complex manganiferous garnet-pyroxenoids	GAQ
A3	Calc-silicate marble unit	CAS
A4	Manganiferous garnet quartzite	GQZ
B1	Quartz-muscovite-sillimanite-K-feldspar ± biotite schist Quartz-sillimanite-garnet-K-feldspar ore	PEL PEO
B2	Garnet-pyroxenoid-quartz-magnetite ore	MPO
C1	A series of quartz-magnetite-pyroxenoids-amphibole ± garnet rocks	MGQ, APM, PXG, etc.
C2	Garnetite rock with calderite-rhodonite-franklinite-magnetite	GTT, GMQ

The C2 unit is finely banded and a diagnostic marker, dominated by an orange to yellow garnet calderite end-member (Stalder and Rozendaal, 2005a). The C2 unit is highly manganiferous (20 wt% MnO), which results in the presence of pyroxmangite, rhodonite, minor tephroite and minor rhodochrosite (Stalder and Rozendaal, 2002; Rozendaal, 2008). Jacobsite, franklinite and magnetite contain insignificant Zn concentrations (Stalder and Rozendaal, 2005a; Rozendaal, 2008).

The C1 unit consists of magnetite quartzite and hematite quartzite (Stalder and Rozendaal, 2002). Magnetite and hematite quartzites both host minor sillimanite, Fe-Mn garnets and muscovite in the northern area, whereas towards the east they grade into quartz-garnet-biotite-magnetite-pyroxenes/pyroxenoids-quartz-magnetite-hematite rock and quartz-garnet-amphibole rocks with variable amounts of pyrrhotite and sphalerite (Rozendaal, 2008).

Two main ore classes have been identified using mineralogical assemblages: sulphidic meta-pelite ore (PEO) and magnetite-garnet-quartz ± pyroxenoid ± amphibole ore (MPO), occurring in B1 and B2 respectively (Rozendaal, 1985; Schouwstra et al., 2010; McClung and Viljoen, 2011). The ore of the B1 unit comprises less mineralised pelitic schist and mineralised meta-pelite ore, while the MPO ore of the B2 unit displays higher Zn grades (Rozendaal, 1985; Schouwstra et al., 2010; McClung and Viljoen, 2011).

The B2 unit thins toward the west and is mineralogically similar to the C1 unit (Rozendaal, 2007). However, it has a significantly higher sulphide content (pyrrhotite and sphalerite) (Stalder and Rozendaal, 2004; Rozendaal, 2007). The manganese content of sphalerite tends to reach higher levels in the upper parts of the garnet magnetite ore (Stumpfl, 1979). The B2 unit is gradational to the B1 unit, where oxidised conditions are changing to reducing conditions and which is marked by the abundance of garnets and the absence of pyroxenoids (Stalder and Rozendaal, 2004).

The B1 unit was deposited in a shallow, stratified, third-order basin, where anoxic bottom waters were overlain by oxic water column (Stalder and Rozendaal, 2004). The B1 unit comprises characteristic, moderately banded pelitic schists, with abundant quartz, sillimanite, muscovite, K-feldspar, pyrrhotite, sphalerite and minor galena. While this unit comprises the bulk of the Zn ore in volume, it is generally of lower grades than the B2 unit, and the sphalerite content decreases towards the base (Rozendaal, 2008).

Generally, the B unit is interpreted to represent original organic-rich mudstones (Stalder and Rozendaal, 2004).

The A4 unit is a garnet quartzite and is marked by the minor concentration of sulphide phases and the appearance of colourless Mn-Fe garnets (Rozendaal, 2008). The unit is discontinuously developed along strike, but is well developed in the North, West and South orebodies (Rozendaal, 2008). It marks the change from pelitic to chemogenic sediments in the footwall (Rozendaal, 2008).

The A3 unit is a banded calc-silicate rock with impure marble. It is a thick unit, but discontinuous along strike (Rozendaal, 2008).

The A2 unit is the most weakly developed unit and consists of quartz, pyroxenoids, garnets and grunerite (Rozendaal, 2008). The biotite gneiss is related to the A unit because it represents calcareous gneiss, marking the transition from marble to pelitic sediments (Rozendaal, 2008).

Manganese distribution in the Gamsberg East orebody was mapped by Rozendaal (2008) from seven drillhole intersections, using mineralogy and mineral chemistry. According to Rozendaal (2008), the metapelite rocks of the Gamsberg East orebody host the lowest Mn content, whereas garnet- pyroxene-, amphibole- and magnetite-bearing rocks host the highest Mn content, up to 30% Mn. Manganese in the pelitic ore occurs mainly within the sphalerite lattice. Manganese in the garnet-magnetite ore (MPO) occurs mainly within garnets, pyroxenoids (pyroxmangite) and amphiboles (Rozendaal, 2008; Schouwstra et al., 2010).

A study by Stumpfl (1979) concluded that the Mn distribution of BHT deposits, including the Gamsberg Zn deposit, represents primary Mn halos. Gertloff (2004), on the other hand, stated that typical Mn halos of the BHT deposits can be explained by the remobilisation of Mn into pore water under reducing conditions. However, Stumpfl (1979) previously reported that the maximum concentration of Mn frequently coincides with high concentrations of base metals, and the metamorphism in all deposits is considered to have been isochemical, with minimal migration of elements. The characteristic Mn concentration of the Gamsberg Zn deposit shows that the Mn content decreases towards the hanging and the footwall of the orebody, while the garnets, which contain a maximum Mn concentration, do not show any compositional variation (Stumpfl, 1979). This implies that rapidly varying conditions of sedimentation prevailed, and Mn therefore was introduced with metalliferous brines (Stumpfl, 1979). Figures 14 (a and b) present the MnO distribution of the Gamsberg deposit and its associated rocks of the Gams Formation (Rozendaal, 2008).

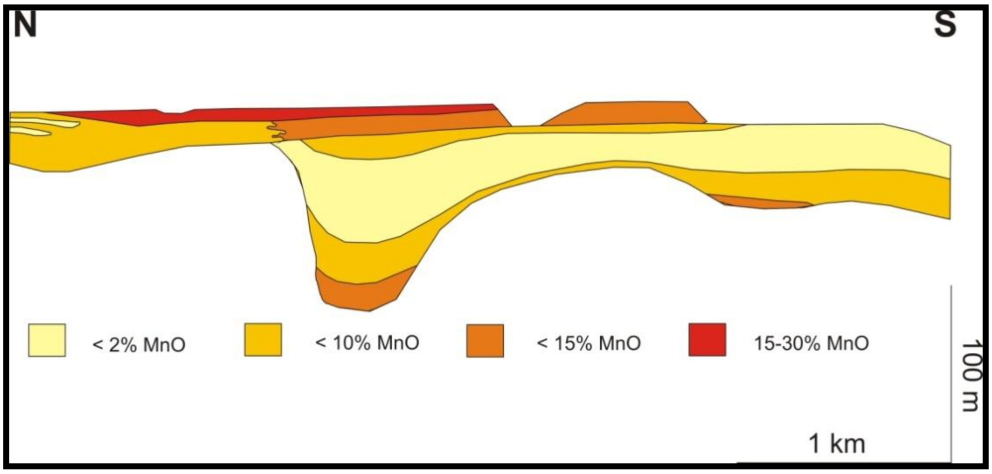

Figure 14a. Simplified manganese distribution with the rock distribution in the N-S section line of the Gamsberg East orebody (Rozendaal, 2008).

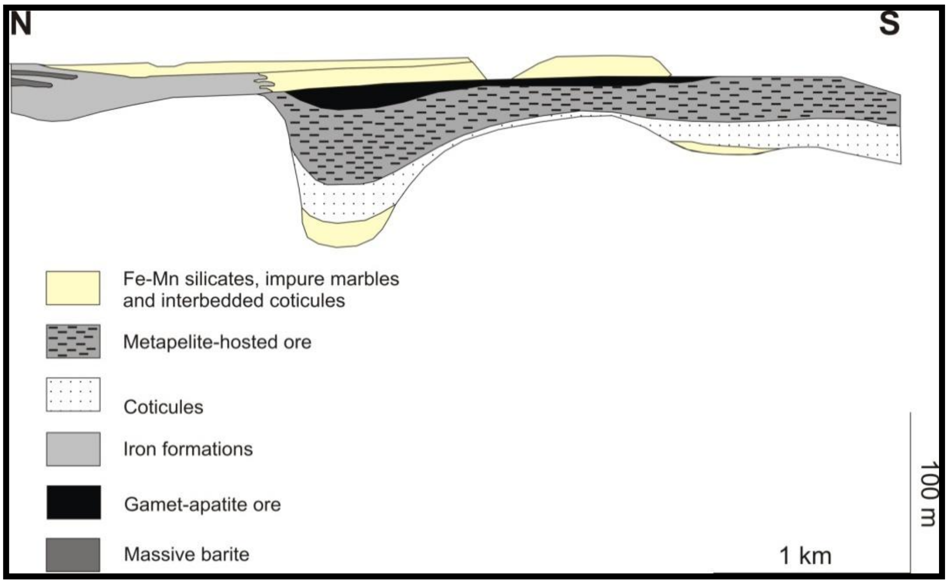

Figure 14b. A N-S cross-section of the Gams Formation of the Gamsberg East orebody (Rozendaal, 2008).

The sphalerite quality of the Gamsberg East orebody is a function of Fe and Mn substitution in its crystal structure, because extensive substitution of Zn by Fe and Mn produces a low Zn potential for metallurgical processing (Rozendaal, 2008; Schouwstra et al., 2010). Rozendaal (2008) and Schouwstra et al. (2010) have reported the Gamsberg East sphalerite compositions associated with the ore types:

Table 2. Average composition of sphalerite of the Gamsberg East orebody (Rozendaal, 2008; Schouwstra et al., 2010).

	Fe_%wt	**Mn_%wt**	**Zn average_%wt**
Meta-pelite ore: "pelitic ore"	9-11	Max of 7%	47.5
Garnet-magnetite ore	9-10	Max of 5%	55.5

In addition to various other approaches (isotopic studies, mineralogy, etc.) to explain the genesis and evolution of the Gamsberg Zn deposit, Stalder and Rozendaal (2002; 2004; 2005c) studied the characteristics of the rare earth elements. A positive Eu anomaly, observed only in the ore-bearing lithologies of the Gamsberg Zn deposit, implies that the deposit is pre-metamorphic and therefore indicates that relatively hot (200 to 250˚C) and reduced metal-rich brines were responsible for the formation of the base metal sulphide ores (Stalder and Rozendaal, 2002; 2004; 2005c).

Section 2: The effects of manganese on the metallurgical processing of the Gamsberg East ore

The zinc concentrate from the Gamsberg North ore contains between 2 and 3%wt Mn, and the prefeasibility studies recommended that the Gamsberg ore be processed on site and that the concentrate should not be sold to the markets, as a hefty penalty is imposed on the Mn content; to date, the zinc markets across the world can only tolerate a zinc concentrate with a maximum of 2%wt Mn concentration. Investigations into improving the Zn concentrate of the Gamsberg ore were carried out as early as 1975 (Ahlrichs, 1975). The challenges regarding the quality of Zn concentrate are brought about by the variation in sphalerite grain size, the wide variation in sphalerite chemistries between PEO and MPO, and the occurrence of alabandite (Schouwstra et al., 2010). Manganese remains a penalty factor for the Gamsberg ore, especially the Gamsberg East ore, as it hosts the highest Mn concentration compared to the rest of the Gamsberg North orebody (Rozendaal, 2008; Schouwstra et al., 2010).

Various options have been presented to improve the quality of the sphalerite concentrate, which improving the recoveries of sphalerite, concentrate cleaning and understanding the distribution of Mn within the Gamsberg Zn deposit (Schouwstra et al., 2010).

According to Schouwstra et al. (2010), the recoveries of sphalerite and Fe sulphides are excellent in both ore types, which shows that the sulphide minerals are generally liberated well in the concentrates. However, recoveries are nonetheless lower for the meta-pelite ore (Schouwstra et al., 2010). Four contributing factors to the lower Zn concentrate grade for meta-pelite ore are: finer sphalerite grain size, Fe sulphide contamination, difference in the Zn content of the sphalerite between meta-pelite and garnet-magnetite ores, and the variation in the Zn content of the sphalerite within the meta-pelite ore (Malysiak et al., 2007; Schouwstra et al., 2010). In order to improve the sphalerite recoveries, Malysiak et al. (2007) recommend that concentrate cleaning and optimised flotation should be taken into consideration. Due to differences in mineralogical characteristics between the garnet-magnetite ore and pelitic ore, the ore types have different flotation responses, therefore the ore types have a different recoveries (Schouwstra et al., 2010). The Zn recoveries in the garnet-magnetite ore are excellent, mainly because most of the Mn occurs within silicate minerals, and Mn is low within the sphalerite lattice (Schouwstra et al., 2010). In the pelitic ore, Mn occurs mainly in the sphalerite and less so in silicate minerals (Schouwstra et al., 2010).

Malysiak et al. (2007) and Schouwstra et al. (2010) investigated the flotation responses of 32 samples from 15 drillholes in the Gamsberg East and South orebodies. Two Zn recovery trends are recognised from the tests (Figures 17 and 18). In Figure 17, the garnet-magnetite ore trend shows less variable and higher Zn recoveries compared to the meta-pelite ore trends. Zinc recoveries of less than 10% were obtained at grades less than 10% Zn grade. Figure 18 shows the concentration of Zn and Mn in the final Zn concentrate. The manganese content of the meta-pelite ore was higher and increased with increasing Zn concentration, while the Mn content decreased with increasing Zn concentration in the garnet-magnetite ore. Lower levels of sphalerite recoveries in the meta-pelite ore were associated with the presence of alabandite (Schouwstra et al., 2010).

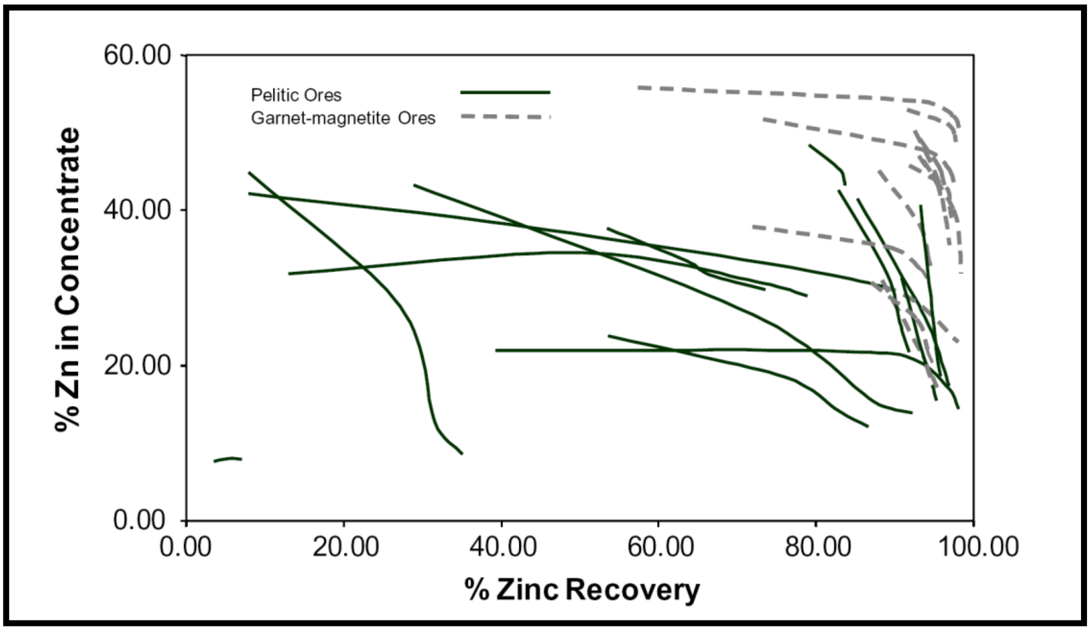

Figure 17. A graph of Zn recovery vs. Zn concentration in the final Zn concentrate of the Gamsberg East ore (Schouwstra et al., 2010).

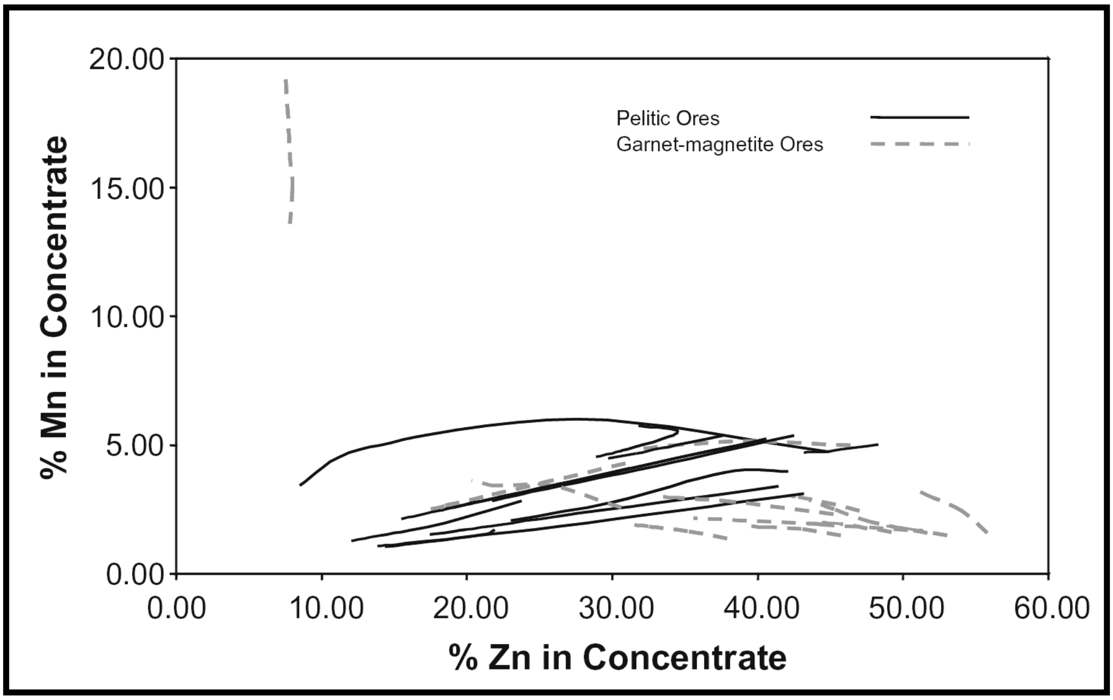

Figure 18. A graph of Mn vs. Zn concentration in the final Zn concentrate of the Gamsberg East orebody (Schouwstra et al., 2010).

The discovery of alabandite in the meta-pelite ore prompted further investigation. According to Schouwstra et al. (2010), the presence of alabandite in the Gamsberg East orebody is not widespread, although its distribution is not understood. ToF-SIMS (Time of Flight Secondary Ion Mass Spectrometer) and

XPS (X-Ray Photoelectron Spectrometer) were used to investigate the reagent absorption and surface analysis of the sphalerite and alabandite (Schouwstra et al., 2010). The meta-pelite ore was then split into two: normal meta-pelite ore (without alabandite) and meta-pelite + alabandite ore (Schouwstra et al., 2010).

Table 3: Summary of the results from surface analysis, reagent absorption and flotation response of sphalerite grains of different ore types (from Schouwstra et al., 2010).

Ore domains	Sphalerite surface analysis	Reagent absorption	Sphalerite flotation response
Meta-pelite ore	Higher Cu surface coverage	High	Good
Meta-pelite + alabandite ore	Poor Cu surface coverage	Low	Poor
Garnet-magnetite ore	Excellent Cu surface coverage	High	Excellent

Table 3 presents the results of the surface analysis, reagent absorption and the flotation responses of sphalerite in different ore types. The results indicate that the meta-pelite ore has a much higher copper surface coverage compared to meta-pelite + alabandite ore; as a result, meta-pelite ore has a good flotation response (Schouwstra et al., 2010). Alabandite from meta-pelite + alabandite concentrate also shows much higher copper surface coverage compared to the sphalerite grains (Schouwstra et al., 2010). The pelitic + alabandite ore also shows higher surface concentrations of copper and xanthate on the alabandite mineral surface compared to the sphalerite mineral surface, therefore the copper and xanthate surface coverage is much higher in the normal pelitic compared to pelitic + alabandite (Schouwstra et al., 2010). The preferential copper and xanthate adsorption on alabandite explains why the sphalerite mineral surface in the meta-pelite + alabandite ore has such low copper absorption and therefore low sphalerite flotation responses (Schouwstra et al., 2010).

The copper ion activation of sphalerite recovery is necessary for sphalerite recoveries because copper-xanthate complexes are more stable compared to copper-zinc complexes. Copper-xanthate complexes induce hydrophobicity of the sphalerite grains, which ultimately results in a high flotation response (Schouwstra et al., 2010).

Alabandite was found to adsorb the flotation reagents to the extent that total zinc recovery was reduced to 7% and the manganese concentration in the concentrate exceeded 14% (Malysiak et al., 2007).

Chapter 4: Research methodology

Section 1: Sampling techniques

4.1.1 Introduction

Over the period of five years from 2005, Anglo American Exploration Division (AAED) drilled a total of 146 ore intersections, which constitute 48 diamond core surface drillholes and 98 multiple deflected drillholes, in the Gamsberg East orebody. All drillhole samples (core, crushed and pulp samples) are stored safely at the Gamsberg Core Archives in Aggeneys.

Appendix 1b presents the section plan of the Gamsberg East orebody, showing the collar position and drillhole traces of most of the drillholes drilled between 2005 and 2010. It also shows the sulphide ore-oxide BIF transition boundaries and fold axial trace of the overturned fold limb located in the Gamsberg East orebody. This section plan also shows the drillhole positions of sampled drillholes.

4.1.2 Sampling procedure

Four drillholes were selected to investigate the outlined aims of the study: drillholes *GAMD033-2-4*, *GAMD041-1-3*, *GAMD045-0-0* and *GAMD054-2-2* (see Figures 19 to 22). The selection of these drillholes was based on existing ICP-MS whole-rock geochemistry and the geological logging database of the samples from the Gamsberg East orebody. Five categories were used to select the four drillholes, namely (see Appendix 1b for the position of the chosen drillholes):

- The drillholes should be representative of the Gams Formation,
- The drillholes should host varying bulk rock Mn concentrations including low, medium and high Mn content,
- Alabandite should be present in some drillholes and absent in others,
- Samples should be taken from the previous sampling intervals used for AAED, and
- Sampling of drillholes should cover a longitudinal section of the Gamsberg East orebody.

Drillholes *GAMD033-2-4* and *GAMD054-2-2* were selected due to the occurrence of alabandite and the high Mn concentrations of the ore intersection – greater than 8 %wt Mn. Drillhole *GAMD041-1-3* was selected due to the absence of alabandite and the relatively high to medium Mn content of between 3 %wt and 8 %wt. Drillhole *GAMD045-0-0* was selected due the absence of alabandite and the low Mn concentration, of less than 2 %wt Mn.

Although only two drillholes were selected that contained alabandite, there are drillholes that are known to contain alabandite. Table 4 present other drillholes whch alabandite was visually observed and estimated during core logging.

Table 4. Other drillholes from the Gamsberg East orebody known to contain alabendite.

Drillhole	Drill core visual estimation
GAMD026	Up to 5% alabandite
GAMD027	Up to 25% alabandite
GAMD029	Alabandite present
GAMD037	Up to 4% alabandite
GAMD044	Up to 10% alabandite

Appendix 3 presents the geological information and sample information tables of the four sampled drillholes. Consistency and continuity were maintained, therefore the same drillhole ID, sample ID and lithology code classification scheme and mineral nomenclature that were used by AAED are used in the present investigation.

About 10 cm long, half NQ core size (47.6 mm diameter) hand specimen samples were collected from the core boxes. The hand specimen samples were used to prepare polished thin sections, as well as polished sections for petrographic work and for mineral chemistry analysis. The crushed samples and pulp were re-sampled to be used for the preparation of the XRF and XRD analysis.

Figures 19 to 22 show the lithological logs, rock names, relative sample positions and codes of the four sampled drillholes.

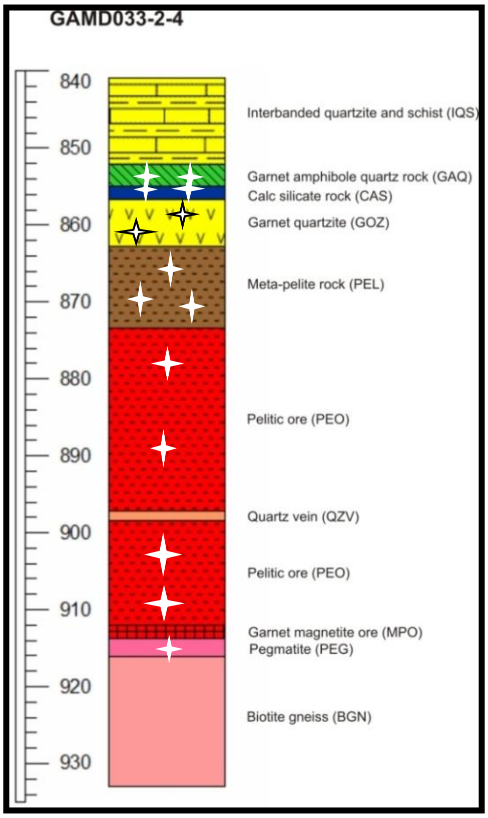

Figure 19. Lithological log, rock description and rock codes of drillhole *GAMD033-2-4 and relative sample positions*.

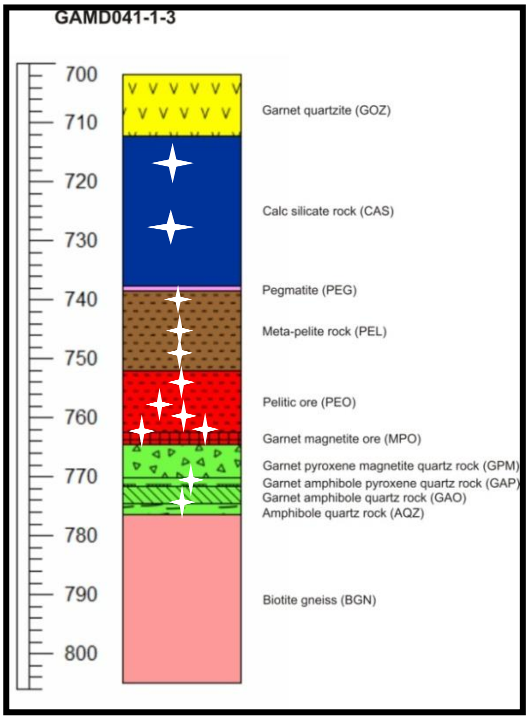

Figure 20. Lithological log, rock description and rock codes of drillhole *GAMD041-1-3 and relative sample positions*.

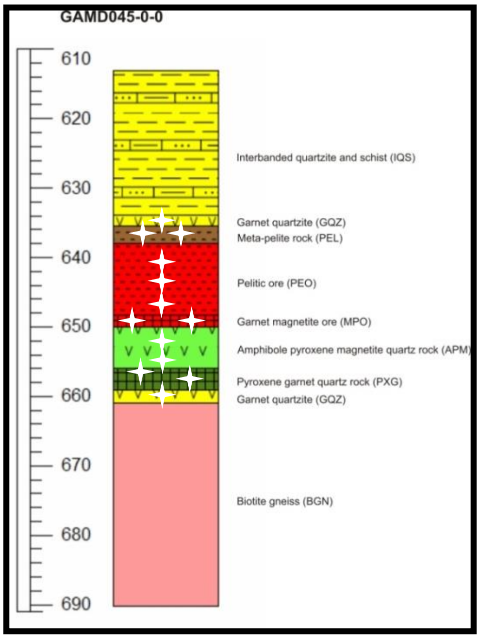

Figure 21. Lithological log, rock description and rock codes of drillhole *GAMD045-0-0 and relative sample positions*.

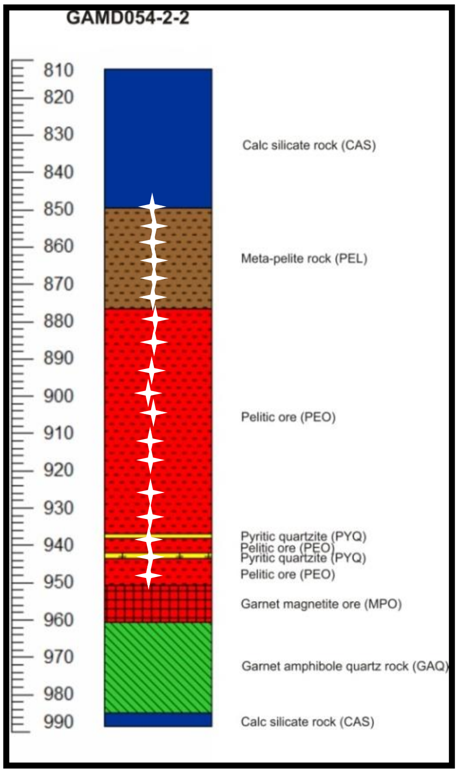

Figure 22. Lithological log, rock description and rock codes of drillhole *GAMD054-2-2 and relative sample positions*.

Section 2: Analytical techniques

4.2.1 Introduction to the geochemical database of the Gamsberg East deposit

Two sets of whole-rock geochemical data were used in this investigation. The first set was analysed at the ALS CHEMEX Laboratories in Johannesburg, using ICP-MS (Inductively Coupled Plasma Mass Spectrometer) and ICP-AES (Inductively Coupled Plasma Atomic Emission Spectrometer) techniques for major and minor element analysis respectively. The dataset consists of 6 000 analyses of the Gamsberg East samples, including a fraction of QAQC (Quality Assurance Quantity Control) samples. All samples were analysed using method code ME-ICP41 and ME-OG46 for 35 elements by Aqua Regia acid digest (Claassen, 2010). Method code ME-OG46 was applied to samples with elements Ag, Cu, Pb and Zn above the detection limit of the ME-ICP41 method code (Claassen, 2010).

The second dataset consisted of four surface drillholes selected for the current investigation. Sixty (60) samples were selected from the four drillholes, and whole-rock chemistry data was generated at the Stoneman XRD-XRF Facility at the University of Pretoria using X-ray techniques. The reason for resampling and reanalysing the samples from the four drillholes for whole-rock geochemistry is because of the absence of silica (SiO_2) from the ICP dataset. Silica content is important because of the approach of the investigation to understanding the relationship between silicate and sulphide minerals. The ICP dataset was also used to validate the XRF data. Whole-rock geochemistry, mineralogy and mineral chemistry were analysed using XRF (X-ray fluorescence), XRD (X-ray diffraction) and EMPA (Electron Microprobe Analyser) techniques respectively.

4.2.2 XRF and XRD techniques for whole-rock geochemistry and bulk mineralogy

XRF spectroscopy is used to determine the bulk chemical composition of a sample with UniQuant (a fundamental parameter software), enabling the qualitative and quantitative analysis of unknown samples. The Quantus software program is used when material samples are fused, reporting qualitative results, and UniQuant is used to report semi-quantitative analysis (Loubser and Verryn, 2008).

The XRF technique has the capability to analyse elements from fluorine to uranium, with the detection limit varying from 0.5 ppm for heavier elements to 100 ppm for lighter elements. With a fundamental parameter approach, every element in a sample is analysed to enable accurate matrix corrections (Loubser and Verryn, 2008).

Sulphide materials are among the materials that are considered difficult to prepare and analyse, therefore sulphide materials need to be oxidised prior to fusion (Willis, 2010). Sulphide samples are difficult to analyse because they do not fuse very well with lithium borate and are best fused prior to analysing. Ideally, oxidation and fusion operations should be combined in a single procedure (Willis, 2010). The fusion technique minimises particle size effects that could cause problems during the measurement process (Loubser and Verryn, 2008). The sulphide materials are risky to process in platinum crucibles because a crucible can be ruined easily in a single fusion unless a safe technique is used (Willis, 2010).

The X-Ray powder diffraction (XRD) technique is used to determine the crystalline phase(s) present in a material sample. The samples are analysed using a PANalytical X'Pert Pro powder diffractometer with X'Celerator detector, and variable divergence and receiving slits with Fe-filtered Co-K_α radiation. The samples are scanned at the required 30^0 angle ranges. The back-loading preparation method is used for sample preparation (Loubser and Verryn, 2008).

The phases are identified using the X'Pert Highscore Plus software program. The quantification of relative phase amounts is estimated by the Rietveld Method using the Autoquan Rietveld software program. Although each phase has unique powder diffraction, it is possible to distinguish between compounds because the diffraction method is sensitive to crystal structure and not just to composition. It also is possible to distinguish between different polymorphs of the same compound. The intensity of each component's pattern is proportional to the amount present (Loubser and Verryn, 2008).

In order to evaluate the accuracy and precision of the XRF technique, the reproducibility of the XRF instrument was measured by recording the analysis of the standard the lab used in the analysis of the 58 samples. The rock samples were split into two batches and one lab standard analysis was inserted between the batches for both major and trace element analysis. Seven and five lab standard analyses were recorded for the major element geochemistry prior and after the analysis of the rock samples respectively. Nine and ten lab standard analyses were recorded for trace element geochemistry before and after the rock sample analysis respectively. For major element geochemistry, seven analyses of the lab standard were recorded in one analysis. Due to time constraints on the XRF machine and cost-related issues it was not viable to analyse the lab standard for a short interval of samples, but overall the reported errors in a form of standard deviation satisfy the reproducibility of the XRF instrument. The limit of detection for the instruments also is reported and, together with instrument errors, provides with true limit of the instrument and the precision of the XRF results.

4.2.3 Petrographic investigation

Seventy-four polished thin sections and 51 polished sections were prepared at the Stoneman XRD-XRF Facilities at the University of Pretoria. The sections were used for mineral phase identification and textural evaluation using light microscopy, backscattered imagery and mineral chemistry analysis. Transmitted light Nikon Eclipse 50í POL was the type of light microscope used to investigate the microscopic properties of the prepared samples.

The polishing of the samples presented a challenge, mainly because of the differences in hardness between mineral grains, like quartz, galena and pyrrhotite, and soft minerals like sphalerite and alabandite. Pitting and the varying relief of mineral grains are typical signs of bad polishing. The other challenge was the oxidation of sulphide minerals like pyrrhotite and alabandite, therefore samples were kept in a vacuum container at all times to avoid having to re-polish often, which can result in losing some mineral species. The use and type of lubricant is important because water-based lubricant breaks down some mineral phases, especially retrogress minerals like micas (including chlorite) and clays, thus it is important to know the type of lubricant to be used.

High quality images of the mineral grains, representative of the textural characteristic of the Gamsberg East orebody, were captured using a high magnification camera installed on the light microscope. The light microscope has magnification limits, therefore for further textural evaluation of the very fine textures, SEM (Scanning Electron Microscopy) technique was instead used.

A diamond marker installed on a light microscope (Nikon Eclipse 200) was used to mark and reference the mineral grains that were chosen for mineral chemistry analysis.

4.2.3 Scanning Electron Microscope (SEM)

Two SEM instruments were used to capture backscattered and secondary electron images for evaluating the textural relationships and identification of mineral phases. The instruments are available at the Microscopy and Microanalysis Laboratory of the University of Pretoria. All samples were carbon coated prior to loading into the instruments.

The Joel JSM-5800LV Scanning Electron Microscope installed with an Energy Dispersive Spectrometer (EDS) detector was used to produce backscattered images and the semi-quantitative analysis of the mineral grains. The working conditions were set to 20 kV energy, with a working distance of 12 mm (BE/C WD1/12 mm). Energy Dispersive Spectrometer analysis was used to rapidly identify mineral phases using chemical composition. Low count-rate, X-ray collimation, extraneous noise and poor spectral resolution, especially regarding peak overlapping, were among the disadvantages of EDS, hence it is a semi-quantitative technique compared to WDS (Wavelength Dispersive Spectroscopy).

The ZEISS Ultra Plus 55 is a Field Emission Gun SEM instrument that is used to capture high resolution secondary electron images to observe sulphide mineral intergrowths. The working conditions were set to 5 keV EHT (electron high voltage) at a working distance of 3.2 mm.

4.2.4 Electron Microprobe Analyser (EMPA) for mineral chemistry analysis

The CAMECA SX 100 is an EMPA instrument available at the Stoneman XRD-XRF Facility of the University of Pretoria. The EMPA technique is used to quantitatively determine the chemical composition of solid materials and qualitatively map element distribution in a material (Reed, 1993; Cherniak et al., 2010). EMPA analysis is considered a non-destructive technique that generates characteristic X-rays by a focused electron beam that bombards and interacts with solid materials (Cherniak et al., 2010). The instrument is equipped with a Wavelength Dispersive Spectrometer (WSD) detector. The instrument is also equipped with the functions of the SEM, and backscattered electron and EDS detectors.

WDS utilises Bragg diffraction through a diffracting crystal to disperse the wavelengths of characteristic X-rays (Reed, 1993). For complete wavelength coverage, the instrument is equipped with multiple spectrometers with different crystals (Cherniak et al., 2010). The standard crystals on the CAMECA SX100 are LIF, PET, TAP and PC3. LIF (Lithium fluoride) is a standard crystal for short wavelengths of less than 3 Armstrong. PET (pentaerythritol) is a standard for the intermediate wavelengths and has a high reflectivity and large thermal expansion coefficient. TAP (thallium acid phthalates) is a standard for long wavelengths and has very high reflectivity. PC3 was not used in this case.

Samples are required to be coated prior to analysis. Non-coated samples will charge when placed on the path of the electron beam, thereby causing the deviation of the electron beam as well as catastrophic decharging (Reed, 1993). Carbon is a suitable choice for coating because its low atomic number causes minimal effects in the X-Ray spectrum, therefore producing the most accurate quantitative analysis (Reed, 1993).

An acceleration voltage of 20 kV with a beam current of 20 nA were used to analyse sulphide and silicate minerals. Three spectrometers were used for analysing Mg, Al, S, Ti, V, Cr, Mn, Fe and Zn in pyrrhotite, pyrite, sphalerite and alabandite grains. Four spectrometers are used to analyse Na_2O, MgO, Al_2O_3,

SiO_2, K_2O, CaO, TiO_2, Cr_2O_3, MnO, FeO and ZnO in garnets, micas, pyroxenes, amphiboles and oxide mineral phases like magnetite, rutile, etc.

The EMPA technique quantifies the elements or molecules by comparing the intensities of X-ray lines from the sample with those of known standards. There generally are two types of errors that could be inherited when using EMPA, namely systematic and random errors. Random errors result from the sampling methodology and the condition of the sample being analysed, while systematic errors are related to the capability of the instrument to produce precise and accurate data.

The intensity measurement (number of counts) requires certain instrumental corrections, such as background subtraction and matrix corrections, commonly in the form of ZAF (atomic number, absorption and fluoresce) corrections. These are typical sources of systematic errors. Other possible errors that could affect accuracy and precision for the quantification of the chemical analysis are variation in carbon coating across the polished section, excitation volume, instrument drift, overlapping of grains and overlapping of X-ray lines, and a change in climate in and outside of the lab, such as changes in temperature, wind velocity, etc. (Reed, 1993).

Section 3: EMPA data evaluation

4.3.1 Error evaluation for mineral chemistry data

The Electron Microprobe Analyser (EMPA) technique was used to quantify the chemical analysis of sulphide (alabandite, Mn-Fe-bearing sphalerite, pyrrhotite and pyrite) and silicate minerals (micas, amphiboles, garnets, pyroxenes, feldspars and clays) precisely and accurately. The sulphide minerals were analysed for Mg, Al, S, Ti, V, Cr, Mn, Fe and Zn, whereas the silicate minerals were analysed for Na_2O, MgO, Al_2O_3, SiO_2, K_2O, CaO, TiO_2, Cr_2O_3, MnO, FeO and ZnO. The analyses were reported in %wt, and then calculated to %atomic (%at) and moles (mol) for mineral formula calculations.

The variability or error, which is a standard deviation reported in Tables 5 to 7, is the measure of the ability of the instrument to reproduce the same results for the set-up conditions. To measure the reproducibility and precision of the EMPA instrument, a test was conducted in which each grain of alabandite, sphalerite and pyrrhotite was analysed ten times on the same spot. Limits of detection for the instrument are presented in Tables 8 and 9.

Table 5. Summary of descriptive statistics of reproducibility of the analysis of alabandite.

Alabandite							
N = 10	**Mn_%wt**	**Fe_%wt**	**Zn_%wt**	**S_%wt**	**Mn_mol**	**Fe_mol**	**Zn_mol**
Minimum	56.90	6.20	0	35.74	0.91	0.11	0
Maximum	57.59	6.37	0.03	36.35	0.92	0.11	0
Mean	57.33	6.27	0.01	35.99	0.92	0.11	0
Median	57.31	6.25	0.01	35.98	0.91	0.11	0
Mode	56.90	6.20	0	35.98	0.91	0.11	0
Std dev. (1σ)	***0.221***	***0.060***	***0.013***	***0.171***	***0.005***	***0.001***	***0***

Table 6. Summary of descriptive statistics of reproducibility of the analysis of sphalerite.

Sphalerite							
N = 10	**Mn_%wt**	**Fe_%wt**	**Zn_%wt**	**S_%wt**	**Mn_mol**	**Fe_mol**	**Zn_mol**
Minimum	7.00	10.48	48.06	34.38	0.12	0.19	0.68
Maximum	7.25	10.72	48.61	34.85	0.12	0.19	0.69
Mean	7.12	10.58	48.40	34.59	0.12	0.19	0.69
Median	7.12	10.55	48.46	34.52	0.12	0.19	0.69
Mode	7.04	10.53	48.47	34.38	0.12	0.19	0.68
Std dev. (1σ)	***0.080***	***0.082***	***0.177***	***0.163***	***0.001***	***0.002***	***0.005***

Table 7. Summary of descriptive statistics of reproducibility of the analysis of pyrrhotite.

Pyrrhotite							
N = 10	**Mn_%wt**	**Fe_%wt**	**Zn_%wt**	**S_%wt**	**Mn_mol**	**Fe_mol**	**Zn_mol**
Minimum	0	59.06	0	39.30	0	0.93	0
Maximum	0.02	59.71	0.03	39.64	0	0.94	0
Mean	0.01	59.35	0.01	39.40	0	0.93	0
Median	0	59.36	0	39.37	0	0.93	0
Mode	0	59.42	0	39.37	0	0.93	0
Std dev. (1σ)	***0.008***	***0.190***	***0.012***	***0.097***	***0***	***0.003***	***0***

Table 8. The limit of detection for the sulphide minerals as calculated by the instrument.

Sulphide minerals' limit of detection			
Elements_ppm	**Alabandite**	**Sphalerite**	**Pyrrhotite**
	Limit of detection	**Limit of detection**	**Limit of detection**
Mg	339	441	366
Al	325	423	342
S	680	763	720
Ti	414	466	435
V	524	592	552
Cr	515	527	476
Mn	571	497	482
Fe	597	491	542
Zn	760	945	782

Table 9. The limits of detection for the silicate minerals as calculated by the instrument.

Silicate minerals' limit of detection (σ= std dev.)	
Elements_ppm	**Limit of detection**
Na	110
Mg	292
Al	316
Si	372
K	388
Ca	346
Ti	438
Cr	464
Mn	446
Fe	445
Zn	696

4.3.2 Data processing using the statistical evaluation technique

About 2 500 data points of sulphide minerals and 545 of silicate and oxide minerals were analysed for mineral chemistry. Of the sulphide minerals, alabandite, sphalerite, pyrrhotite and pyrite were analysed, while mica minerals (biotite, muscovite and chlorite), amphiboles, garnets, pyroxenes, feldspars and clay minerals were the silicate minerals analysed. Rutile, pyrophanite, jacobsite, franklinite and magnetite were the oxide minerals analysed.

An exploratory data evaluation was used to clean the datasets. This technique involves data sorting, grouping and elimination. The sulphide minerals dataset was sorted into GOOD DATA and BAD DATA analyses. The GOOD DATA analyses were all the analyses with a Total %wt between 98.5 %wt and 101.5 %wt. The BAD DATA analyses were all the analyses with a Total %wt of less than 98.5 %wt and greater than 101.5 %wt. The GOOD DATA-BAD DATA criteria were based on the assumption that all elements of interest were analysed, and other elements that might be present are less significant or even below the detection limit. The assumption was based on analyses of alabandite, sphalerite and pyrrhotite that had been analysed or tested using the SEM installed with EDS (Energy Dispersive Spectrometer). Tables 10a and 10b show the summarised analytical results from the EDS analysis. Petrographic observations revealed that elements such as As, Ag and Pb, which were reported in alabandite and sphalerite, and were detected from inclusions of these minerals. Systematic errors such as spectral deconvolution (peak overlap), spectral artefacts and error limits of ± 2 %wt are some reasons why EDS is considered a semi-quantitative analysis.

Table 10a. Semi-quantitative analysis of sulphide minerals from the EDS analyser.

EDS semi-quantitative analysis: Sulphide minerals										
	n	**S %wt**	**Mn %wt**	**Fe %wt**	**Zn %wt**	**Pb %wt**	**Ag %wt**	**As %wt**	**Mo %wt**	**Sb %wt**
Alabandite	***19***	35.16	58.73	5.64	0.38		0.07	0.11		
Sphalerite1	***14***	33.57	7.86	11.09	47.24	0.16	0.01	0.01		
Sphalerite2	***5***	32.86	2.30	8.56	54.94	0.02				
Pyrrhotite	***38***	38.77	0.31	60.19	0.27	0.11	0.04	0.08		
Pyrite	***17***	53.01	0.25	46.00	0.48	0.21	0.01			
Galena	***8***	13.25	0.17	0.94	0.29	84.38	0.08			
Silver inclusion in alabandite1	***1***	21.30	3.80	31.30			31.10	0.04	1.40	10.70
Silver inclusion in alabandite2	***1***	14.20	20.5	4.70	0.02		60.40			

Table 10b. Semi-quantitative analysis of silicate and oxide minerals from the EDS analyser.

EDS semi-quantitative analysis: Silicate and oxide minerals										
	n	**O %wt**	**Si %wt**	**Al %wt**	**Mg %wt**	**Mn %wt**	**Fe %wt**	**Zn %wt**	**Ti %wt**	**Ca %wt**
Pyroxenes	***2***	44.90	23.40		7.55	9.20	14.00			
Garnet1	***15***	39.32	16.39	9.41	0.48	24.67	6.75	0.09		2.41
Garnet2	***2***	44.90	16.93	6.26	6.83	1.22	15.30	0.13		
Pyrophanite	***3***	27.20				21.37	0.09	0.01	31.37	
Mn-oxide	***1***	42.40		0.02		55.80	0.09			

The GOOD DATA was then grouped by minerals. This process was followed by eliminating the mixed and bad analyses and transferring them into the BAD DATA group. The BAD DATA group was further investigated using SEM backscattered images to inspect the position of the points, the quality of the surfaces and any other possible reason that might have introduced errors. The majority of the mixed analysis resulted from poor surface conditions and the position of the analysis point being too close to the mineral boundary. For silicate minerals that contain water, a maximum of 5 %wt H_2O was added. The minerals with a Total %wt between 98.5 and 101.5 %wt were accepted as part of the GOOD DATA group.

The GOOD DATA group was then used for statistical analysis, including descriptive statistics (central tendency), cumulative frequency distribution in the form of histograms and probability plots, scatter plots and, in some cases, box-plot analysis. Statistical analysis was coupled with interpretation.

In order to demonstrate the process of data cleaning, histograms (Figures 23 to 26) of S and Fe in sphalerite and Fe and Mn in alabandite were used to show the outliers and extreme values, which fall far outside 3Ϭ (standard deviation). These outliers and extreme values were investigated and then eliminated from the dataset. The graphs only demonstrate the cleaning process, and are not suitable for distribution analysis.

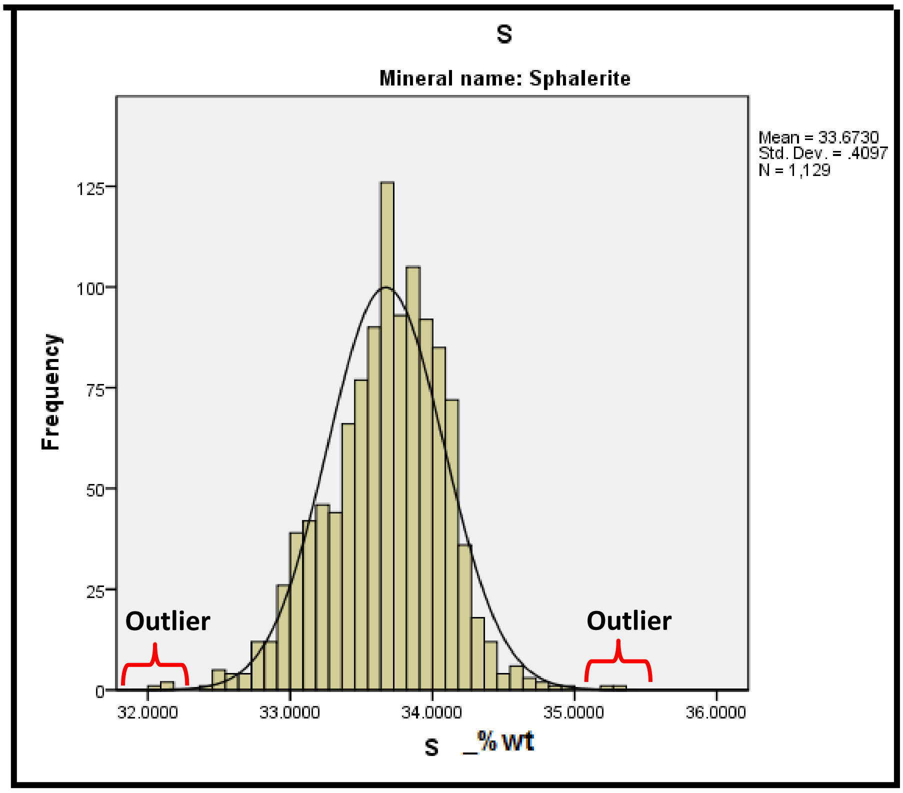

Figure 23. Histogram showing the distribution of the sulphur content of sphalerite and outliers.

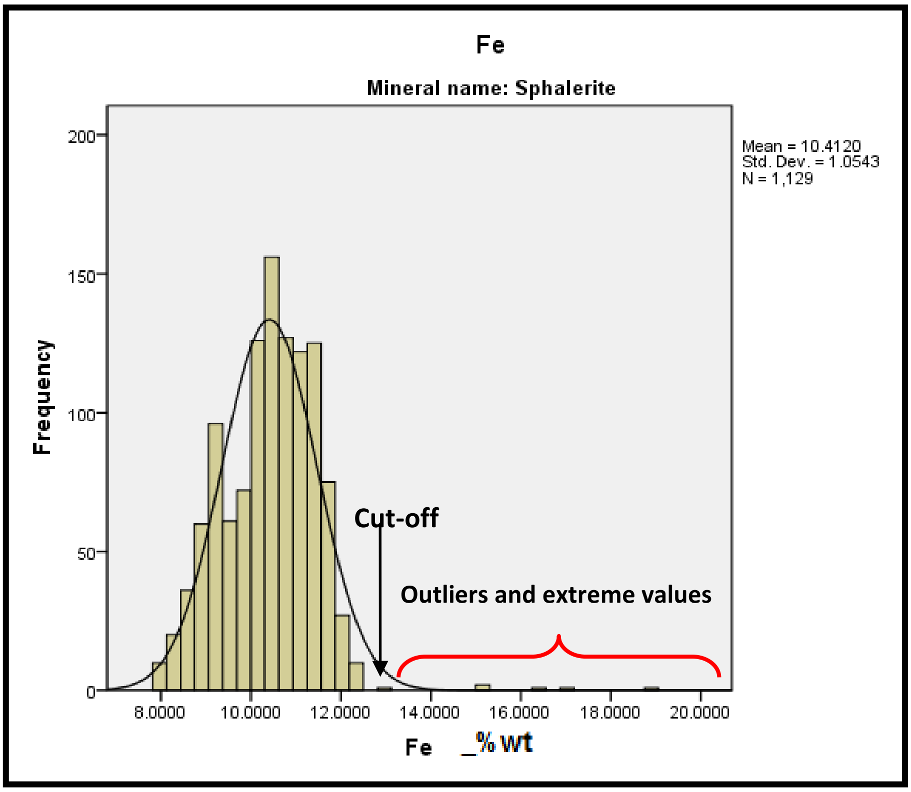

Figure 24. Histogram showing the distribution of the iron content of sphalerite and outliers.

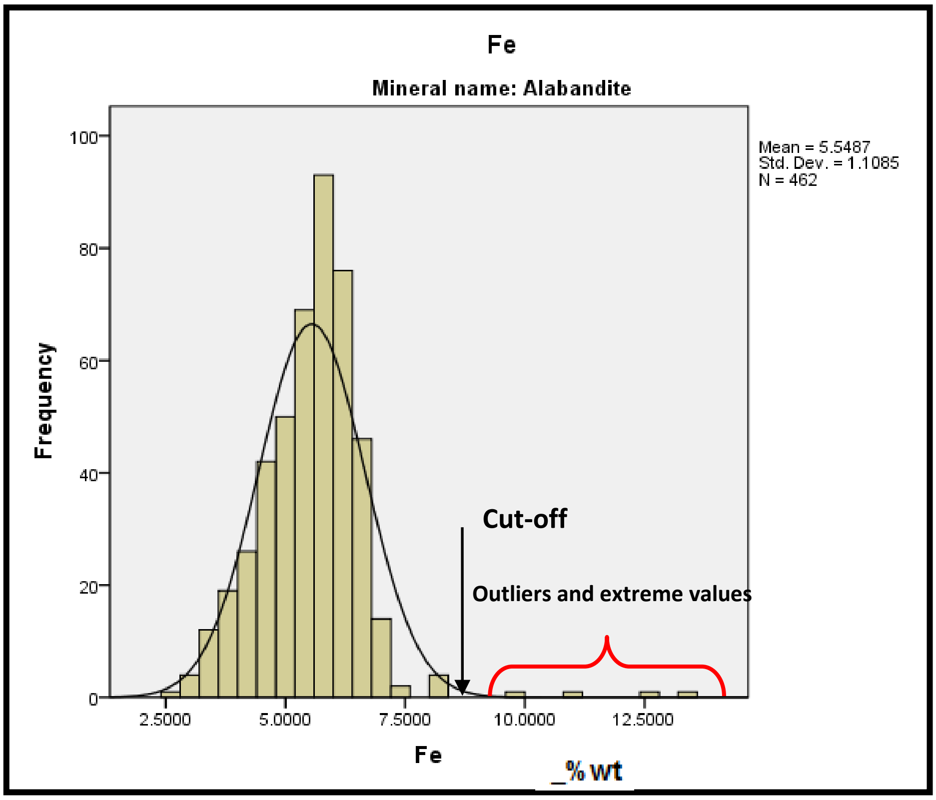

Figure 25. Histogram showing the distribution of the iron content of alabandite and outliers.

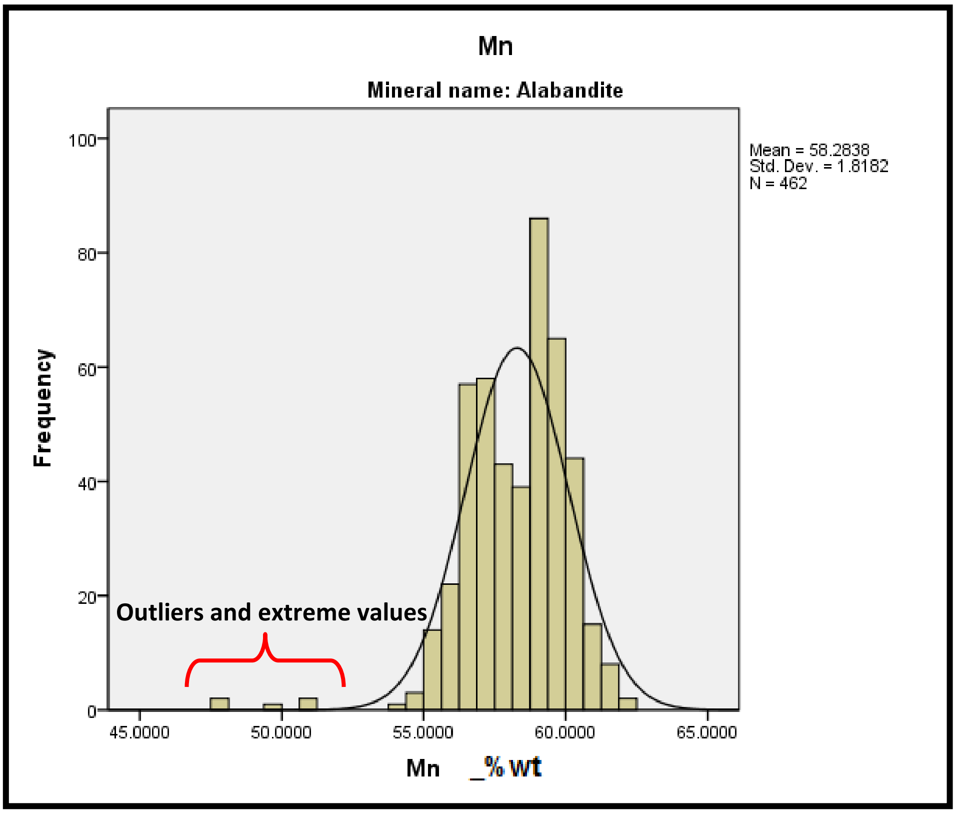

Figure 26. Histogram showing the distribution of the manganese content of alabandite and outliers.

Alabandite and sphalerite mineral chemistry analyses were the core of this study and will be discussed at length. There were 799 and 333 analyses of sphalerite and alabandite respectively. These analyses were separated into several categories according to mineral assemblages:

- sphalerite coexisting with alabandite
- alabandite coexisting with pyrrhotite
- alabandite coexisting with pyrite
- alabandite in silicate mineral matrix (not coexisting with other sulphide minerals)
- alabandite as exsolution lamella in other sulphide minerals

Chapter 5: Results

Section 1: Petrography, whole-rock geochemistry and mineralogy

5.1.1 Petrography

The four sampled drillhole intersections of the Gamsberg East orebody represent the Gams Formation around the fold closure on the eastern part of the Gamsberg Zn deposit. All four drillholes are proximal to the overturned fold hinge in the Gamsberg East orebody. The A unit from all drillholes generally consists of garnet-amphibole-quartz rock, calc-silicate rock and a garnet-quartzite “halo”. Sphalerite occurs mainly within the B unit, with only a very small amount present in some rocks in the C unit. The B unit is the economic unit and consist of pelitic schist, meta-pelite ore and garnet-magnetite ore. The C units consist of a series of garnet-, amphibole-, pyroxene-, quartz- and magnetite-bearing rocks, classified as BIF (Banded Iron Formation). The silicate minerals in the BIF occur in varying proportion, hence there is a variation in rock types (e.g. garnet-amphibole-magnetite-quartz rock (GAM), garnet-amphibole-pyroxene-magnetite-quartz rock (GAP), amphibole-magnetite-pyroxene-quartz rock (AMP), etc.).

Not all of the Gams Formation units is present in all four drillholes. The C unit is absent in drillhole *GAMD033-2-4*, but are well developed in the A and B units. The base of the B2 unit is in contact with a pegmatite, and the garnet-magnetite ore (MPO) is absent. Franklinite, jacobsite, arsenopyrite and alabandite are present in the garnet quartzite and pelitic schist. The Gams Formation intersection of drillhole *GAMD041-1-3* is well developed, with all units present. The A unit of drillhole *GAMD045-0-0* is only represented by a thin garnet quartzite unit, but the B and C units are well developed. The units in drillhole *GAMD054-2-2* are well developed and contain a duplication of calc-silicate rock, present within the A unit and below the C1 unit.

The development and variation in thickness of the units shows a pinch-and-swell form or structure. There is a general increase in unit thicknesses towards the fold closure in the NE direction, which coincides with the general NE plunge of the orebody.

The rocks of the Gams Formation are generally medium grained, foliated and banded. Pelitic schist is the most foliated rock unit, while meta-pelite ore is partly foliated and highly banded with remobilised pyrrhotite. Garnet-magnetite ore is occasionally banded, and granular. Meta-pelite ore contains nodules that are composed primarily of fine-grained quartz, feldspar, muscovite, biotite and clay minerals. Finer grains of pyrrhotite and sphalerite minerals are also present within these nodular shapes.

Three distinct sphalerite populations are observed in the hand specimen: light brown- (honey-coloured), reddish brown-, and very dark- (reddish black) coloured sphalerite. The light brown (honey-coloured) sphalerite is associated with remobilised textures. The reddish brown sphalerite is present throughout the ore-bearing rocks. The very dark sphalerite occurs mainly within the pelitic schist and the top part of the meta-pelite ore. It is mostly associated with the occurrence of alabandite, arsenopyrite and Mn-bearing oxide minerals, like franklinite and jacobsite.

The alabandite found at the Gamsberg East orebody is black in colour, has a metallic lustre and a black streak. It has been identified as coarse grained (vein-like texture in drillhole *GAMD054-2-2*), and also as medium-grained in some parts of the rock types. Alabandite occurs mainly within pelitic schist, but minor concentrations are present in calc-silicate rock, garnet-quartzite, and meta-pelite ore.

Appendices 4, 5a, 5b and 5c present detailed handspecimen descriptions, thin section petrographic descriptions, polished section petrographic descriptions and back-scattered images, respectively.

5.1.2 Whole-rock geochemistry datasets

The whole-rock geochemistry dataset consists of a pair of ICP and XRF analyses, made up of 57 samples. The dataset analysed by the ICP technique is historical whole-rock geochemistry data of the Gamsberg East samples, collected since 2005 by the Anglo American Exploration Division. The dataset consist of 32 elements, reported as elements in parts per million (ppm) and weight percentages (%wt).

The XRF dataset was collected for the purpose of the current investigation. It consists of major elements reported as oxides in weight percentages (%wt) and trace elements reported as elements in parts per million (ppm). The XRF dataset is used for two reasons:

1. To validate the ICP data so that a 3D model of manganese distribution in the Gamsberg East orebody can be generated using a 3D software package and geostatistical parameters for estimation purposes. There are 6 000 data entries in the ICP dataset from 146 Gams Formation drillhole intersections, whereas the XRF dataset consists of only 57 data entries from four drillhole intersections. As a result of the higher volume of data in the ICP dataset compared to the XRF dataset, the ICP dataset was the best candidate to generate a 3D model.

2. The XRF data was used to investigate the geochemical behaviour of the Gams Formation in the Gamsberg East orebody.

5.1.2.1 XRF and ICP validation

A statistical software package, IBM SPSS Statistics 21, was used to compute and present the information from the two sets of data. (See the HELP menu for all definitions and calculation parameters used by the software.) The analysis of histograms, descriptive statistics, box plots and scatter plots was used to show the compatibility of the XRF and ICP datasets and the geochemical behaviour of the Gams Formation of the Gamsberg East orebody.

Histograms

Statistical analysis of the data was executed for most elements to show the distribution of data. Figures 27 to 32 show only the distribution of SiO_2, TiO_2, Al_2O_3, MnO, FeO, and ZnO of the XRF analysis. The choice of elements to demonstrate the distribution of bulk-rock geochemistry is limited by mineral abundance in the lithological units of the Gams Formation, such as quartz, micas, rutile, magnetite, sphalerite, pyrrhotite and alabandite. These minerals are dominant in each lithological unit of the Gams Formation in the Gamsberg East orebody.

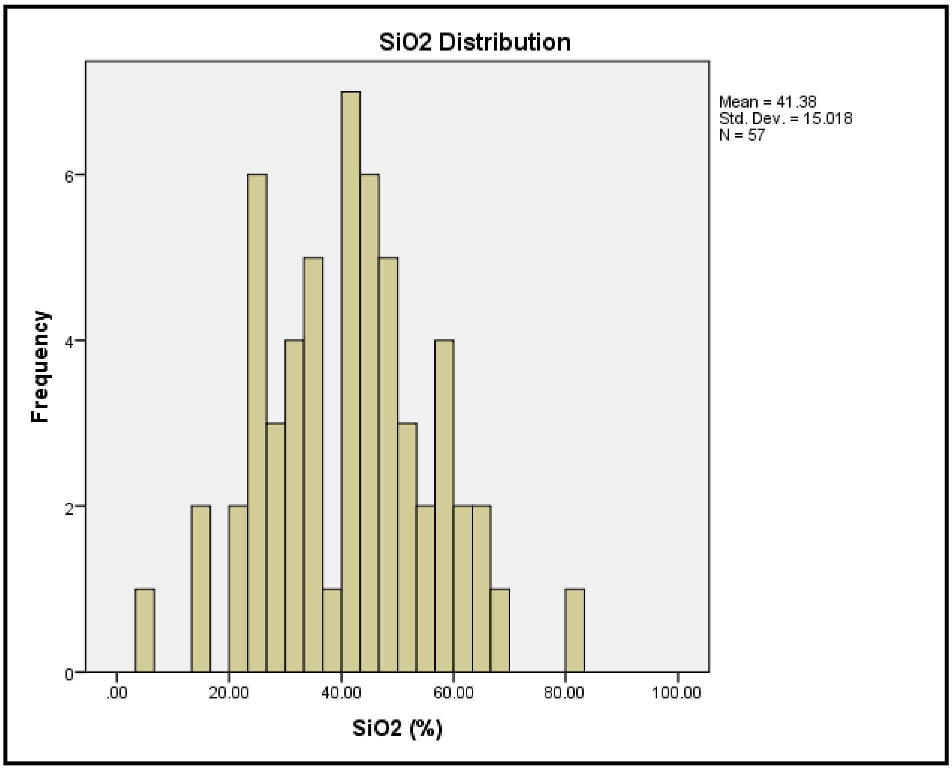

Figure 27. The histogram shows the distribution, mean and standard deviation of silica (SiO_2) (XRF) for all samples.

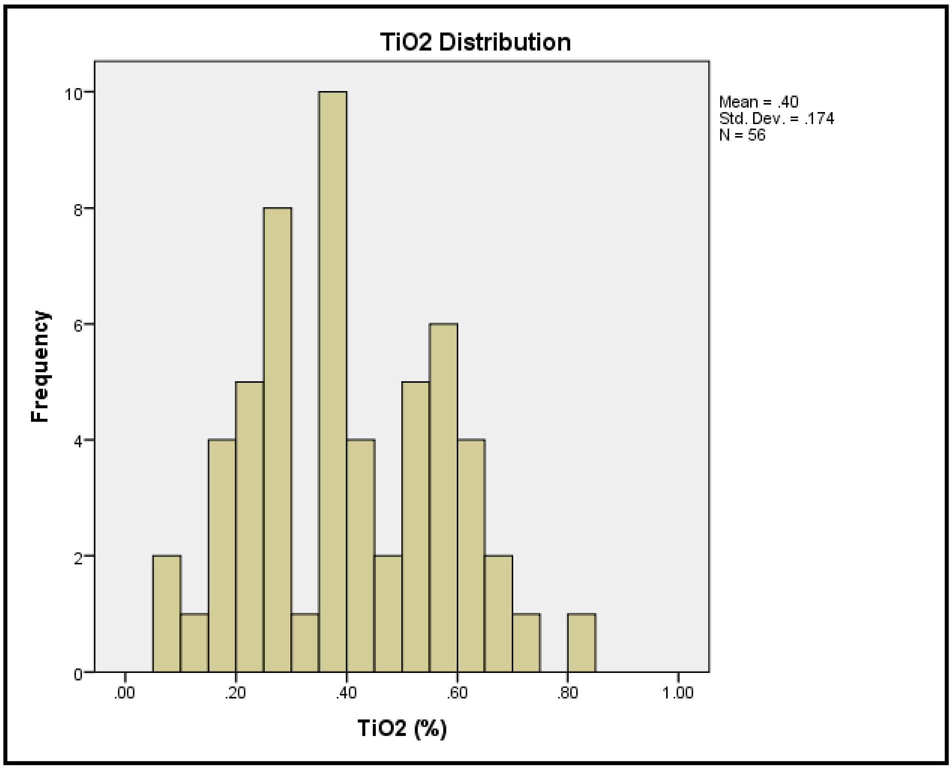

Figure 28. The histogram shows the distribution, mean and standard deviation of TiO_2 (XRF) for all samples (n=56 instead of n=57: 1 null).

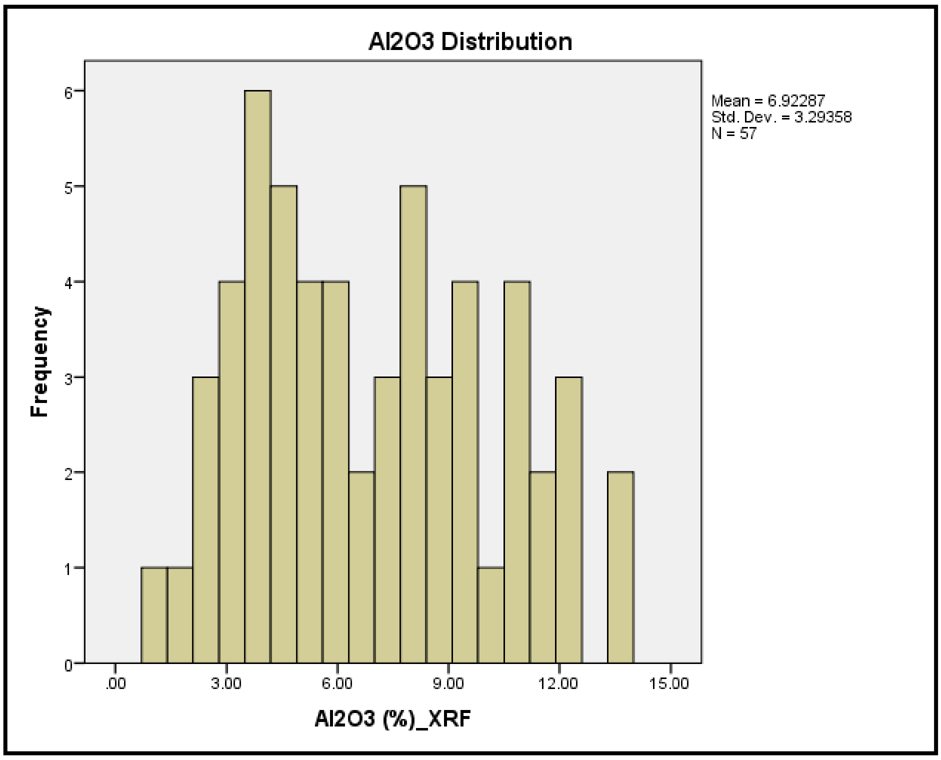

Figure 29. The histogram shows the distribution, mean and standard deviation of Al_2O_3 (XRF) for all samples.

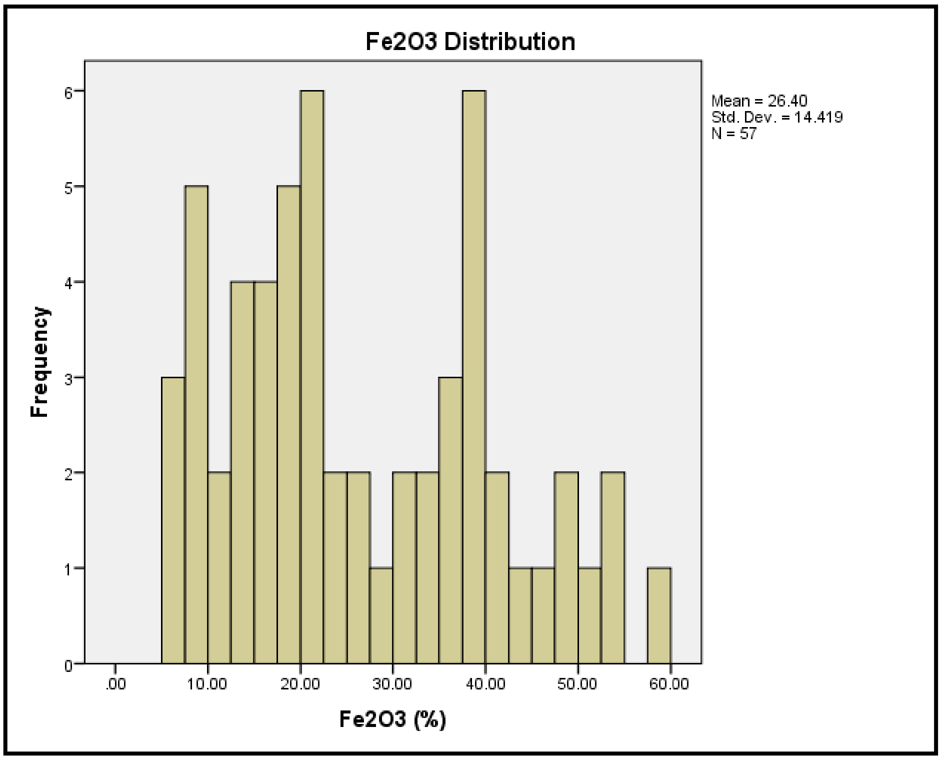

Figure 30. The histogram shows the distribution, mean, and standard deviation of Fe_2O_3 (XRF) for all samples.

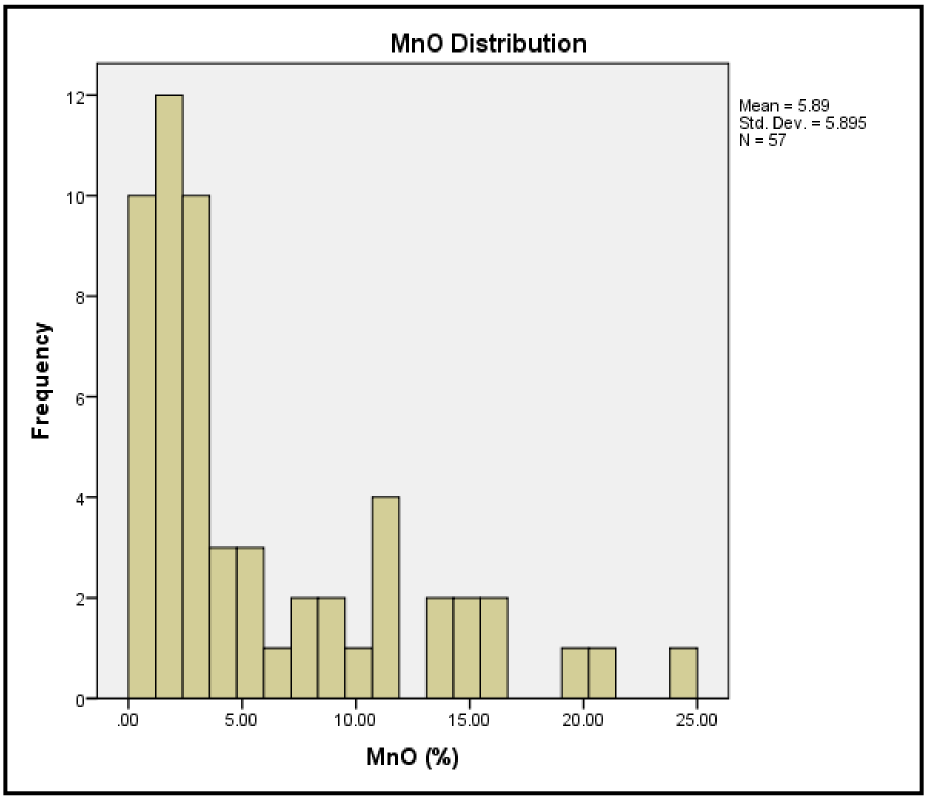

Figure 31. The histogram shows the distribution, mean and standard deviation of MnO (XRF) for all samples.

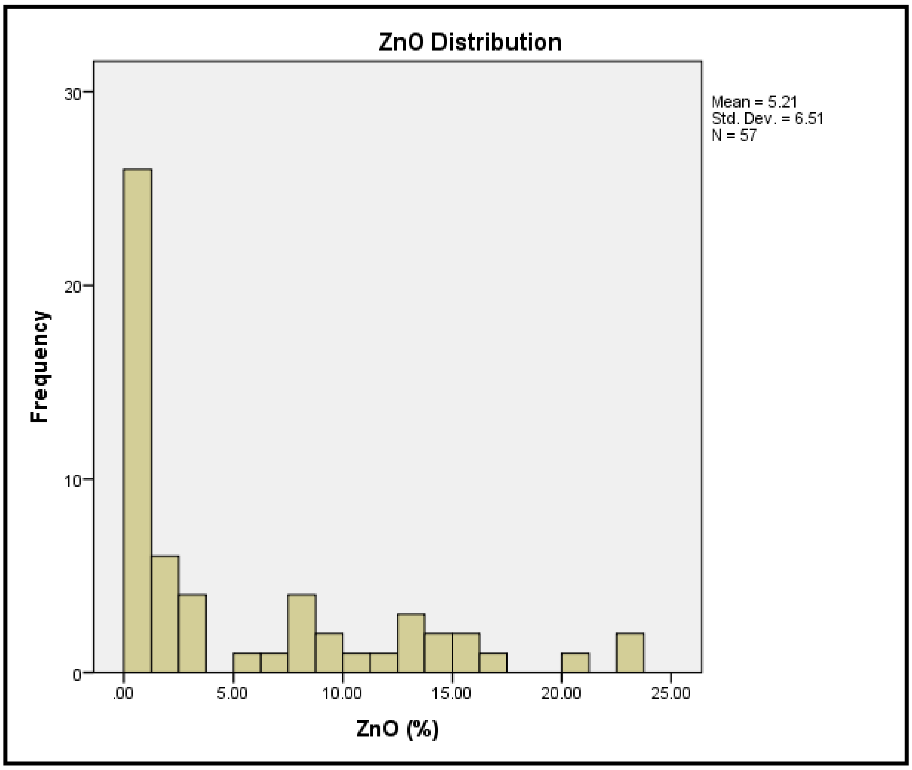

Figure 32. The histogram shows the distribution, mean and standard deviation of ZnO (XRF) for all samples.

Visual inspection of the histograms presented in Figures 27 to 32 shows that the SiO_2, TiO_2, Al_2O_3, MnO, FeO and ZnO data is not normally distributed, is skewed and has a number groups, which signifies different lithological units. For these reasons, a non-parametric data analysis was used for to describe the central tendencies of the distribution of the chosen elements. A Binomial Test and Spearman's correlation coefficient were used to describe the central tendency of the data and to show compatibility of the ICP and XRF datasets.

In the context of this thesis, only Mn, Zn and Fe are of direct relevance, therefore some of the other major elements and their relationship will no longer be considered further. A major emphasis also is placed on the B unit of the Gams Formation (pelitic schist, meta-pelite ore, and garnet-magnetite ore), specifically due its mineral assemblages associated with sulphide minerals (alabandite, sphalerite and pyrrhotite). Other elements and lithology units will be used where necessary.

Descriptive statistics and binomial tests

The compatibility of the ICP and XRF datasets was tested by comparing the descriptive statistics, box-plot analysis, scatter plots and correlation coefficients. Table 11 presents the descriptive statistics of Mn, Fe and Zn for both ICP and XRF, from 57 samples.

Table 11. Table showing comparison of the descriptive statistics of Mn, Fe and Zn from the ICP and XRF data.

Descriptive statistics	**N**	**Minimum**	**Maximum**	**Percentiles**		
				25th	50th (Median)	75th
Mn (ppm*10000)_ICP	**57**	0.096	16.65	0.55	1.14	2.29
MnO (%)_XRF	**57**	0.38	24.28	1.55	3.18	9.72
Fe (%)_ICP	**57**	0.61	42.60	9.06	15.05	27.05
Fe_2O_3 (%)_XRF	**57**	5.09	59.39	14.91	22.16	38.43
Zn (ppm*10000)_ICP	**57**	0.015	20.90	0.17	1.13	7.79
ZnO (%)_XRF	**57**	0.03	22.71	0.23	1.62	9.1
Zn (ppm*10000)_XRF	**57**	0.02	18.65	0.1171	0.9698	6.25

There are significant differences between the ICP and XRF data presented in Table 11. The XRF data is always higher than the ICP data for most of the comparable elements. Only the concentration of the semi-quantitative Zn ppm_XRF is lower than both the Zn (ppm)_ICP and ZnO (%)_XRF concentrations.

This descriptive statistical analysis does not take into account the differences in mineral assemblages (lithologies) of the samples. Therefore, Tables 12 to 15 present the statistical analysis of the four drillholes for pelitic schist, meta-pelite ore and garnet-magnetite ore. The differences between ICP and XRF analysis are minimal as compared in Table 11.

Table 12 shows the descriptive statistics of the pelitic schist and meta-pelite ore of drillhole *GAMD033-2-4*. A comparison of the minimum, maximum, median, 25th and 75th percentiles of Mn, Zn and Fe shows that the XRF data is always higher than that of the ICP data, except for the Zn semi-quantitative analysis. The maximum Mn concentrations of ICP data in the pelitic schist (PEL) are that of the upper detection limit of the ICP technique. This shows that the over-grade "over-detection limit" analysis is missing from the database. Removing the oxygen factor (molecule vs. element) does not improve the inaccuracy between the XRF and the ICP concentrations, so the XRF concentration remains slightly higher than the ICP.

Table 12. Descriptive statistics of Mn, Zn and Fe for ICP and XRF data in drillhole *GAMD033-2-4*, showing the distribution in pelitic schist (PEL) and meta-pelite ore (PEO).

		GAMD033-2-4					
		Minimum	**Maximum**	**Percentiles**			**N**
				25th	**50th (MEDIAN)**	**75th**	
PEL	Mn (ppm)_ICP	4240	50000	4240	4790	50000	**3**
	MnO (%wt)_XRF	0.62	20.61	0.62	1.08	20.61	
	Zn (ppm)_ICP	2900	11300	2900	8900	11300	
	ZnO (%wt)_XRF	0.27	1.74	0.27	1.20	1.74	
	Zn (ppm)_XRF	1489	9916	1489	7196	9916	
	Fe (%)_ICP	6.21	37.40	6.21	19.30	37.40	
	Fe_2O_3 (%wt)_XRF	7.90	38.52	7.90	26.94	38.52	
PEO	Mn (ppm)_ICP	14200	28100	14412	18675	26650	**4**
	MnO (%wt)_XRF	1.79	3.47	1.90	2.49	3.29	
	Zn (ppm)_ICP	57100	91500	60650	79900	90750	
	ZnO (%wt)_XRF	8.25	13.17	8.55	10.70	12.87	
	Zn (ppm)_XRF	53242	88783	58213	75139	85875	
	Fe (%)_ICP	25.50	31.50	25.83	28.30	31.08	
	Fe_2O_3 (%wt)_XRF	35.34	40.14	35.62	37.09	39.54	

Table 13 shows the descriptive statistics of pelitic schist, meta-pelite ore and garnet-magnetite ore of GAMD041-1-3. A comparison of the minimum, maximum, median, 25th and 75th percentiles shows that major analyses of the XRF analysis have higher concentrations than the ICP analysis. Once again, the over-grade analysis value for Mn in the PEL is missing, with the maximum value at 50 000 ppm. The garnet-magnetite ore (MPO) shows extreme variation between the ICP and the XRF concentration of manganese. The Mn_ICP concentration is below 30 000 ppm (3 %wt), while XRF shows an Mn concentration well above 18 %wt MnO. The Fe concentration also shows higher variation in the garnet-magnetite ore than in other lithologies.

Table 13. Descriptive statistics of Mn, Zn and Fe for ICP and XRF data in drillhole *GAMD041-1-0*, showing the distribution in pelitic schist (PEL), meta-pelite ore (PEO) and garnet-magnetite ore (MPO).

		GAMD041-1-3					
		Minimum	**Maximum**	**Percentiles**			**N**
				25th	**50th (MEDIAN)**	**75th**	
PEL	Mn (ppm)_ICP	4150	50000	4150	4840	50000	**3**
	MnO (%wt)_XRF	0.54	10.25	0.54	0.60	10.25	
	Zn (ppm)_ICP	363	9820	363	2100	9820	
	ZnO (%wt)_XRF	0.09	1.31	0.09	0.24	1.31	
	Zn (ppm)_XRF	319	6611	318	1165	6611	
	Fe (%)_ICP	9.53	11.7	9.53	10.20	11.70	
	Fe_2O_3 (%wt)_XRF	13.54	19.23	13.54	14.67	19.23	
PEO	Mn (ppm)_ICP	6030	28400	6030	16650	28400	**3**
	MnO (%wt)_XRF	0.65	3.46	0.65	1.59	3.46	
	Zn (ppm)_ICP	26400	209000	26400	89900	209000	
	ZnO (%wt)_XRF	2.34	22.63	2.34	8.65	22.63	
	Zn (ppm)_XRF	13362	186284	13362	61889	186284	
	Fe (%)_ICP	17.20	42.60	17.20	39.70	42.60	
	Fe_2O_3 (%wt)_XRF	20.70	53.98	20.70	44.95	53.98	
MPO	Mn (ppm)_ICP	26300	26700	-	-	-	**2**
	MnO (%wt)_XRF	7.72	11.02	-	-	-	
	Zn (ppm)_ICP	181000	192500	-	-	-	
	ZnO (%wt)_XRF	20.08	22.71	-	-	-	
	Zn (ppm)_XRF	159295	186453	-	-	-	
	Fe (%)_ICP	14.15	15.05	-	-	-	
	Fe_2O_3 (%wt)_XRF	21.06	21.37	-	-	-	

Table 14 shows the minimum and maximum of pelitic schist, meta-pelite ore and garnet-magnetite ore for drillhole *GAMD045-0-0*. Only two samples were taken from each lithology, therefore the distribution of the samples cannot be demonstrated properly. The manganese concentration of garnet-magnetite ore shows the highest differences when comparing the minimum and maximum of the ICP and XRF analyses (all the ICP values are lower than 14 000 ppm Mn (1.4 %wt), while the XRF analysis presents values greater than 8 %wt MnO). The Fe concentration in the garnet-magnetite ore also shows high variation, unlike in the other lithologies.

Table 14. Descriptive statistics of Mn, Zn and Fe for ICP and XRF data in drillhole *GAMD045-0-0*, showing the distribution in pelitic schist (PEL), meta-pelite ore (PEO) and garnet-magnetite ore (MPO).

		GAMD045-0-0					
		Minimum	**Maximum**	**Percentiles**			**N**
				25th	**50th (MEDIAN)**	**75th**	
PEL	Mn (ppm)_ICP	963	1245	-	-	-	**2**
	MnO (%wt)_XRF	0.38	0.52	-	-	-	
	Zn (ppm)_ICP	1820	2610	-	-	-	
	ZnO (%wt)_XRF	0.33	0.51	-	-	-	
	Zn (ppm)_XRF	1872	2997	-	-	-	
	Fe (%)_ICP	27.30	27.6	-	-	-	
	Fe_2O_3 (%wt)_XRF	35.03	38.38	-	-	-	
PEO	Mn (ppm)_ICP	4200	6870	-	-	-	**2**
	MnO (%wt)_XRF	0.81	1.45	-	-	-	
	Zn (ppm)_ICP	42400	56000	-	-	-	
	ZnO (%wt)_XRF	5.32	6.75	-	-	-	
	Zn (ppm)_XRF	27780	44609	-	-	-	
	Fe (%)_ICP	26.70	36.6	-	-	-	
	Fe_2O_3 (%wt)_XRF	38.87	47.51	-	-	-	
MPO	Mn (ppm)_ICP	11400	13100	-	-	-	**2**
	MnO (%wt)_XRF	8.67	11.19	-	-	-	
	Zn (ppm)_ICP	121000	138500	-	-	-	
	ZnO (%wt)_XRF	14.79	16.35	-	-	-	
	Zn (ppm)_XRF	108016	129377	-	-	-	
	Fe (%)_ICP	19.2	20.6	-	-	-	
	Fe_2O_3 (%wt)_XRF	30.29	30.57	-	-	-	

Table 15 shows the descriptive statistics of pelitic schist and meta-pelite ore from drillhole *GAMD054-2-2*. The comparison of the minimum, maximum, median, 25th and 75th percentiles of Zn shows good compatibility between the ICP and the XRF dataset compared to the other elements. The Fe concentrations are extremely variable, with the XRF concentrations always higher than the ICP concentrations. The XRF Mn concentrations are also always higher than that of the ICP concentrations in all lithologies. The effect of over-grade analysis is shown by the 75th percentile of Mn in the PEL, with the ICP Mn concentration of 150 000 ppm (15 %wt), and the 20.46 %wt MnO of the XRF analysis.

Table 15. Descriptive statistics of Mn, Zn and Fe for ICP and XRF data in drillhole GAMD054-2.2, showing the distribution in pelitic schist (PEL) and meta-pelite ore (PEO).

		GAMD054-2-2					
		Minimum	**Maximum**	**Percentiles**			**N**
				25th	**50th (MEDIAN)**	**75th**	
PEL	Mn (ppm)_ICP	5430	166500	9795	62500	150000	**6**
	MnO (%wt)_XRF	0.95	24.28	1.45	9.66	20.46	
	Zn (ppm)_ICP	392	11700	1253	1905	4868	
	ZnO (%wt)_XRF	0.06	1.87	0.16	0.24	0.78	
	Zn (ppm)_XRF	274	9698	894	1443	4269	
	Fe (%)_ICP	4.71	16.3	8.75	11.28	13.53	
	Fe_2O_3 (%wt)_XRF	7.86	26.28	13.35	17.68	22.80	
PEO	Mn (ppm)_ICP	6750	40000	15938	21550	32350	**12**
	MnO (%wt)_XRF	1.52	5.58	2.25	2.87	4.20	
	Zn (ppm)_ICP	22100	118500	34450	76750	99625	
	ZnO (%wt)_XRF	2.94	15.47	4.71	9.83	13.51	
	Zn (ppm)_XRF	18846	124753	26953	61043	97573	
	Fe (%)_ICP	13.00	34.10	17.30	27.10	31.80	
	Fe_2O_3 (%wt)_XRF	18.63	59.39	26.08	40.80	51.32	

In general, the ICP concentrations were lower than those of the XRF major elements analysis and slightly higher than the XRF trace elements analysis. The Zn concentration is less variable in all rock units, which signifies that sphalerite is the main Zn-bearing mineral and, as a sulphide mineral, it easily releases the Zn during sample preparation for the ICP analysis. In the ICP sample preparation, sulphide minerals dissolve completely, while oxide and silicate minerals dissolve partially, therefore the concentration of elements from the ICP analysis is controlled by the mineral assemblage. The manganese concentrations in the ICP dataset represent the sulphide mineral distribution rather than the whole-rock geochemistry.

Any interpretation of the results should always consider limitations and differences of the ICP and XRF techniques, such as:

1. Difference in the sample preparation methods,
2. Matrix effects,
3. Step-wise analysis as a result of upper detection limits of the ICP technique,
4. Correction for inter-elemental spectral interferences, and
5. Reporting units (the ICP data is reported as elements in ppm and %, the qualitative XRF analysis is reported as molecules in %wt, and the semi-quantitative XRF is reported as elements in ppm).

Box-plot analysis of Mn data

Figure 33 shows an illustration of a box plot graph with an explanation of the components. The box plot was used in this instance to graphically present the distribution of the manganese data of the XRF and ICP data.

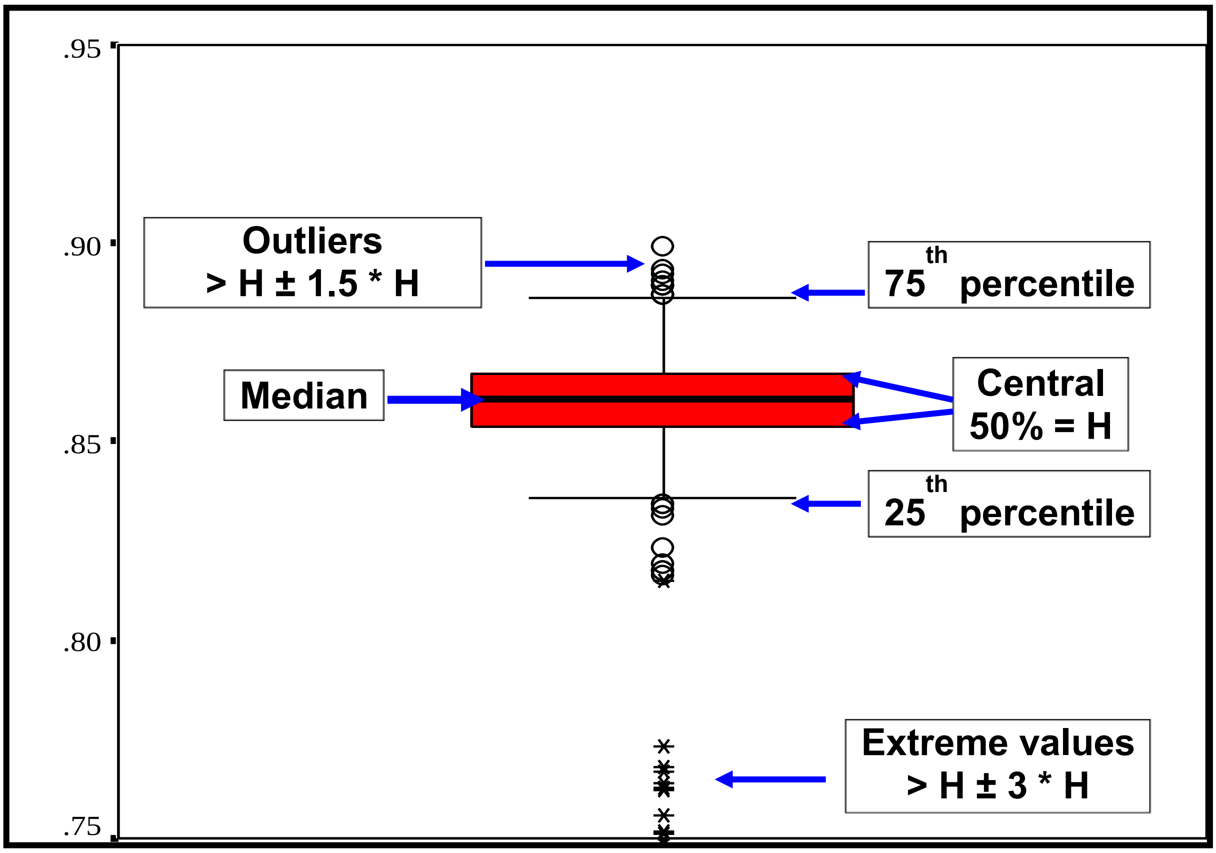

Figure 33. Graph showing the illustration of a box plot.

Figures 34a and 34b show box-plot graphs of the Mn distribution in pelitic schist and meta-pelite ore respectively. In Figure 34a, the Mn_XRF concentration has a larger spread than the Mn_ICP concentration for all drillholes. The Mn_ICP concentration in drillholes *GAMD033-2-4* and *GAMD041-1-3* shows the 75th percentile to be 50 000 ppm, which is the upper detection limit of the ICP analysis for Mn analysis. Drillhole *GAMD045-0-0* has less than three samples, hence the distribution cannot be demonstrated by a box-plot graph. The medians of XRF data are higher than those of the ICP data.

Figure 34b shows that the median and spread of data are comparable in drillholes *GAMD033-2-4* and *GAMD054-2-2*, whereas drillhole *GAMD041-1-3* shows a lower median in the XRF analysis than in the ICP analysis, and drillhole *GAMD045-0-0* shows a higher median in the XRF analysis than in the ICP analysis. In general, the correlation of Mn data between XRF and ICP is poorer in the pelitic schist than in meta-pelite ore.

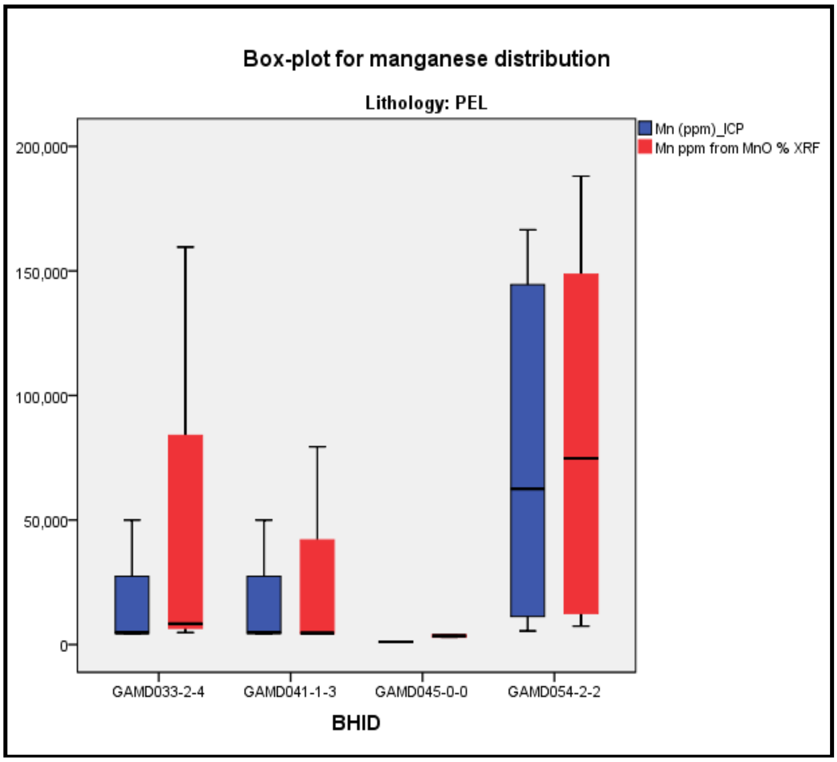

Figure 34a. A box-plot graph showing a comparison of XRF and ICP analysis for the Mn concentration of pelitic schist.

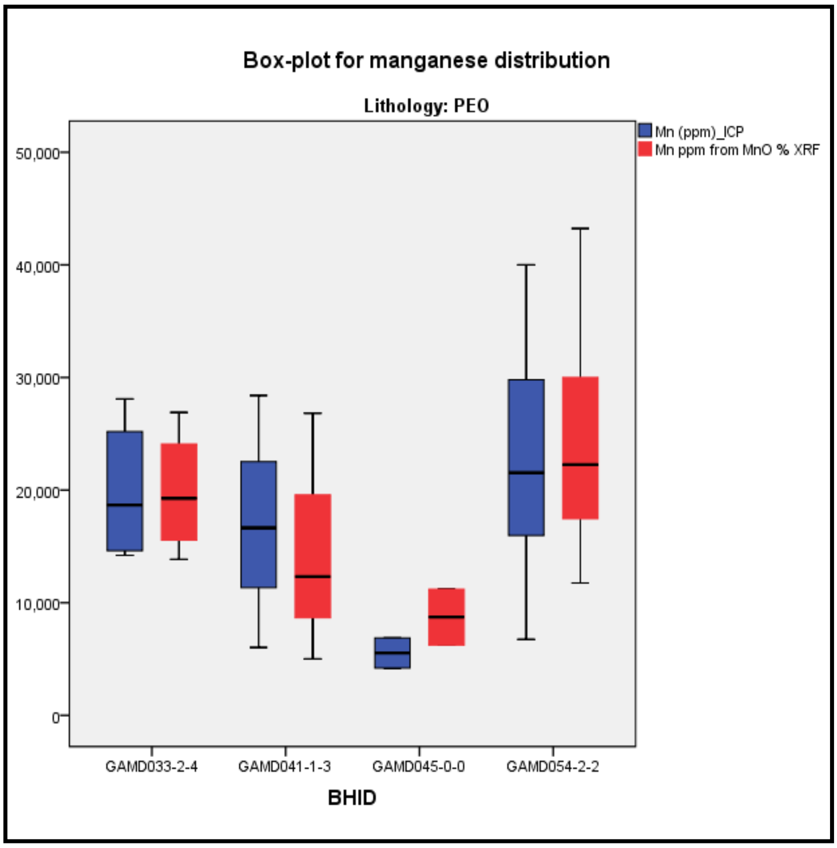

Figure 34b. A box plot shows a comparison of the XRF and ICP analysis of the Mn concentration of meta-pelite ore.

Compatibility of the ICP and XRF data

The compatibility of the ICP and XRF data is further tested by presenting the difference between the ICP and XRF analysis when taking into consideration the mineral assemblages and sample preparation methods for the ICP technique. Table 10 presents the factor ***(f)*** of Mn, Fe and Zn. It is a ratio calculated by dividing the XRF concentrations by the ICP concentrations. The manganese concentrations from the XRF analysis were converted to Mn_ppm from MnO_%wt for accurate comparisons with the ICP analysis. See Chapter 4, Section 2 for an elaboration of the sample preparation methods for the ICP technique.

Table 16. Table presents the factor ***(f)*** of Mn, Fe and Zn data of different mineralogical assemblages and sample preparation methods.

Drillhole_ID	Lithology	Mn (*f*)	Fe (*f*)	Zn (*f*)	ICP sample preparation	Comments
GAMD033-2-4	**GAQ**	9.14	4.58	1.39	ME ICP-41	Variable in Mn
	CAS	8.75	9.73	1.54	ME ICP-41	Variable in Fe
	GQZ	3.89	2.14	2.12	ME ICP-41	Variable in Fe
	PEL	1.44	1.23	1.74	ME ICP-41	
	PEO	1.01	1.33	1.47	ME ICP-41+Zn OG-46	
GAMD041-1-3	**CAS**	2.81	2.28	1.02	ME ICP-41	Variable in all three elements
	PEL	0.99	1.5	2.3	ME ICP-41	Mn OG-46 sample excluded
	PEO	0.84	1.21	1.46	ME ICP-41+Zn OG-46	Variable in Zn
	MPO	2.74	1.45	1.24	ME ICP-41+Zn OG-46	Variable in Mn
	BIFs	6.34	1.84	1.82	ME ICP-41	Variable in Fe
	GQZ	13.34	1.54	2.15	ME ICP-41	
GAMD045-0-0	**PEL**	3.28	1.34	1.73	ME ICP-41	Mn OG-46 sample excluded
	PEO	1.56	1.38	1.71	ME ICP-41+Zn OG-46	Variable in Mn
	MPO	6.25	1.53	1.32	ME ICP-41+Zn OG-46	
	BIFs	11.68	1.73	1.72	ME ICP-41	
GAMD054-2-2	**PEL**	0.23			Mn OG-46	
	PEL	1.17	1.61	1.85	ME ICP-41	
	PEO	1.18	1.55	1.59	ME ICP-41+Zn OG-46	

An ***(f)*** value of zero (nil) shows that the XRF and ICP concentrations are equal, and the further away from zero, the more different the concentrations. The ***(f)*** values greater than 3 observed in Mn ***(f)*** are from the lithologies of the A unit, BIFs and MPO units. These lithologies host significant quantities of Mn-bearing minerals such as garnets, pyroxenoids, amphiboles, jacobsite and franklinite. The pelitic schist and meta-pelite ore units have lower ***(f)*** values for all three elements, and this signifies that there is good compatibility between the XRF and ICP datasets. The lesser ***(f)*** value in Zn concentrations signifies that most of the Zn is hosted by sphalerite.

Re-analysis of Certified Reference Materials (CRMs)

A re-analysis of the CRMs was undertaken to test the accuracy of the XRF technique at the University of Pretoria, which was used to analyse the 57 samples for the purpose of this thesis. The three CRMs – LG (low-grade Zn), MG (medium-grade Zn) and HG (high-grade Zn) – were used as standards for the QAQC (Quality Assurance Quality Control) of the Gamsberg East ore sampling programme.

Table 17 presents comparisons of the analysis of the three CRMs. The concentration reported by Ore Research and Exploration PTY Ltd. are mean concentrations of data submitted to ten laboratories across the world. Both, the fusion (XRF sample preparation technique) and three-acid digest (ICP sample preparation technique), were analysed and compared. The concentrations are reported as elements in %wt and Cu is reported in ppm.

Table 17. Results of the analysis of Gamsberg Certified Reference Material (CRM
1 SD = standard deviation (1σ).

Gamsberg Certified Reference Material (ICP and XRF)_Ore Research and Exploration PTY Ltd.												
	3-Acid digest	**1 SD**	**Fusion**	**1 SD**	**3-Acid digest**	**1 SD**	**Fusion**	**1 SD**	**3-Acid digest**	**1 SD**	**Fusion**	**1 SD**
	LG		**LG**		**MG**		**MG**		**HG**		**HG**	
Fe (%wt)	20.68	**0.37**	21.06	**0.85**	23.76	**0.56**	23.53	**0.54**	21.28	**0.42**	20.98	**0.84**
Mn (%wt)	1.08	**0.03**	1.27	**0.03**	0.72	**0.02**	0.77	**0.03**	1.37	**0.04**	1.57	**0.04**
Cu (ppm)	151	**5**	153	**7**	125	**5**	129	**6**	111	**5**	108	**9**
Zn (%wt)	4.19	**0.07**	4.22	**0.13**	6.26	**0.15**	6.30	**0.18**	10.06	**0.14**	9.99	**0.20**
Pb (%wt)	0.58	**0.02**	0.55	**0.01**	0.62	**0.02**	0.60	**0.02**	0.59	**0.02**	0.56	**0.01**

Gamsberg Certified Reference Material (XRF major analysis)_University of Pretoria												
%wt	**LG1**	**LG2**	**LG3**	**AVERAGE**	**MG1**	**MG2**	**MG3**	**AVERAGE**	**HG1**	**HG2**	**HG3**	**AVERAGE**
Fe_2O_3	26.77	26.42	27.05	**26.75**	31.33	32.16	31.85	**31.78**	29.24	28.30	29.04	**28.86**
MnO	1.47	1.47	1.53	**1.49**	0.94	0.92	0.89	**0.92**	2.01	1.97	1.98	**1.99**
CuO	0.03	0.03	< 0.01	**0.03**	0.04	< 0.01	0.02	**0.03**	0.03	< 0.01	0.02	**0.03**
ZnO	4.94	4.89	5.05	**4.96**	7.66	7.94	7.98	**7.86**	12.81	12.64	12.81	**12.76**
PbO	0.27	0.28	0.37	**0.31**	0.31	0.34	0.35	**0.33**	0.35	0.29	0.34	**0.33**

A comparison of the two datasets shows that the XRF analysis from the University of Pretoria generally reports higher concentrations, but there is some correlation between the techniques.

Correlation coefficients

To further demonstrate the compatibility of the XRF and ICP techniques, correlation coefficients were used. Spearman's correlation coefficient was used to calculate the correlation coefficients of the XRF and ICP datasets. Spearman's correlation coefficient is chosen over Pearson's correlation coefficient, "the R^2", because the Mn, Zn and Fe datasets have a non-parametric distribution.

Table 18 presents the Spearmen's correlation coefficients computed by the IBM SPSS 21 statistical software package. For the total sample, the correlation coefficient of Mn was the lowest, while Zn and Fe were high. These high coefficients indicate that, for Zn and Fe, the XRF and ICP datasets are compatible, while the low coefficient of Mn indicates that the ICP and XRF analyses are not compatible for Mn analysis.

On the other hand, the correlation coefficient of Mn calculated for individual rock types shows a much higher coefficient. Pelitic schist and meta-pelite ore have coefficients of 0.995 (N = 14) and 0.974 (N = 21) respectively, while garnet-bearing rock units have a very low correlation coefficient. The compatibility of XRF and ICP data seems to be mineralogically controlled.

Table 18. Spearman's correlation coefficients of Mn, Zn and Fe.

All samples N = 57	**Spearman's correlation coefficient**
Mn (ppm)_ICP vs. MnO (%wt)_XRF	0.561
Zn (ppm)_ICP vs. ZnO (%wt)_XRF	0.993
Zn (ppm)_ICP vs. Zn (ppm)_XRF	0.986
ZnO (%wt)_XRF vs. Zn (ppm)_XRF	0.994
Fe (%)_ICP vs. Fe_2O_3 (%wt)_XRF	0.968
Mn (ppm)_ICP vs. MnO (%wt)_XRF ***(N=14, Pelitic schist)***	***0.995***
Mn (ppm)_ICP vs. MnO (%wt)_XRF ***(N=14, Meta-pelite ore)***	***0.974***

The manganese scatter-plot analysis

Scatter plots are used to demonstrate the relationships between two elements. A comparison of the Mn dataset between the XRF and ICP techniques is also presented to unpack issues around compatibility.

Figures 35a and b shows the relationships of Mn_ICP and Mn_XRF in the four drillholes. There are two systematic linear trends and a group of scattered samples, displayed in Figure 35a. A diagonal trend (t1) is made up mainly of samples from drillhole *GAMD054-2-2*, and some samples from drillholes *GAMD041-1-3* and *GAMD045-0-0*. Trend t1 is an expected trend for compatible analysis techniques, and trend t2 shows no correlation between the two techniques. Trend (t2), which shows lower Mn_ICP concentrations than Mn_XRF, is made up mainly of samples from drillholes *GAMD033-2-4* and *GAMD045-0-0*. Samples in trend t2 and the cluster are mostly from the A and C units of the Gams Formation, as shown in Figure 35b. Pelitic schist and meta-pelite ore are the main components of trend t1.

Differences in mineralogical assemblages and different sample preparation techniques could be possible reasons for the under-reporting of the Mn concentration in the ICP technique. A good correlation of the ICP and XRF techniques in pelitic schist and meta-pelite ore suggests that most Mn is associated with sulphide minerals, unlike with silicate and oxide minerals.

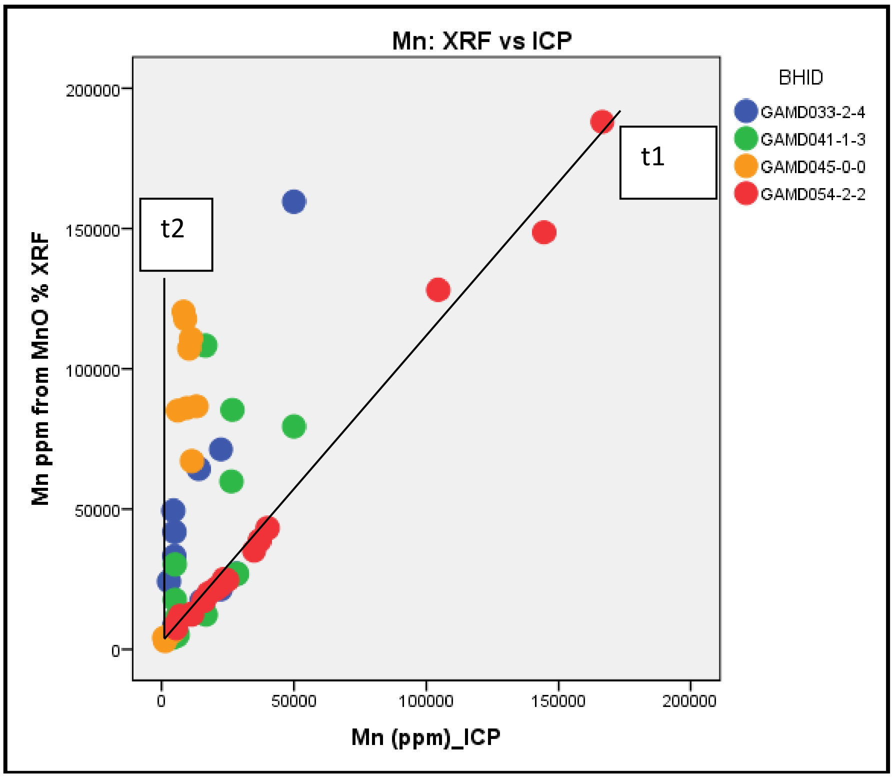

Figure 35a. The relationship between Mn (ppm) _XRF and Mn (ppm) _ICP data, categorised by drillhole ID. t1 and t2 are trends from the comparison.

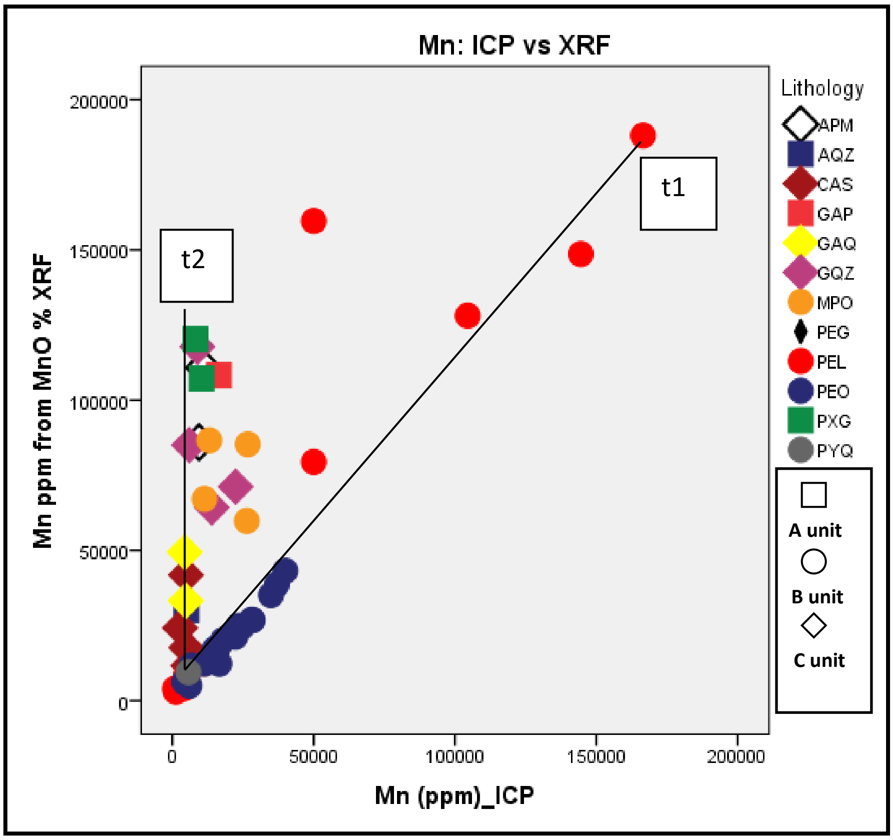

Figure 35b. The relationship between Mn (ppm) _XRF and Mn (ppm) _ICP data, categorised into lithologies. t1 and t2 are trends from the comparison.

Figures 36 to 38 show the scatter plot of Mn and associations with the occurrence of alabandite within the pelitic schist of drillhole *GAMD054-2-2*, and the meta-pelite ore units of drillholes *GAMD033-2-4* and *GAMD054-2-2*. The pelitic schist (PEL) in Figure 36 hosts alabandite, but an anomalous concentration of alabandite is associated with the high concentration of Mn above 10 %wt MnO or 100 000 ppm Mn. All meta-pelite ore (PEO) samples associated with alabandite are shown in Figures 37 and 38. Manganese concentrations greater than 2 %wt or (20 000 ppm) within meta-pelite ore are associated with the occurrence of alabandite.

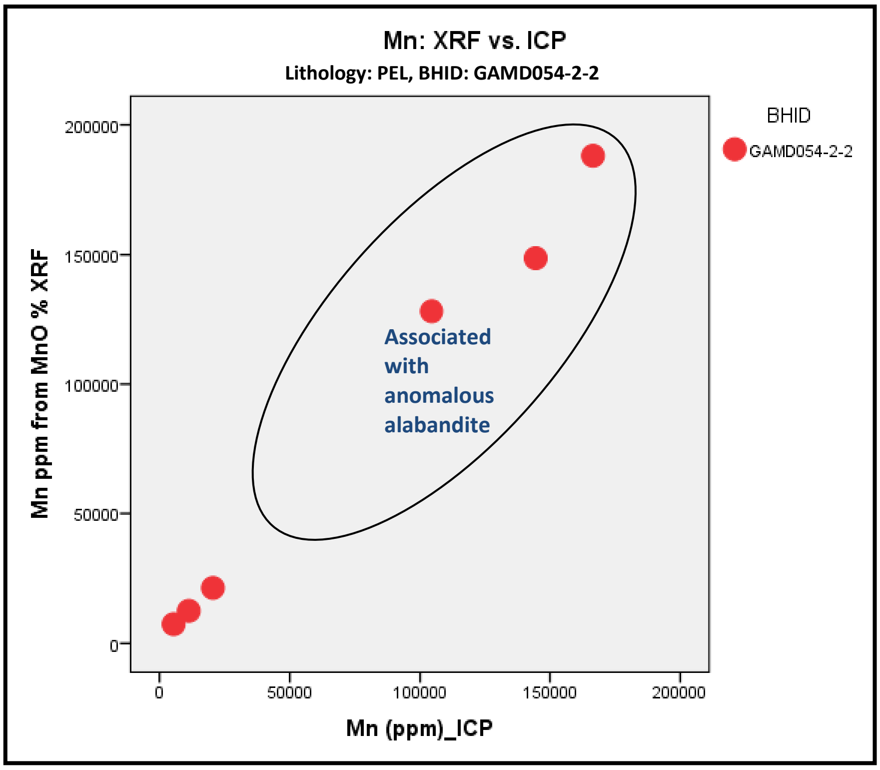

Figure 36. The relationship between Mn (ppm) _XRF and Mn (ppm) _ICP data, of PEL in drillhole GAMD054-2-2.

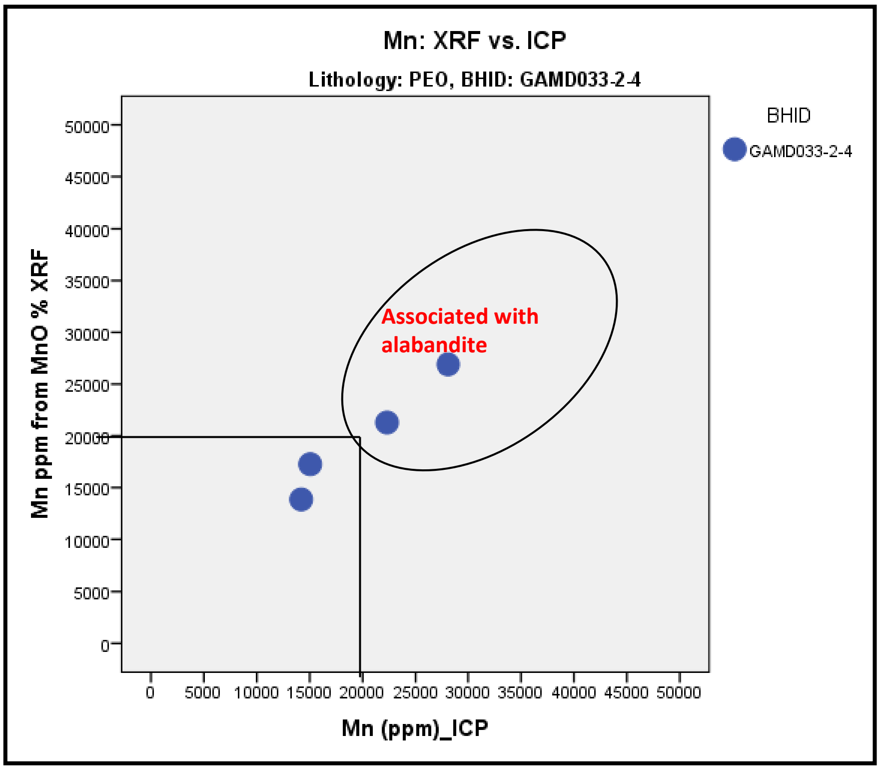

Figure 37. The relationship between Mn (ppm) _XRF and Mn (ppm) _ICP data, of PEO in drillhole GAMD033-2-4.

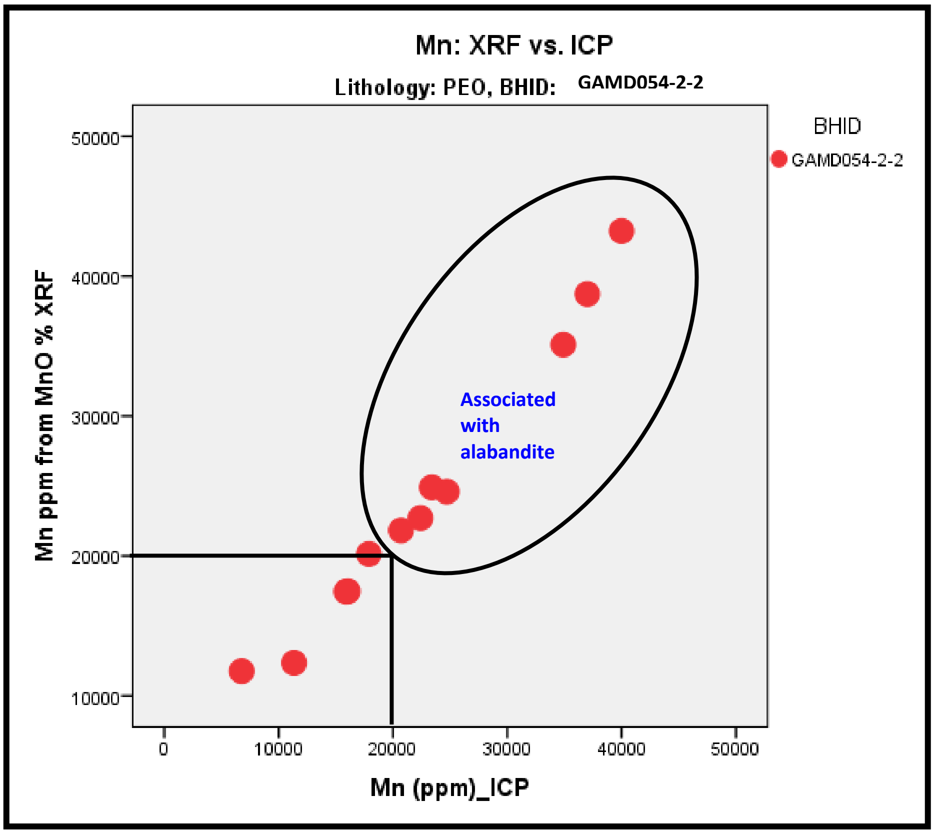

Figure 38. The relationship between Mn (ppm) _XRF and Mn (ppm) _ICP data, of PEO in drillhole GAMD054-2-2.

The zinc scatter plot analysis

Figures 39 to 41 show the relationships of Zn in the XRF (major and trace element analysis) and ICP analysis. The relationship between ZnO_XRF and Zn_ICP, in Figure 39, shows a positive correlation between the ICP and XRF major element analysis (ZnO). Samples from drillhole *GAMD041-1-3* have a higher Zn concentration than all the other drillholes. The major element analysis (MnO) has slightly higher concentrations than Zn_ICP.

The relationship between Zn_XRF and Zn_ICP in Figure 40 shows a positive correlation, but Zn_XRF concentrations are slightly lower than those of the ICP analysis. Figure 41 shows the relationship of Zn in the major element and trace element XRF analysis. The trace element (Zn_XRF) concentration was slightly lower than ZnO_XRF. Overall there was good compatibility between XRF and ICP for the Zn analysis. The ZnO therefore will be used further to represent whole-rock Zn concentration of the four drillholes.

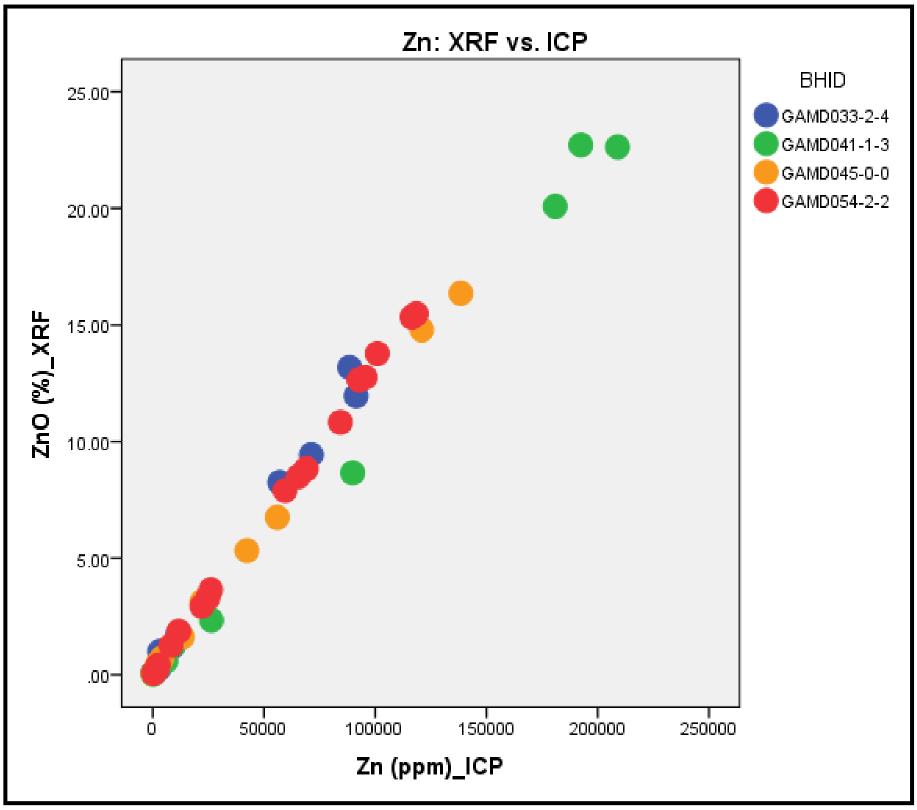

Figure 39. The relationship between ZnO (%wt) _XRF and Zn (ppm) _ICP data of all four drillholes.

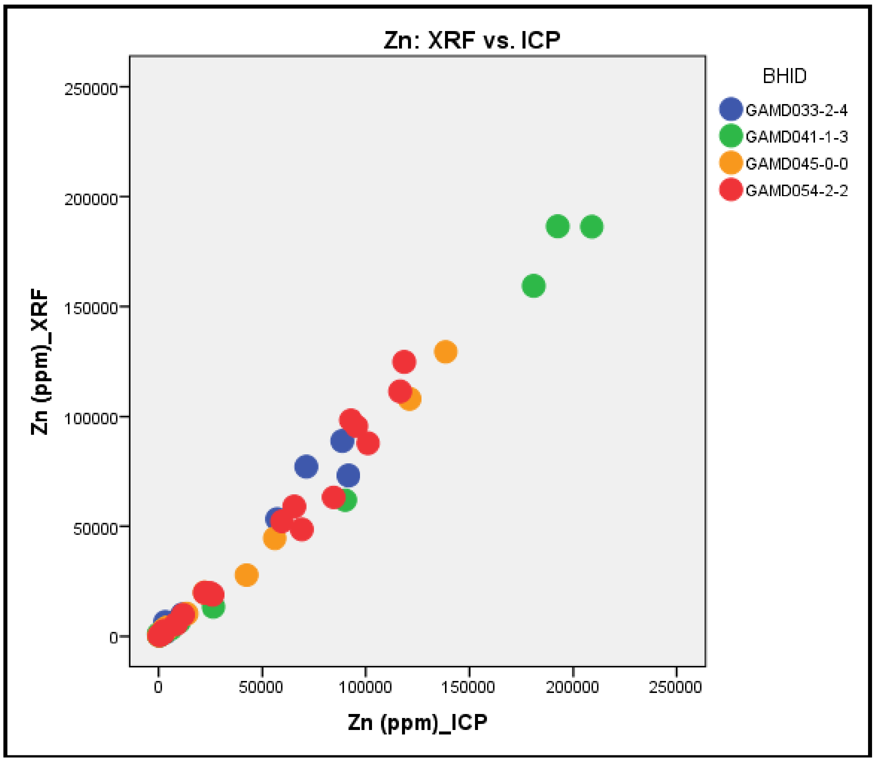

Figure 40. The relationship between Zn (ppm) _XRF and Zn (ppm) _ICP data categorised by drillhole ID.

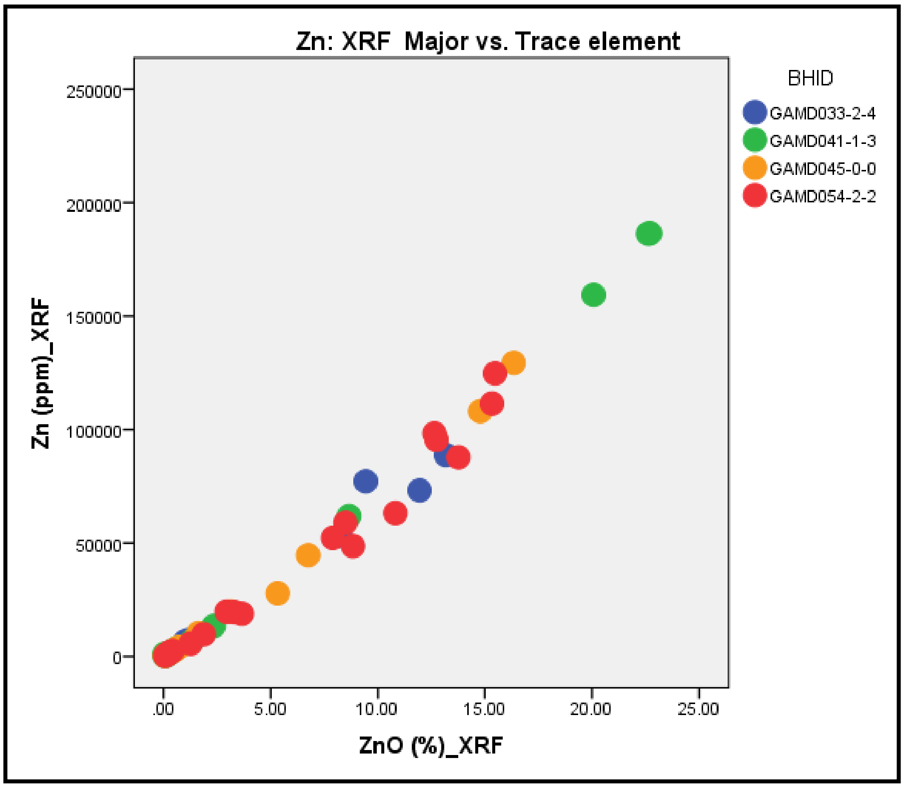

Figure 41. The relationship between ZnO (%wt) _XRF and Mn (ppm) _ICP data categorised by drillhole ID.

The iron scatter-plot analysis

Figure 42 shows the relationship of Fe concentration between the XRF and ICP analysis. The relationship shows a positive correlation, with the XRF analysis reporting a slightly higher concentration than the ICP analysis. The higher concentration of Fe, above 40 %wt Fe, shows different trends compared to Fe concentration below 40 %wt. The effects of mineralogical assemblage, already discussed earlier, could be playing a role in understanding the difference between the XRF and ICP analyses for Fe concentrations.

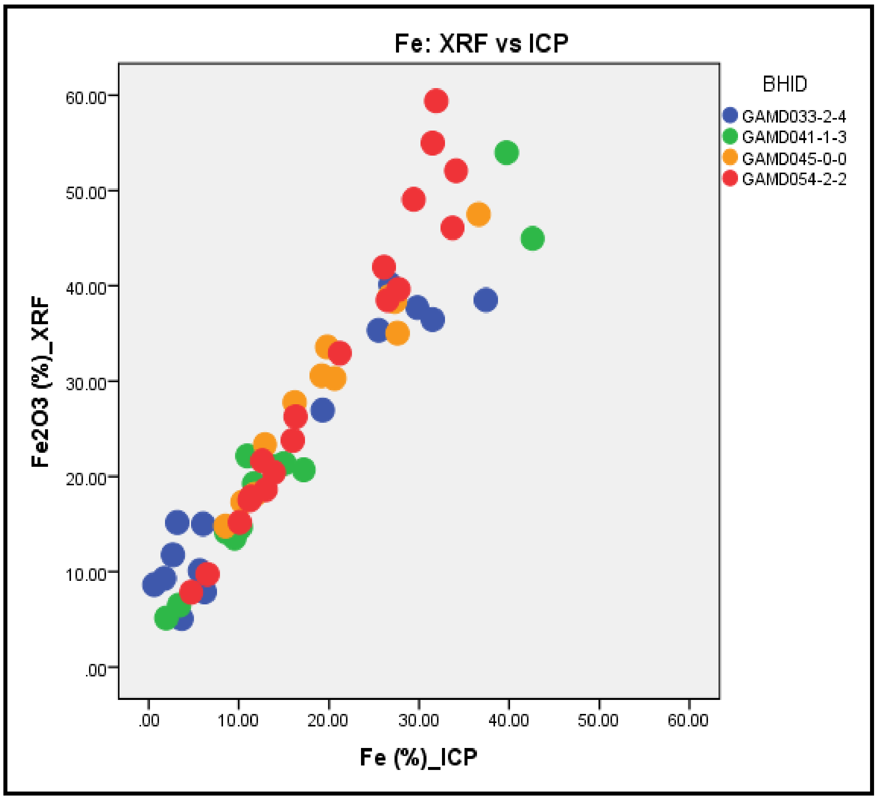

Figure 42. The relationship between Fe_2O_3 (%wt) _XRF and Fe (%) _ICP data, categorised by drillhole ID.

The ICP sample preparation technique is affected by mineral assemblages as some are minerals partially digested. The excellent correlation of Zn and Fe indicates that Zn and Fe are associated mainly with sphalerite and Fe sulphides. The same applies to Mn within the pelitic schist, were the Mn concentration is related to sphalerite and occasionally to alabandite. The silicate and oxide minerals associated with Mn do not dissolve easily, therefore not releasing all the elements from a mineral specimen. Sulphide minerals, on the other hand, dissolve excellently, withe most of the Mn reported by the ICP analysis associated with sphalerite and/or alabandite. The missing value of over-grade Mn analysis (> 50 000 ppm Mn_ICP) in the historical database compromises the Mn_ICP dataset.

5.1.3 Mineral abundance, mineral assemblages and litho-geochemistry

5.1.3.1 Mineral abundance

The XRD technique was used to quantify the mineral abundances of the 49 samples. A semi-quantitative approach was carried out, and therefore the reported quantity of minerals does not reflect exact quantities. The minerals were identified accurately from various XRD spectras. A 2σ (standard deviation) was used to accept the quantities.

In order to demonstrate the accuracy or precision of the XRD analysis, a scatter-plot relationship between silica vs. quartz was assumed, with a reference line representing a monomineralic rock-type relationship between a mineral and associated major element. The quantity of quartz as a common constituent of the sample rocks should never exceed the silica content, as there are other silicate minerals such as amphiboles, micas, etc. present in the analysed samples. Other elements, such as Fe, Mn and Zn, have complex relationships with their associated minerals, hence they are not used to evaluate the accuracy or precision of the XRD dataset. Figure 43 shows the scatter-plot relationship between quartz and silica content, categorised by lithologies.

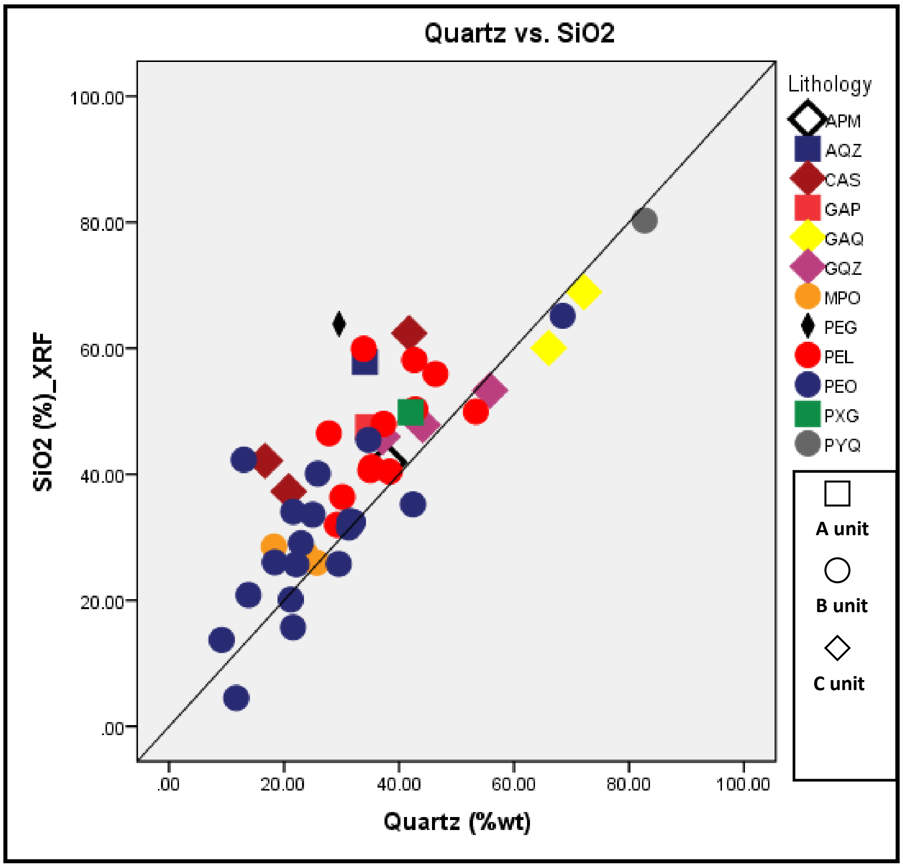

Figure 43. The relationship between quartz (%wt) and SiO_2_XRF, categorised by drillhole ID. A reference line cuts the graph diagonally.

The relationship between quartz and SiO_2 illustrated in Figure 43 shows that some meta-pelite ore samples have a higher quartz concentration than silica content. This is due to a large error margin of 2 %wt quartz (average 2 sigma) reported by the instrument. The quantities of minerals in the rock sample should not be treated as exact amounts. Quantification is guided by what has been observed from hand specimens and microscopy. Chlorite is grouped with clays, as it is impossible to differentiate the two minerals from the XRD spectra, and the same goes for biotite/phlogopite and sillimanite/kyanite.

Alabandite analysis

A coarse-grained alabandite sample from a pelitic schist of drillhole *GAMD054-2-2* was sampled separately and analysed. Alabandite is associated mainly with the pelitic schist and meta-pelite ore of the B1 unit of drillholes *GAMD033-2-4* and *GAMD054-2-2*. Minor concentrations were recorded in the A unit, but no alabandite was recorded within the garnet-magnetite ore and the C unit. Figure 44 shows the positions of alabandite and pyrrhotite on the XRD spectra, and Table 19 presents the concentrations of minerals occurring within the alabandite sample.

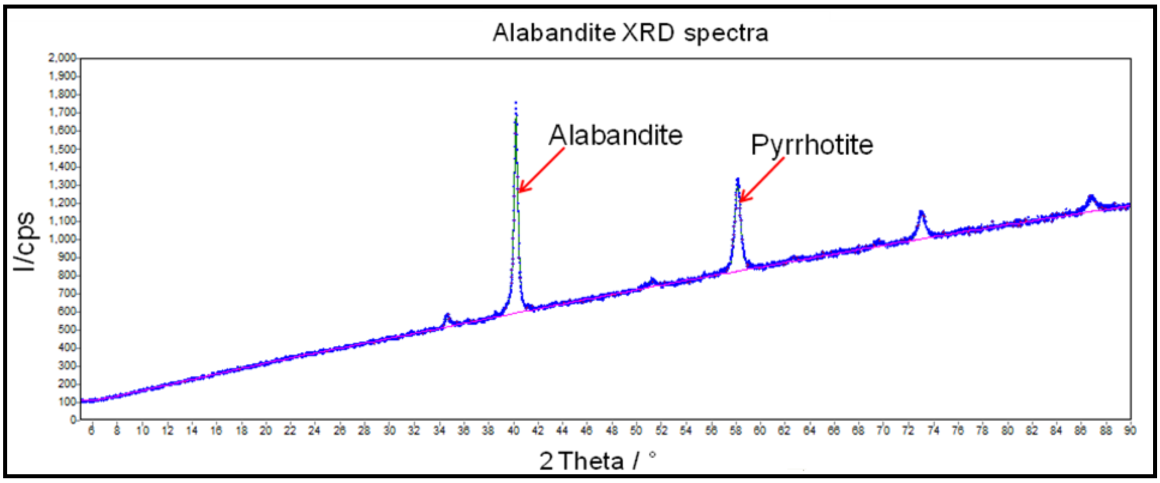

Figure 44. XRD spectra of alabandite, showing the positions of the alabandite and pyrrhotite peaks.

Table 19: Mineralogical composition of vein alabandite sample.

XRD: Alabandite sample mineralogical composition	
Alabandite (%wt)	87.325
Arsenopyrite (%wt)	1.793
Pyrite (%wt)	1.172
Pyrrhotite (%wt)	9.708
Sphalerite (%wt)	<0.01

5.1.3.2 Drillhole *GAMD033-2-4*

Mineral abundance and petrography

Table 20 present the mineral abundance of the sampled intersection of drillhole *GAMD033-2-4*. Alabandite is present within the A and B units and its maximum content is hosted within the pelitic schist. Pyrrhotite is the most common sulphide mineral, with pyrite present only in the pelitic schist and meta-pelite ore. Sphalerite is hosted within the pelitic schist and meta-pelite ore, with the maximum content hosted by meta-pelite ore. Galena is present within the A horizon. The most common silicate minerals are biotite/phlogopite and quartz. Garnets are present within the A unit, with less than 1% present within the top of the pelitic schist. Chlorite/clay minerals are present mainly in the garnet quartzite and pelitic schist.

Table 20. Mineral abundance in each sampled intersection of drillhole GAMD033-2-4.

	GAMD033-2-4									
Lithology	**GAQ**	**CAS**	**GQZ**	**PEL**	**PEL**	**PEL**	**PEO**	**PEO**	**PEO**	**PEG**
Alabandite (%wt)		2.95		10.06				0.71		
Biotite/phlogopite (%wt)	11.44	15.40		30.51	5.08	7.48		1.25	10.83	
Calcite (%wt)		70.26								
Chlorite incl. clays (%wt)			15.80		3.09	3.71				
Franklinite (%wt)		0.57	2.21							
Galena (%wt)		0.42	0.24							
Garnets (%wt)	15.59		19.26	0.33						
Hematite (%wt)										0.71
Hornblende [Fe-Mg] (%wt)	6.93									
Magnetite (%wt)		1.63								
Microcline (%wt)								7.83		
Muscovite (%wt)					9.08			6.81	6.39	20.36
Orthoclase (%wt)					4.21				6.21	21.22
Plagioclase (%wt)										21.10
Pyrite (%wt)						0.27			13.30	
Pyrrhotite (%wt)		3.37	9.96	5.75	28.62	44.14	42.90	31.81	25.23	
Quartz (%wt)	66.04	20.80	37.10	53.36	42.81	38.34	29.51	31.27	22.95	29.56
Sillimanite/Kyanite (%wt)					5.03	4.27	4.19	6.81	5.96	4.63
Sphalerite (%wt)					2.08	1.78	23.44	13.50	9.14	2.41

The summary of the mineral assemblages and rock classification of the sampled intersection of drillhole *GAMD033-2-4* is presented in Table 21. The summary is supported by photomicrographs of the representative rock samples, displaying mainly silicate mineral assemblages, in Figure 45.

Table 21. Summary of mineral assemblages of the sampled intersection of Gams Formation of drillhole GAMD033-2-4.

Gams Formation unit	**Mineral assemblages**	**Rock names**
A2	quartz-garnet-mica(biotite)-pyrrhotite-amphibole	Garnet-amphibole-quartz rock
A3	calcite-quartz-mica(phlogopite) ± pyrrhotite ± alabandite ± magnetite ± franklinite ± galena	Calc-silicate rock
A4	quartz-garnet-micas-feldspar-pyrrhotite-magnetite ± franklinite ± pyrite ± sphalerite	Garnet-quartz rock
B1	quartz-pyrrhotite-micas-alabandite-feldspar-sillimanite ± sphalerite ± garnet ± pyrite	Pelitic schist
	pyrrhotite-quartz-sphalerite-sillimanite-micas-pyrite-feldspar ± pyrite ± alabandite	Meta-pelite ore
Pegmatite	feldspar-quartz-mica(muscovite)-sillimanite ± sphalerite ± hematite	Pegmatite

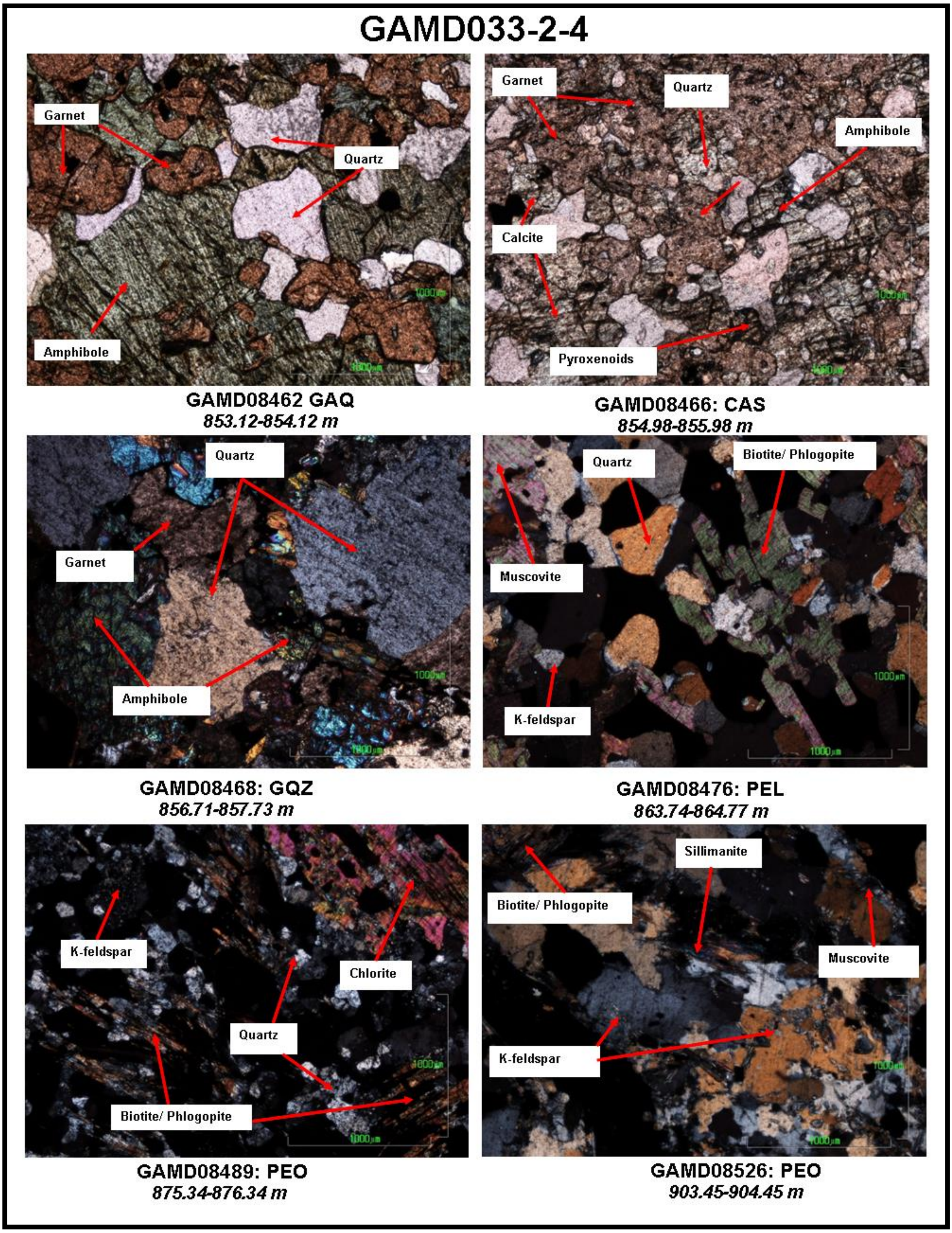

GAMD08462 GAQ
853.12-854.12 m

GAMD08466: CAS
854.98-855.98 m

GAMD08468: GQZ
856.71-857.73 m

GAMD08476: PEL
863.74-864.77 m

GAMD08489: PEO
875.34-876.34 m

GAMD08526: PEO
903.45-904.45 m

Figure 45. Photomicrographs showing the characteristic silicates mineral assemblages of the GAMD033-2-4 drillhole.

Six photomicrographs, shown in Figure 45, present the mineral assemblages of the representative lithologies of the intersection of Gams Formation in drillhole *GAMD041-1-3*. Quartz and amphiboles are the most common constituents. Sillimanite needles are well developed and restricted only to the pelitic schist and meta-pelite ore. The biotite/phlogopite and feldspar grains are slightly altered, as observed in the pelitic schist and meta-pelite ore, unlike those present in the A unit. Garnets are clearly distinct, showing a typical anhedral (round) form with no evidence of zonation.

Lithogeochemistry

Figure 46 shows the relationship between rock types, mineral abundance, whole-rock geochemistry and the behaviour of certain elements and minerals with depth in the Gams Formation intersection of drillhole *GAMD033-2-4*. There is a distinct difference between the rock units, where sharp contacts are displayed by the major elements and associated minerals. The upper contact of the pelitic schist is characterised by a distinct anomaly of manganese and alabandite.

The upper contact of meta-pelite ore marks the anomalous increase in zinc and sphalerite. The A unit is characterised by the enrichment of most major elements, with the exception of the zinc content. The zinc content increases slightly with depth from the A unit to the B1 unit. The zinc content increases sharply at the base of the pelitic schist (PEL) into the meta-pelite ore (PEO), where it reaches a maximum content towards the base of B unit, with 13.17 %wt ZnO and 9.14 %wt sphalerite content, although the maximum sphalerite content of 23.44 %wt is present at the top of the B2 unit, with 11.96 %wt ZnO. The Mn content increases with depth from the top of the A unit to the top of PEL, where it reaches its maximum of 20.61 % MnO, and then decreases abruptly to 0.62 %wt MnO at the base of PEL, after which it increases slightly to PEO (3.74 %wt MnO) and then decreases with depth towards the base of the B unit. Alabandite is present within the calc-silicate rock (2.95 %wt), is highest in the PEL (10.06 %wt) and lowest within PEO (0.71 %wt).

The SiO_2 content decreases with increasing depth, and has an inverse relationship with the Fe_2O_3 content. The quartz and pyrrhotite contents mimic the trend of the SiO_2 and the Fe_2O_3 content respectively. The occurrence of mica minerals, feldspars, sillimanite, amphiboles and clay minerals is associated with the distribution of K_2O and Al_2O_3, hence their relationships were compared. The mica mineral content is at its maximum at the top of the pelitic schist (PEL), and lowest in the meta-pelite ore. The minimum concentration of Al_2O_3 is at the top of the meta-pelite ore, and its maximum concentration is within the garnet quartzite (GQZ). A pegmatite unit hosts the highest Al_2O_3 and K_2O contents, and therefore the highest content of feldspars. The first appearance of sillimanite/kyanite is with the pelitic schist, common within the B unit.

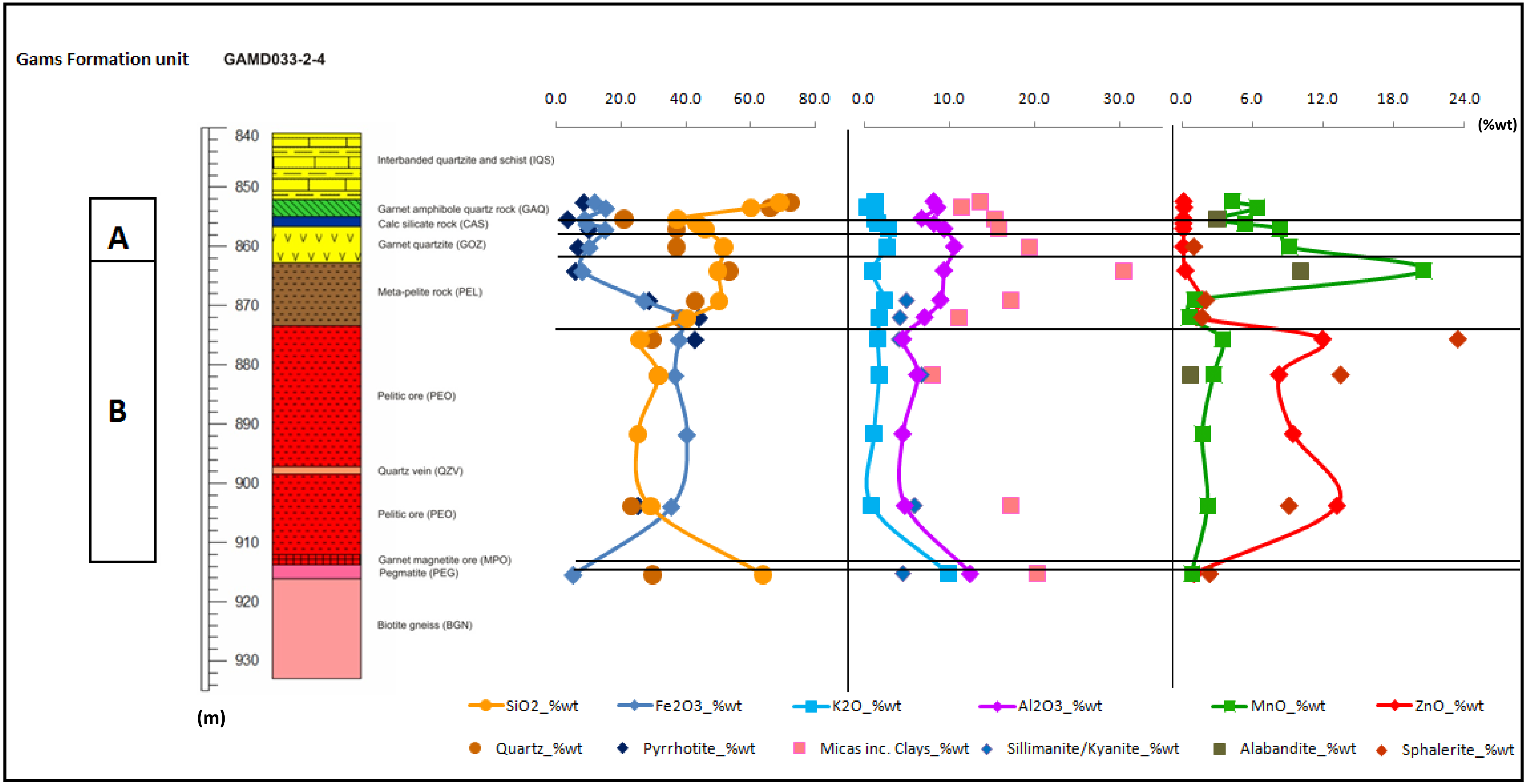

Figure 46. Lithogeochemical presentation of drillhole GAMD033-2-4.

5.1.3.3 Drillhole *GAMD041-1-3*

Mineral abundance and petrography

Table 22 presents the mineral abundance of the sampled intersection of drillhole *GAMD041-1-3*. Alabandite is absent from all rock units in this drillhole intersection, although jacobsite and franklinite are present within PEL and AQZ respectively. Pyrrhotite is present throughout, reaching its maximum within the meta-pelite ore. Pyrite is also present in the B unit and in the AQZ. Sphalerite is hosted in the pelitic schist, meta-pelite ore and the garnet-magnetite rock, with its maximum content hosted by garnet-magnetite ore. Galena is present in magnetite-bearing rocks. The most common silicate minerals are biotite/phlogopite, chlorite/clays and quartz. Garnets are present within the A unit, with less than 1% present within the top of the pelitic schist. Sillimanite/kyanite is restricted mainly to the pelitic schist.

Table 22. Mineral abundance in each sampled intersection of drillhole GAMD041-1-3.

GAMD041-1-3										
Lithology	**CAS**	**CAS**	**PEL**	**PEL**	**PEO**	**PEO**	**PEO**	**MPO**	**GAP**	**AQZ**
Actinolite (%wt)									3.11	
Biotite/phlogopite (%wt)		6.90	19.10	4.39	10.25	10.33	9.10		13.47	18.21
Calcite (%wt)	33.97	6.43								
Chlorite incl. clays (%wt)	14.47	21.27	22.70		0.13	3.88				20.94
Cummingtonite (%wt)									9.74	4.41
Diopside (%wt)	8.68	9.44								
Epidote (%wt)	5.99	1.84								3.16
Franklinite (%wt)										1.22
Galena (%wt)								0.94	0.10	0.14
Garnets (%wt)	0.60	2.54							19.41	
Hematite (%wt)								0.63		2.31
Hornblende [Fe-Mg] (%wt)	6.08	8.53		3.88		3.47		9.45	5.20	2.57
Jacobsite (%wt)				1.10						
Magnetite (%wt)	0.93									2.17
Microcline (%wt)				14.16						
Muscovite (%wt)			17.00	12.12	14.50	8.37				
Orthoclase (%wt)			1.66	4.22	2.08	0.58				3.33
Paragonite (%wt)				2.19						
Plagioclase (%wt)	9.37									
Pyrite (%wt)			6.58	1.73	2.18		21.00	6.17		0.29
Pyrrhotite (%wt)	3.22	1.30	2.49	9.60	47.20	50.61	19.00	20.94	14.30	7.04
Quartz (%wt)	16.68	41.75	27.80	42.65	21.58	9.15	32.00	18.23	34.67	34.08
Sillimanite/Kyanite (%wt)			3.01	3.74	1.71					
Sphalerite (%wt)			0.25	0.21	0.37	13.60	18.00	43.64		0.13

The summary of the mineral assemblages and the rock classification of the sampled intersection of drillhole *GAMD041-1-3* are presented in Table 23. This summary is supported by photomicrographs of representative rock samples, displaying mainly silicate mineral assemblages, in Figure 47.

Table 23. Summary of mineral assemblages of the sampled intersection of the Gams Formation of drillhole GAMD041-1-3.

Gams Formation unit	**Mineral assemblages**	**Rock name**
A3	calcite-quartz-pyroxene-mica-amphiboles-feldspars-garnets ± pyrrhotite ± magnetite	Calc-silicate rock
B1	quartz-micas-feldspar-sillimanite(kyanite)-amphiboles-pyrrhotite-garnets ± sphalerite ± garnet ± pyrite ± jacobsite	Pelitic schist
	pyrrhotite-quartz-micas-sphalerite-feldspar-amphiboles-sillimanite(kyanite) ± pyrite	Meta-pelite ore
B2	sphalerite-pyrrhotite-quartz-garnets-amphiboles-magnetite-pyrite ± hematite ± galena ± spinel ± pyroxenes	Garnet-magnetite ore
C2	quartz-garnet-amphiboles-mica(phlogopite)-pyrrhotite-pyroxenes ± galena ± magnetite ± sphalerite	Garnet-amphibole-pyroxene-quartz rock
	quartz-amphiboles-mica(phlogopite)-feldspar-pyrrhotite-epidote -garnets-franklinite ± pyrite ± sphalerite ± galena	Amphibole-quartz rock

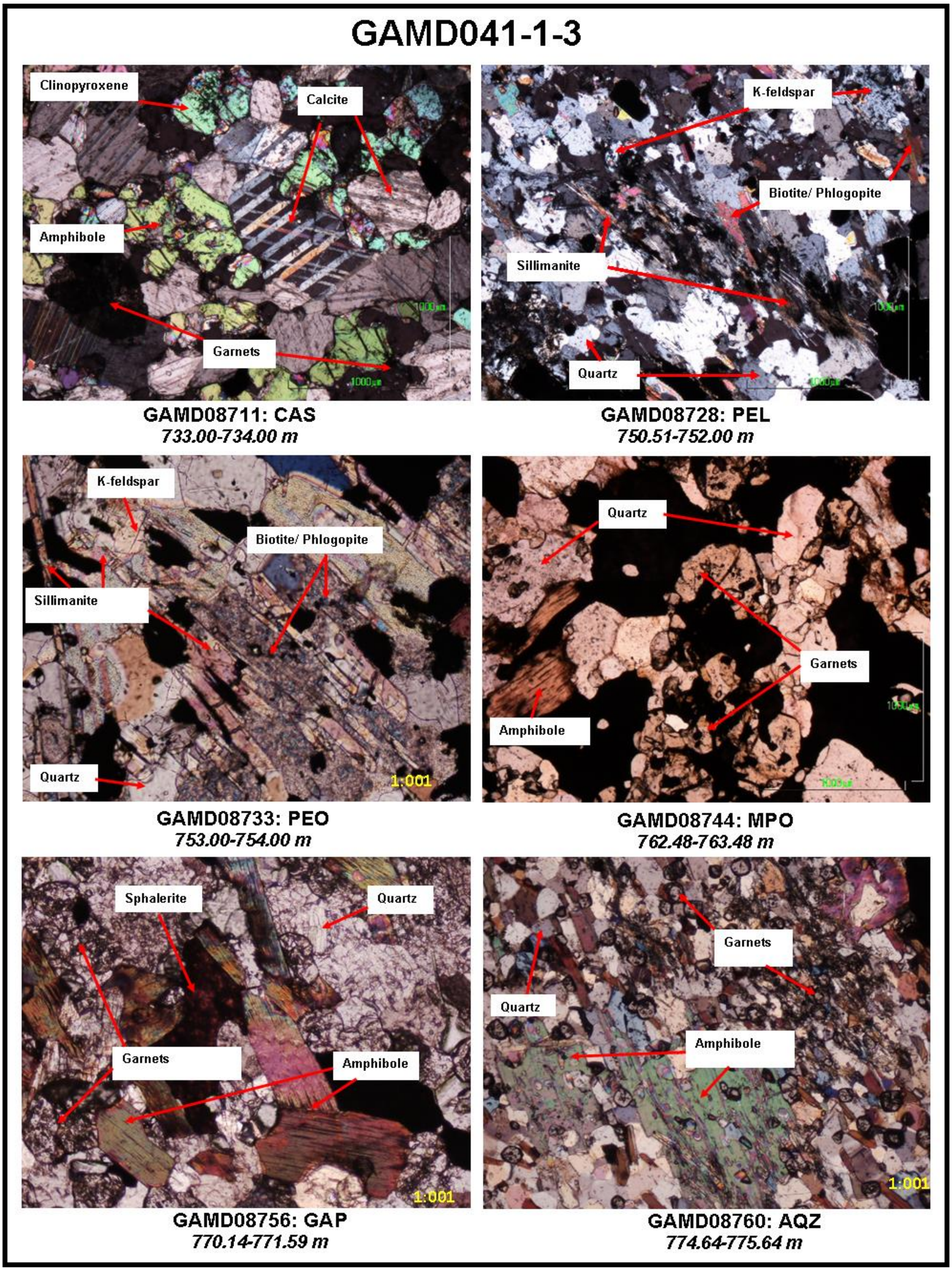

GAMD08711: CAS
733.00-734.00 m

GAMD08728: PEL
750.51-752.00 m

GAMD08733: PEO
753.00-754.00 m

GAMD08744: MPO
762.48-763.48 m

GAMD08756: GAP
770.14-771.59 m

GAMD08760: AQZ
774.64-775.64 m

Figure 47. Photomicrographs showing the characteristic silicate mineral assemblages of drillhole GAMD041-1-3.

Six photomicrographs, shown in Figure 47, show the mineral assemblages of representative lithologies of the intersection of the Gams Formation in drillhole *GAMD041-1-3*. Quartz, biotite/phlogopite and amphiboles are the most common constituents. Sillimanite needles are well developed and restricted to the pelitic schist and meta-pelite ore. The biotite/phlogopite and feldspars grains are slightly altered in the pelitic schist and the meta-pelite ore. Garnets are clearly distinct, showing a typical anhedral (round) form with no evidence of zonation.

Lithogeochemistry

Figure 48 shows the relationship between rock types, mineral abundance, whole-rock geochemistry and the behaviour of certain elements and minerals with depth in the Gams Formation intersection of drillhole *GAMD041-1-3*. There is a distinct difference between the rock units, where sharp contacts are displayed by major elements and associated minerals. The upper contact of the pelitic schist is characterised by a distinct anomaly of manganese, and the presence of jacobsite instead of alabandite.

The manganese content increases abruptly from calc-silicate rock, from about 2 %wt MnO, into the top of the pelitic schist, slightly above 10 %wt MnO, and then decreases abruptly towards the base of the pelitic schist into the meta-pelite ore, where MnO has the lowest concentration. The garnet-magnetite ore (MPO) and the C unit host a significantly high MnO content, but the AQZ, at the base of the C unit, hosts the lowest MnO content. High quantities of MnO are associated with the garnet-bearing rocks.

The sphalerite content is below 1 %wt in the pelitic schist and the A unit, but highest in the meta-pelite ore and garnet-magnetite ore. The sphalerite content in the garnet-magnetite ore is unusually higher than the Zn concentration.

The iron content increases steadily from the A unit towards the base of the B1 unit, where it reaches its maximum, then decreases significantly towards the B2 and into the C unit. The iron content increases abruptly from the pelitic schist into the meta-pelite ore, and again decreases abruptly into the garnet magnetite ore. The pyrrhotite content is equal to the iron content within the B unit, and this signifies that Fe sulphide minerals are the most abundant Fe-bearing mineral.

The Al_2O_3 content is highest in the pelitic schist and increases towards the bottom contact of the C unit. The Al_2O_3 trend is similar to the silica trend. The mica content is anomalously high towards the upper contact of the pelitic schist. The K_2O is slightly high in the calc-silicate rock and dips at the upper contact of the pelitic schist, then increases slightly, decreases in the meta-pelite ore and increases towards the bottom contact of the C unit.

The silica content generally decreases significantly from the A unit into the top of the B1 unit. Towards the bottom contact of the calc-silicate rock silica content is high. The pegmatite unit occurs between the calc-silicate rock and the pelitic schist. The silica content in the B unit decreases with depth, while the pelitic schist contains the highest silica and quartz content. The silica and iron content has an inverse relationship, and the same applies to the pyrrhotite and quartz contents.

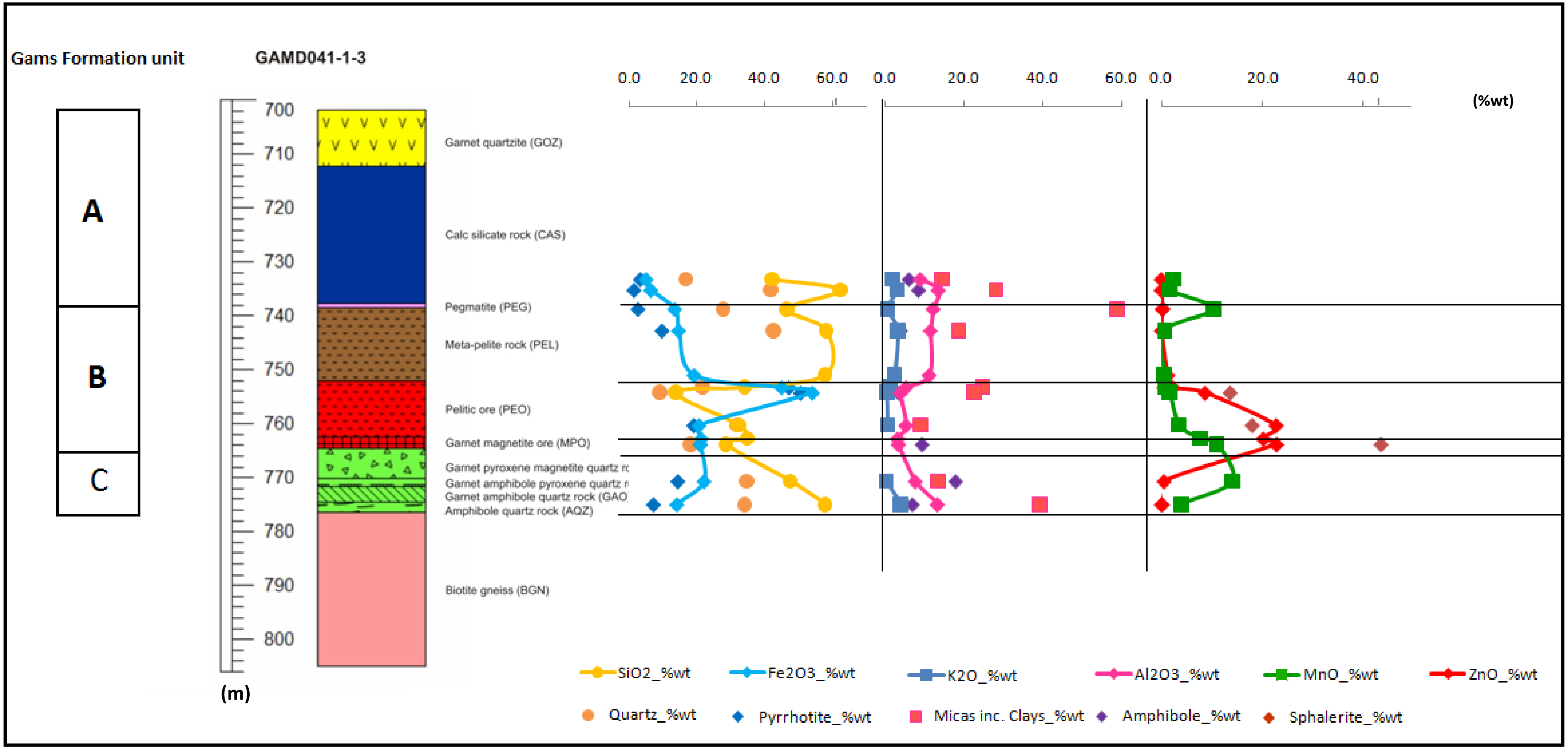

Figure 48. Lithogeochemical presentation of drillhole GAMD041-1-3.

5.1.3.4 Drillhole *GAMD045-0-0*

Mineral abundance and petrography

Table 24 presents the mineral abundance of the sampled intersection of drillhole *GAMD045-0-0*. Pyrrhotite and quartz are present throughout the sampled intersection, with the exception of one meta-pelite ore sample, which has no quartz but the maximum pyrrhotite content. Pyrite is absent throughout the meta-pelite ore. Sphalerite is hosted in the pelitic schist, and in the meta-pelite ore, garnet-magnetite rock and the rocks of the C unit. The highest concentrations of sphalerite are hosted within garnet-magnetite ore and meta-pelite ore. Galena is present within the garnet quartzite, garnet-magnetite ore and the amphibole-magnetite magnetite rocks. The most common silicate minerals are biotite/phlogopite, chlorite/clays, muscovite and quartz. Sillimanite/kyanite, muscovite and orthoclase are restricted mainly to the pelitic schist.

Table 24. Mineral abundance in each sample intersection of drillhole GAMD045-0-0.

GAMD045-0-0										
Lithology	**GQZ**	**PEL**	**PEL**	**PEO**	**PEO**	**MPO**	**MPO**	**APM**	**PXG**	**GQZ**
Biotite/phlogopite (%wt)		6.76	6.41	2.90	2.47	6.58			6.32	8.04
Chlorite incl. clays (%wt)	4.18		3.95		6.22				10.91	10.00
Cummingtonite (wt%)								10.65		
Diopside (%wt)	1.82					5.02			11.38	
Epidote (%wt)	1.51					5.60		8.12	12.51	
Galena (%wt)	0.61						2.19	0.27		
Garnets (%wt)	27.47									
Hematite (%wt)	0.43						2.47	0.43		0.44
Hornblende [Fe-Mg] (%wt)			5.08		3.58			7.66		3.26
Magnetite (%wt)							14.30	19.47	0.79	
Muscovite (%wt)		5.60	6.66	9.58	14.77					
Orthoclase (%wt)		8.77	5.07	13.73						
Pyrite (%wt)	0.51	0.36					8.04	2.38		
Pyrrhotite (%wt)	18.39	44.17	35.62	54.69	36.27	31.67	14.20	10.85	16.06	21.36
Quartz (%wt)	44.09	30.13	34.98		24.98	23.67	25.70	37.90	42.04	55.82
Sillimanite/Kyanite (%wt)		3.60	2.21	9.90	1.17					
Sphalerite (%wt)		0.59		9.16	10.53	23.61	33.10	2.27		1.09

The garnet quartzite is the only unit of drillhole *GAMD045-0-0* that represents the A unit. It is also present below the C unit. The compositions of the garnet quartzites are different. The GQZ in the C unit contain garnets or magnetite. Table 25 presents a summary of mineral assemblages, supported by the petrographic microphotographs of mainly silicate minerals in Figure 49.

Table 25. Mineral assemblages of the sampled intersection of the Gams Formation of the GAMD045-0-0.

Gams Formation unit	**Mineral assemblages**	**Rock name**
A4	quartz-garnet-amphibole-chlorite-galena-pyroxene-pyrrhotite ± epidote ± pyrite	Garnet quartzite
B1	quartz-pyrrhotite-micas-feldspar-sillimanite(kyanite)-amphiboles ± sphalerite ± garnet ± pyrite ± apatite	Pelitic schist
	pyrrhotite-quartz-micas-sphalerite-amphiboles-sillimanite(kyanite)-feldspar ± pyrite ± apatite	Meta-pelitic ore
B2	sphalerite-magnetite-pyrrhotite-quartz-mica-pyrite-garnet ± pyroxene ± hematite ± galena ± epidote ± apatite	Garnet-magnetite ore
C1	quartz-magnetite-amphibole-pyrrhotite-garnets-pyroxene-epidote ± sphalerite ± galena ± pyrite	Amphibole-pyroxene-magnetite-quartz rock
C2	quartz-pyrrhotite-pyroxene-garnets-micas-epidote-(chlorite/phlogopite)-amphiboles ± hematite ± sphalerite	Pyroxenoids-garnet rock
	quartz-pyrrhotite-chlorite-phlogopite-amphiboles ± hematite ± sphalerite	Garnet quartzite*

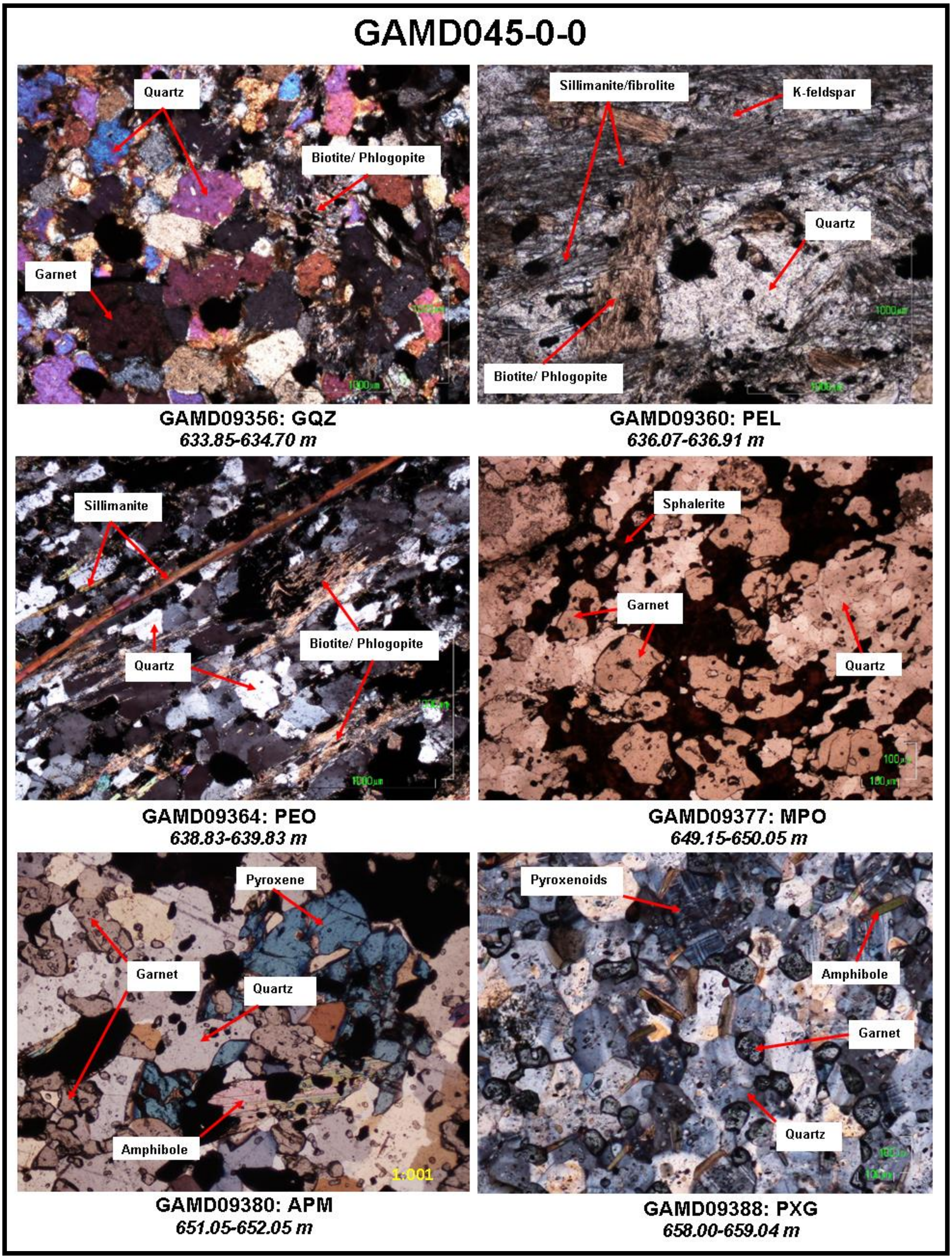

GAMD09356: GQZ
633.85-634.70 m

GAMD09360: PEL
636.07-636.91 m

GAMD09364: PEO
638.83-639.83 m

GAMD09377: MPO
649.15-650.05 m

GAMD09380: APM
651.05-652.05 m

GAMD09388: PXG
658.00-659.04 m

Figure 49. Photomicrographs showing the characteristic silicate mineral assemblages of GAMD045-0-0 drillhole.

Six photomicrographs, shown in Figure 49, present mineral assemblages from representative lithologies of drillhole GAMD045-0-0. Quartz is the most common constituent. Sillimanite (fibrolite) is restricted to the pelitic schist and meta-pelite ore only. The sections from pelitic schist and meta-pelitic ore are altered slightly, with most of the feldspars broken down into muscovite and sillimanite. Clay minerals are observed mostly within micas, especially the biotite/phlogopite grains. Garnets are clearly distinct, showing a typical anhedral (round) form, with no evidence of zonation.

Lithogeochemistry

Figure 50 shows the relationship between rock types, mineral abundance, whole-rock geochemistry, and the behaviour of certain elements and minerals with depth in the Gams Formation intersection of drillhole *GAMD045-0-0*. Compared to the other three drillholes, *GAMD045-0-0* has the thinnest units, with a poorly developed A unit.

Manganese content is high in the garnet quartzite (above 15 %wt MnO), and low in the pelitic schist and meta-pelite ore, below 1.5 %wt MnO. The manganese content increases from 8 %wt MnO in the garnet-magnetite ore to a maximum of 16 %wt MnO in the C unit. No alabandite or Mn-bearing spinel minerals was recorded in the garnet quartzite, pelitic schist, or meta-pelitic ore. The high manganese content is associated with garnet- and pyroxene-bearing rock of the A unit, garnet-magnetite ore, and C unit.

The zinc and sphalerite contents increase sharply from top contact of meta-pelite ore, and reach their maximum content in the garnet-magnetite ore. The zinc content is significantly higher than sphalerite in the garnet-magnetite compared to the ratios in the pelitic schist. The zinc content is low in the A unit, pelitic schist and in the C unit.

The iron content is low in the A and C unit and high in the meta-pelite ore. The pyrrhotite content mimics the trend of the iron content. The pyrrhotite content is significantly lower than the iron content due to the presence of magnetite in the C unit. The iron content is inversely related to the silica content, with an exception in the meta-pelite ore and garnet-magnetite ore, where they are both decreasing.

The silica content decreases with increasing depth, and has an inverse relationship with iron content. The quartz and pyrrhotite content mimic the trend of the SiO_2 and the Fe_2O_3 contents respectively. The silica content is low in the meta-pelite ore and highest in the A and C units. The quartz content mimics the silica content.

The Al_2O_3 is low in the meta-pelite ore, garnet-magnetite ore, and in the upper C unit. It is high in the garnet quartzite and pelitic schist and towards the bottom contact of the C unit. However, the mica mineral content is at its maximum at the top of the pelitic schist (PEL), and lowest in the meta-pelite ore. The minimum concentration of Al_2O_3 is at the top of the meta-pelite ore, and its maximum concentration is within the garnet quartzite (GQZ). A pegmatite unit hosts the highest Al_2O_3 and K_2O contents and therefore the highest content of feldspars.

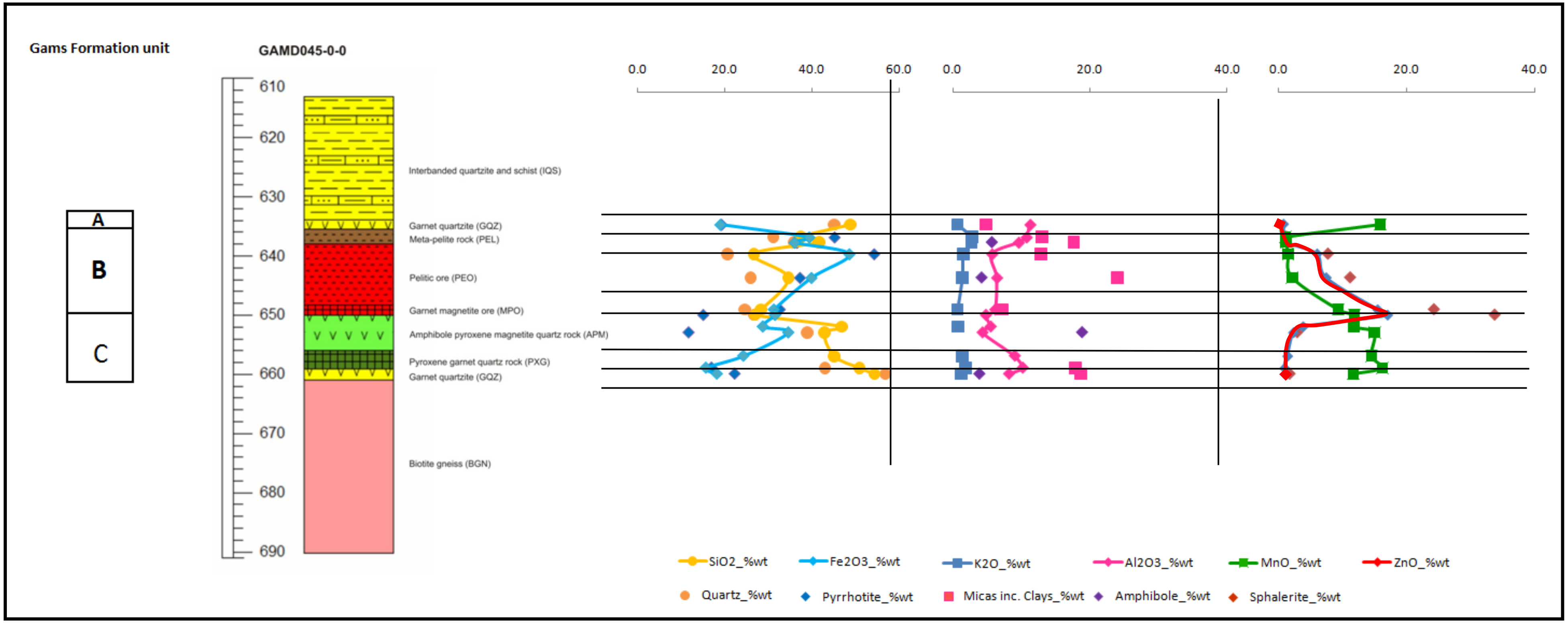

Figure 50. Lithogeochemical presentation of drillhole GAMD045-0-0.

5.1.3.5 Drillhole *GAMD054-2-2*

Mineral abundance and petrography

Table 26 presents the mineral abundance of the samples of drillhole *GAMD054-2-2*. Alabandite is present within the pelitic schist and meta-pelite ore, with its maximum of 16% at the top of the pelitic schist. The alabandite content decreases with depth and is absent towards the bottom contact of the meta-pelite ore. The sphalerite content is significantly high in the meta-pelite ore, with a concentration of above 2 %wt and a maximum of 20.2 %wt. The pelitic schist hosts concentrations below 0.5 %wt. Pyrrhotite, quartz and micas are the most common minerals, making up at least 80% of the rock samples in most cases. Pyrite is present at a lower concentration, of below 2%, with the exception of two meta-pelite ore samples with a concentration of slightly above 5% and 12%.

Table 27 presents the summary of the mineral assemblages of the intersection from drillhole *GAMD054-2-2.* The B unit, which constitutes pelitic schist, pyritic quartzite and meta-pelite ore, is the only sampled unit of the *GAMD054-2-2* drillhole. All the units are well developed and significantly wide. Mineral assemblages in Table 27 are supported by the petrographic microphotographs in Figure 51, which shows the representative B unit.

Table 27. The mineral assemblages of the sampled section of the Gams Formation of drillhole GAMD054-2-2.

Gams Formation unit	Mineral assemblages	Rock name
B1	quartz-pyrrhotite-feldspars-micas-alabandite-silllimanite(kyanite)-amphiboles-pyrite ± garnets ± sphalerite	Meta-pelite rock
	pyrrhotite-quartz-sphalerite-micas-sillimanite(kyanite)-alabandite-amphiboles-feldspar ± pyrite ± hematite ± galena	Pelitic ore
	quartz-muscovite-pyrrhotite ± sphalerite ± pyrite	Pyritic quartzite

GAMD054-2-2																			
Lithology	**PEL**	**PEL**	**PEL**	**PEL**	**PEL**	**PEO**	**PEO**	**PEO**	**PEO**	**PEO**	**PEO**	**PEO**	**PEO**	**PEO**	**PEO**	**PYQ**	**PEO**	**PYQ**	**PEO**
Alabandite (%wt)	4.67	16.00	10.71	1.32		0.85	0.66	2.44	0.96		1.58	0.18	0.34						
Biotite/phlogopite (%wt)	11.58	5.22	6.14	17.93	3.48	2.17	7.11		5.43	7.18		2.61	4.74	10.19	8.31		3.69		2.98
Chlorite incl. clays (%wt)	11.20	2.41	1.40		3.92	3.15	2.90		2.48	4.52	3.50	2.36	3.04		2.95		3.18		
Galena (%wt)											0.08		0.20						
Hematite (%wt)	0.63	0.71			0.12				1.76		0.17	0.80							
Hornblende [Fe-Mg] (%wt)	6.10	1.27	1.88		3.22		1.91			5.98	1.58		16.99		6.77	1.89			1.73
Microcline (%wt)				22.00		2.61					6.50	7.12							
Muscovite (%wt)	8.83	10.22	9.74		12.84	9.98	7.74	1.29	5.17	4.87			5.53	6.31	28.90	7.22	14.4	6.75	8.01
Orthoclase (%wt)	2.11	6.29	4.81		2.02				1.14				7.67	5.46			30.3		1.15
Paragonite (%wt)	1.90				5.40														
Pyrite (%wt)	1.67	1.16	1.36	1.41	1.96		0.15						5.04	12.30		1.44		1.68	
Pyrrhotite (%wt)	4.95	27.50	20.30	14.76	28.42	56.64	60.80	64.40	43.62	41.55	46.00	34.74	17.44	44.40	14.11	9.93	34.5	8.35	15.46
Quartz (%wt)	46.4	29.21	35.21	33.85	37.33	22.11	13.82	11.67	21.56	31.44	21.17	42.43	25.85	18.36	34.67	78.96	13.0	82.73	68.47
Sillimanite/Kyanite (%wt)			8.39	8.72	1.21								7.67						
Sphalerite (%wt)			0.03		0.08	2.48	0.21	20.20	17.87	4.47	19.38	9.75	5.49	2.94	4.29	0.57	0.96	0.50	2.19

Table 26. Mineral abundance in each sample intersection of drillhole GAMD054-2-2.

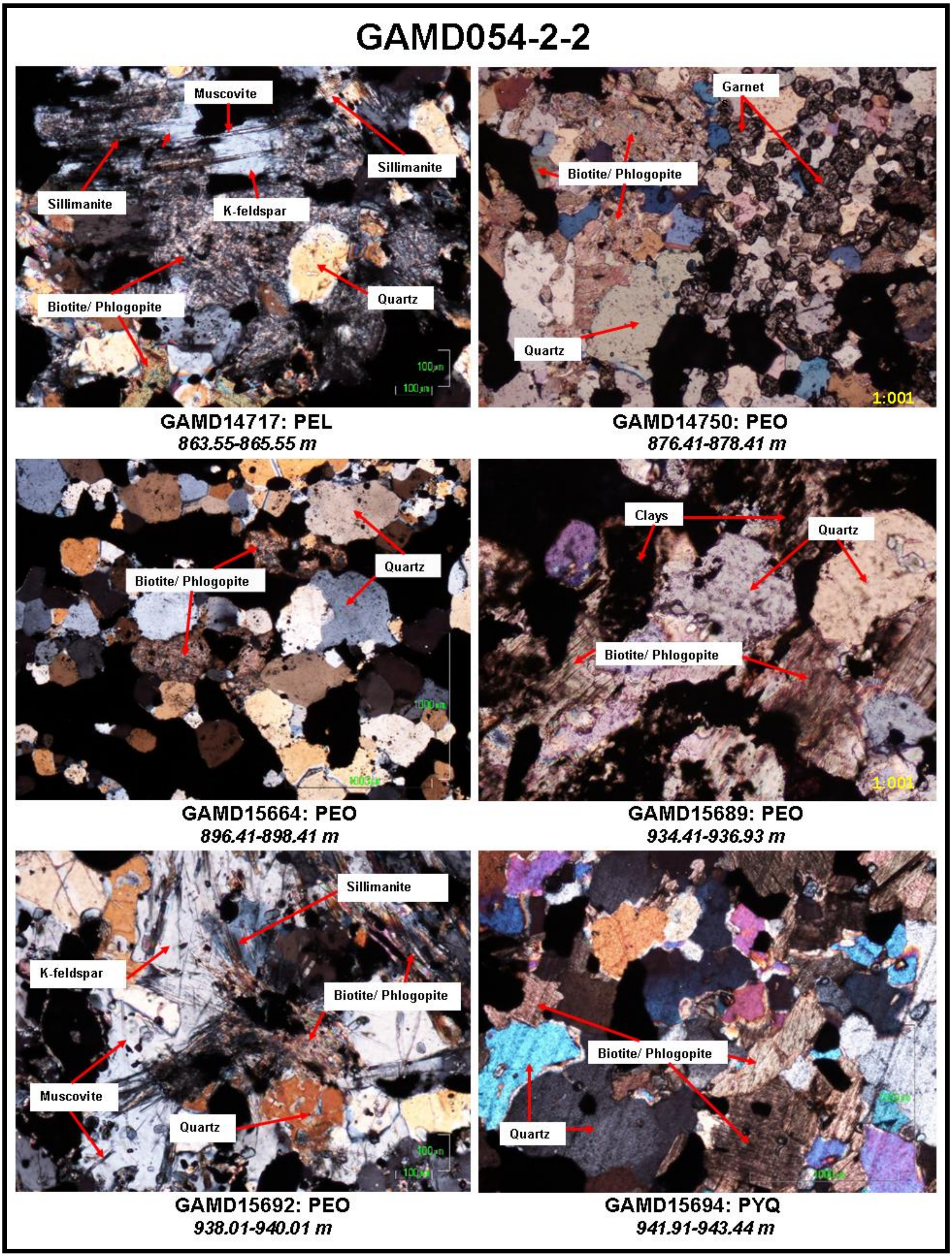

Figure 51. Photomicrographs showing the characteristic silicate mineral assemblages of drillhole GAMD054-2-2.

The six photomicrographs in Figure 51 show the mineralogical assemblages of the four sampled lithologies of drillhole *GAMD054-2-2*. Quartz and biotite/phlogopite are the most common minerals. Biotite/phlogopite shows some degree of alteration. Garnets grains are present within the meta-pelite ore, with only a sample at the upper contact meta-pelite ore. The feldspar grains in the pelitic schist are altered and the muscovite needle-like, and clay minerals are present as by-products.

Lithogeochemistry

Figure 52 shows the relationship between rock types, mineral abundance, whole-rock geochemistry and the behaviour of certain elements and minerals with depth in the Gams Formation intersection of drillhole *GAMD054-2-2*. There is a distinct difference between the rock units, where sharp contacts are displayed by abrupt changes in major elements and associated minerals.

The upper contact of the pelitic schist is characterised by a distinct anomaly of manganese and alabandite. The Mn content decreases with depth and no alabandite is recorded towards the lower contact of meta-pelite ore.

The sphalerite and zinc content in the pelitic schist is significantly low, with a concentration of less than 0.1% sphalerite. The sphalerite and zinc contents are high in the meta-pelite ore and display a zigzag trend. The zinc and sphalerite contents are low within the pyritic quartzite, which occurs as thin bands towards the lower contact of the meta-pelite ore.

The iron concentration increases sharply at the contact of the pelitic schist and meta-pelite ore, and decreases towards the lower contact of the meta-pelite ore. The pyrrhotite content mimics the iron content, except within the pyritic quartzite. The iron content starts with a lower concentration at the top contact of the pelitic schist and increases significantly at the same sample where the anomalous manganese concentration occurs, then decreases and eventually increases towards the lower contact into the meta-pelite schist.

The silica content is inversely proportional to the iron content. The quartz content generally mimics the trend of the silica content. The silica and quartz contents are mostly high within the pelitic schist and generally low within the meta-pelite ore, although a zigzag trend is displayed.

The K_2O and Al_2O_3 are significantly higher within the pelitic schist and lower within the meta-pelite ore. There is a significant increase in K_2O and Al_2O_3 between the two bands of pyritic quartzite, where the mica minerals also are spiking. The mica contents are higher within the pelitic schist, accompanied by a significant content of feldspars. The feldspar content is higher in the middle of the meta-pelite ore unit.

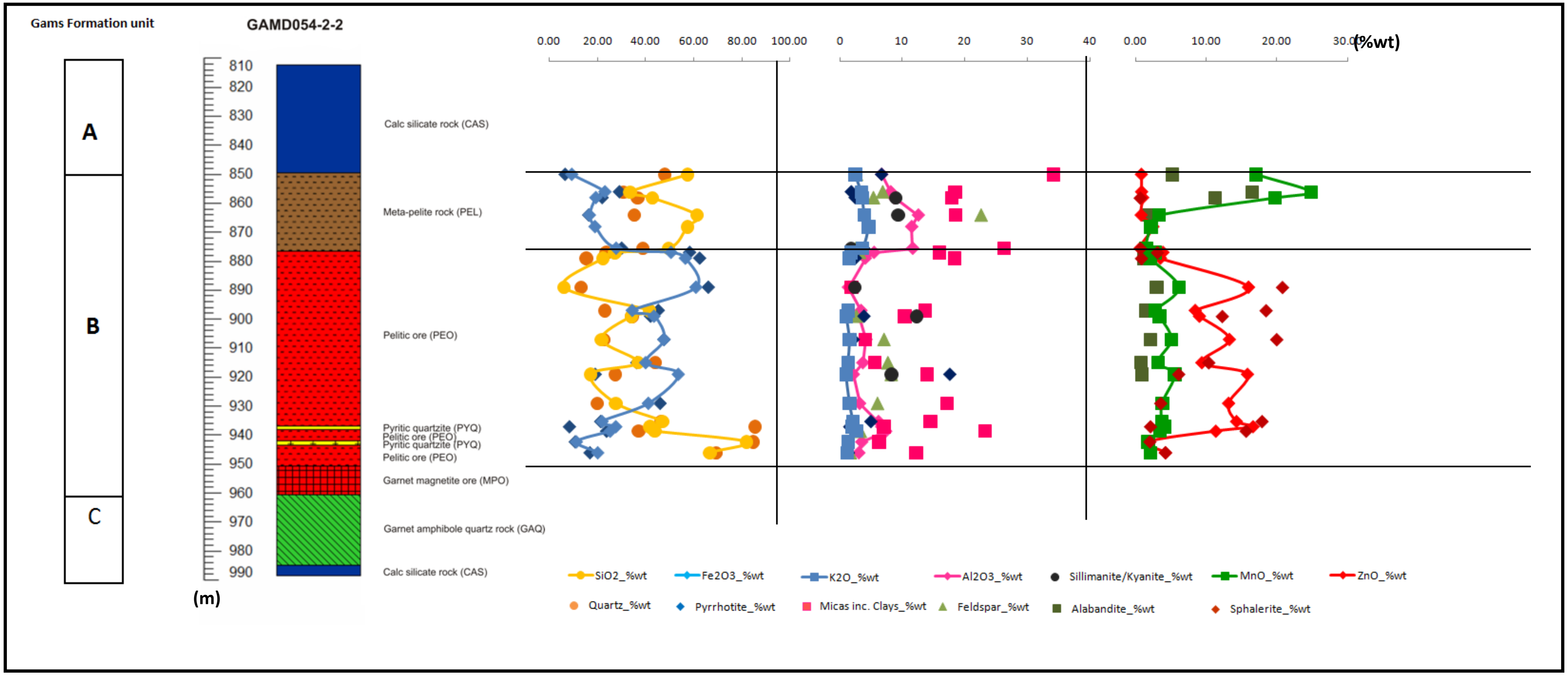

Figure 52. Lithogeochemical presentation of drillhole GAMD054-2-2.

Section 2: Sulphide mineral textures

In this section, representative samples showing textural relationships typical of sulphide minerals in the four drillholes are presented.

5.2.1 Textural relationships of alabandite

Typically, three textures occur: alabandite hosting minute exsolution and/or inclusion blebs of pyrrhotite, pyrite and other sulphide minerals; inclusion- and/or exsolution-free alabandite that coexists with sphalerite and pyrrhotite; and alabandite as inclusion and/or exsolution in sphalerite. There also are three associated, distinct pyrrhotite grain size distributions occurring within alabandite, namely (see Figures 53, 54 and 55 for illustration):

1. Large (> 50 microns) subhedral-anhedral grains, often encasing sphalerite
2. Small (10 to 50 microns) grains of pyrrhotite orientated in three different orientations, along the cubic cleavages of alabandite
3. Fine-grained (< 10 microns) grains that occur along the grain boundaries of alabandite crystals

In general, pyrrhotite exsolution/inclusion blebs form along the cubic cleavage planes of alabandite, forming cloth-like textures in three different orientations. Pyrrhotite grains are not equigranular, but vary from less than 1 µm to ca. 1 mm in diameter. There usually is a lack of small pyrrhotite grains around the large and subhedral-anhedral pyrrhotite grains (see Figure 53).

Sphalerite grains tend to be enclosed and/or partly enclosed by large pyrrhotite exsolution grains (> 50 microns) (see Figures 53 to 55). Pyrite, arsenopyrite and covellite are closely associated with large- and medium-grained pyrrhotite exsolution grains (see Figure 54 (A)). Pyrite occurs as minute exsolution/ inclusion blebs, and as remobilised grains, but often idiomorphic. Arsenopyrite occurs mainly as large idiomorphic grains. In Figure 55 (A), pyrite seems to be at the late stage, and fracture-filling with graphite over-printed on the pyrrhotite and alabandite.

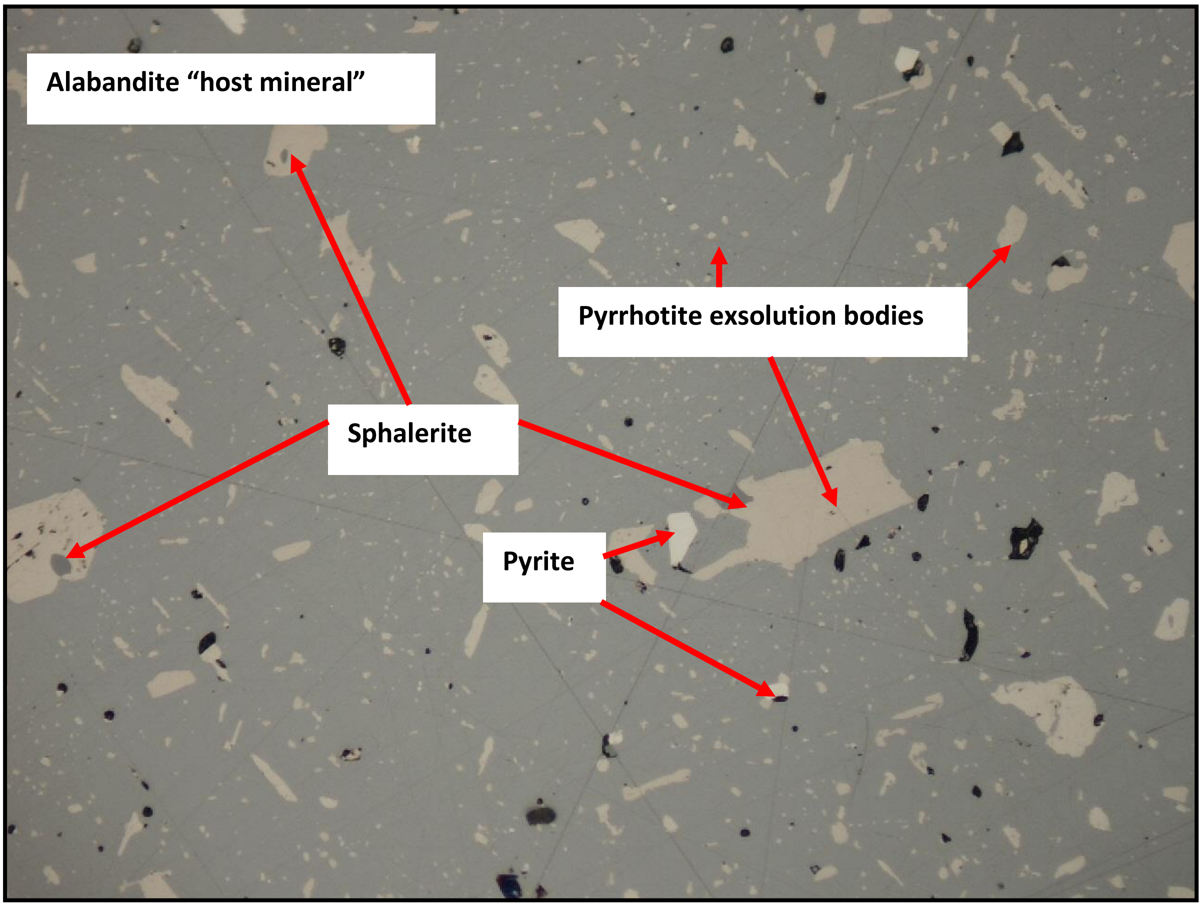

Figure 53. Photomicrograph of alabandite sample from a remobilised vein in drillhole GAMD054-2-2. Field of view = 2.5 mm.

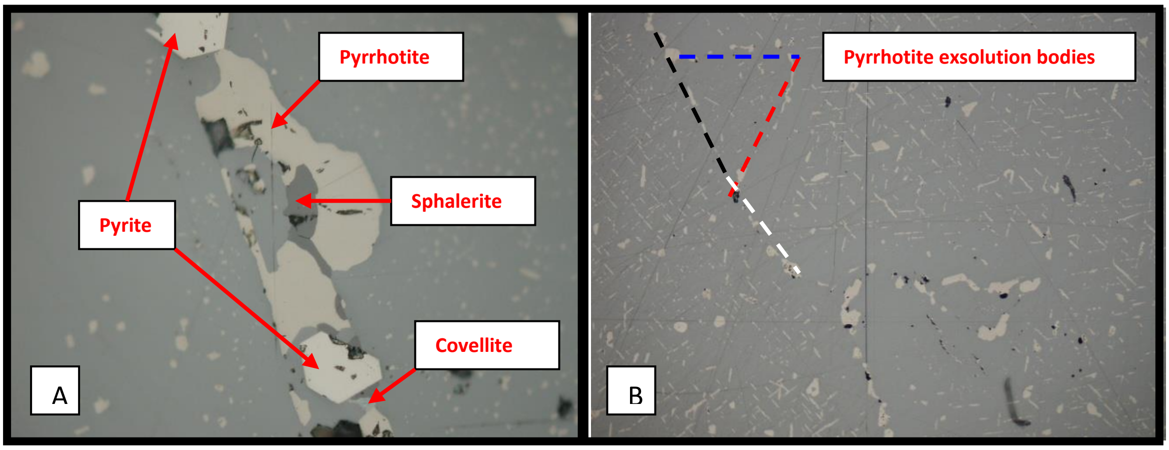

Figure 54. Photomicrographs of alabandite samples showing exsolution. Field of view = 0.25 mm (A) and 1.2 mm (B).

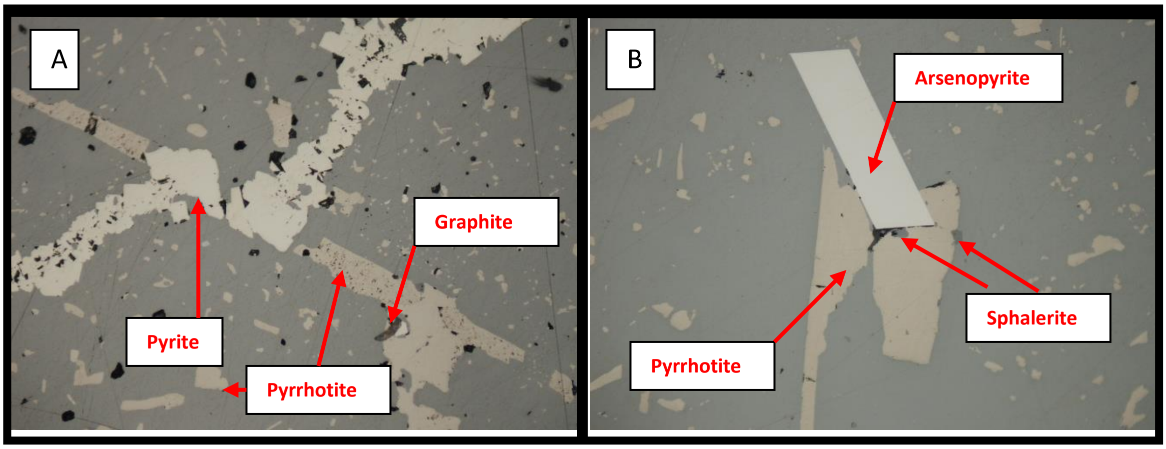

Figure 55. Photomicrographs of alabandite textural relationships between pyrite arsenopyrite and pyrrhotite. Field of view = 0.25 mm (A) and 0.25 mm (B).

The secondary electron imaging of alabandite in Figure 56 shows pyrrhotite grains distributed in three different orientations, evident in three colour-coded broken lines. Alabandite is homogenous and only hosts varying sizes of pyrrhotite grains.

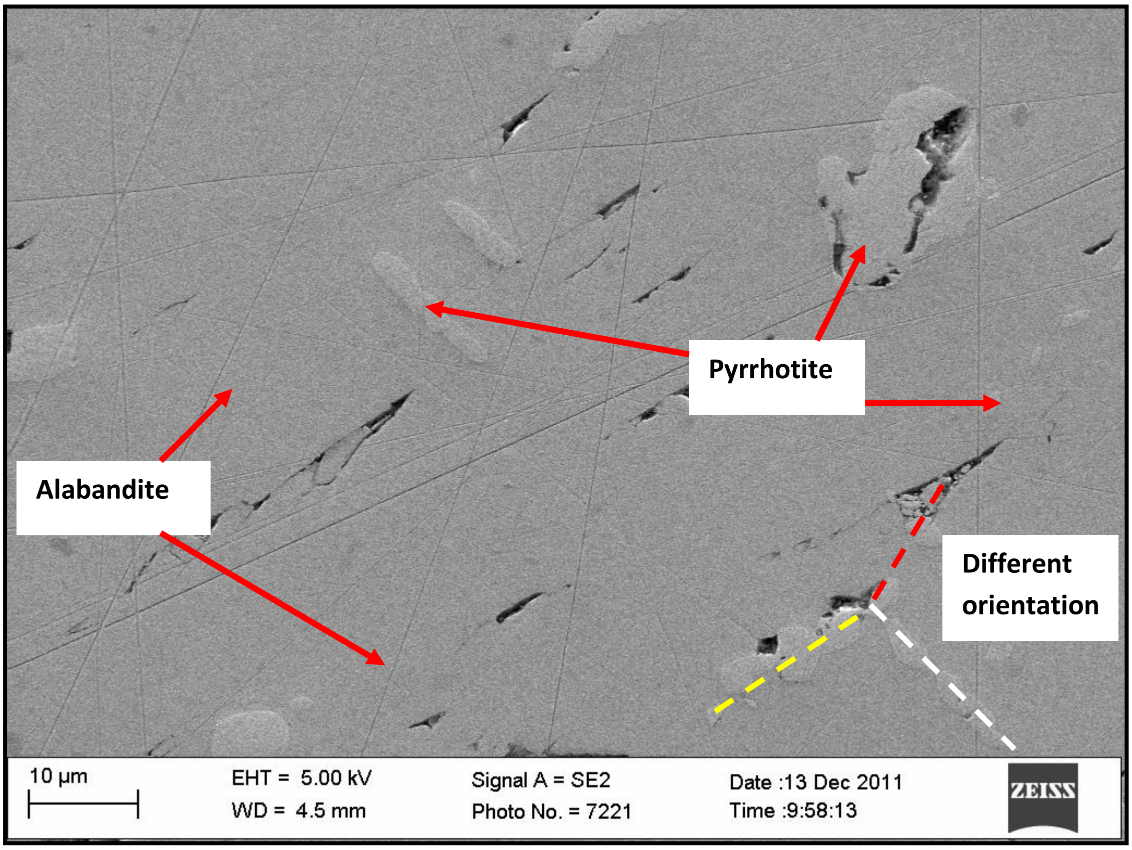

Figure 56. Secondary electron imaging of granular alabandite sample.

5.2.2 Textural relationships of coexisting alabandite-sphalerite-pyrrhotite

Sample GAMD08489 in Figure 57, a pelitic schist sample, shows coexisting alabandite, sphalerite and pyrrhotite mineral phases, representative of drillhole *GAMD033-2-4*. Typically, alabandite is anhedral and found between pyrrhotite and sphalerite. With this texture, alabandite does not host any minute exsolution/ inclusion grains of either sphalerite or pyrrhotite, but these can occur as small grains at the contact of alabandite with other minerals. In Figure 57 there are grains of alabandite within a sphalerite grain boundary, shown by the white broken line.

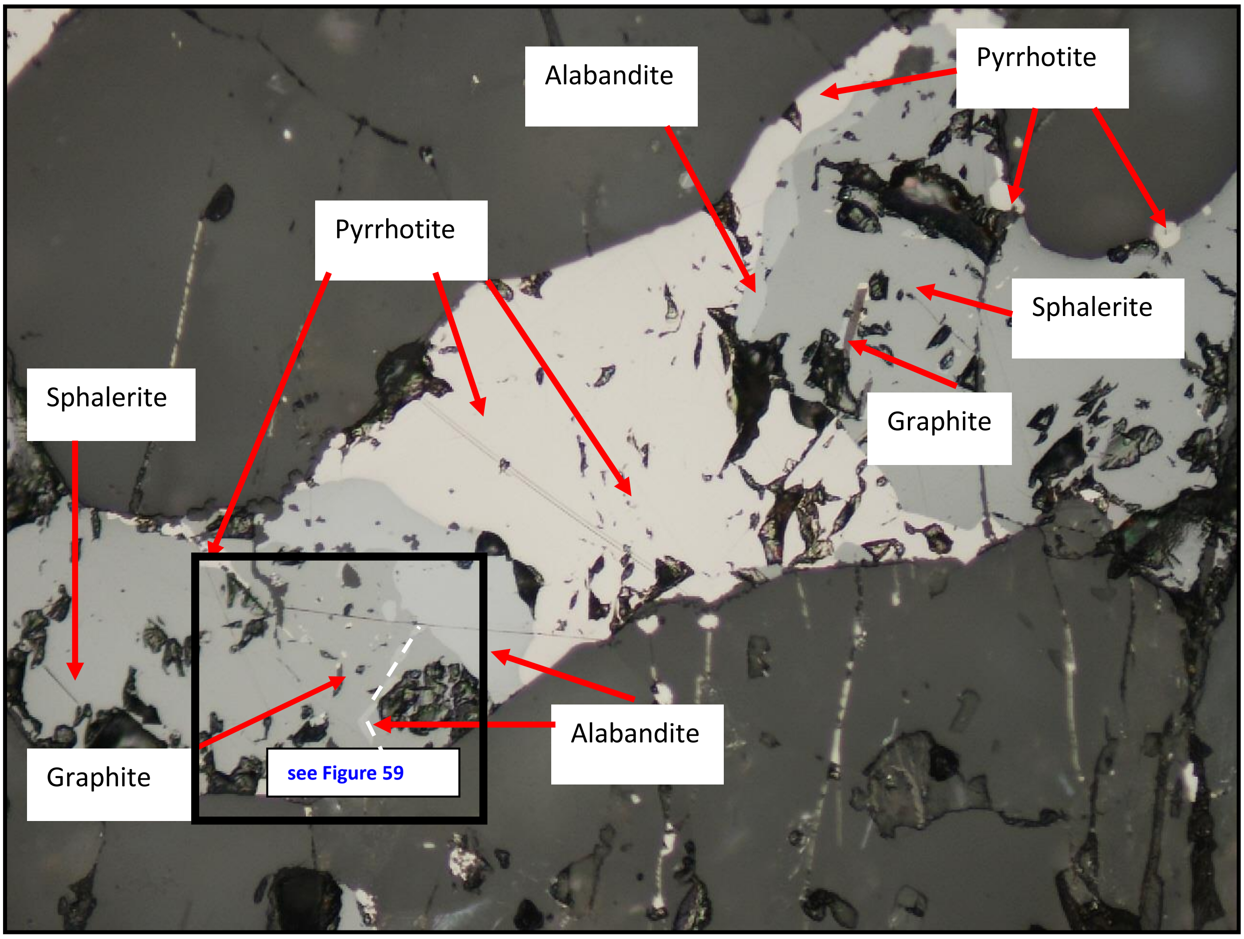

Figure 57. Photomicrograph of sample GAMD08489 of drillhole *GAMD033-2-4*. Field of view = 0.6 mm.

Tabular graphite grains (average of 0.4 microns x 4 microns) typically occur within sphalerite. Less than 10 micron grains of alabandite and pyrrhotite coexist with graphite inclusions. The high-resolution images in Figure 58 (A and B) show the textural relationships of graphite, alabandite and pyrrhotite grains within sphalerite. In most cases, graphite imprints or cross-cuts pyrrhotite or alabandite grains whenever they coexist.

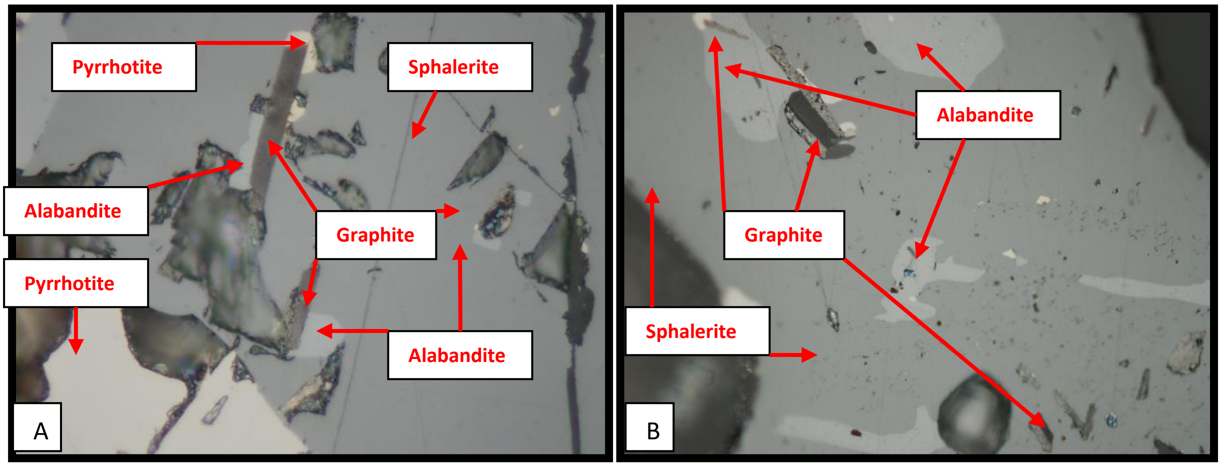

Figure 58. Photomicrographs showing textural relationships of alabandite, sphalerite, pyrrhotite and graphite. Field of view (A) = 0.12 mm and (B) = 0.25 mm.

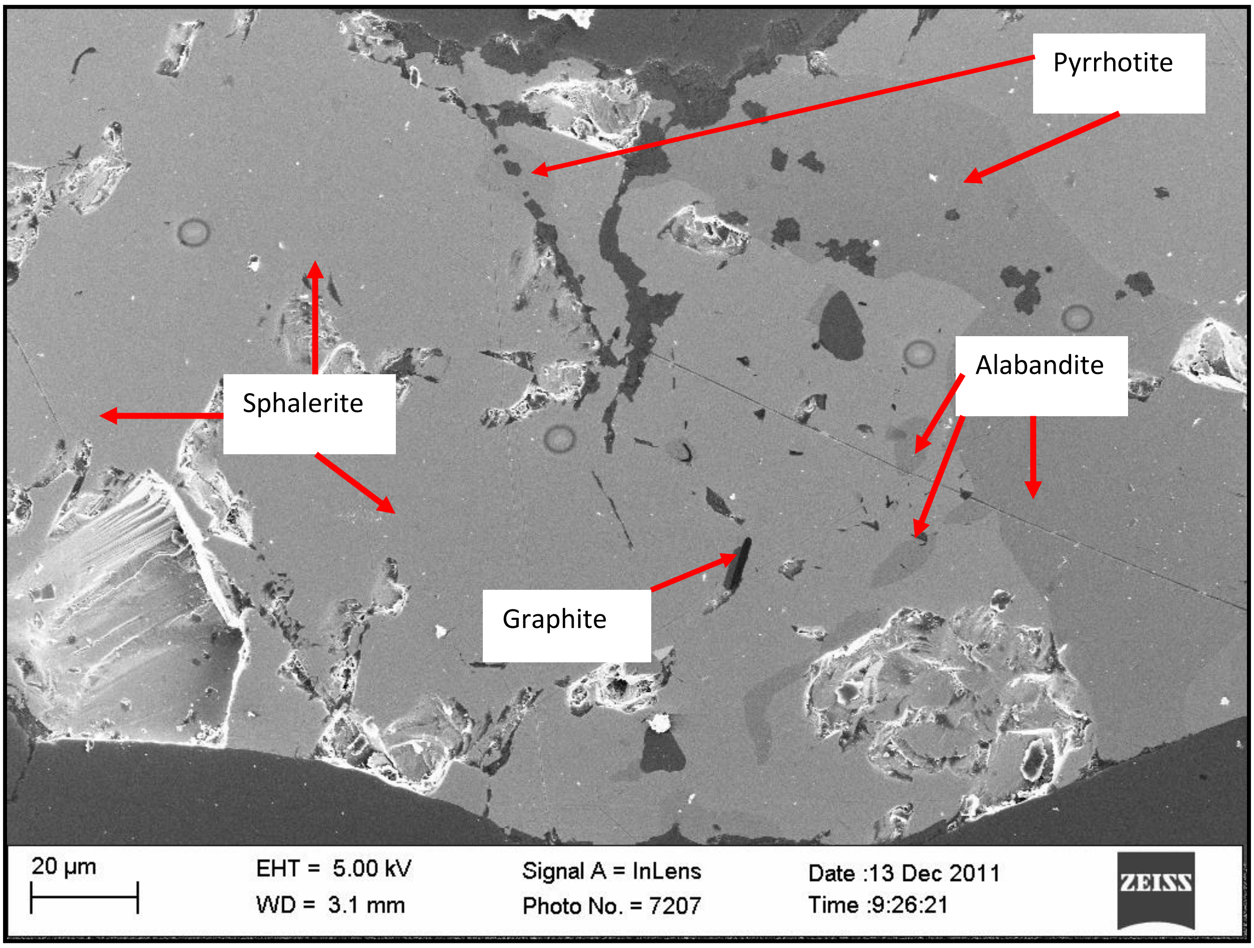

Figure 59. Secondary electron imaging of portion in Figure 57.

Secondary electron imaging in Figure 59, a high resolution of a portion of Figure 55, shows the textural relationships between coexisting pyrrhotite, alabandite and sphalerite grains. The contacts between mineral grains are defined well, with no reaction effects between mineral phases. In this case, alabandite does not host any exsolved mineral phases or inclusions. Alabandite occurs along crystal planes of sphalerite.

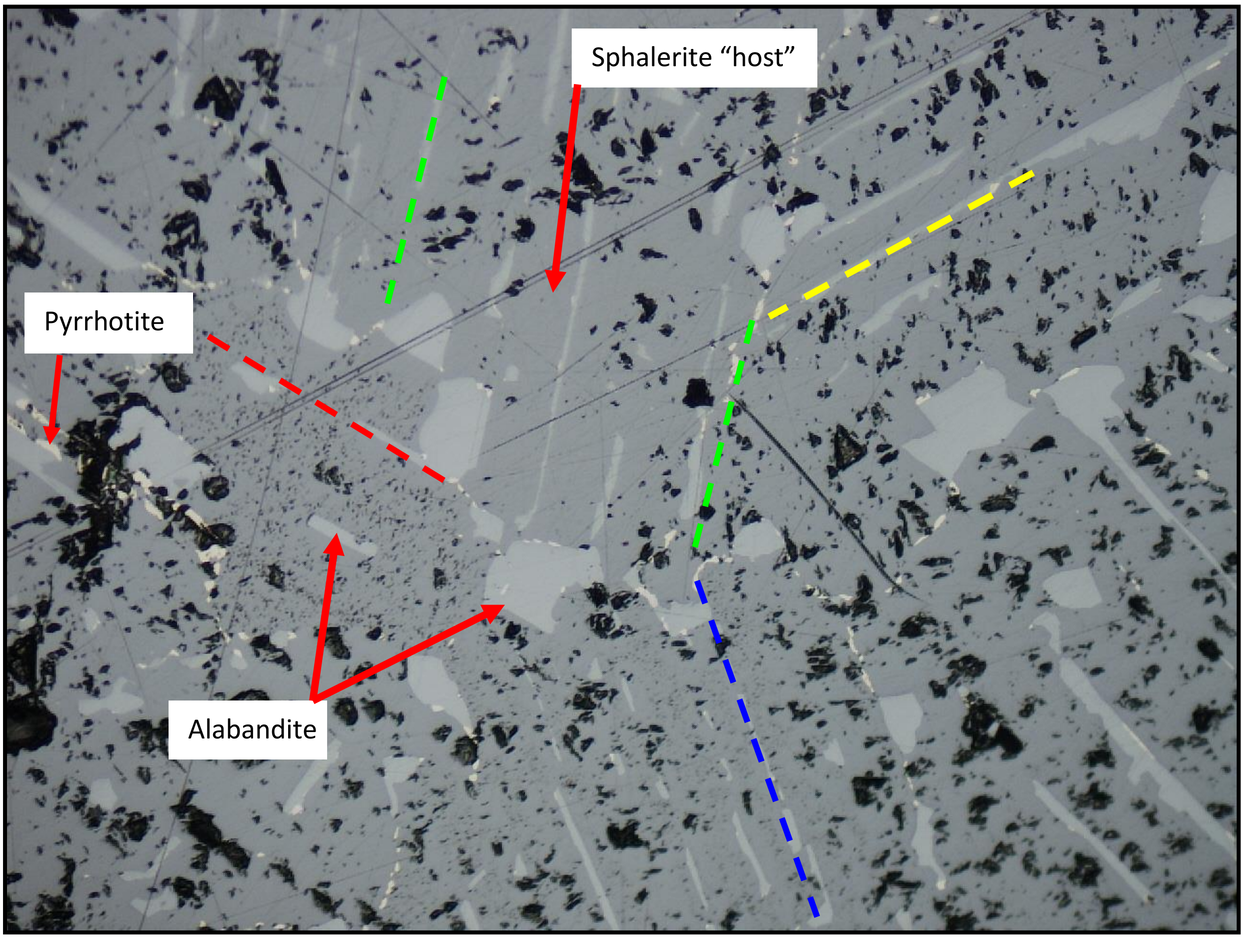

Figure 60. Textural relationships between coexisting alabandite, pyrrhotite and sphalerite of sample GAMD14750 of drillhole *GAMD054-2-2*. Field of view = 1.2 mm

Figure 60 shows another textural relationship between alabandite and sphalerite. Alabandite and pyrrhotite grains are present along the crystal planes of sphalerite, depicted by the blue, green, yellow and red dotted lines. Alabandite grains show subhedral to anhedral grain forms, with elongated tabular grains being the most common. Larger, anhedral grains of alabandite are distributed along the crystal planes of sphalerite, while elongated grains occur away from the vertices.

Pyrrhotite grains are less than 5 microns, while alabandite grains range from 5 microns to less than 50 microns.

Figure 61A shows an alabandite grain (ca. 125 microns) surrounded by quartz and micas, with pyrrhotite grains on the boundary and within alabandite. There is a 10 micron inclusion of quartz within the alabandite grain. Smaller alabandite grains occur within a silicate matrix, without any association with pyrrhotite or sphalerite. Figure 61B shows the "imprints" within an alabandite "background" and chalcopyrite and pyrrhotite conforming to the shape of these imprints. The "imprints" are alabandite grains and could have a different texture to the usual observed so far.

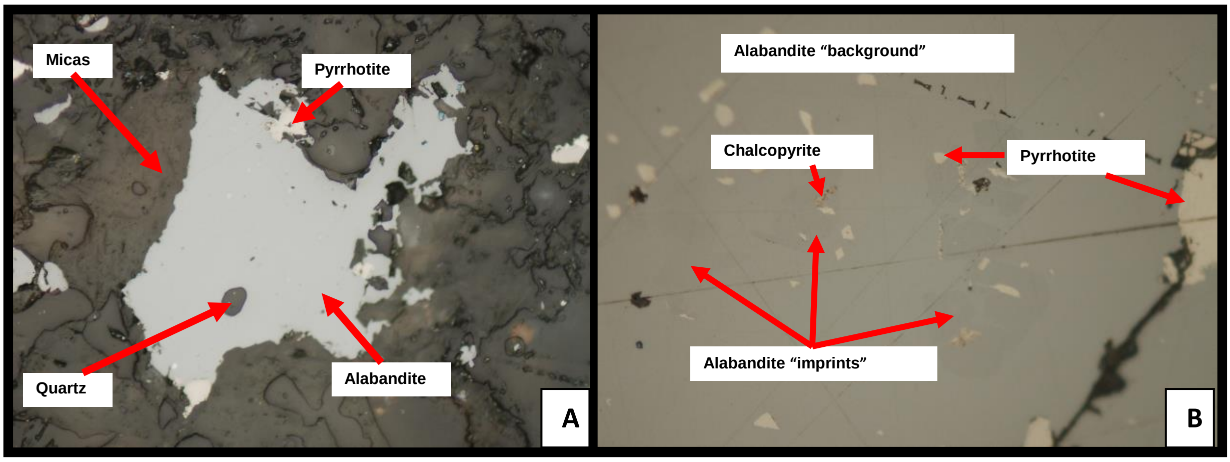

Figure 61. Photomicrographs showing textural relationship between alabandite with silicates and other sulphide minerals. Field of view (A) = 0.6 mm and (B) = 0.25 mm.

5.2.3 Textural relationships of sphalerite without alabandite

Figure 62 shows the textural relationships of sphalerite in the absence of alabandite. The image shows sphalerite coexisting with pyrophanite, rutile, pyrrhotite, garnet and quartz. Rutile grains of less than 50 micron occur within quartz. Pyrophanite occurs as a rim around a rutile grain.

Sphalerite is uniform throughout, without exsolution blebs or inclusions, but small sphalerite, along with rutile, is included within the quartz.

Pyrrhotite occurs between garnets, pyrophanite and sphalerite. There are distinct boundaries between coexisting mineral phases, with no obvious reaction textures.

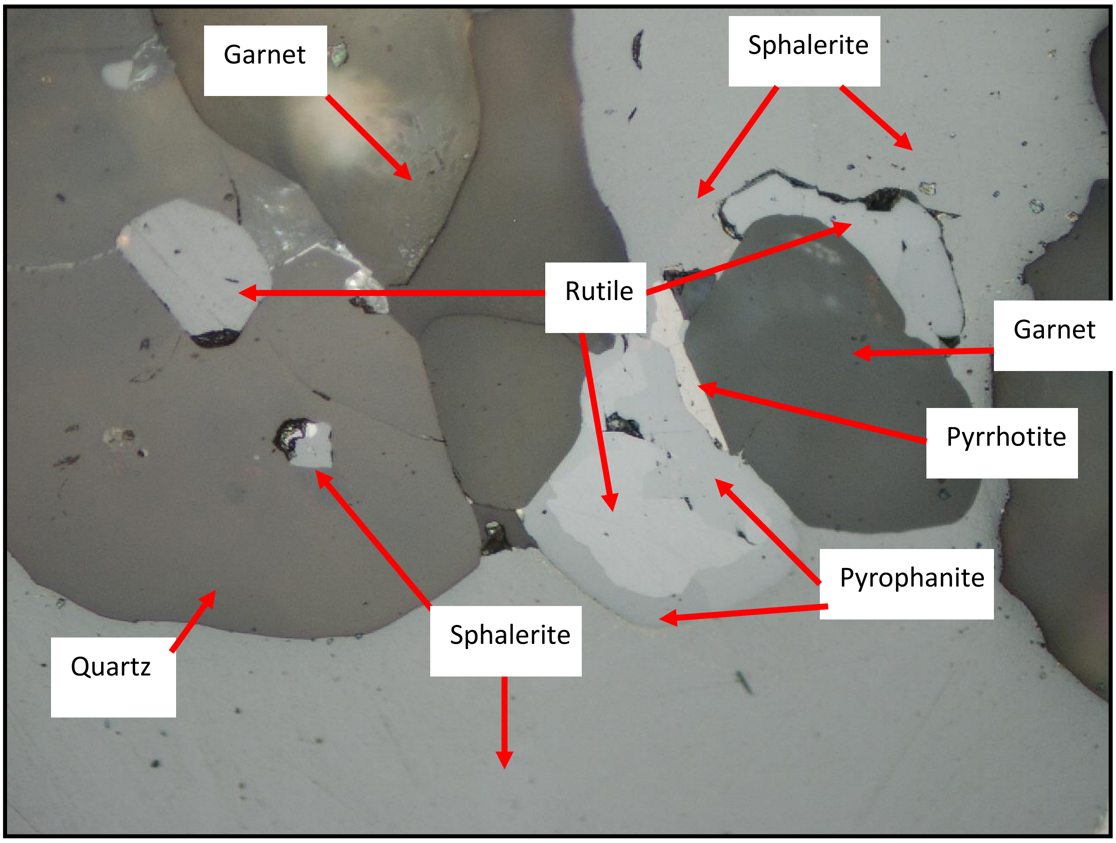

Figure 62. Photomicrograph of sample GAMD08744 of drillhole GAMD041-1-3. Field of view = 0.6 mm.

Figure 63 shows a high-resolution version of Figure 62. The image confirms that the grain boundaries between mineral phases are distinct, with no obvious reaction rims between coexisting mineral phases.

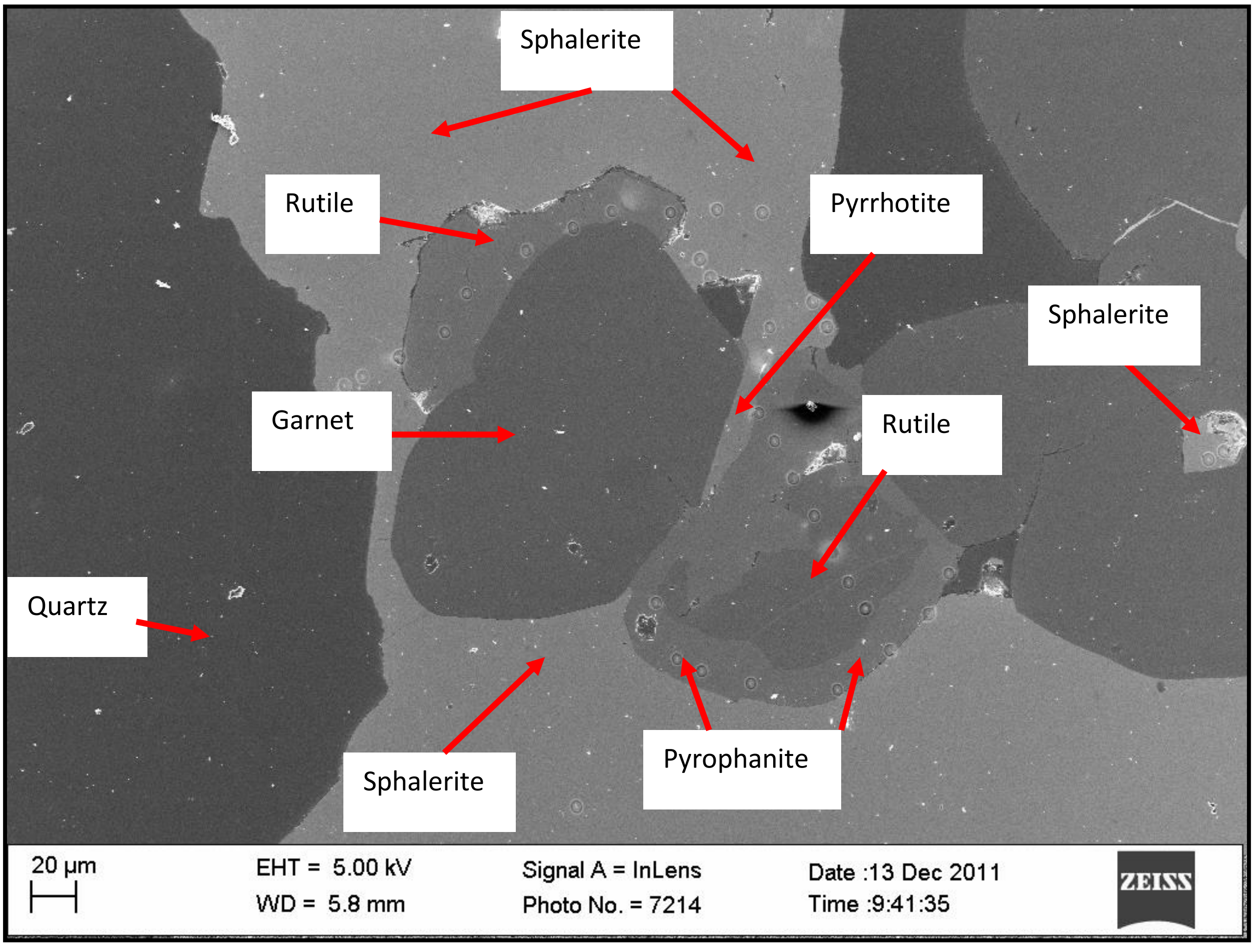

Figure 63. Secondary electron imaging showing high-resolution textural relationships in Figure 62.

Figures 64 and 65 show additional textures of alabandite-free samples. Figure 64 shows meta-pelite ore, with sphalerite coexisting with pyrrhotite, chalcopyrite and galena. Pyrrhotite, galena and chalcopyrite are orientated along “cracks” of sphalerite, with varying grain sizes (less than 1 µm to 0.5 mm). Other pyrrhotite grains are large and surround the sphalerite grain.

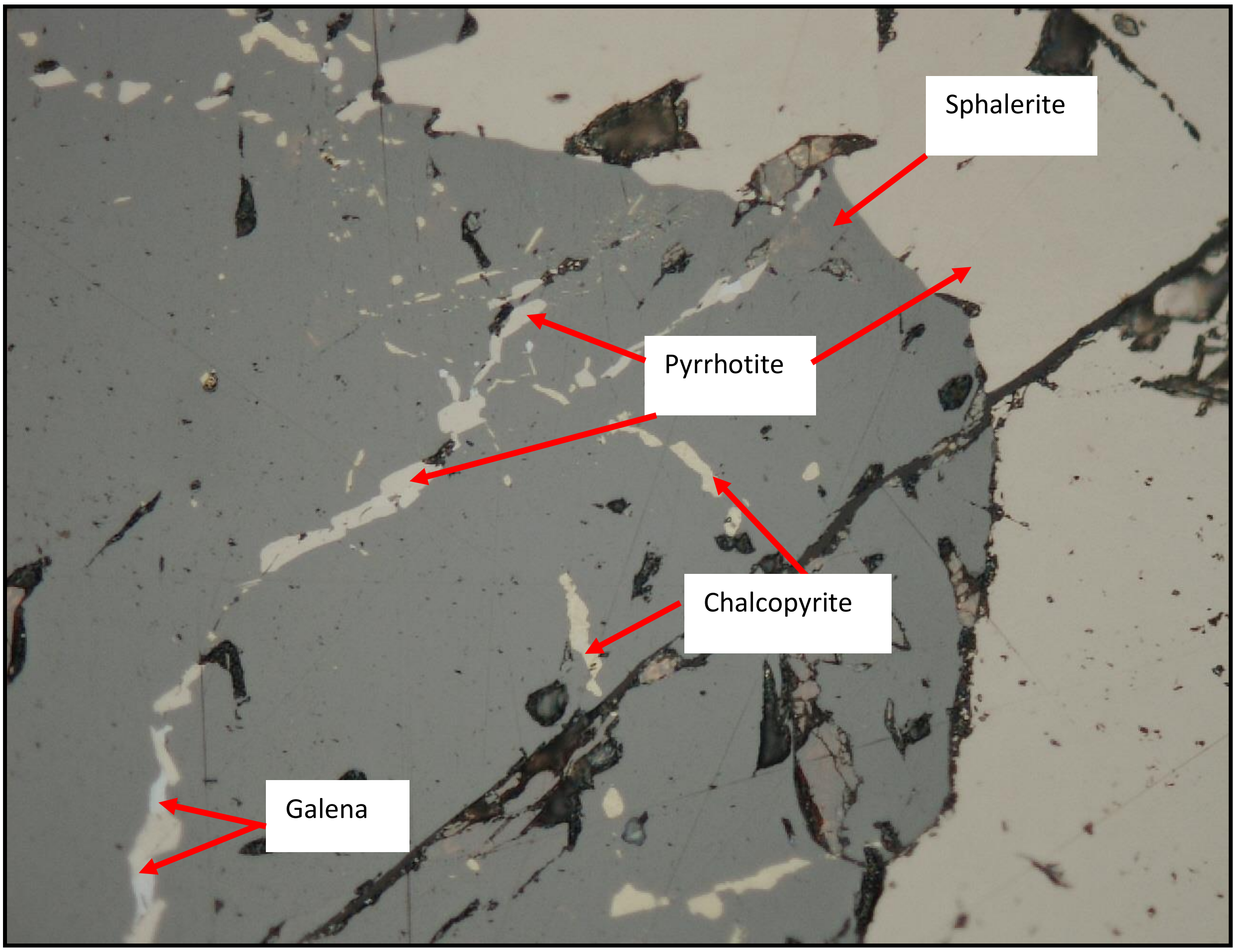

Figure 64. Photomicrograph of sample GAMD09364 of drillhole GAMD045-0-0. Field of view = 0.6 mm.

Figure 65A shows a sphalerite grain with inclusions of graphite and rutile. Figure 65B shows sphalerite coexisting with pyrrhotite and galena grains. This texture could be interpreted as replacement texture.

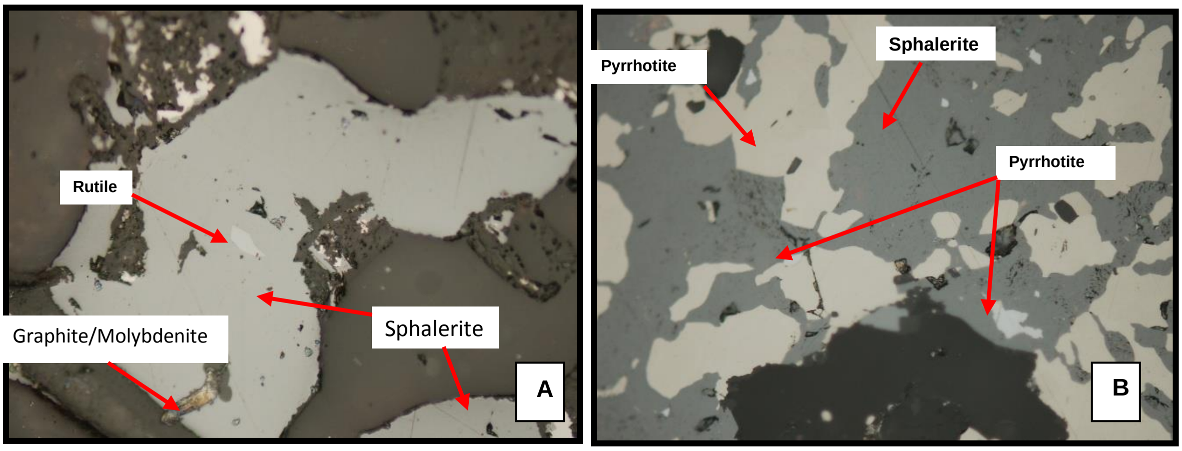

Figure 65. Photomicrographs showing textural relationships between alabandite-free samples. Field of view (A) = 0.25 mm and (B) = 0.12 mm.

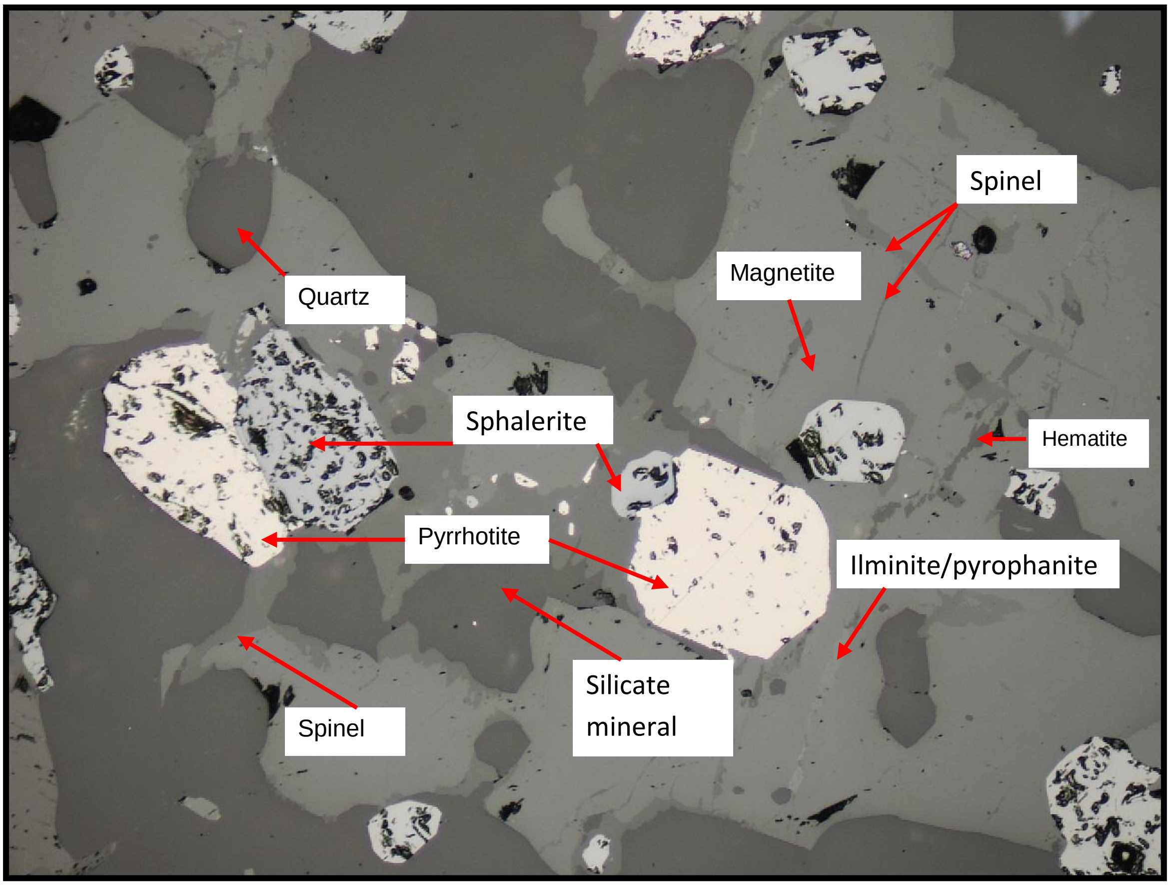

Figure 66. Photomicrograph of sample GAMD09381 of drillhole *GAMD045-0-0*. Field of view = 1.2 mm.

Figure 66 shows a sample from amphibole-pyroxene-magnetite-quartz rock, displaying coexisting magnetite, sphalerite, pyrrhotite and silicate minerals. Magnetite is closely associated with spinel, hematite and Ti-bearing minerals, where other spinel minerals, hematite and Ti-bearing minerals occur as lamella. The spinel mineral could be jacobsite, franklinite or titano-magnetite.

Sphalerite is closely associated with pyrrhotite, but there are other isolated subhedral sphalerite and isolated pyrrhotite grains occurring within silicate minerals and magnetite.

Chapter 6: Sulphide, silicate and oxide mineral chemistry

Section 1: Statistical analysis and data presentation of alabandite and sphalerite chemistries

6.1.1 Alabandite mineral chemistry data

6.1.1.1 Normal distribution tests for alabandite dataset

In order to choose the correct statistical analysis, the distribution or behaviour of the dataset had to be determined, as this would assist with interpreting the data and could be used for summary reports of the dataset to prevent misrepresentation of the dataset. The data were tested for normal distribution (central limit theorem) using probability plots, histograms and box plots. The data are presented in both %wt (weight percentage) and %at (atomic percentage). The %at is used in particular to remove the effects of atomic mass of the four elements present in alabandite.

The alabandite dataset was tested for a normal distribution of S, Mn, Fe and Zn using probability plots and histograms. Figures 67 and 68 show alabandite probability plots of S, Mn, Fe and Zn in %wt and %atomic. For a distribution to be normal it will plot very close to the reference line within the probability plot. The probability plots of S, Mn and Zn (%wt) showed a skewed distribution with more than one population group, showing that the data was not distributed normally. Iron (%wt) was the only component that plotted very close to the reference line and therefore was distributed normally.

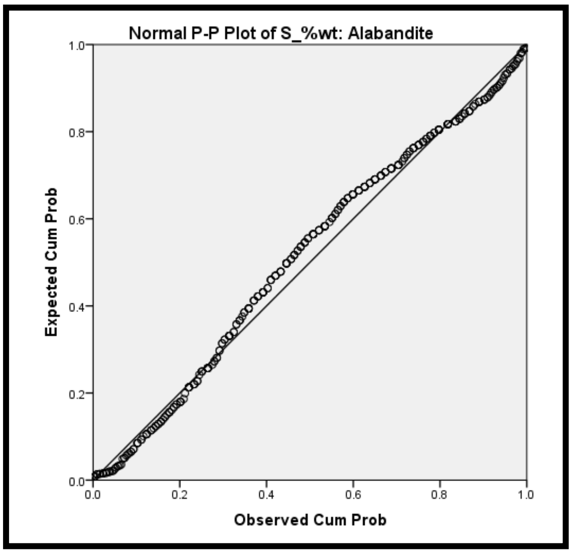

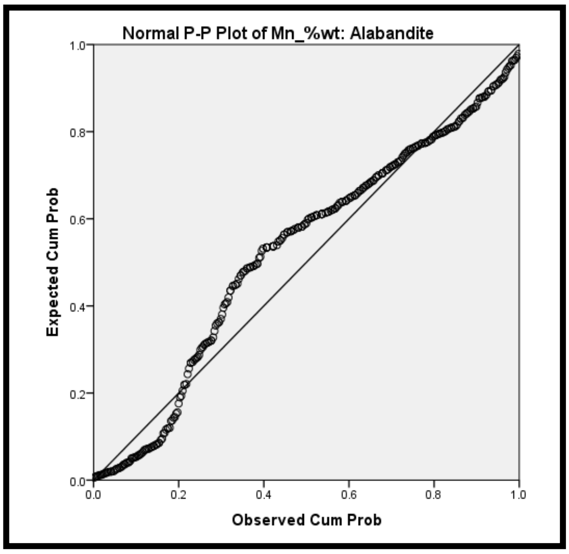

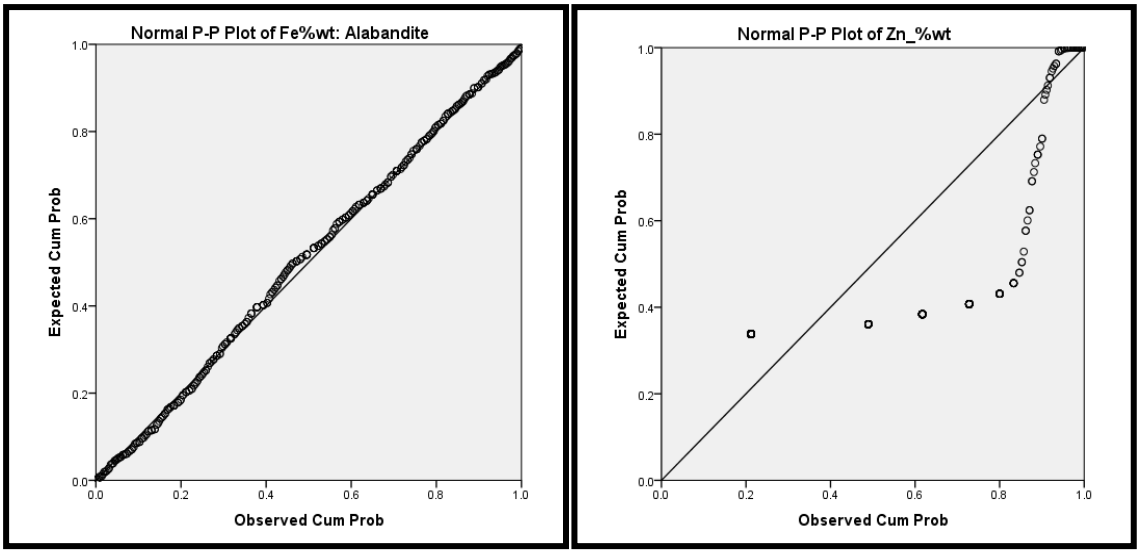

Figure 67. Probability plots of S, Mn, Zn and Fe (%wt) in the alabandite.

Figure 68 shows the probability plots of S, Mn, Fe and Zn (%atomic). The sulphur distribution was negatively and positively skewed, with at least two population groups. The manganese distribution was positively skewed with a number of kinks (groups). Iron distribution showed the highest probability of being normally distributed, plotting very close to the reference line. The zinc distribution was negatively skewed with a lot of kinks.

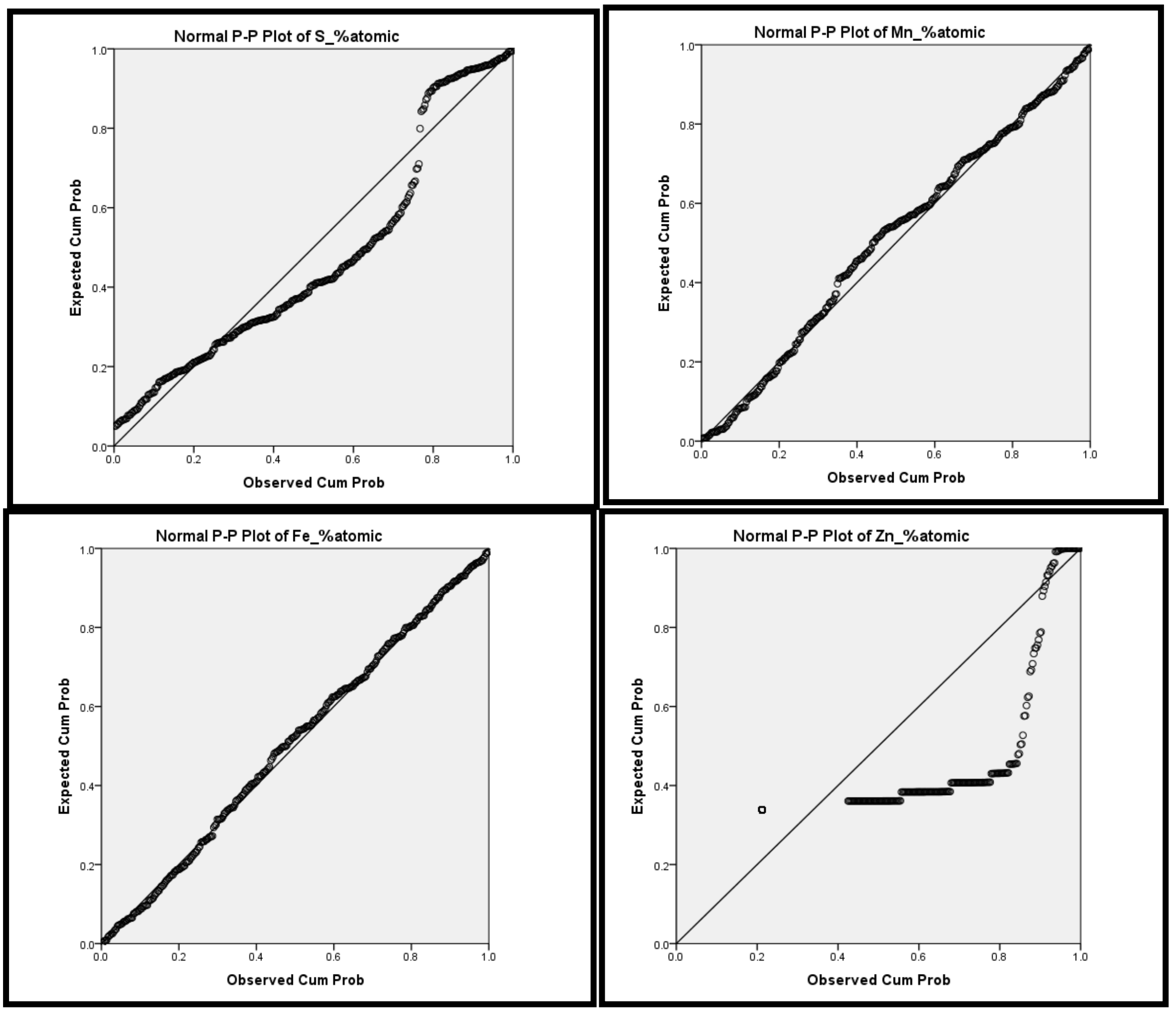

Figure 68. Probability plots of S, Mn, Zn and Fe (%atomic) in the alabandite.

The distribution of Mn, Fe and S in alabandite was further analysed with frequency distribution charts, as shown in Figures 69 to 71 (%wt) and Figures 72 to 74 (%atomic). The zinc concentration in alabandite was lower than 1 %wt (maximum of 0.88 %wt), and therefore was too small to be considered a major element. Only the sulphur, manganese and iron distributions were investigated further by frequency distribution.

Figure 69 shows the distribution of Mn in alabandite in three groups. Figure 70 shows how Fe in alabandite is normally distributed, implying that the Fe concentration in alabandite is dependent on other elements. The sulphur distribution in Figure 71 is positively skewed and not normally distributed. Based on the assumption that sulphur controls the crystal lattice of monosulphides, the sulphur distribution was expected to be normal, which was not the case in the alabandite analyses. For this reason %atomic was used to further understand the distribution of S in alabandite.

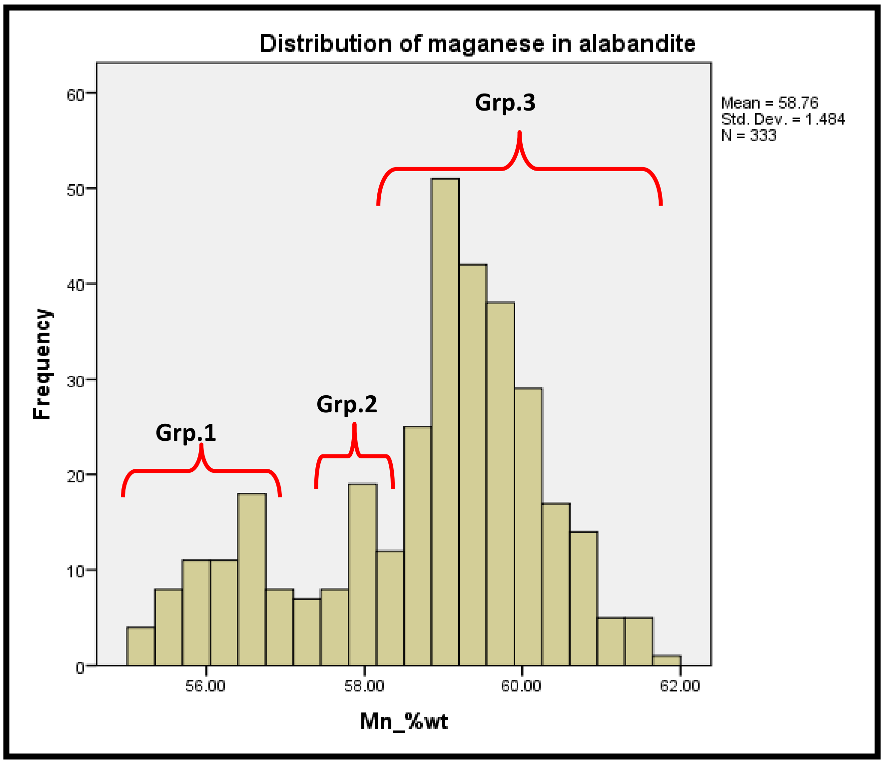

Figure 69. Histogram showing the frequency distribution of the manganese (%wt) content in alabandite.

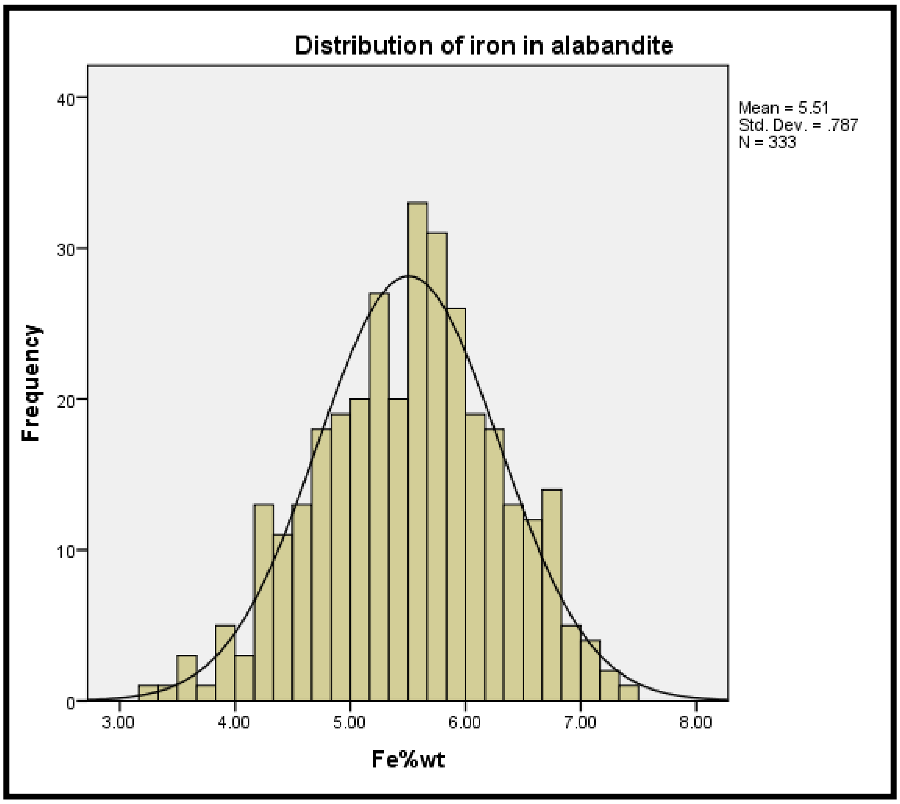

Figure 70. Histogram showing the frequency distribution of the iron (%wt) content in alabandite.

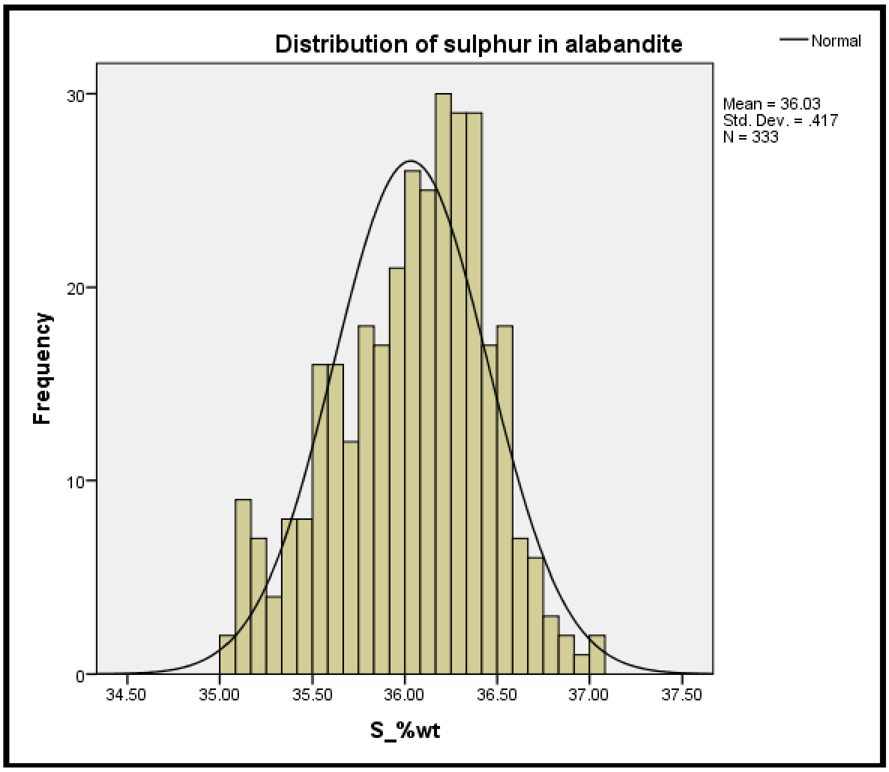

Figure 71. Histogram showing the frequency distribution of the sulphur (%wt) content in alabandite.

Figure 72 shows the distribution of S (%atomic) in alabandite. Two distinct groups (Group 1 and Group 2) of sulphur are observed. There are 255 data analyses in Group 1 and 79 in Group 2. Although the distinction is observed in %atomic, it is important to never lose the distributions in %wt, since the summary statistics will be reported in %wt.

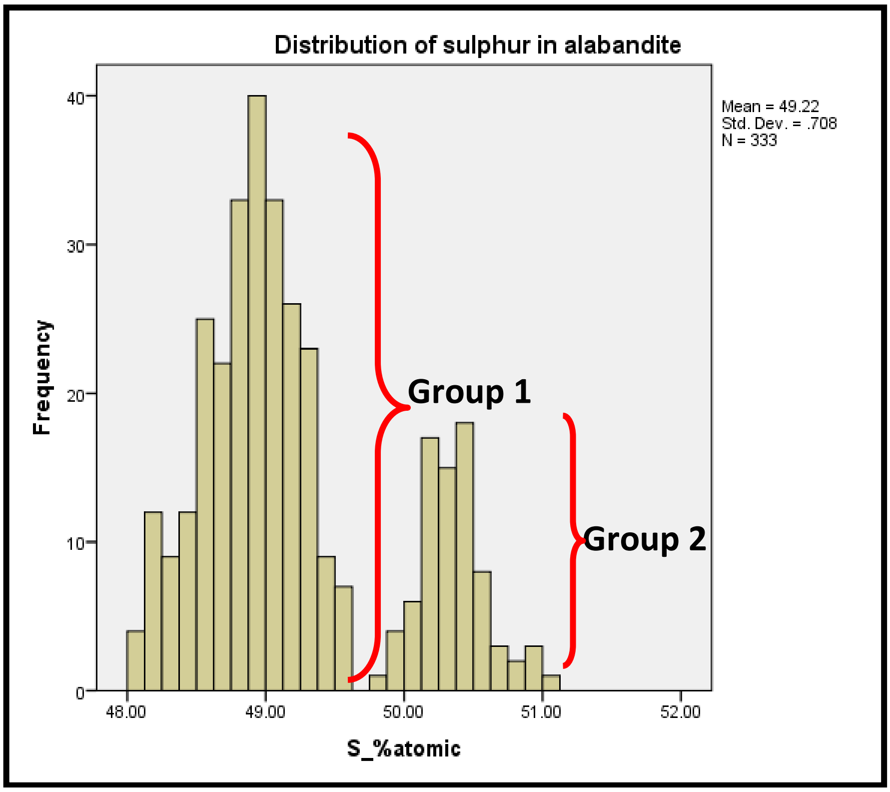

Figure 72. Histogram showing the frequency distribution of the sulphur (%at) content in alabandite, and two population groups.

Figures 73 and 74 show the distribution of sulphur (%atomic and %wt respectively) in alabandite for Groups 1 and 2, as derived from Figure 72. Group 1 ranges from 48.06 to 49.61 %atomic S (35.02 to 36.72 %wt S) and Group 2 ranges from 49.82 to 51.02 %atomic S (35.94 to 37.04 %wt). The gap between the two groups is 0.99 %wt S (0.21 %atomic S) and the mean difference of sulphur between the two groups is 0.55 %wt (1.48 %atomic).

The two groups of sulphur populations in alabandite were investigated for analytical artefacts by checking if the samples were analysed under similar set-up conditions. Investigating the entry records versus point analysis revealed that the point analyses from the same polished section or sample, recorded a few minutes and distances (in mm) apart, yielded analyses that fell into both Groups 1 and 2. This was to rule out the possibility of errors introduced by the instrument. The possibility of undetected elements was investigated by EDS analysis, mentioned in section 4.3.2. There is no evidence to suggest undetected elements from the analysis.

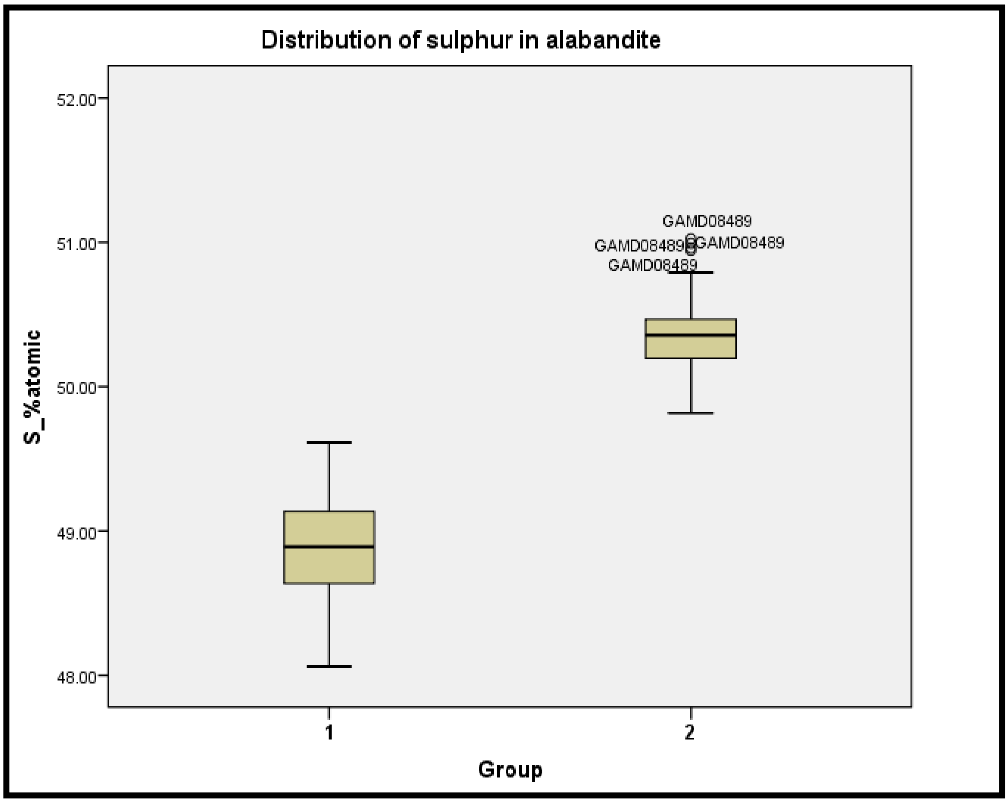

Figure 73. Box plot showing the distribution of sulphur (%atomic) in alabandite for Group 1 and Group 2.

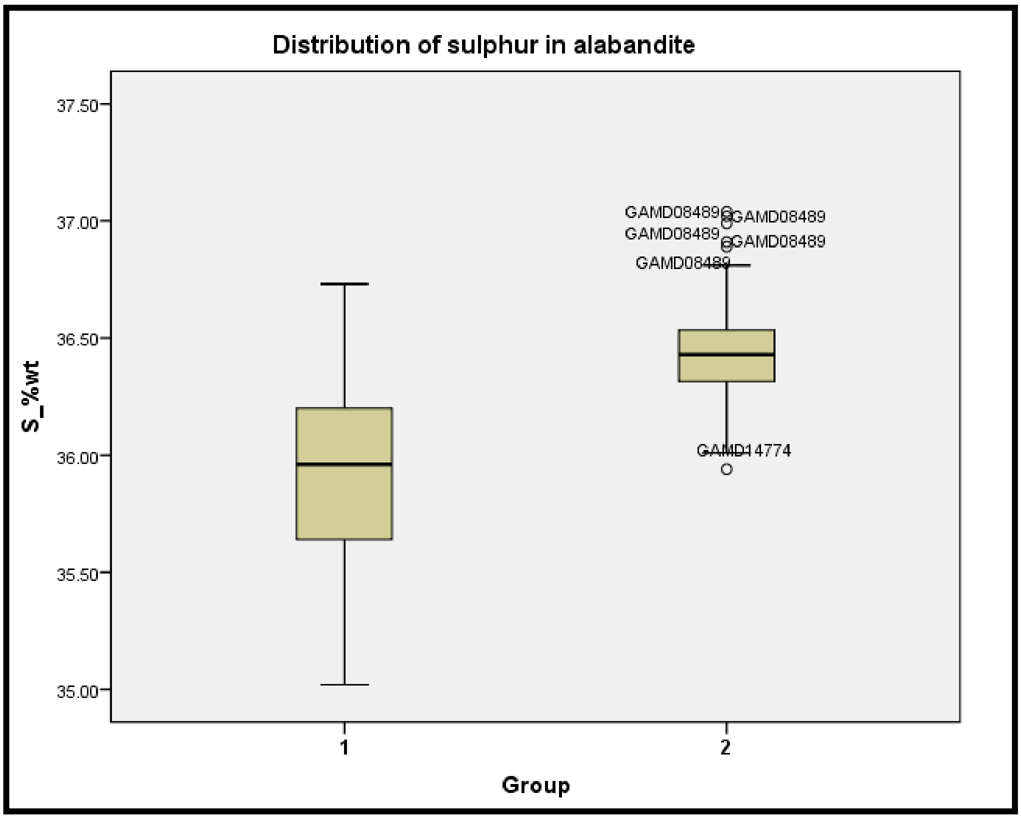

Figure 74. Box plot showing the distribution of sulphur (%wt) in alabandite for Group 1 and Group 2.

Figure 75 shows the frequency distribution of manganese in alabandite for Groups 1 and 2 combined, in %atomic. The distribution of manganese is slightly positively skewed. The manganese distribution in %atomic does not show different groups, in contrast to Figure 69, which shows three population groups of manganese in %wt. Despite the %wt groups, Groups 1 and 2 derived from the sulphur distribution in %atomic were accepted and analysed further.

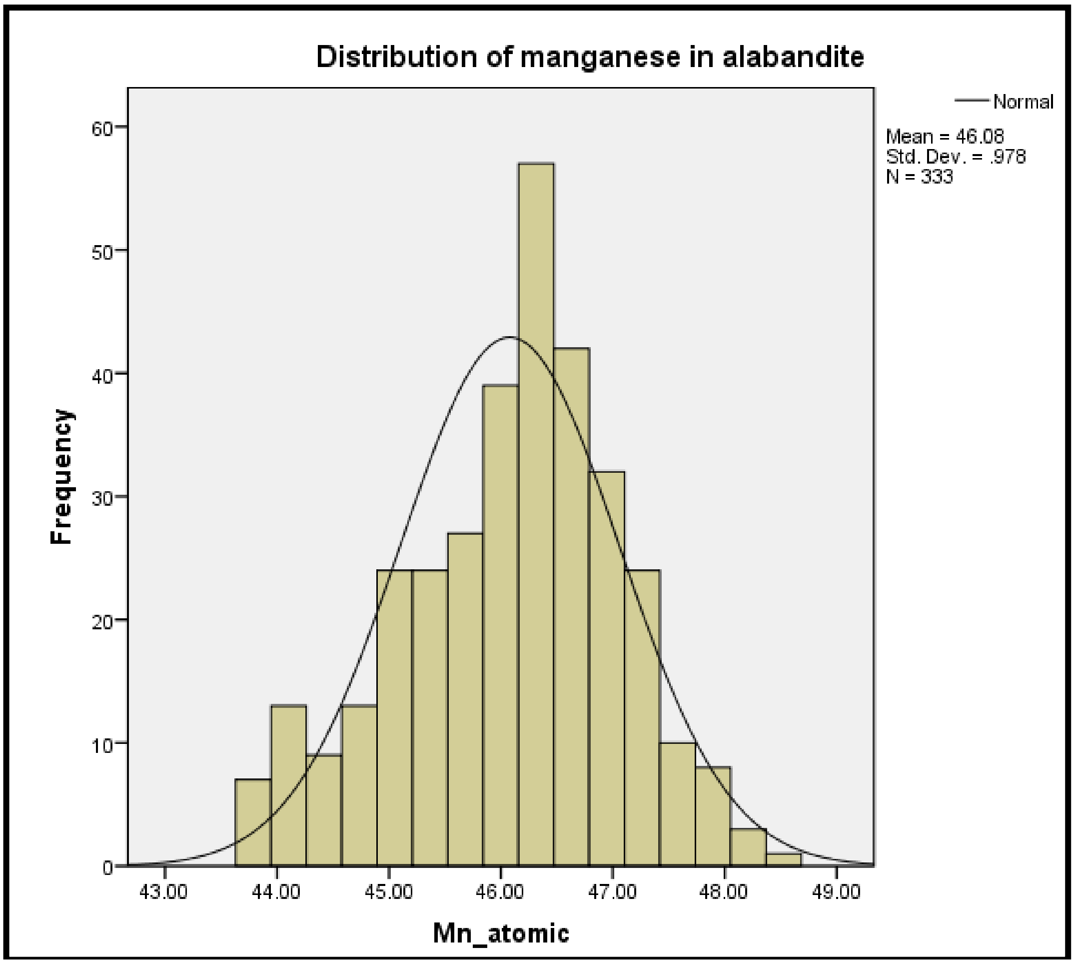

Figure 75. Histogram showing the frequency distribution of the manganese content of alabandite.

The box-plot diagrams in Figures 76 and 77 show the distribution of manganese (%atomic and %wt respectively) in alabandite for Group 1 and Group 2. Group 1 had a higher manganese concentration than Group 2. The mean difference of manganese between the two groups was 1.62 %atomic (2.91 %wt) and the median difference was 1.58 %atomic (2.79 %wt).

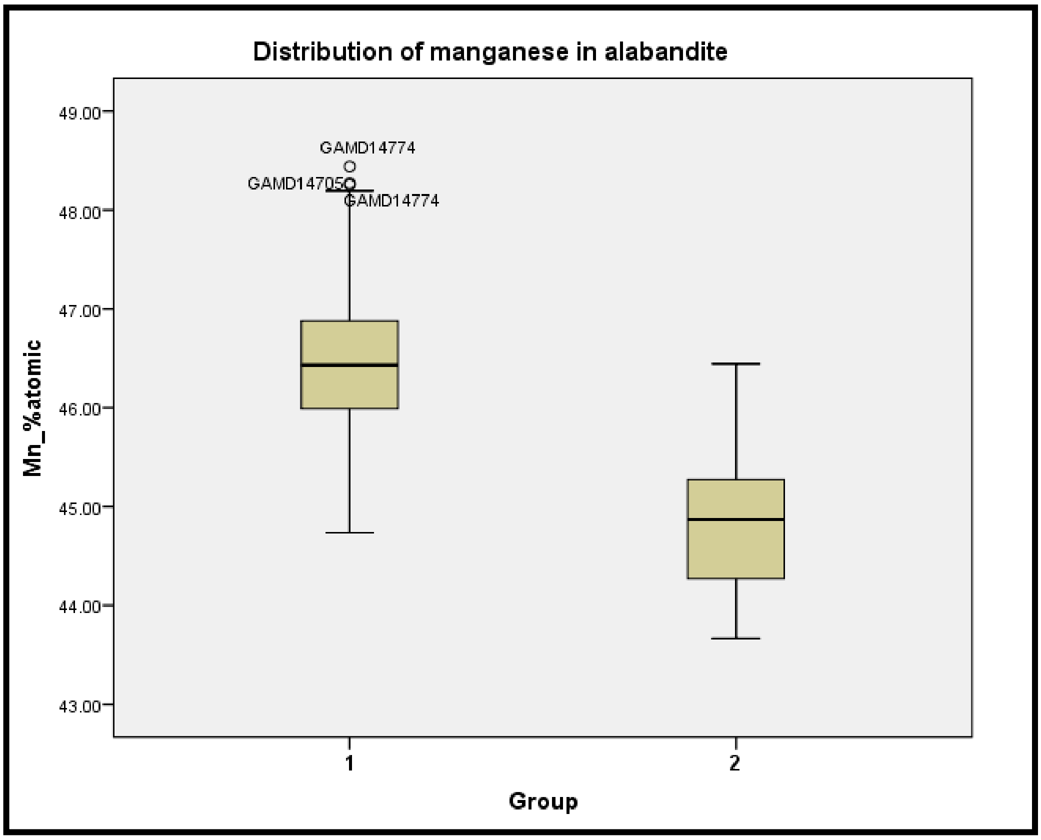

Figure 76. Box plot showing the distribution of manganese in alabandite (%atomic).

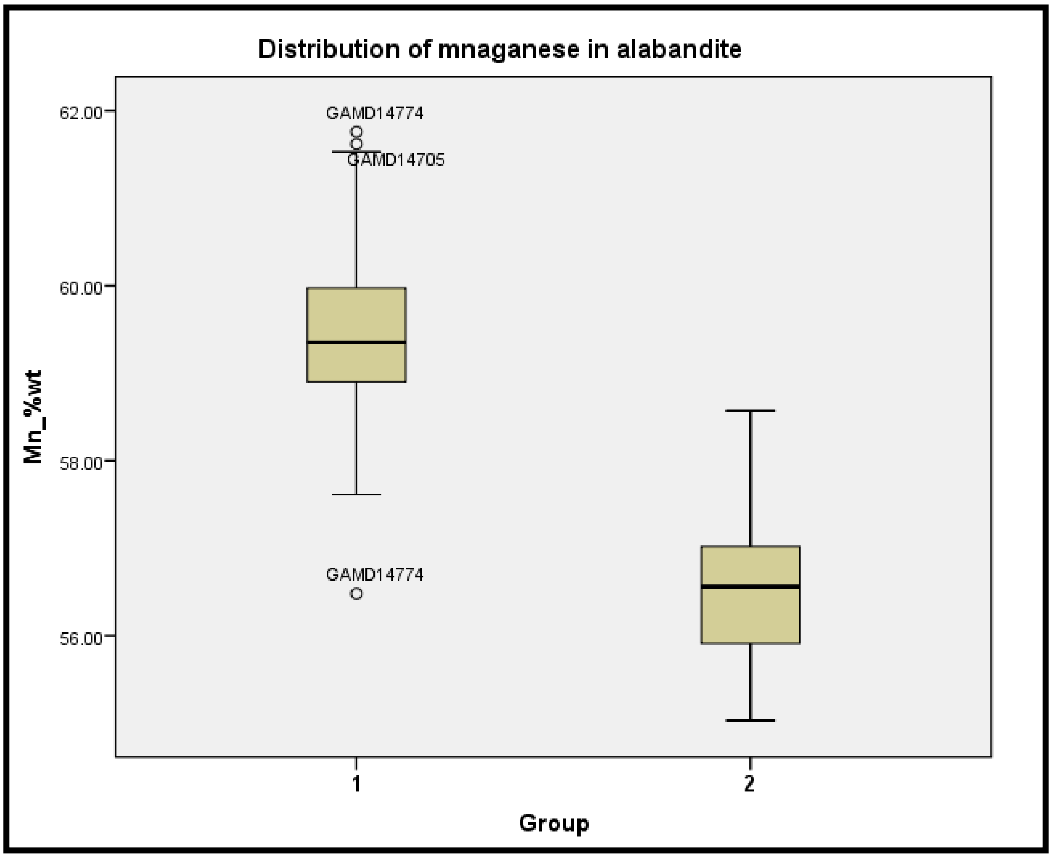

Figure 77. Box plot showing the distribution of manganese in alabandite (%wt).

Figure 78 shows the frequency distribution of iron in alabandite in %atomic. This distribution is normal and iron shows a normal distribution in both %atomic and %wt.

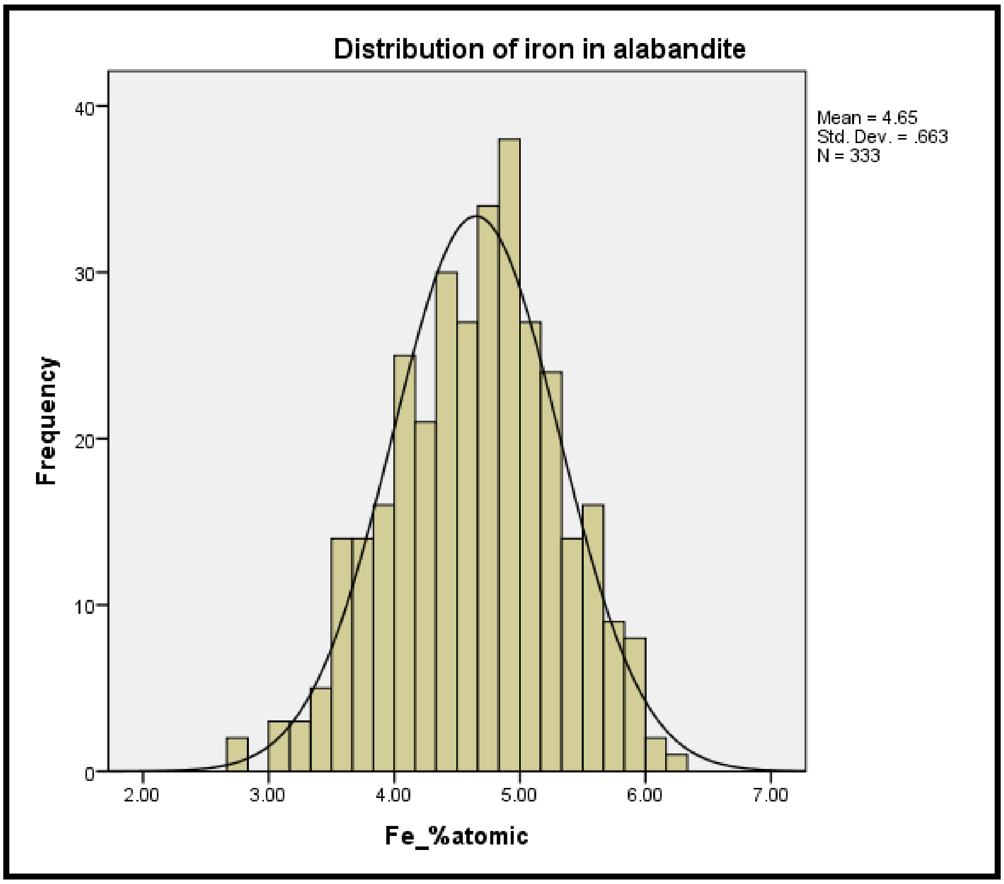

Figure 78. Histogram showing the frequency distribution of iron in alabandite (%atomic).

Figures 79 and 80 show box plot diagrams of the distribution of iron (%atomic and %wt respectively) in alabandite for Groups 1 and 2. The medians are relatively similar, but the iron concentration in Group 1 has a larger range than that in Group 2.

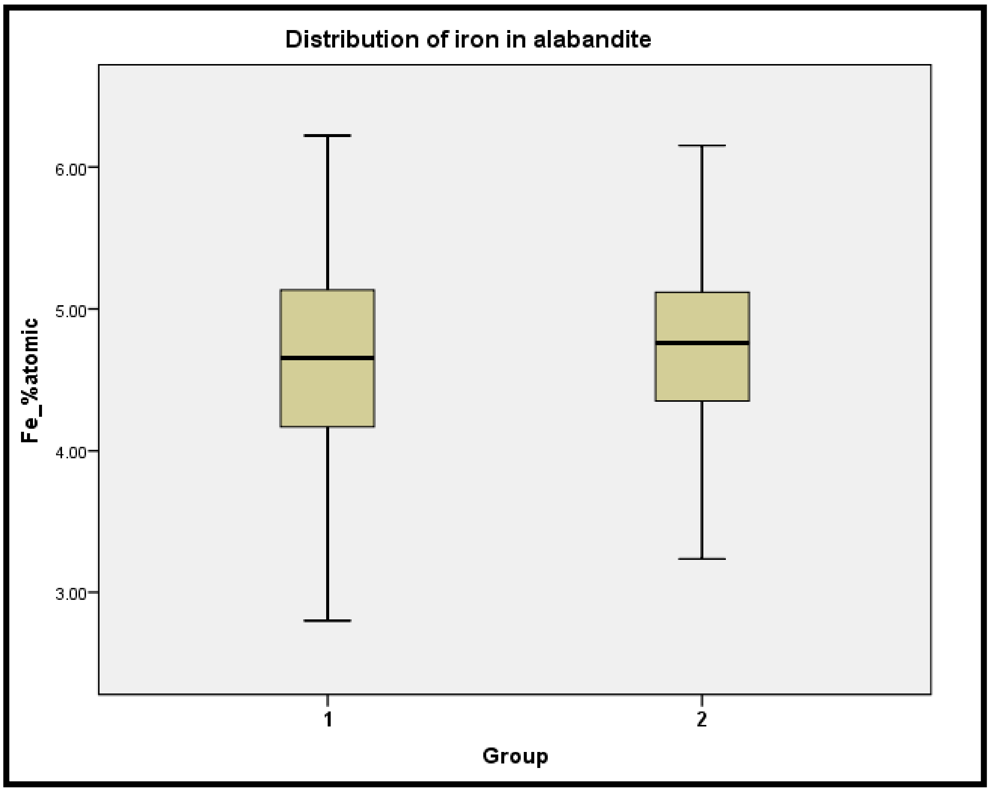

Figure 79. Box plot showing the distribution of the iron content in alabandite in Groups 1 and 2.

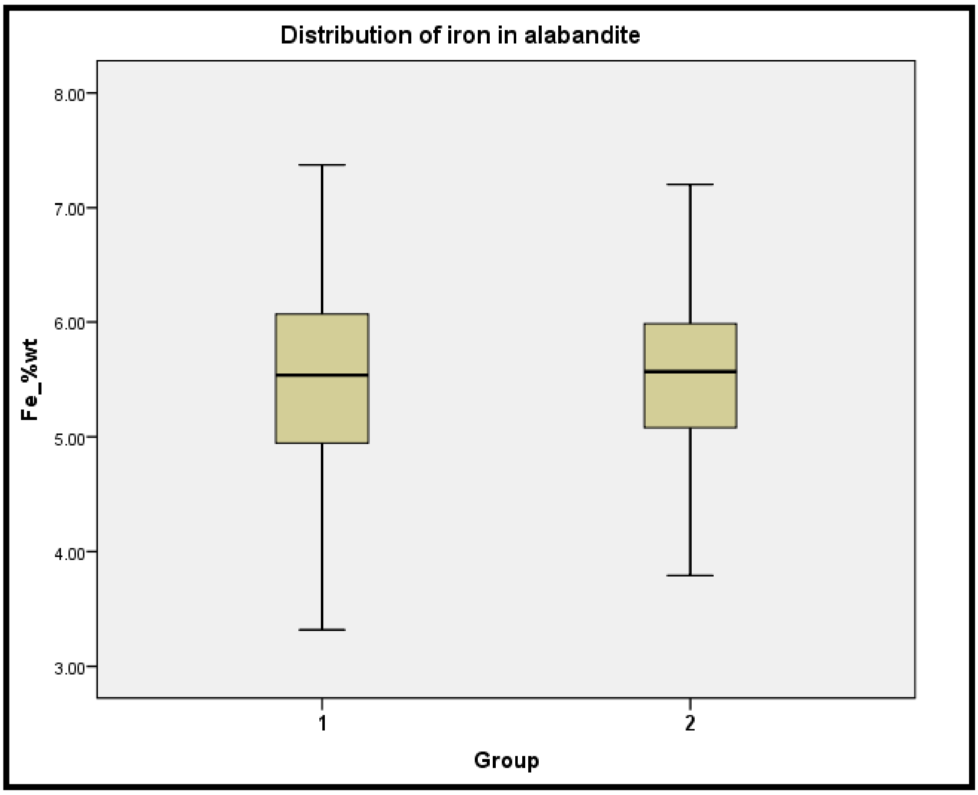

Figure 80. Box plot showing the distribution of the iron content in alabandite in Groups 1 and 2.

The populations of iron in %wt and %atomic are normally distributed, and this means that the iron concentration in alabandite is not controlled by the same factors controlling the distribution of manganese. With the assumption that sulphur controls the crystal lattice of monosulphide minerals, the two distinct groups of sulphur signify that there were at least two different alabandite populations.

6.1.1.2 Scatter plots of alabandite mineral chemistry

Scatter plots were used in this section to investigate the binomial relationships between sulphur, iron, manganese and zinc in alabandite. These relationships will be presented in both %wt and %at, with the %at discussed only where necessary. The alabandite dataset was categorised into sample_ID and mineralogical assemblages. The sample IDs were linked to rock types and the stratigraphic position of the sample. Mineralogical assemblages represent relationships between coexisting minerals.

The relationship between Mn %at and S %at in Figure 81 shows two distinct clusters (Clusters 1 and 2), with a notable gap between the two clusters. The data was categorised by sample_ID and most of the samples fell within both of the clusters, with the exception of samples *Alabandite 1* and *GAMD15677*. Cluster 1 had higher Mn and lower S concentrations compared to Cluster 2, which had lower Mn and higher S concentrations.

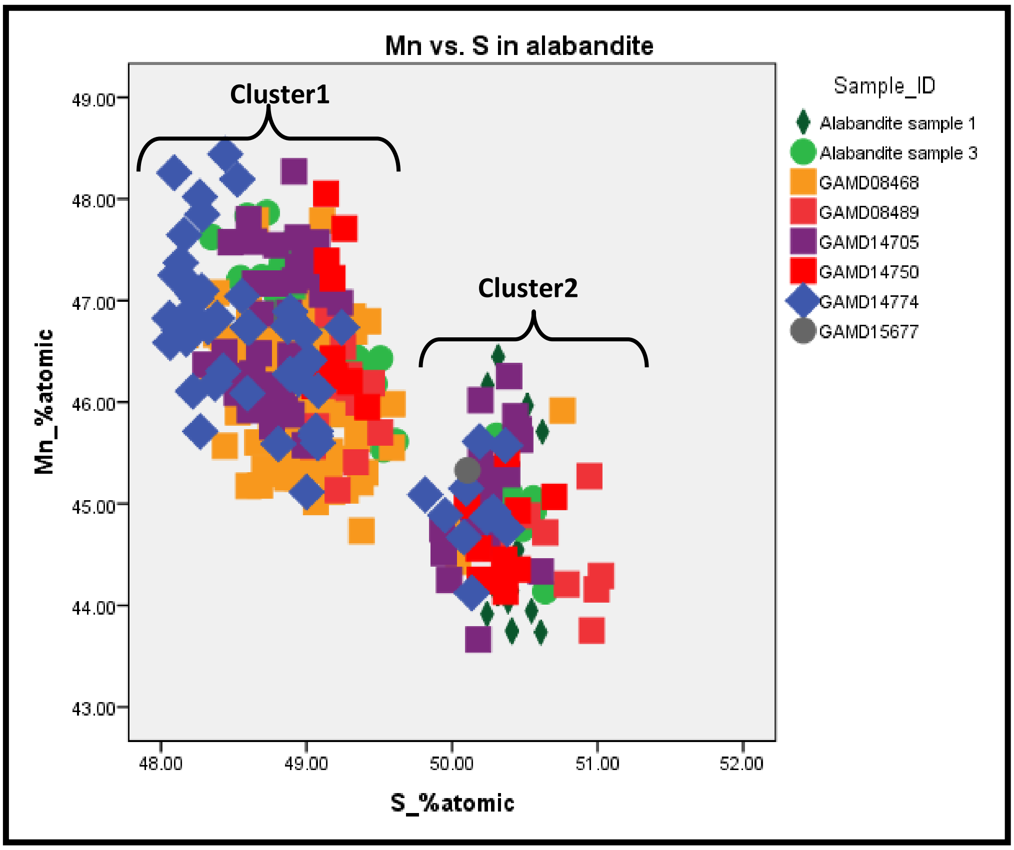

Figure 81. A scatter plot showing the relationship between Mn and S in alabandite.

The scatter plots in Figures 82 and 83 show the relationship between Mn %wt and Fe %wt in alabandite. In Figure 82 the data is categorized into sample_IDs. There is an inverse relationship between Mn %wt and Fe %wt, with two distinct trends (T1 and T2). Both trends share similar samples, with the exception of samples *Alabandite 1* and *GAMD15677*. Sample *Alabandite 1* is coarse grained and sample *GAMD15677* is fine grained, but all other samples are either coarse or fine grained. The two trends are strongly related to Mn distribution as the range of Fe content is almost similar in both trends. Trend 1 (T1) has higher Mn compared to Trend 2 (T2). There is also a noticeable gap between the two trends.

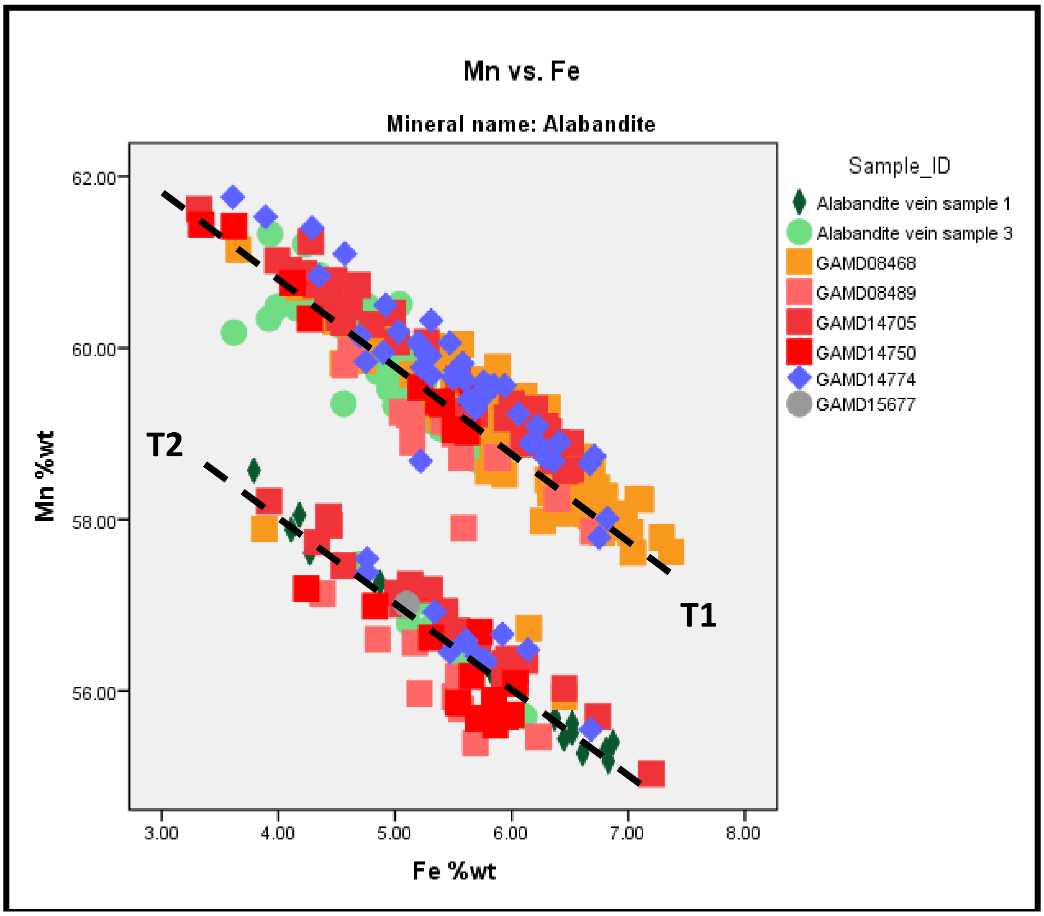

Figure 82. A scatter plot showing the relationship between Fe and Mn in alabandite for all samples analysed. T1 and T2 represent the trends shown by the data.

The mineralogical assemblage in Figure 83 does not show any distinction between the two trends, as all mineralogical assemblages are present in both trends. The photomicrographs of some of the alabandite-bearing rocks show allotromorphic (anhedral) textures with no visible boundaries in alabandite grains. These textures prevent the identification of individual alabandite grains, meaning the mineral boundaries are indistinguishable. For this reason there is uncertainty whether or not the points analysed represent a single grain or are across grains. However there are alabandite grains that were positive identified as individual grains.

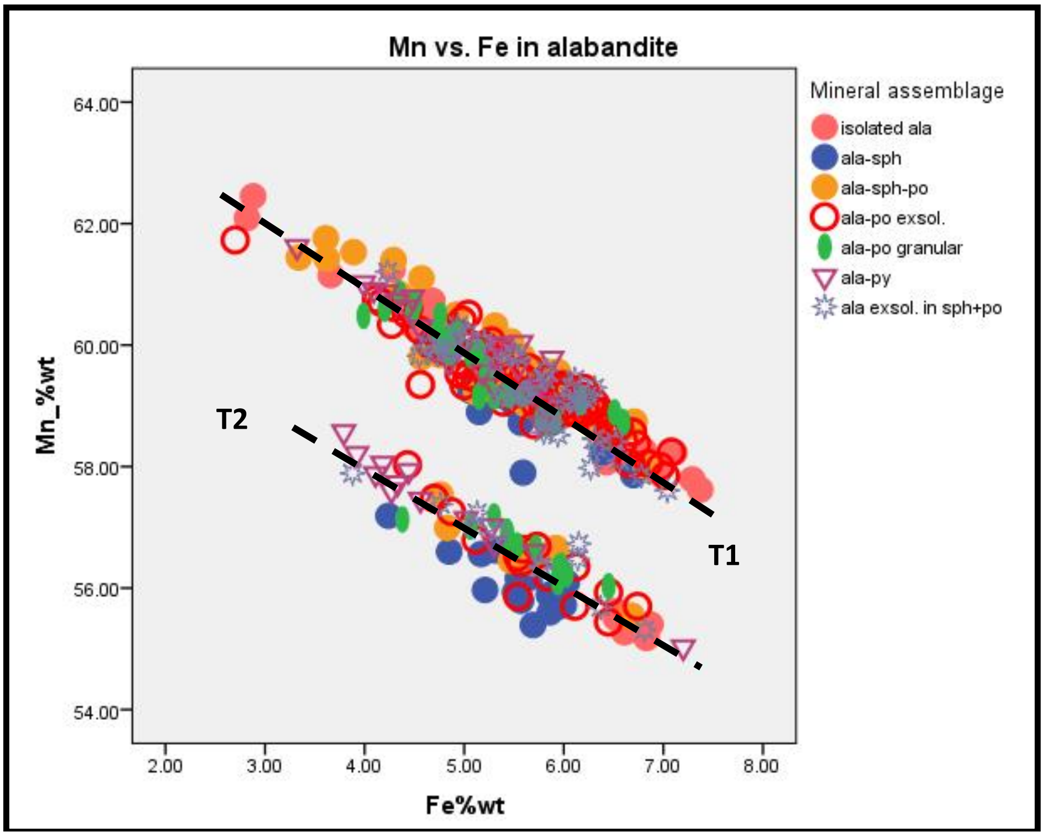

Figure 83. Scatter plot showing the relationship between Fe and Mn in alabandite. The data is categorised into mineral assemblages. T1 and T2 represent the trends shown by the data.

The relationship between Mn %at and Fe %at in Figure 84 shows that there are two trends. There also is a gap between the two trends, even though the gap is smaller compared to that observed in Figures 82 and 83. There is an overlap between samples GAMD14774 and GAMD08489. These two samples are from the meta-pelite ore of drillholes *GAMD054-2-2* and *GAMD033-2-4* respectively.

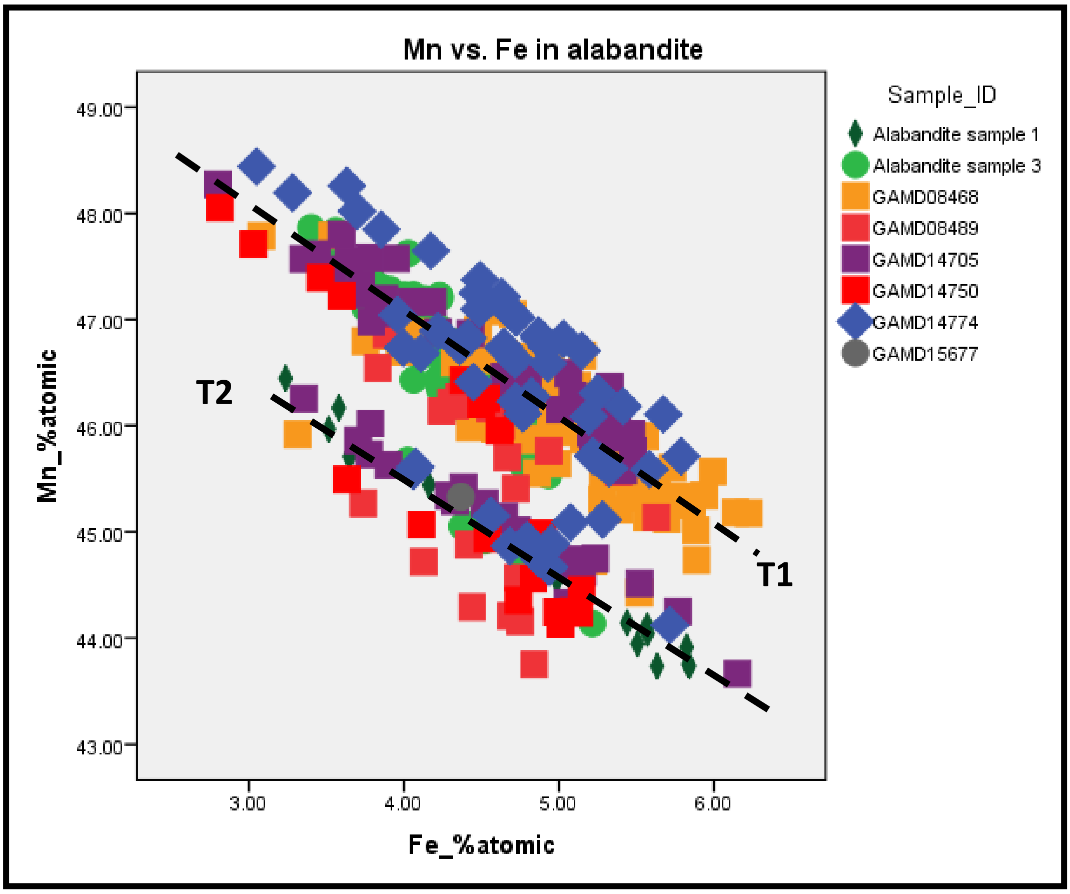

Figure 84. A scatter plot showing the relationship between Mn and S in alabandite for all samples analysed.

To further understand the behaviour of Fe and Mn in alabandite, the data was broken down into individual drillholes and further into individual samples. Figures 85 and 86 show the relationship between Fe and Mn in alabandite for drillholes *GAM033-2-4* and *GAMD054-2-2*, while Figures 87 to 89 show the relationship between Fe+Zn and Mn in alabandite for individual samples.

In Figures 85 and 86, the samples are in order of increasing depth. The two samples from drillhole *GAMD033-2-4* plot in both trends, as observed in Figure 85. Sample GAMD08468 (from Garnet Quartzite) plots in both trends, but with more points on the trend with higher Mn concentration. Sample GAMD08489 (from meta-pelite ore) plots in both trends and is distributed almost equally. The two samples are about 18 m apart.

The samples GAMD14705, 14750 and 14774 in Figure 86 are 21 m, 12 m and 30 m apart respectively. Samples Alabandite 1 and GAMD15677 are the only samples present in the one with the lower Mn trend, whereas all samples are present in both trends. Samples GAMD14705 and GAMD14750 are from pelitic schist and samples GAMD14774 and GAMD15677 are from meta-pelite ore. Samples Alabandite 1 and 3 are from an alabandite vein with pelitic schist from drillhole *GAMD054-2-2*.

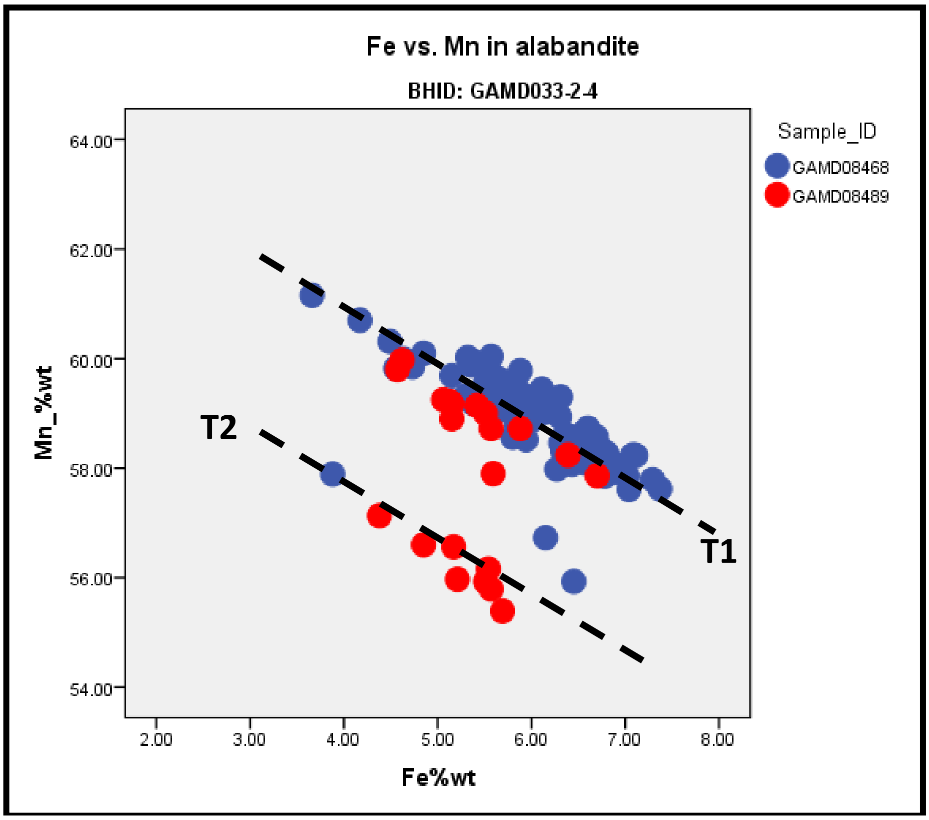

Figure 85. Relationship between Fe and Mn of alabandite in drillhole *GAMD033-2-4*.

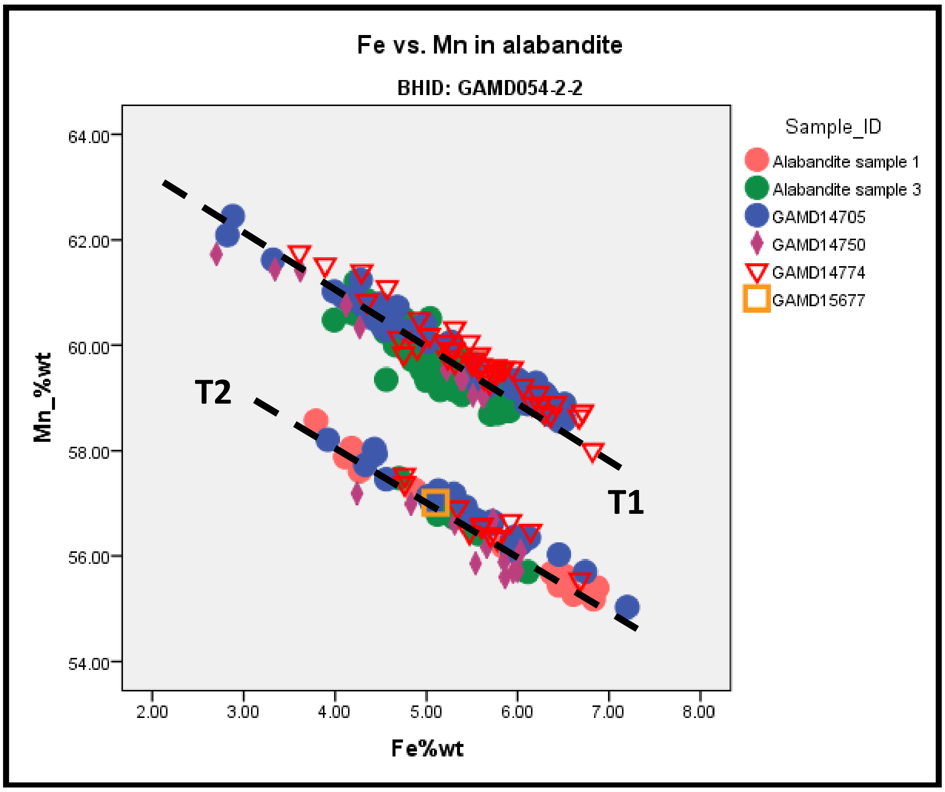

Figure 86. Relationship between Fe and Mn of alabandite in drillhole *GAMD054-2-2*.

Figure 87 shows the relationship between Fe+Zn and Mn in the alabandite of Alabandite 1 and 3. The data is categorised into mineralogical assemblages. The Fe+Zn concentration of Alabandite 1 is higher than that of Alabandite 3, and Alabandite 1 has a lower Fe+Zn concentration than Alabandite 3. The Mn concentration of Alabandite 3 is higher than that of Alabandite 1, with Alabandite 3 having the lowest Mn concentrations. There is only one trend in Alabandite sample 1, with two clusters, and this trend has a low Mn concentration. Isolated alabandite and alabandite as exsolution grains in sphalerite and pyrrhotite are apart from each other, whereas alabandite with pyrrhotite exsolution grains fills in the gap between the two clusters. These observations suggest that there is a completion of Fe in alabandite coexisting with Fe-sulphides as the iron content lower in alabandite compared to alabandite that is not coexisting with Fe-sulphides. There are two trends in Alabandite sample 3. Alabandite coexisting with pyrrhotite and alabandite exsolution grains in sphalerite and pyrrhotite are present only in T1. The other two mineral assemblages are present in both trends.

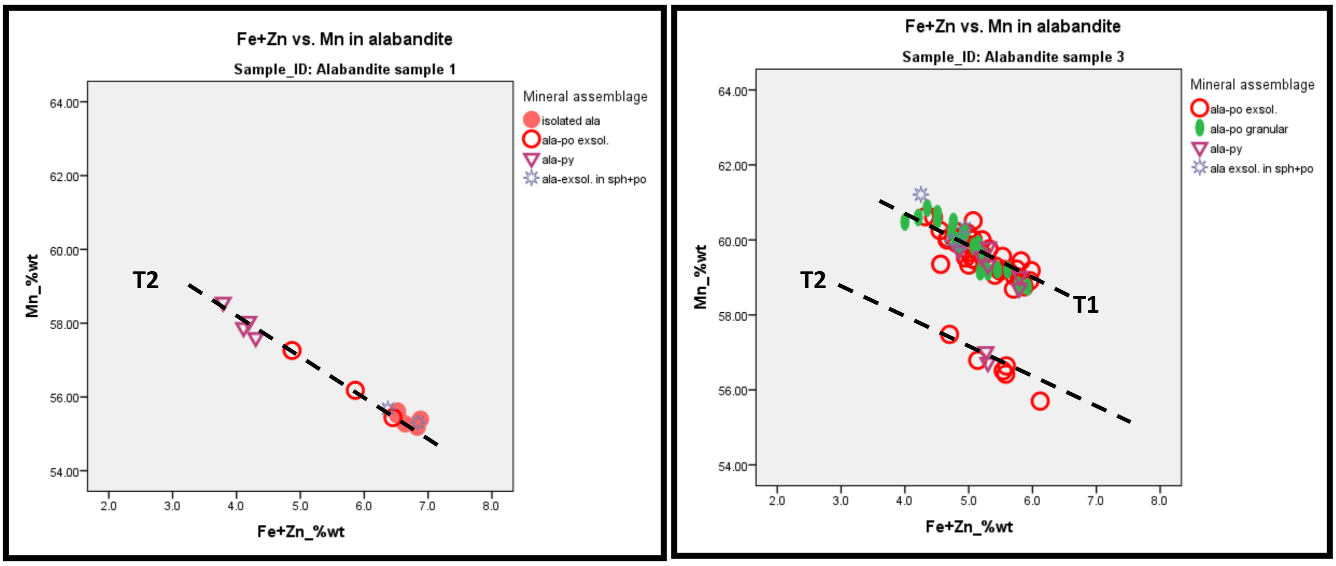

Figure 87. Relationship between Fe+Zn and Mn of vein alabandite from drillhole *GAMD054-2-2*.

Figure 88 shows the relationship between Fe+Zn and Mn in alabandite for samples GAMD08468 (from garnet quartzite) and GAMD08489 (from meta-pelite ore). Two trends can be observed in both samples. The Mn concentration is higher in GAMD08468 than in GAMD08489. In GAMD08468, most of the samples are in T1. Alabandite with pyrrhotite exsolution grains and alabandite as exsolution grains in sphalerite and pyrrhotite make up T2. In sample GAMD08489, coexisting alabandite is present only in T1, whereas the other two mineralogical assemblages are present in both trends.

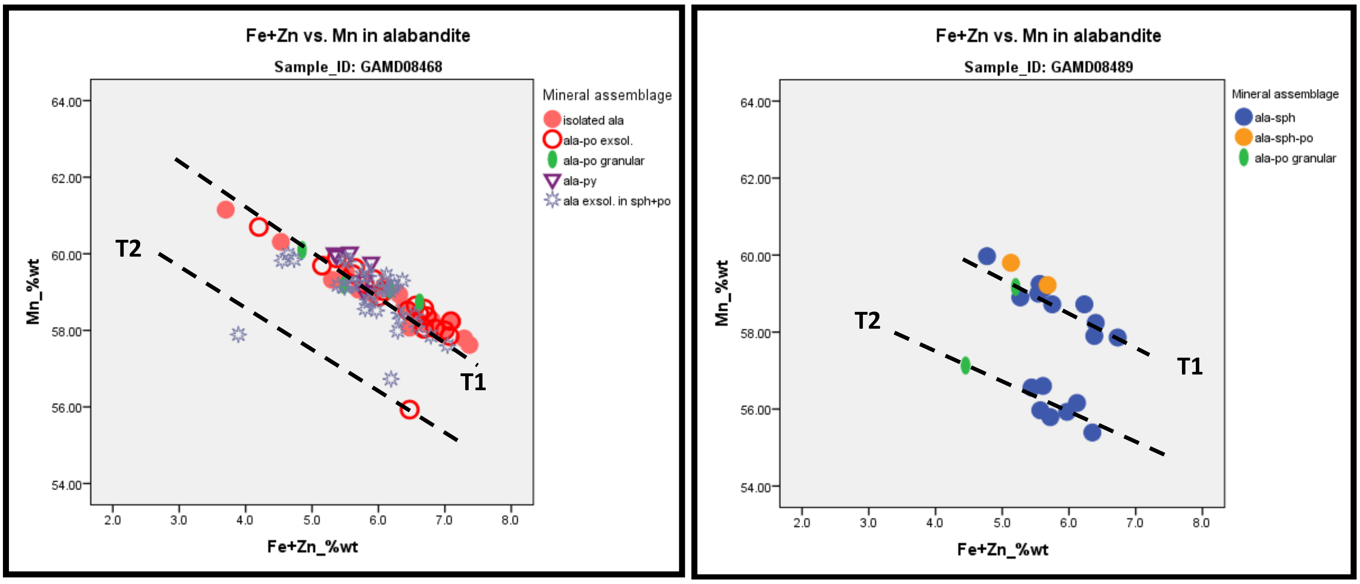

Figure 88. Relationship between Fe+Zn and Mn of the alabandite from drillhole *GAMD033-2-4*.

Figure 89 shows the relationship between Fe+Zn and Mn in the alabandite of samples GAMD14705 (from pelitic schist) and GAMD14750 (meta-pelite ore). There are two trends in both samples. The range of the Fe+Zn concentration and the Mn concentration of sample GAMD14705 is higher than that of sample GAMD14750. Isolated alabandite in sample GAMD14705 is present only in T1, and alabandite exsolution grains in sphalerite and pyrrhotite are present only in T2. In sample GAMD14750, all mineral assemblages are present in both trends.

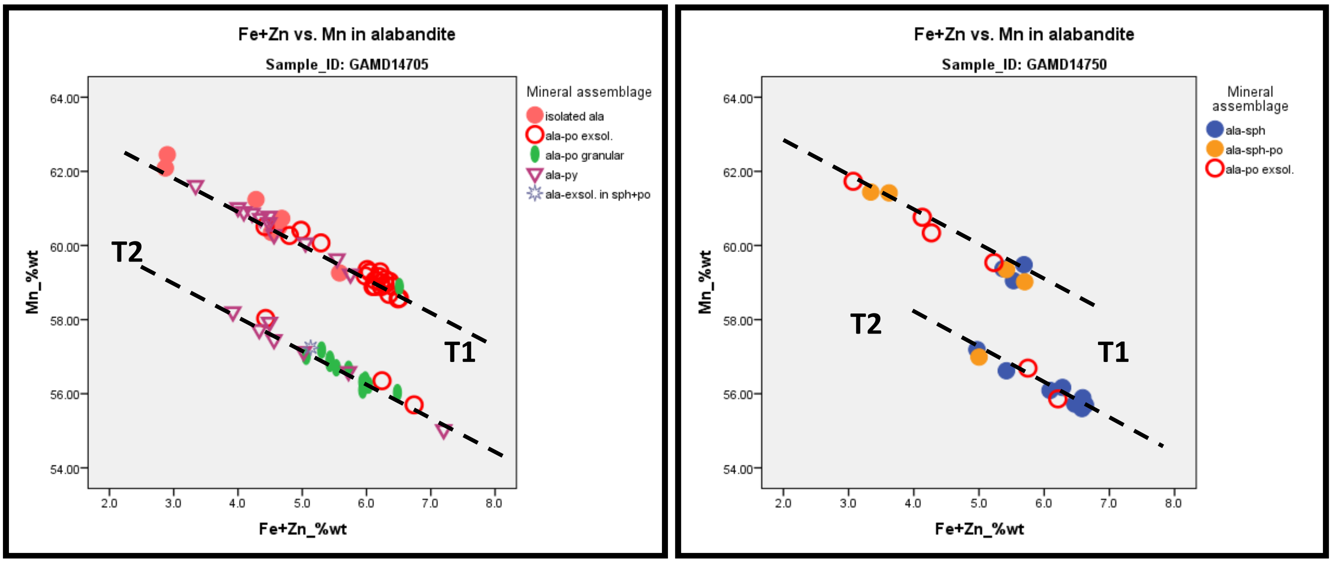

Figure 89. Relationship between Fe+Zn and Mn of the alabandite from drillhole *GAMD054-2-2*.

The gap observed in Figures 82, 83 and 84 is strongly associated with Mn distribution. The mean difference between the two groups/clusters or trends is 0.55 %wt S (1.48 %at S) and 2.91 %wt Mn (1.62 %at Mn), which means that these amounts basically are the maximum concentrations of other metals needed to close the gap. Further analysis or investigation of the gap between the two trends is critical, as it could point out if there are missing element(s) and/or the existence of different oxidation states of Mn (Mn^{3+}, Mn^{4+} etc.) and/or Fe (Fe^{3+}) to balance the charge. It should be noted that EMPA treats all of the Fe in the analysis as Fe^{2+} and ignores Fe^{3+}. The recalculation of Fe into Fe^{2+} and Fe^{3+} does not close the gap between two trends or clusters.

In summary, there are three consistent observations shown by the scatter-plot relationships of S, Mn, Fe and Zn in the alabandite in Figures 82 to 87, namely:

1. There are two distinct trends of Mn and two groups of sulphur,
2. The two trends are strongly associated with Mn distribution in relation to sulphur distribution
3. However the two trends can not be distinguished using mineral textures and mineral assemblages.

6.1.1.3 Cross-sections through alabandite

Cross-sections through the alabandite grains are presented in this section to investigate the compositional variation in individual alabandite grains. The point analysed was from a rim through the core to the adjacent rim. Intervals were not fixed, but all the analyses presented here are of individual grains. The coexisting mineral grains also were noted. The graph is accompanied by the composition and chemical formula of the alabandite grain presented.

Figure 90 shows a cross-section through the alabandite grain coexisting with pyrite from sample GAMD08468 of drillhole *GAMD033-2-4*. The concentration of Mn and Fe throughout the alabandite is homogenous and remains constant from rim to rim. The variations are accounted for by the error estimated for the chemical components. The mineral formula of this alabandite is $Mn_{0.93}Fe_{0.10}S$.

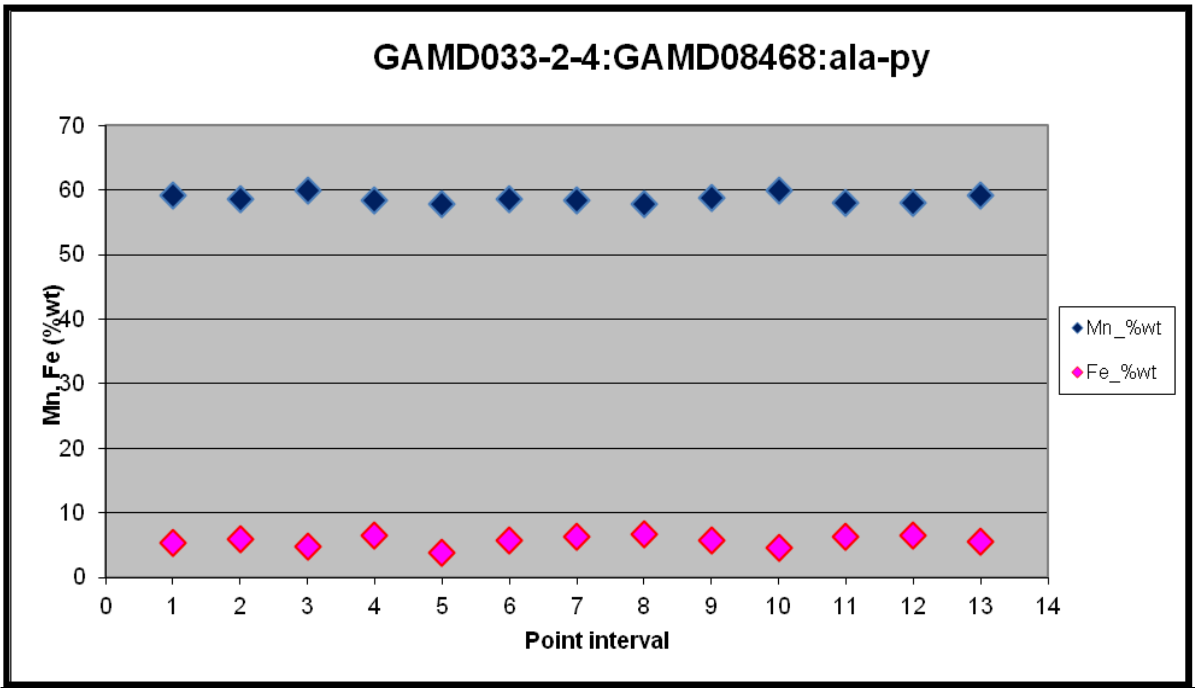

Average chemical analysis N = 13				Chemical formula N = 13			
Mn_%wt	**Fe_%wt**	**Zn_%wt**	**S_%wt**	Mn_mol	Fe_mol	Zn_mol	S_mol
58.68	5.71	0.01	36.26	0.93	0.10	0.00	1
± 0.221	*± 0.060*	*± 0.125*	*± 0.171*	*± 0.05*	*± 0.001*	*0.00*	

Figure 90. Cross-section through alabandite, which coexists with pyrite, and a table showing the chemical composition of the alabandite mineral chemistry error.

Figure 91 provides a cross-section, composition and chemical formula of the alabandite isolated from other sulphide minerals, but coexisting with silicate minerals. The sample of alabandite is from sample GAMD08468. The concentration of Mn and Fe throughout the alabandite is homogenous, remains constant from rim to rim and does not show any zonation. The variations are accounted for by the error estimated for the chemical components. The mineral formula of this alabandite is $Mn_{0.94}Fe_{0.11}S$.

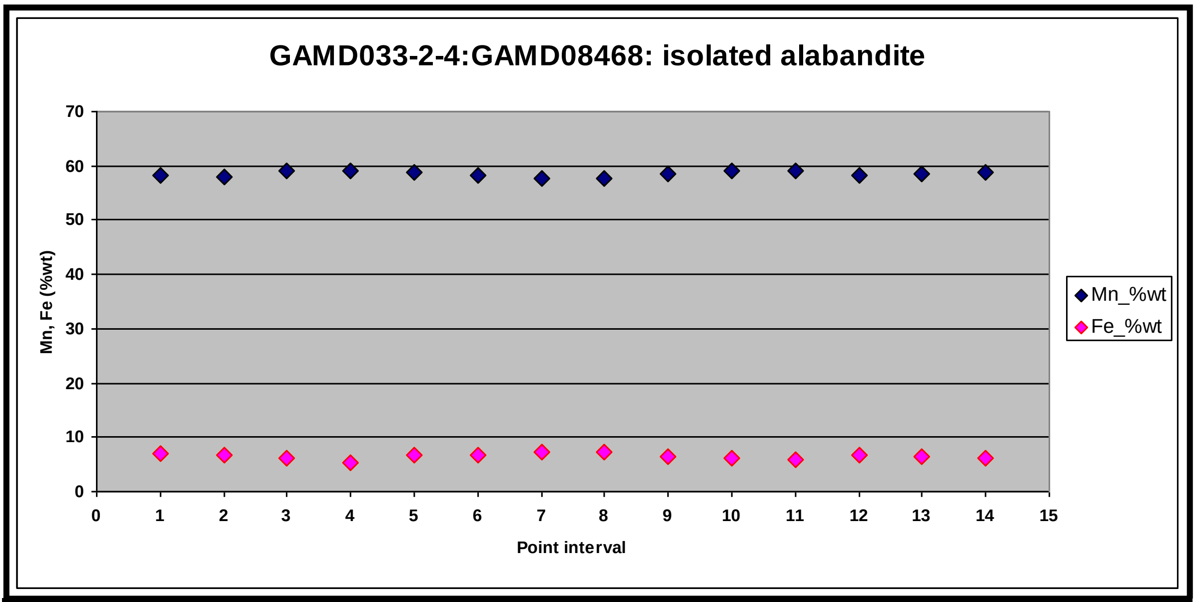

Average chemical analysis N = 14				Chemical formula N = 14			
Mn_%wt	**Fe_%wt**	**Zn_%wt**	**S_%wt**	Mn_mol	Fe_mol	Zn_mol	S_mol
58.51	6.53	0.02	35.78	0.94	0.11	0.00	1
± *0.221*	± *0.060*	± *0.125*	± *0.171*	± *0.05*	± *0.001*	*0.00*	

Figure 91. Cross-section through alabandite, which coexists with silicate minerals, and the chemical formula of the alabandite mineral chemistry error.

Figure 92 shows the cross-section, composition and chemical formula of the alabandite coexisting with pyrrhotite and sphalerite. The example is from sample GAMD14774 of drillhole *GAMD054-2-2*, which is meta-pelite ore. The concentration of Mn and Fe through the alabandite is homogenous, remains constant from rim to rim and does not show any zonation. The variations are accounted for by the error estimated for the chemical components. The mineral formula of this alabandite is $Mn_{0.92}Fe_{0.10}S$.

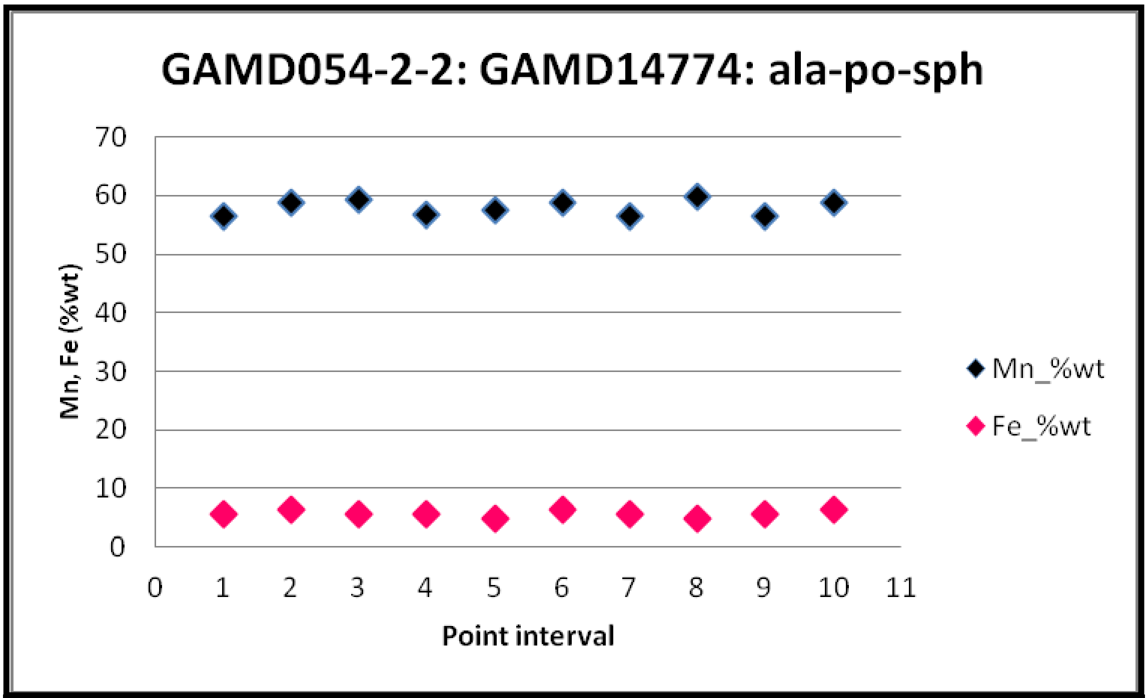

Average chemical analysis N = 10				Average chemical formula N = 10			
Mn_%wt	**Fe_%wt**	**Zn_%wt**	**S_%wt**	Mn_mol	Fe_mol	Zn_mol	S_mol
57.91	5.64	0.06	36.31	0.92	0.10	0.00	1
± 0.221	*± 0.060*	*± 0.125*	*± 0.171*	*± 0.05*	*± 0.001*	*0.00*	

Figure 92. Cross-section through alabandite that coexisted with silicate minerals and the chemical formula of the alabandite mineral chemistry error.

6.1.2 Sphalerite mineral chemistry data

6.1.2.1 Normal distribution tests for sphalerite dataset

The sphalerite dataset was tested for a normal distribution of S, Mn, Fe and Zn using probability plots and histograms. Figures 93 and 94 show sphalerite probability plots for S, Mn, Fe and Zn in %wt and %atomic respectively.

Figure 93 shows the probability plots of S (%wt), Mn (%wt), Fe (%wt) and Zn (%wt). The probability plots of Mn (%wt) and Zn (%wt) show a skewed distribution and therefore are not distributed normally. The probability plot of S (%wt) and Fe (%wt) shows kinks and therefore also is not distributed normally.

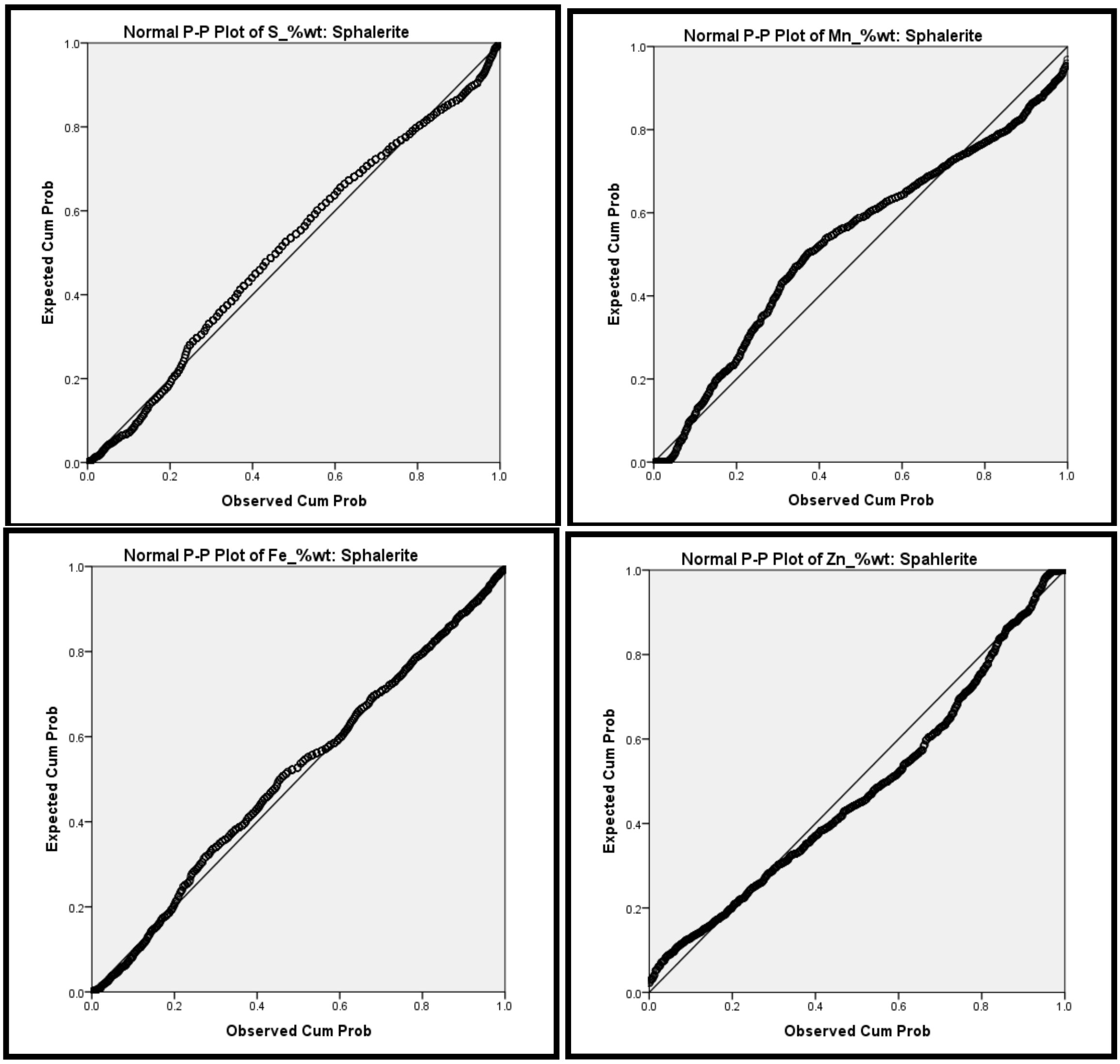

Figure 93. Probability plots of S, Mn, Zn and Fe (%wt) in the sphalerite population.

Figure 94 shows the probability plots of S (%at), Mn (%at), Fe (%at) and Zn (%at). The sulphur and iron distribution show a higher probability than a normal distribution. The manganese distribution is positively skewed and therefore not distributed normally. The zinc distribution is negatively skewed, therefore also is not distributed normally.

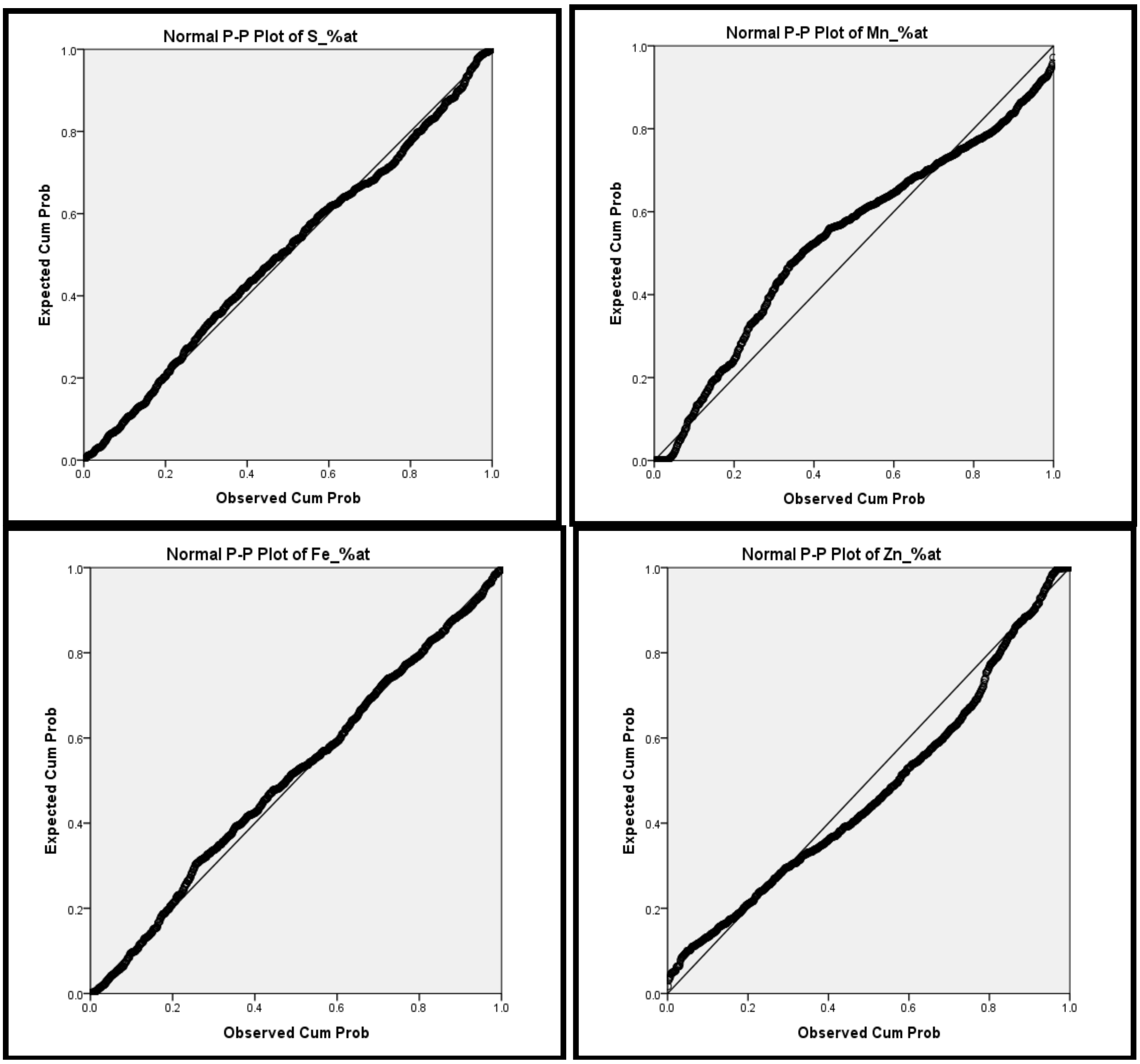

Figure 94. Probability plots of S, Mn, Zn and Fe (%at) in the sphalerite population.

A further analysis of the distributions of S, Mn, Zn and Fe (in %wt and %at) was undertaken using histograms. Figures 95 to 98 show distributions in %wt, and Figures 99 to 102 show the distributions in %at.

The sulphur distribution in Figure 95 shows a slightly positively skewed distribution. Figure 96 shows a positively skewed distribution of manganese. Both distributions are not normally distributed. Figure 97 shows that the distribution of Fe has the highest probability of being normally distributed, as the data fits into a normal distribution curve. Figure 98 shows a negatively skewed Zn distribution that is not normally distributed.

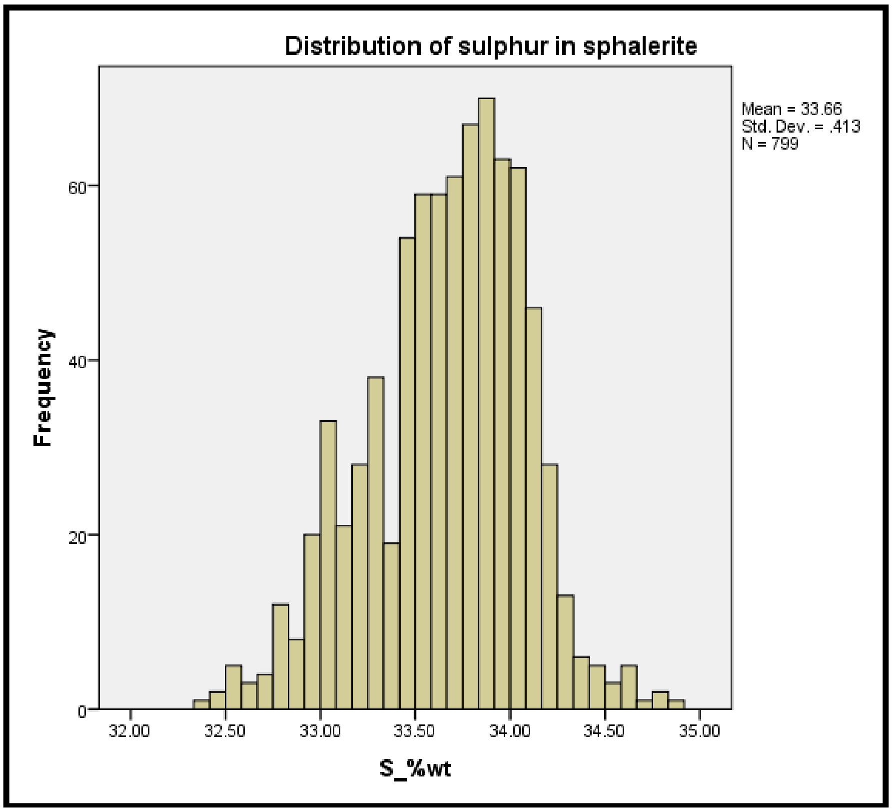

Figure 95. Histogram showing the frequency distribution of the sulphur content in sphalerite.

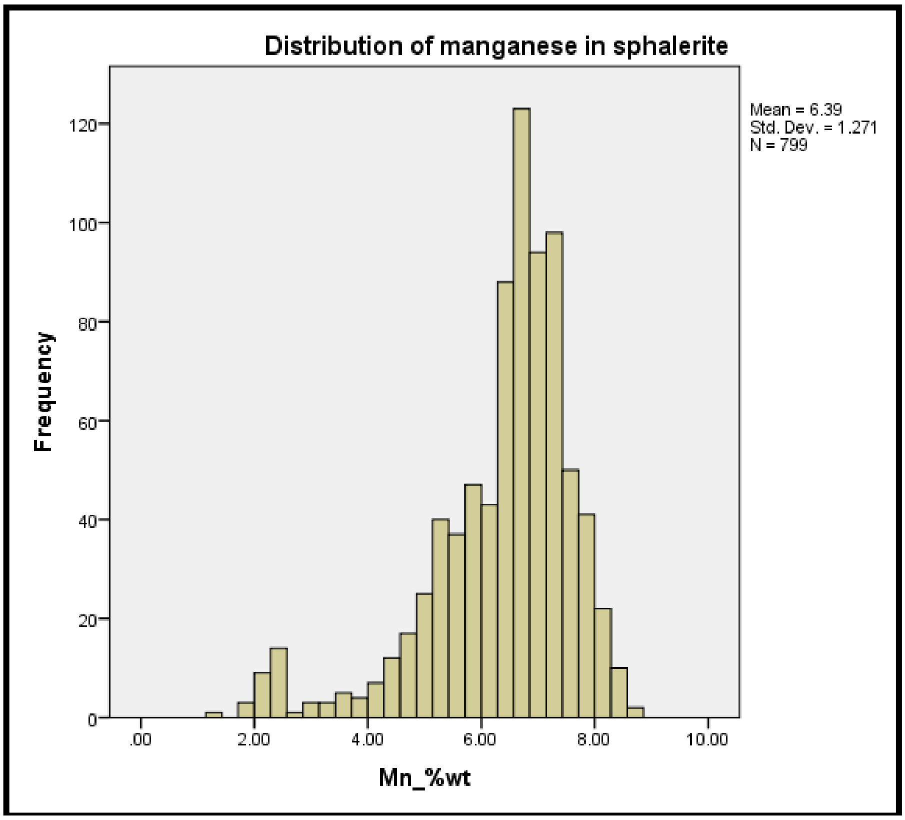

Figure 96. Histogram showing the frequency distribution of the manganese content in sphalerite.

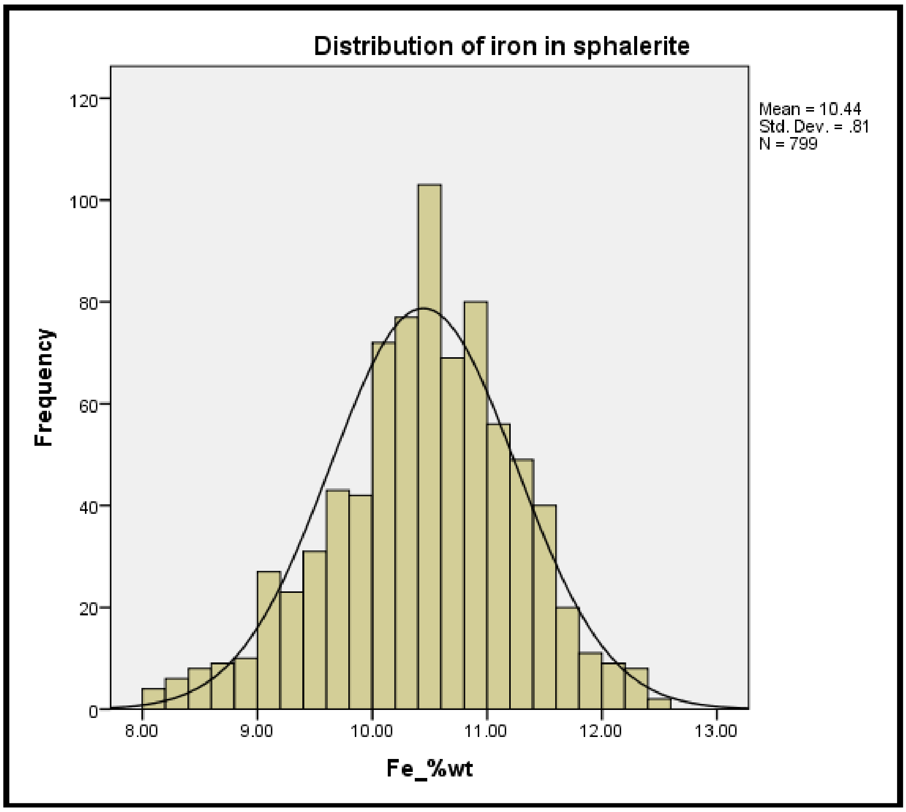

Figure 97. Histogram showing the frequency distribution of the iron content in sphalerite.

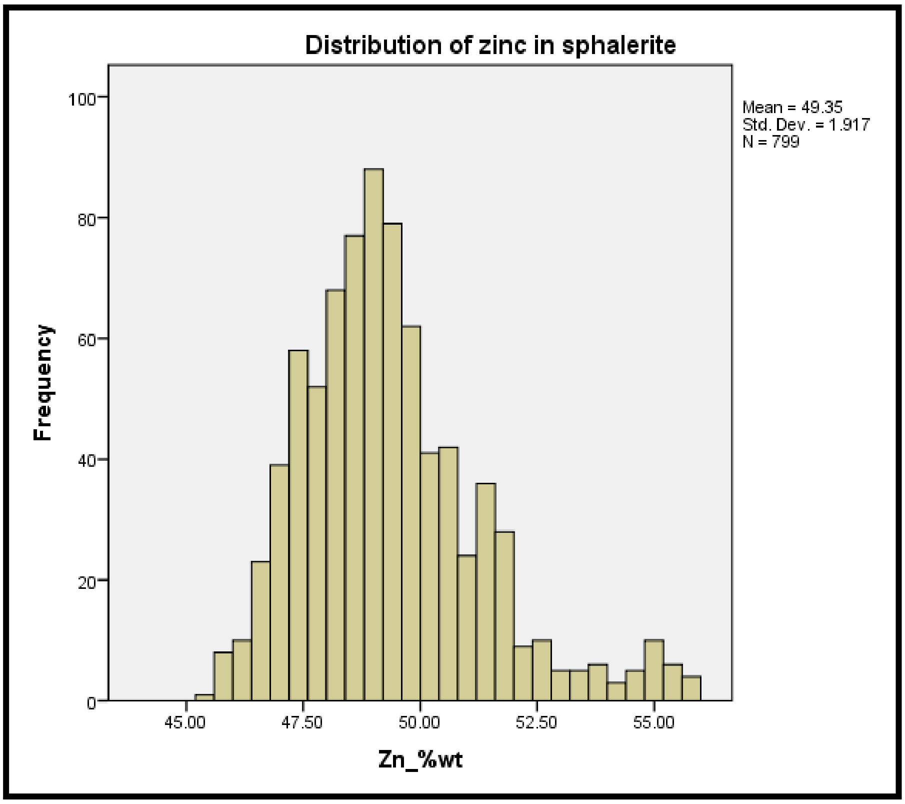

Figure 98. Histogram showing the frequency distribution of the zinc content in sphalerite.

The histograms in Figures 99 to 102 show the distributions (in %at) of sulphur, manganese, iron and zinc. The aim of using %at to further investigate the distribution of elements in sphalerite is to remove the effects that atomic mass has on the EMPA analysis. The objective still was to distinguish whether the elements were normally distributed or not.

The distribution of sulphur in Figure 99 shows that sulphur is normally distributed and it has a single population. Sulphur as a single anion in the monosulphide minerals is expected to be normally distributed, which also is the case in the sphalerite analysis.

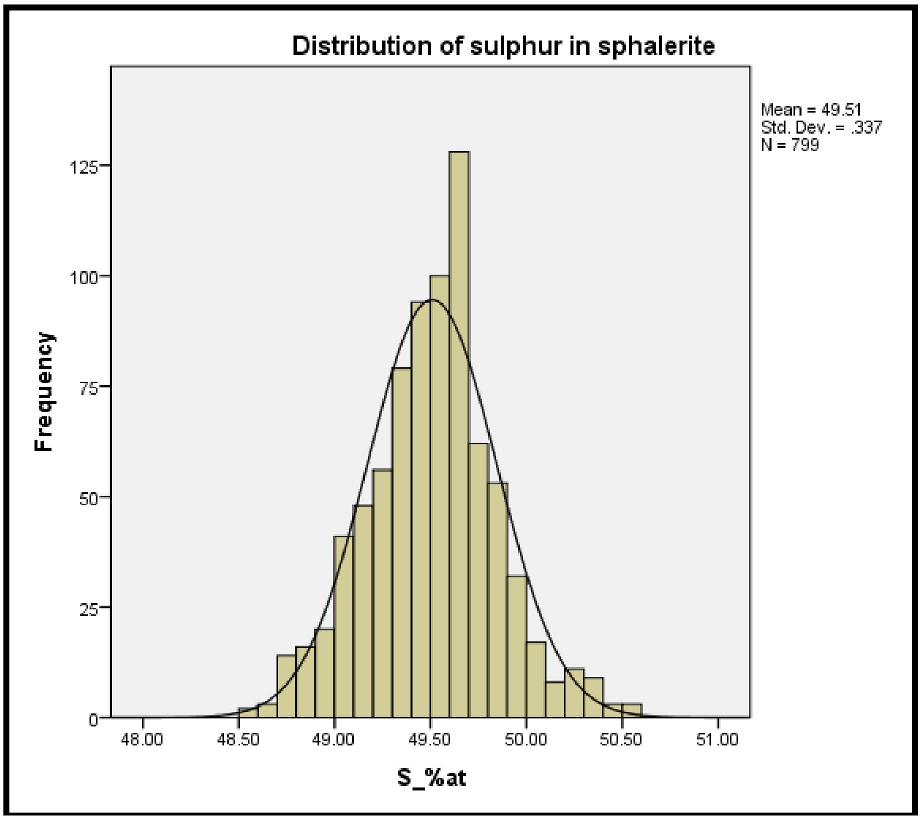

Figure 99. Histogram showing the frequency distribution of the zinc content in sphalerite.

The manganese distribution (%at) in Figure 100 shows a positively skewed distribution, with at least three population groups denoted by G1, G2 and G3. Groups G1 and G2 are positively skewed. Group G3 shows a probability of normal distribution. A further analysis of the manganese distribution was used to investigate this using box plots and scatter plots, as reported in the following sections.

The distribution of iron (%at) in Figure 101 shows a normal distribution, as the data fits into the normal distribution curve. The iron content, like the sulphur distribution, has a single population group. The single population group for iron means that factors that affected the distribution of Fe in sphalerite are not similar to those that affected other elements, such as manganese.

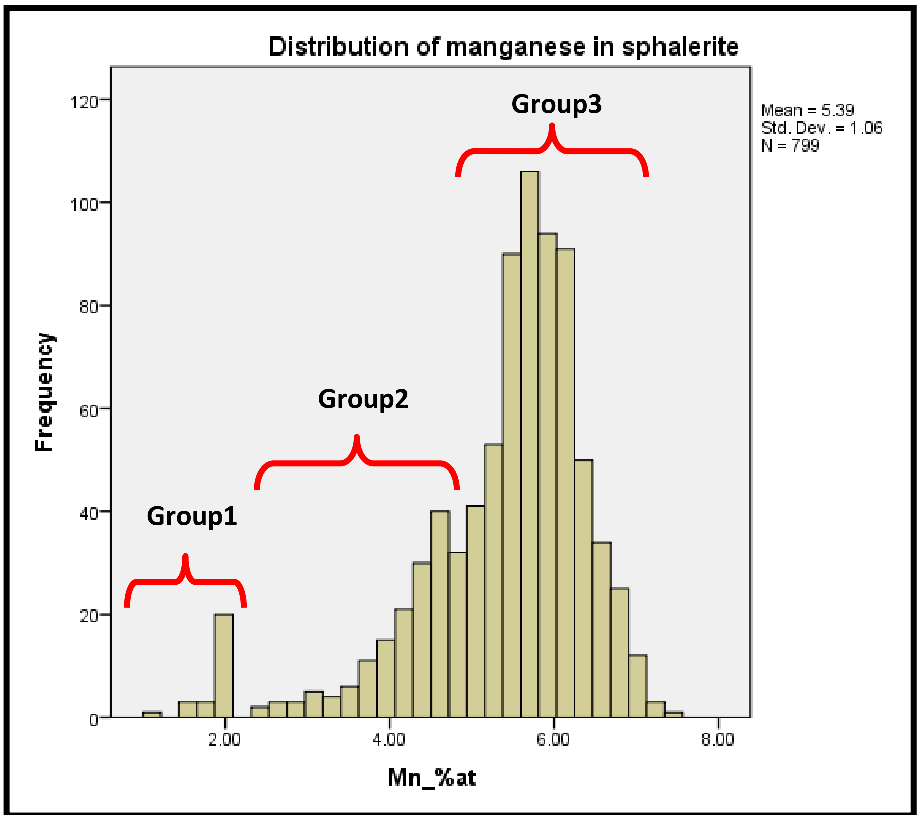

Figure 100. Histogram showing the frequency distribution of the manganese content in sphalerite.

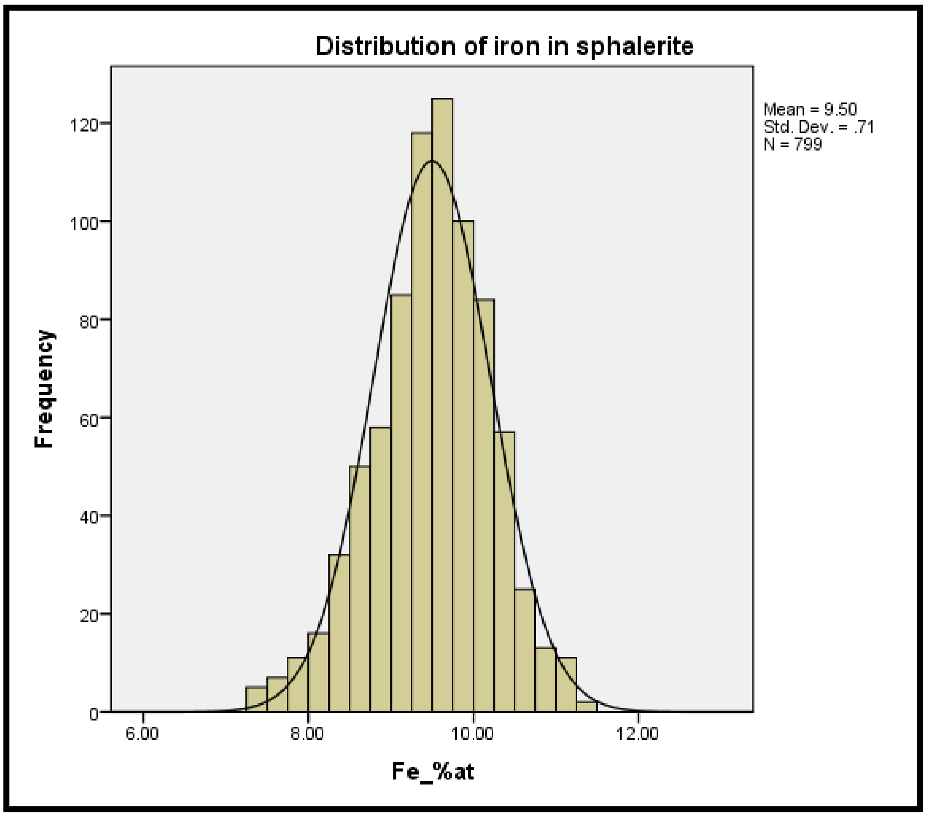

Figure 101. Histogram showing the frequency distribution of the iron content in sphalerite.

The distribution of zinc (%at) in Figure 102 shows a negatively skewed distribution with at least three groups, denoted by Groups 1, 2 and 3. This observation shows that the Zn distribution is not normally distributed and is negatively skewed. Further analysis of the manganese distribution was undertaken using box plots and scatter plots, as discussed in the following sections.

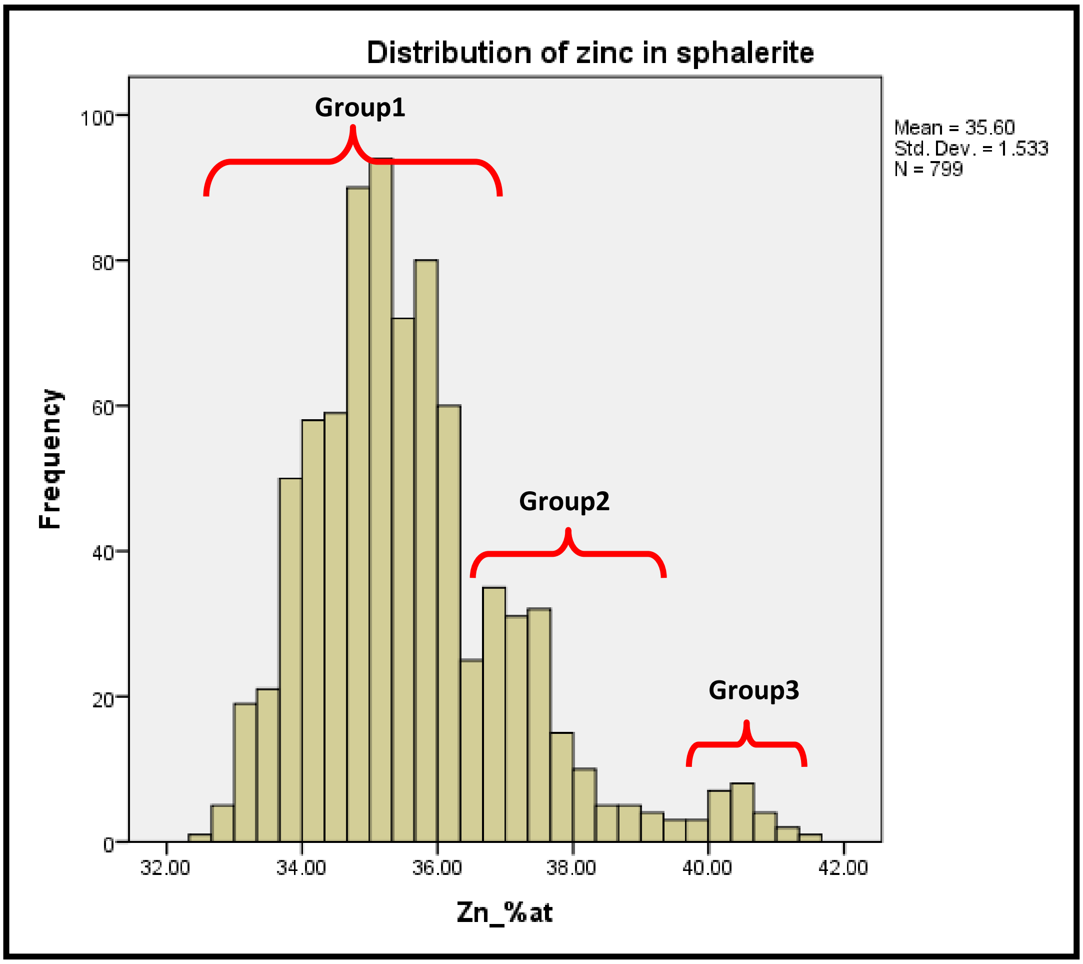

Figure 102. Histogram showing the frequency distribution of the zinc content in sphalerite.

Group 1 in manganese distribution + Group 3 in zinc distribution = Group A

Group 2 in manganese distribution + Group 2 in zinc distribution = Group B

Group 3 in manganese distribution + Group 1 in zinc distribution = Group C

6.1.2.2 Box plot of Mn and Zn distribution in sphalerite

The box plot of the manganese and zinc distributions in sphalerite is presented in Figures 103 - 106 to further understand the nature of the three groups present in both distributions. Rock types and coexisting mineral relationships are presented. The stratigraphic sequence of the rock type is pelitic schist, meta-pelite ore and garnet-magnetite ore. The coexisting mineral relationships are:

1. **Sph-silicate:** Sphalerite grains within the silicate mineral matrix (mica minerals)
2. **Sph-po:** Sphalerite coexisting mainly with large pyrrhotite grains
3. **Silicate-sph-po:** Sphalerite and pyrrhotite coexisting within the silicate mineral matrix
4. **Sph-ala:** Sphalerite coexisting with alabandite
5. **Sph-py:** Sphalerite coexisting with pyrite
6. **Sph-free exsolution:** Sphalerite grains free from other sulphide mineral grains
7. **Py-sph-po:** Sphalerite enclosed by pyrite and pyrrhotite
8. **Sph-grt:** Sphalerite coexisting with garnet

Figure 103 shows a box plot of manganese (%at) in sphalerite in the pelitic schist, meta-pelite ore and garnet-magnetite ore. The manganese content of sphalerite in the pelitic schist has no outliers or extreme values. In the meta-pelite ore, the distribution of manganese in sphalerite has outliers in samples GAMD08521 and GAMD15697. The garnet-magnetite ore has outliers and an extreme value, both from sample GAMD09376. The outliers and extreme value in %at translate into a manganese concentration of less than 3.02 %wt. The meta-pelite ore (PEO) has a larger range of manganese concentration in sphalerite compared to both the pelitic schist (PEL) and the garnet-magnetite ore (MPO). The manganese concentration decreases with depth because the median of manganese in the pelitic schist is the highest, while that in the meta-pelite ore is second lowest and in the garnet-magnetite ore is the lowest.

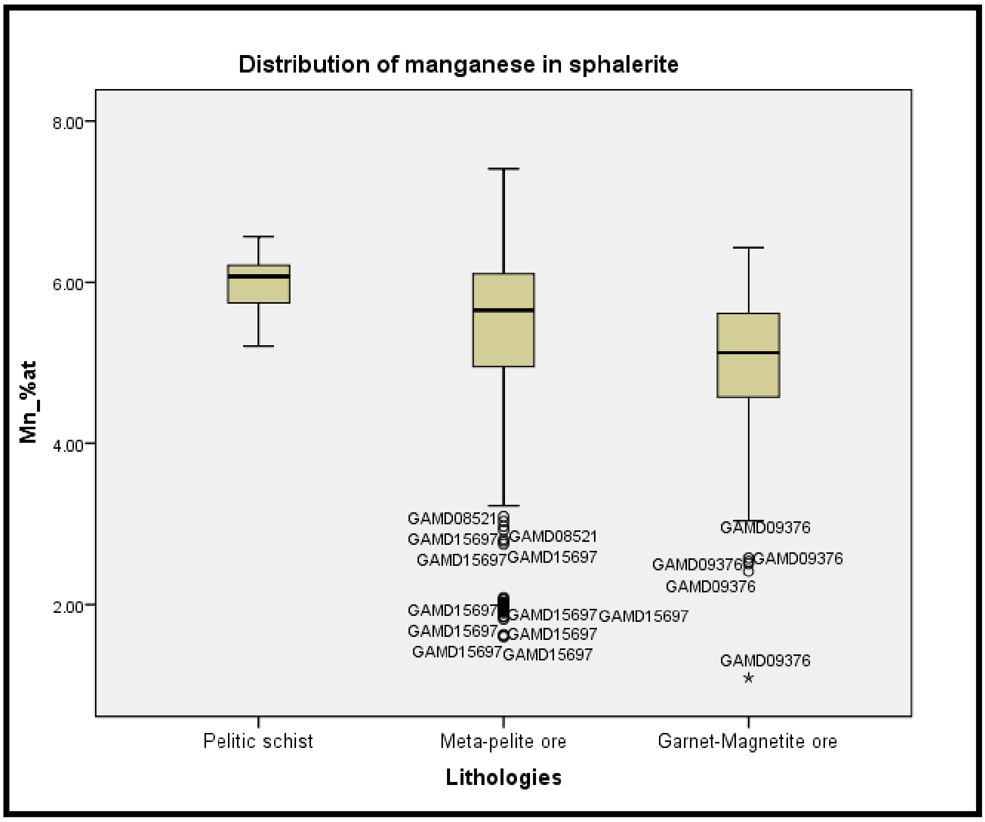

Figure 103. Box plot showing the distribution of manganese in sphalerite in the pelitic schist, meta-pelite ore and garnet-magnetite rocks.

Figure 104 shows a box plot of manganese (%at) in sphalerite with different coexisting phase relationships. The manganese concentration in sphalerite is the highest when sphalerite grains are not coexisting with Fe sulphides, whereas the sphalerite grains coexisting with Fe sulphide minerals have a relatively lower manganese concentration in sphalerite. Sphalerite grains coexisting with Fe sulphide minerals have a wider range of manganese concentrations, whereas the sphalerite grains not coexisting with Fe sulphide minerals have a narrow range of Mn concentration. Sphalerite coexisting with garnet has a Mn concentration with a narrow range and its median is similar to that of the Fe sulphide minerals. The outliers and extreme values represent a different sphalerite group.

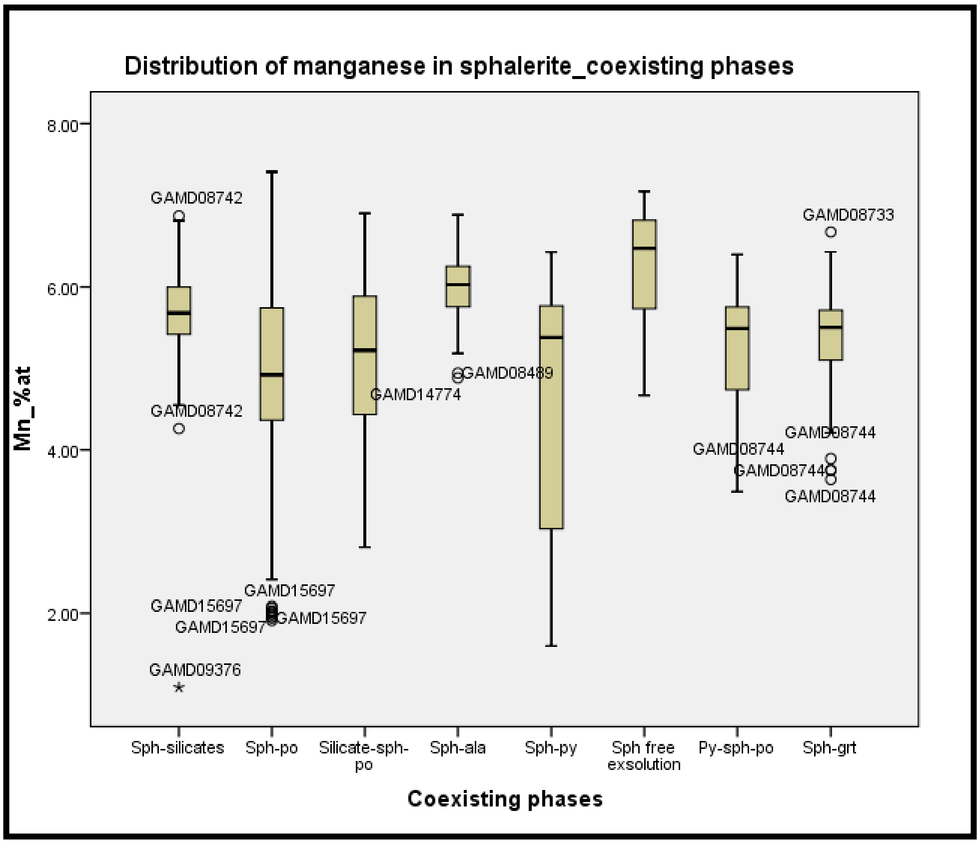

Figure 104. Box plot showing the distribution of manganese (%at) in the sphalerite for coexisting mineral phases.

Figure 105 shows the box plot of zinc (%at) in sphalerite in the pelitic schist, meta-pelite ore and garnet-magnetite ore. The zinc concentration in sphalerite in the pelitic schist is the lowest. In the meta-pelite ore, the distribution of zinc in sphalerite has outliers from sample GAMD15697. The garnet-magnetite ore has outliers from samples GAMD09376 and GAMD08744, and one extreme value from sample GAMD09376. The outliers and extreme value in %at translate into a zinc concentration of greater than 53.58 %wt. Meta-pelite ore has a larger range of zinc concentration in sphalerite compared to both pelitic schist and garnet-magnetite ore. The zinc concentration increases with depth because the median of the pelitic schist is the lowest, that of the meta-pelite ore is second highest and of the garnet-magnetite ore is the highest.

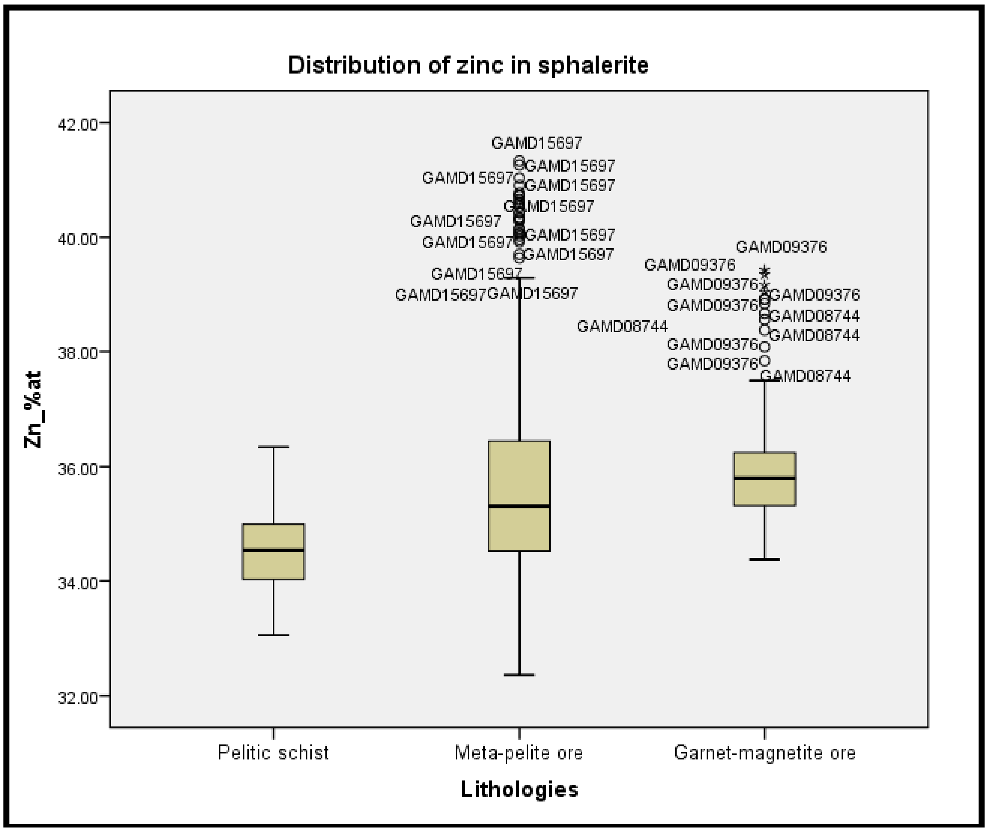

Figure 105. Box plot showing the distribution of zinc in sphalerite in the pelitic schist, meta-pelite ore and garnet-magnetite ore.

Figure 106 shows a box plot of zinc (%at) in sphalerite with different coexisting phase relationships. The zinc concentration in sphalerite is lower when sphalerite grains are not coexisting with Fe sulphides, whereas the sphalerite grains coexisting with Fe sulphide minerals have relatively higher zinc concentrations in sphalerite. The coexisting sphalerite grains with Fe sulphides have a wider range of zinc concentrations, whereas the sphalerite grains not coexisting with Fe sulphide minerals have a narrow range of Mn concentration. Coexisting sphalerite with garnet has a Mn concentration with a narrow range and its median is close to the Fe sulphides. The outliers and extreme values represent a different sphalerite group.

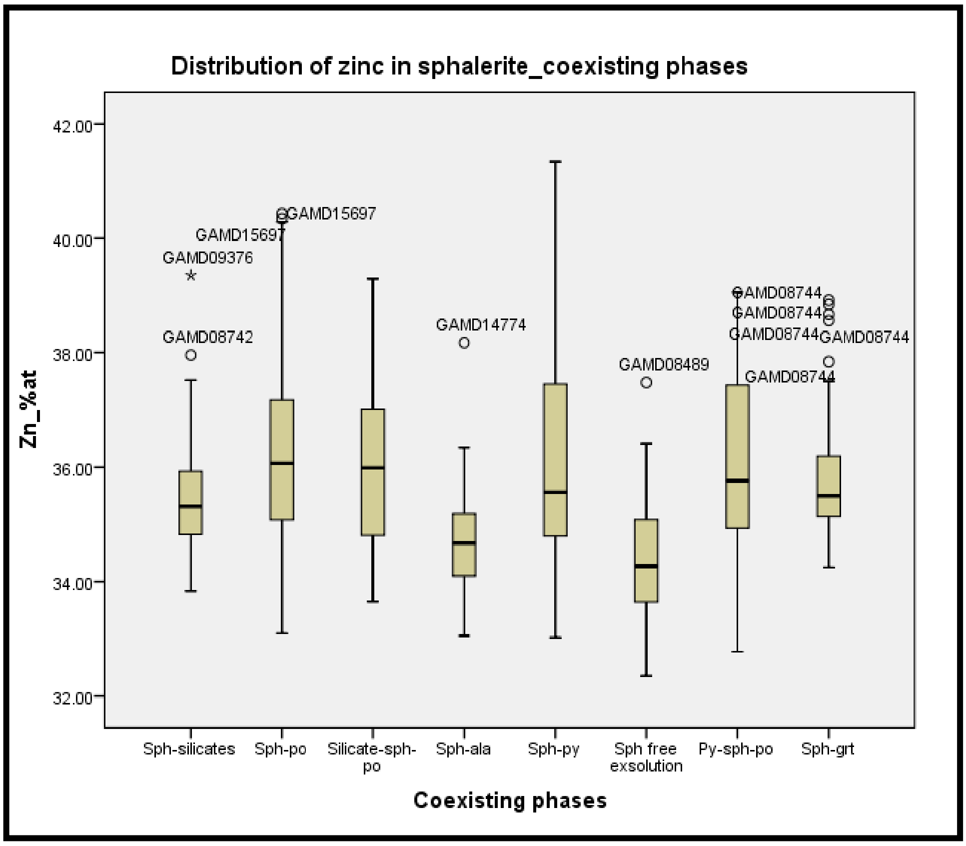

Figure 106. Box plot showing the distribution of manganese (%at) in the sphalerite for coexisting mineral phases.

There are three observations to be drawn from Figures 105 to 108 about the distribution of manganese and zinc concentrations in sphalerite:

1. The outliers and extreme values represent a group of sphalerite with a manganese concentration of below 3.02 %wt and a zinc concentration of above 53.58 %wt.
2. The manganese concentration in sphalerite decreases with depth, and the zinc concentration in sphalerite increases with depth.
3. Sphalerite coexisting with Fe sulphide minerals has a wider range of manganese and zinc concentrations. A narrow range of both manganese and zinc is observed in sphalerite coexisting with minerals other than Fe sulphide minerals.

6.1.2.3 Scatter-plot analysis of sphalerite mineral chemistry

Scatter plots are used in this section to further explore the relationships between iron, manganese and zinc in sphalerite. The sphalerite dataset was categorised into rock types, sample_ID and coexisting mineral phase relationships.

Figure 107 shows the relationship between manganese and iron in sphalerite, presented in %wt. There is one strong trend, showing a direct proportional relationship between manganese and iron. There also is a trend containing about 2 %wt Mn and scattered samples with no particular relationship. The meta-pelite ore (PEO) has the widest range of both manganese and iron. The pelitic schist (PEL) has sphalerite within the narrow range of both manganese and iron, and has a higher iron and manganese content than garnet-magnetite ore (MPO). The MPO unit hosts sphalerite with the most varying composition, as most of its samples are scattered.

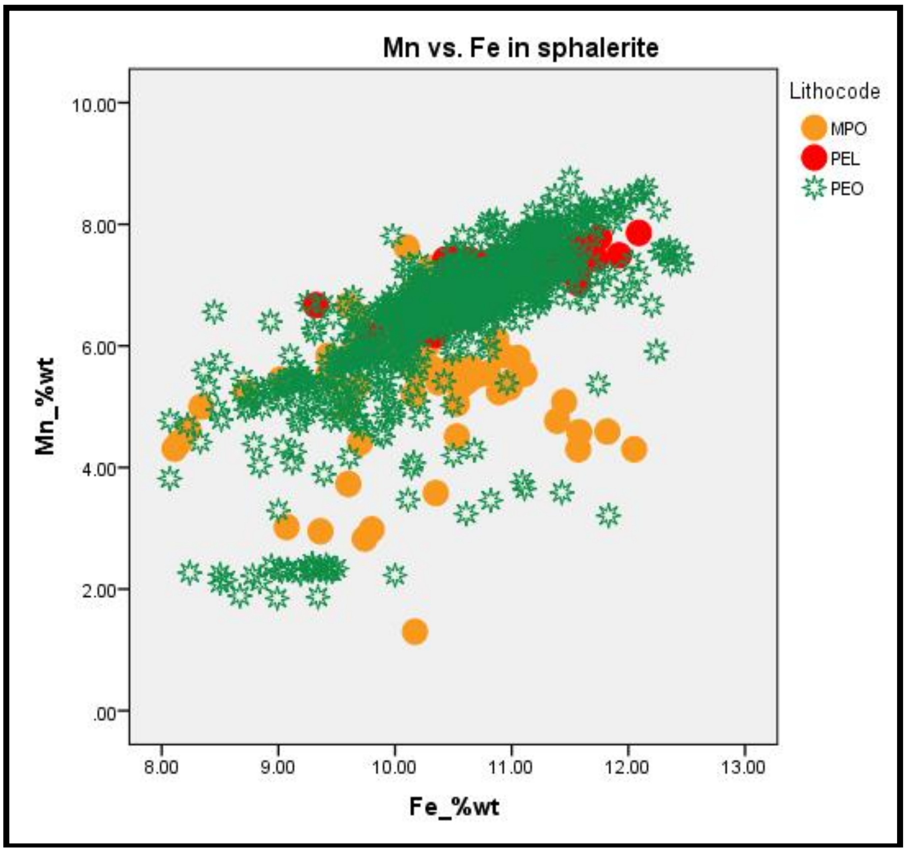

Figure 107. Scatter plot showing the relationship between the Mn and Fe (%wt) in sphalerite.

Figure 108 shows the relationship between manganese and zinc in sphalerite presented in %wt. The sphalerite composition generally shows an inverse relationship between manganese and zinc. The PEO unit hosts sphalerite with the widest range of zinc concentrations compared to the PEL and MPO. The PEO's sphalerite also has a cluster of samples with a high zinc concentration and low manganese concentration. The PEL unit hosts sphalerite that relatively speaking has the lowest zinc concentration and the highest manganese concentration compared to the PEO and MPO.

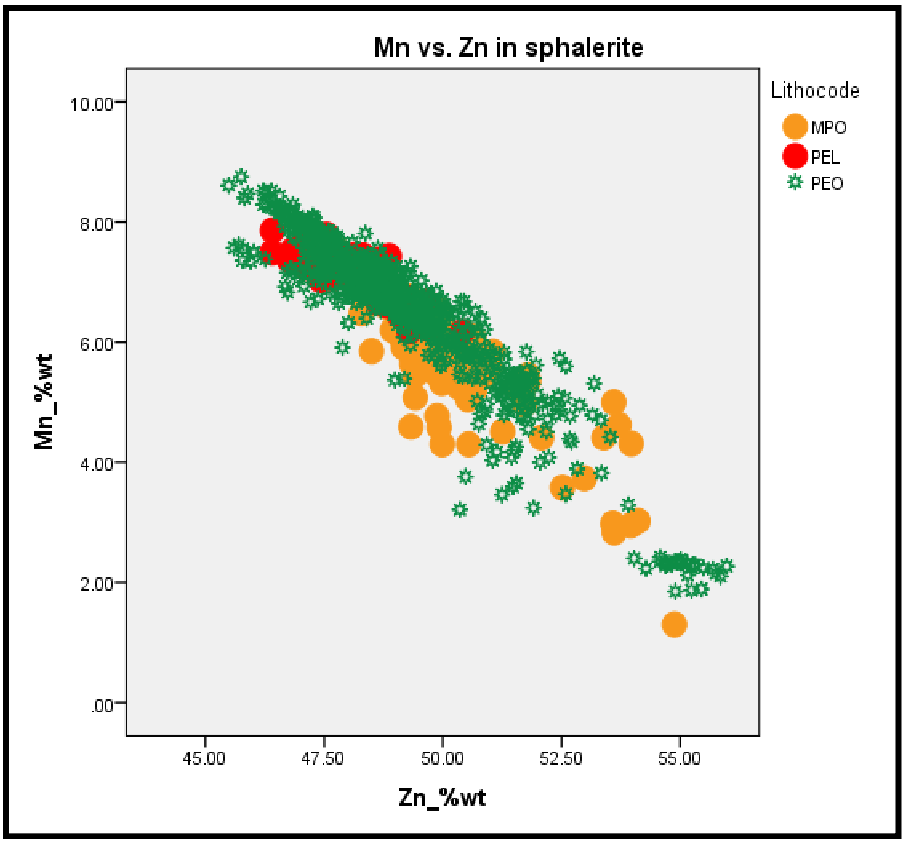

Figure 108. Scatter plot showing the relationship between Mn and Zn (%wt) in sphalerite.

Figure 109 shows the relationship between iron and zinc in sphalerite, presented in (%wt). The sphalerite composition shows an inverse relationship between iron and zinc. There are two strong trends with scattered samples and a wide range, and a trend with a high zinc concentration and low iron concentration. The trends are made up mainly from samples of PEO and PEL, whereas MPO has a varying sphalerite composition as most of its samples are scattered. The PEL unit hosts sphalerite with a higher iron concentration and lower zinc concentration compared to the MPO unit.

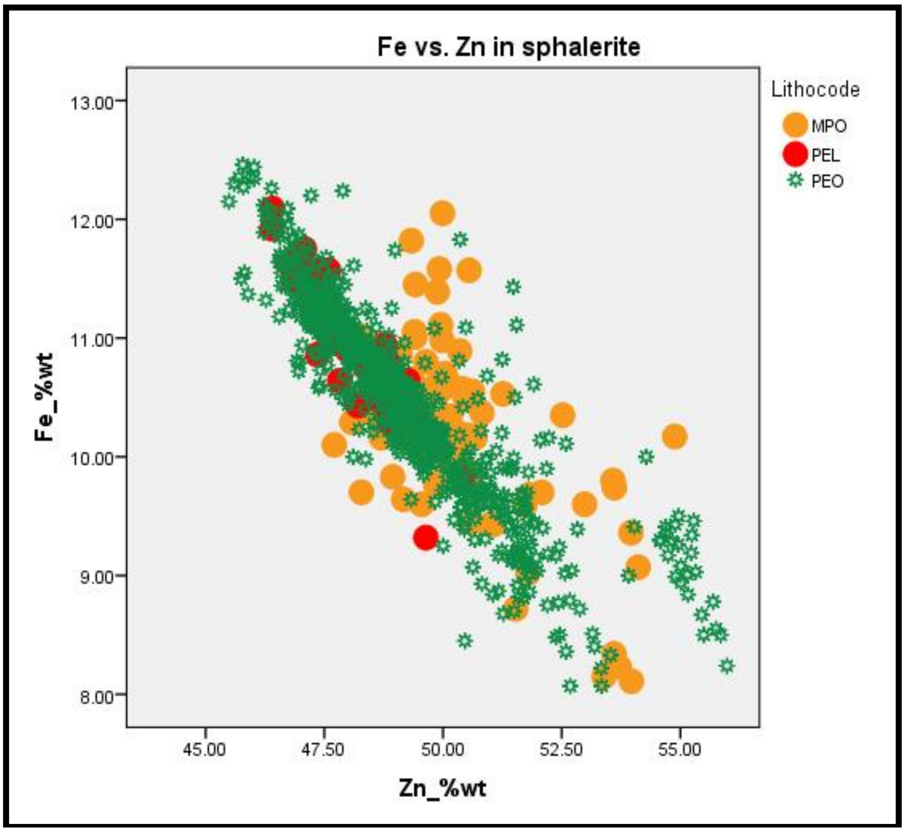

Figure 109. Scatter plot showing the relationship between Fe and Zn (%wt) in sphalerite.

The relationships between Fe+Mn and Zn in the sphalerite from individual drillholes were explored to further understand the distributions of iron, manganese and zinc. Iron and manganese are grouped together because both have an inverse relationship with zinc in sphalerite, as observed in Figures 107 to 109. The samples are ordered by increasing depth.

Figure 110 shows the relationship between Fe+Mn and Zn in sphalerite hosted by samples from drillhole *GAMD033-2-4*. The range of zinc in sphalerite from the three sample units is very similar, despite the difference in depth. In this case the sphalerite composition does not vary with depth. It should be noted that all three sample are from a meta-pelite ore rock unit.

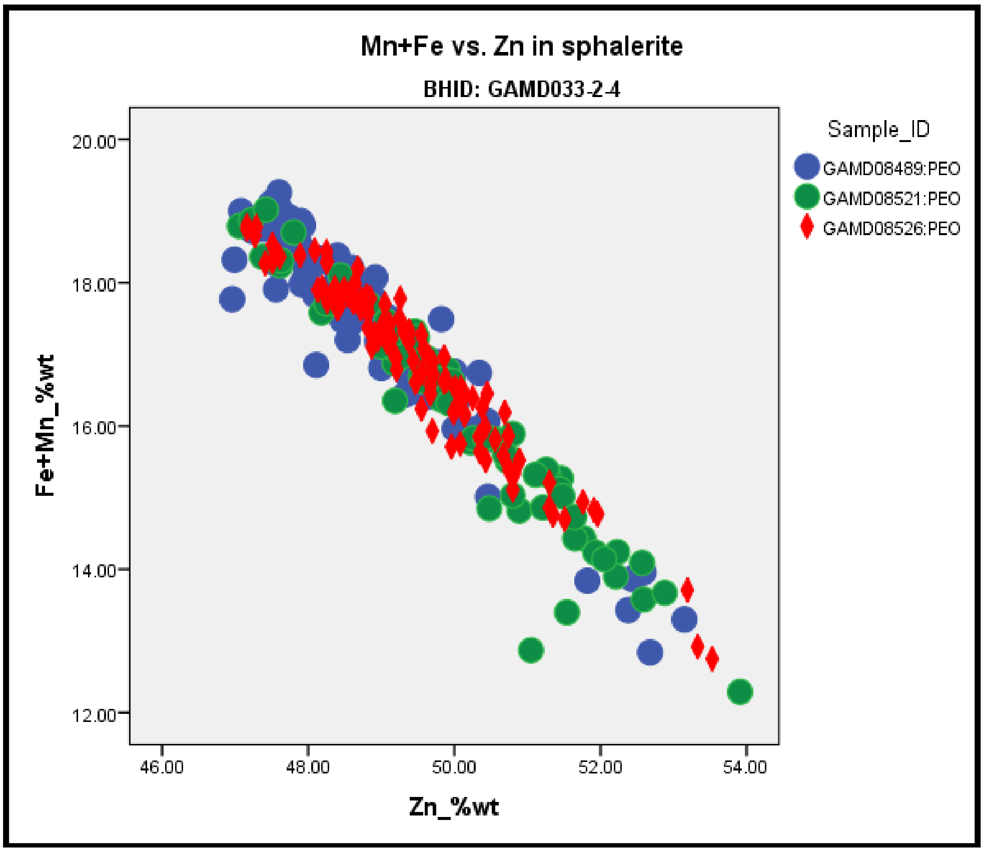

Figure 110. Scatter plot showing the relationship between Fe+Mn and Zn in sphalerite from drillhole GAMD033-2-4.

Figure 111 shows the relationship between Fe+Mn and Zn in sphalerite hosted by samples from drillhole *GAMD041-1-3*. The zinc concentration in the sphalerite increases with depth, as the lowest zinc concentration in sphalerite is within the topmost PEO from sample GAMD08733 and the highest zinc concentration in sphalerite occurs within the MPO from sample GAMD08744, and the PEO from sample GAMD08742 has a sphalerite composition in the middle between the sample units. The MPO sample also hosts a group sphalerite with the highest zinc concentration and the lowest Fe+Mn concentration.

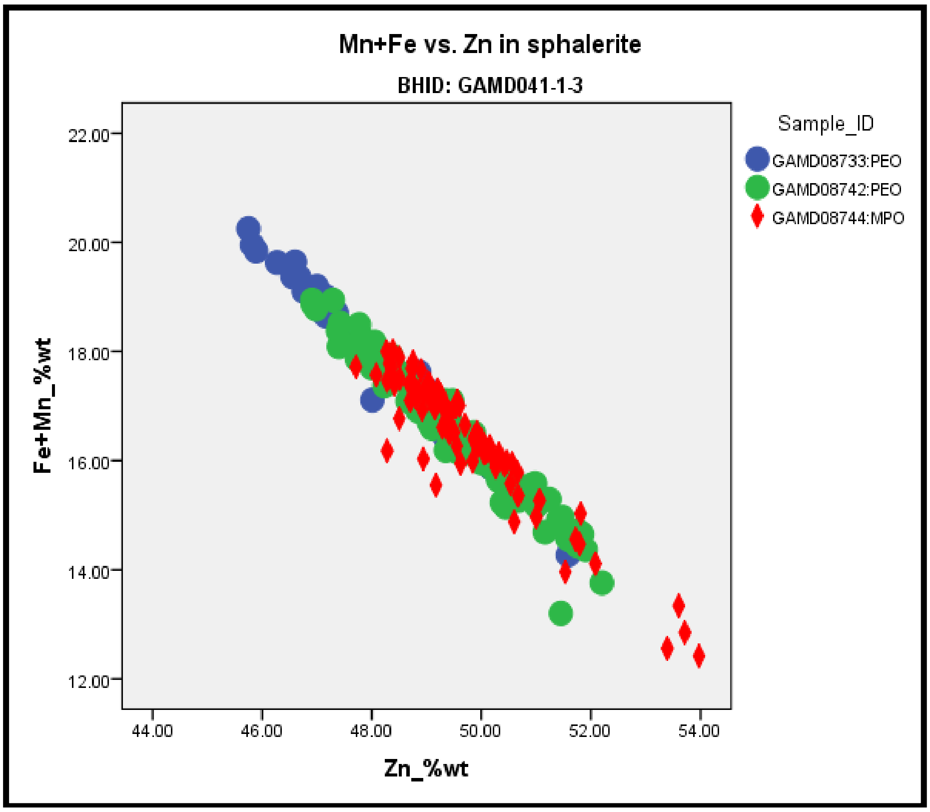

Figure 111. Scatter plot showing the relationship between Fe+Mn and Zn in the sphalerite from drillhole GAMD041-1-3.

Figure 112 shows the relationship between Fe+Mn and Zn in sphalerite hosted by samples from drillhole *GAMD045-0-0*. The sphalerite hosted by MPO had the lowest and highest zinc concentration, while the PEO hosting sphalerite had a zinc concentration in the middle between the other two. The ranges of Zn and Fe+Mn are very narrow compared to those in drillholes *GAMD033-2-4* and *GAMD041-1-3.*

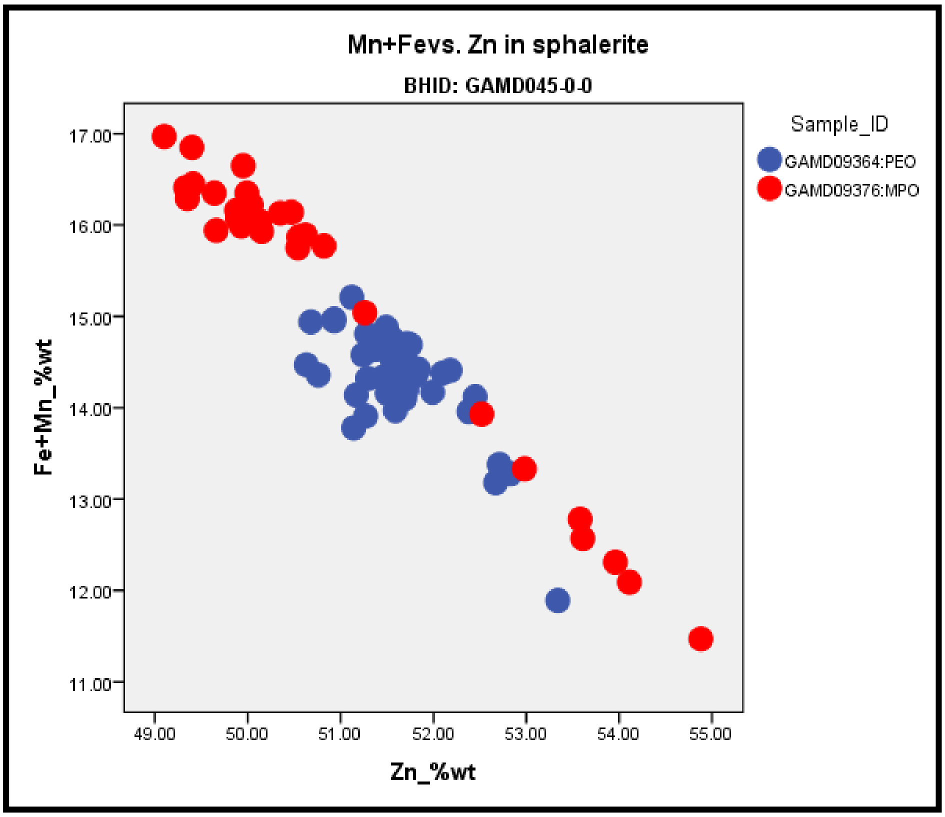

Figure 112. Scatter plot showing the relationship between Fe+Mn and Zn in the sphalerite from drillhole GAMD045-0-0.

Figure 113 shows the relationship between Fe+Mn and Zn in sphalerite hosted by samples from drillhole *GAMD054-2-2*. The three topmost samples (GAM14750, GAMD14774 and GAMD15677) host sphalerite almost similar in range to zinc and Fe+Mn. Sample 15697 hosts sphalerite with two distinct trends and hosts the highest zinc concentration and lowest Fe+Mn. One sample from GAMD14774 had a sphalerite composition in the same cluster as sample GAMD15697. The maximum Zn concentration of PEL was about 50 %wt.

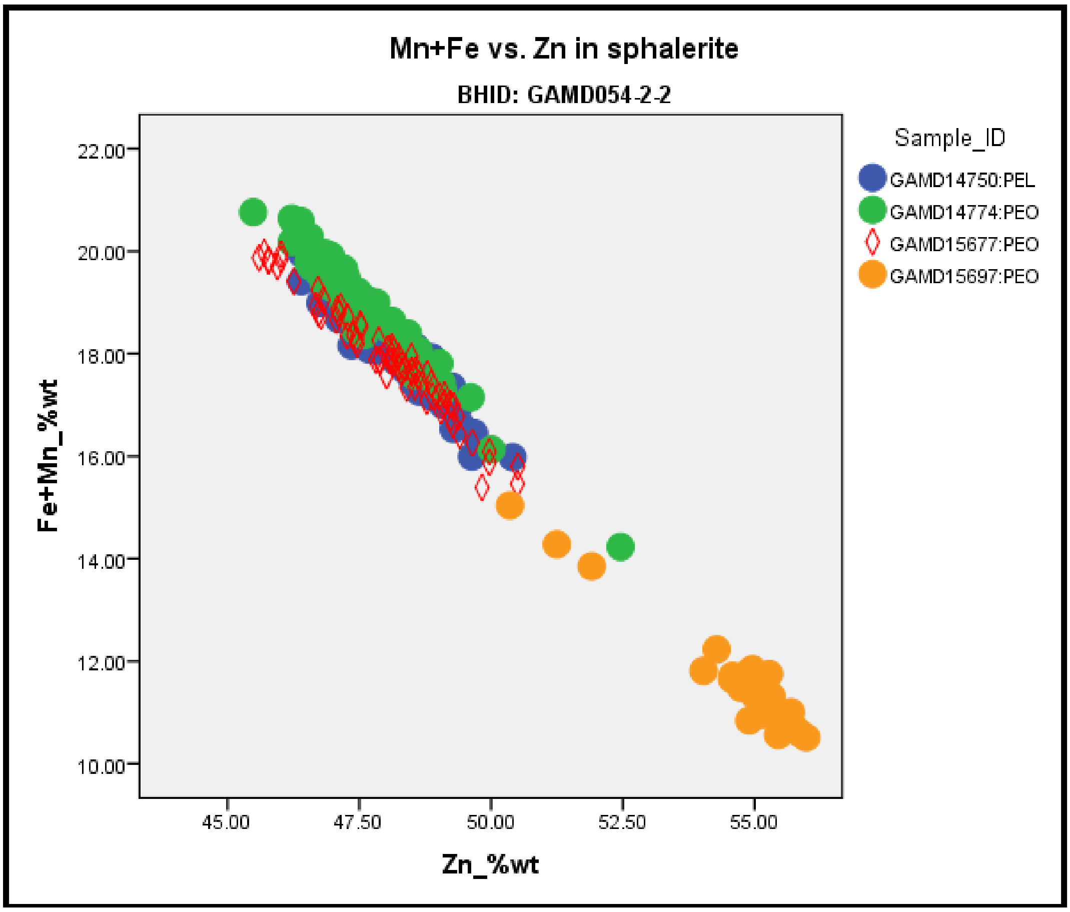

Figure 113: Scatter plot showing the relationship between Fe+Mn and Zn in the sphalerite from drillhole GAMD054-2-2.

In general there was a strong signature that the zinc concentration in sphalerite increases with depth, while the Fe+Mn concentration decreases with depth. The PEO unit hosts sphalerite with compositions that are similar, and PEO occasionally host samples with a sphalerite composition in the same range as the MPO unit's sphalerite, and even with a higher zinc concentration. There is a unique group with a high zinc and lower manganese concentration, mostly with a zinc concentration above 52 %wt.

The three groups in the manganese and zinc distribution in sphalerite can be related to depth, coexisting mineral relationships and rock types. A group or trend with the highest zinc and lowest iron and manganese concentrations is related to the remobilised sphalerite grains with a honey-colour. This honey-coloured sphalerite is present in meta-pelite ore and garnet-magnetite ore. The other two groups are as a result of the compositional variation of sphalerite, particularly from the variation in manganese and zinc, as manganese substitutes zinc in sphalerite.

6.1.2.4 Cross-sections of sphalerite

Cross-sections through sphalerite grains are presented in this section to investigate the compositional variation of individual sphalerite grains. The point analysed was from a rim through the core to the adjacent rim. Intervals were not fixed, but all analyses presented here are of individual sphalerite grains. The coexisting mineral grains were also noted. The graph is accompanied by the composition and chemical formula of the sphalerite grain presented. Minute variations are accounted for by the error estimated for the chemical components.

Figure 114 shows a cross-section through sphalerite coexisting with alabandite from drillhole *GAMD033-2-4* of sample GAMD08489. The concentration of Mn, Fe and Zn in sphalerite is homogenous, as the Mn, Fe and Zn remained constant from rim to rim and do not show any zonation. The mineral formula of this sphalerite is $Mn_{0.12}Fe_{0.20}Zn_{0.70}S$.

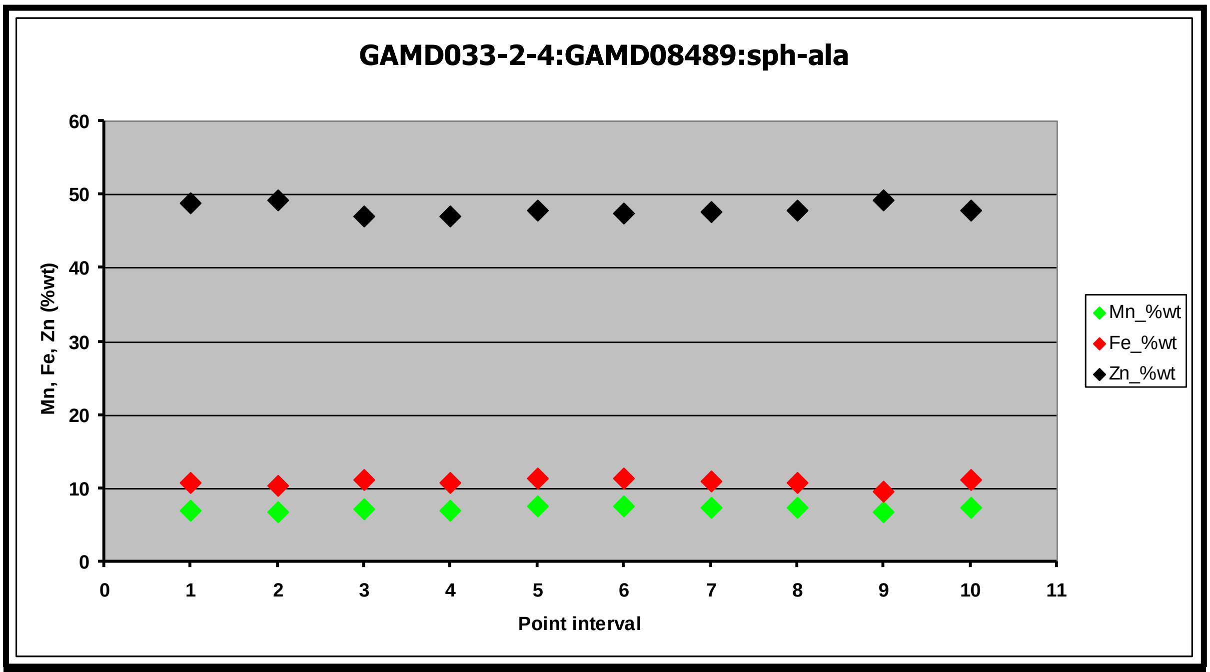

Average chemical analysis N = 10				Average chemical formula N = 10			
Mn_%wt	**Fe_%wt**	**Zn_%wt**	**S_%wt**	**Mn_mol**	**Fe_mol**	**Zn_mol**	**S_mol**
7.19	10.79	48.01	33.79	0.12	0.20	0.70	1
± 0.795	*± 0.082*	*± 0.177*	*± 0.163*	*± 0.011*	*± 0.002*	*± 0.047*	

Figure 114. Cross-section through sphalerite that coexist with alabandite, along with a table presenting the chemical composition, mineral formula and error estimations.

Figure 115 shows a cross-section through sphalerite coexisting with pyrrhotite and silicate minerals from drillhole *GAMD054-2-2* of sample GAMD15677. The concentration of Mn, Fe and Zn in the sphalerite is homogenous, remains constant from rim to rim and does not show any zonation. The mineral formula of this sphalerite is $Mn_{0.12}Fe_{0.20}Zn_{0.70}S$.

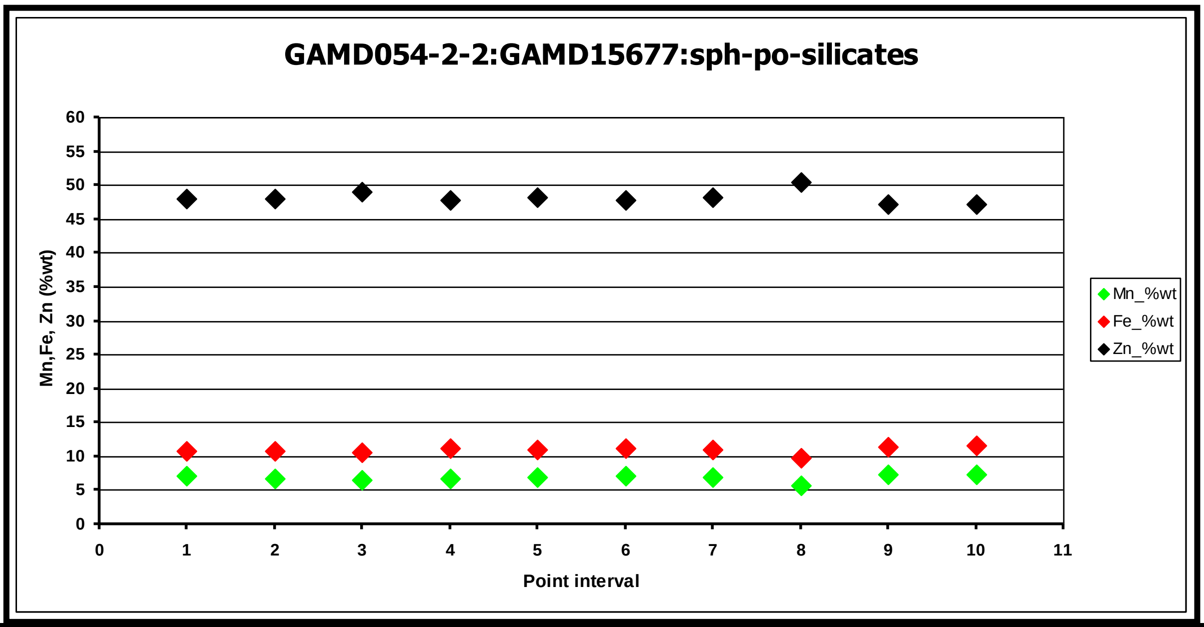

Average chemical analysis N = 10				Average chemical formula N = 10			
Mn_%wt	**Fe_%wt**	**Zn_%wt**	**S_%wt**	**Mn_mol**	**Fe_mol**	**Zn_mol**	S_mol
6.82	10.92	48.21	33.14	0.12	0.20	0.71	1
± 0.795	*± 0.082*	*± 0.177*	*± 0.1627*	*± 0.011*	*± 0.002*	*± 0.047*	

Figure 115. Cross-section through sphalerite that coexists with pyrrhotite and silicate minerals, along with a table presenting the chemical composition, mineral formula and error estimations.

Figure 116 shows a cross-section through sphalerite coexisting with pyrrhotite from drillhole *GAMD054-2-2* of sample GAMD15677. The concentration of Mn, Fe and Zn in the sphalerite is homogenous, remains constant from rim to rim and does not show any zonation. The mineral formula of this sphalerite is $Mn_{0.04}Fe_{0.18}Zn_{0.81}S$. This sphalerite composition is associated with remobilised honey-coloured sphalerite.

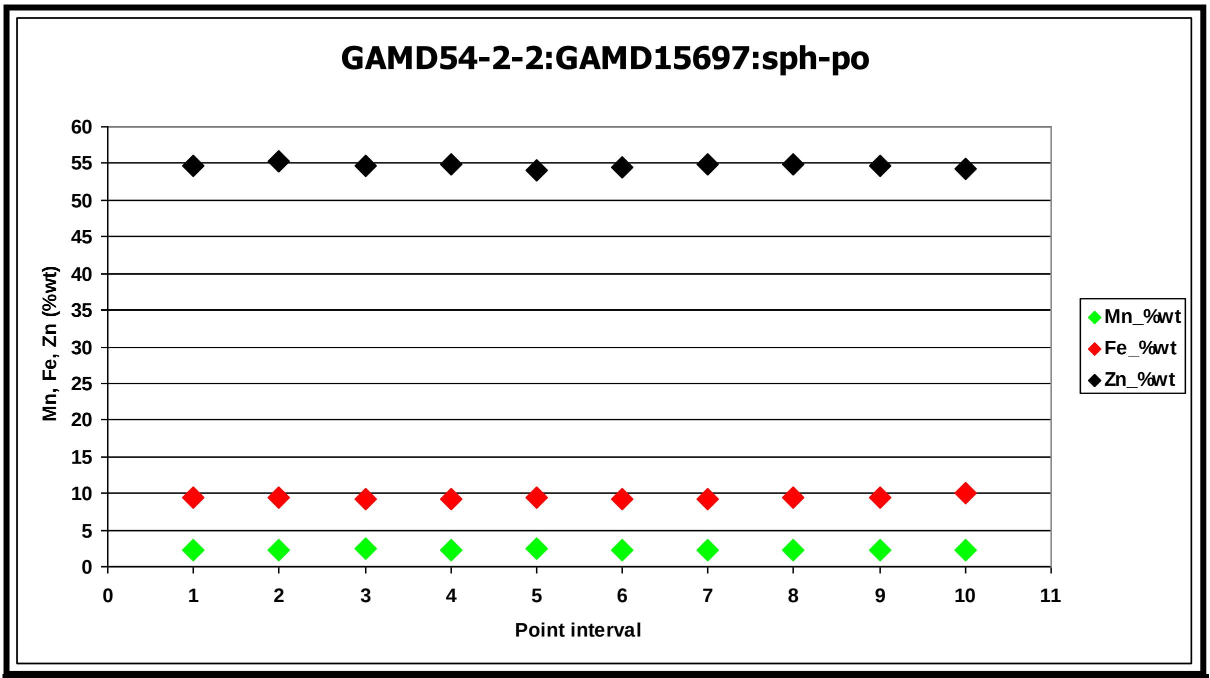

Average chemical analysis N = 10				Average chemical formula N = 10			
Mn_%wt	Fe_%wt	Zn_%wt	S_%wt	Mn_mol	Fe_mol	Zn_mol	S_mol
2.33	9.42	54.68	32.95	0.04	0.18	0.81	1
± 0.795	*± 0.082*	*± 0.177*	*± 0.163*	*± 0.011*	*± 0.002*	*± 0.047*	

Figure 116. Cross-section through sphalerite that coexists with pyrite, along with a table presenting the chemical composition, mineral formula and error estimations.

6.1.3 The relationship between coexisting sphalerite and alabandite

The mineral relationships between coexisting alabandite and sphalerite are presented in this section to investigate the behaviour of manganese, iron and zinc in coexisting phases. An alabandite grain enclosed by sphalerite grains on adjacent sides was used to demonstrate the coexisting mineral relationships. A cross-section through coexisting sphalerite and alabandite grains was used and the point intervals were not fixed. A table presenting the ratios of the averages of manganese, iron and zinc compositions from individual grains accompanies the cross-section.

Figure 117 shows the concentrations of manganese, iron and zinc through the sphalerite on the left side of alabandite, in the central alabandite and in the sphalerite on the right side. There are no compositional variations towards the edges/rims of the coexisting mineral grains. The ratios between alabandite and sphalerite minerals on both sides show that the Zn ratio and S are the same, whereas the Fe and Mn ratios vary slightly, although the variations are within the error margin (0.082 %wt Fe and 0.795 %wt Mn).

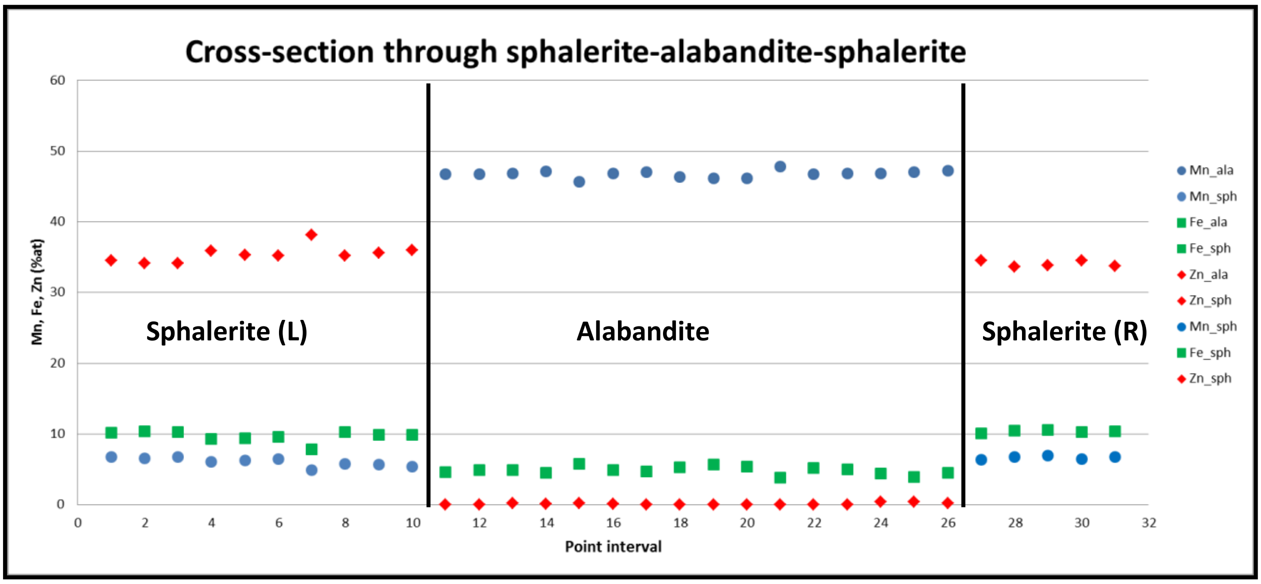

Mn_{ala}/Mn_{sph}	Fe_{ala}/Fe_{sph}	Zn_{ala}/Zn_{sph}	S_{ala}/S_{sph}	Relationships
7.73	0.50	0.00	0.99	Alabandite coexisting with sphalerite L
7.05	0.47	0.00	0.99	Alabandite coexisting with sphalerite R

Figure 117. Cross-section through coexisting sphalerite and alabandite, along with a table presenting the ratios of the average manganese, iron and zinc composition of the individual grains.

The ratios of manganese, iron, zinc and sulphur of other coexisting alabandite and sphalerite grains are presented in Table 28, along with the phase relationships and the number of point analyses involved in the calculation of the averages (in %wt) of individual phases (N, alabandite, sphalerite). The Mn ratios range from 7.037 to 7.836, despite phase relationships. The variation in Fe ratios is minute, ranging from 0.408 to 0.500. The Zn ratio is very small and close to non-existent. The S ratio is very close to 1.0, as expected, since both minerals are monosulphides. The ratios of metals of coexisting alabandite and sphalerite do not seem to be affected much by the phase relationships, as the variations fall within the error margins.

Table 28. Ratios of Mn, Fe, Zn and S of the coexisting alabandite and sphalerite.

Sample_ID	Mn_{ala}/Mn_{sph}	Fe_{ala}/Fe_{sph}	Zn_{ala}/Zn_{sph}	S_{ala}/S_{sph}	Phase relationships	N
GAMD08489_12	7.836	0.473	0.009	1.006	Alabandite within sphalerite	3;5
GAMD14750_10	7.715	0.473	0.001	0.999	Alabandite in contact with sphalerite	4;14
GAMD14774_10	7.054	0.408	0.001	0.988	Alabandite in contact with sphalerite	7;11
GAMD14774_4	7.037	0.485	0.002	0.985	Alabandite within sphalerite	5;10
GAMD14774_4	7.734	0.500	0.003	0.988	Alabandite in contact with sphalerite	16;10
GAMD14774_4	7.050	0.468	0.003	0.986	Alabandite in contact with sphalerite	16;5

Section 2: Distribution of manganese in silicate and oxide minerals

The distribution of manganese in the silicate and oxide minerals is shown in Figure 118. Pyrophanite ($MnTiO_3$) hosts the highest manganese concentration (43 %wt MnO) and is present within the MPO. The second highest manganese-bearing minerals are the garnet groups and spinel groups. The spinel groups are jacobsite, with about 33.5 %wt MnO, occurring within garnet quartzite (GQZ), and franklinite, with about 20 %wt MnO, occurring within the MPO. The most dominant garnet end members are spessartine, with about 32 %wt MnO, almandine, with about 20 %wt MnO, and grossular, with 12 %wt MnO concentrations. The garnet minerals are hosted within calc-silicate rock (CAS), amphibole-quartz rock (AQZ), garnet-amphibole-pyroxenoids-quartz rock (GAP) and garnet-magnetite ore (MPO).

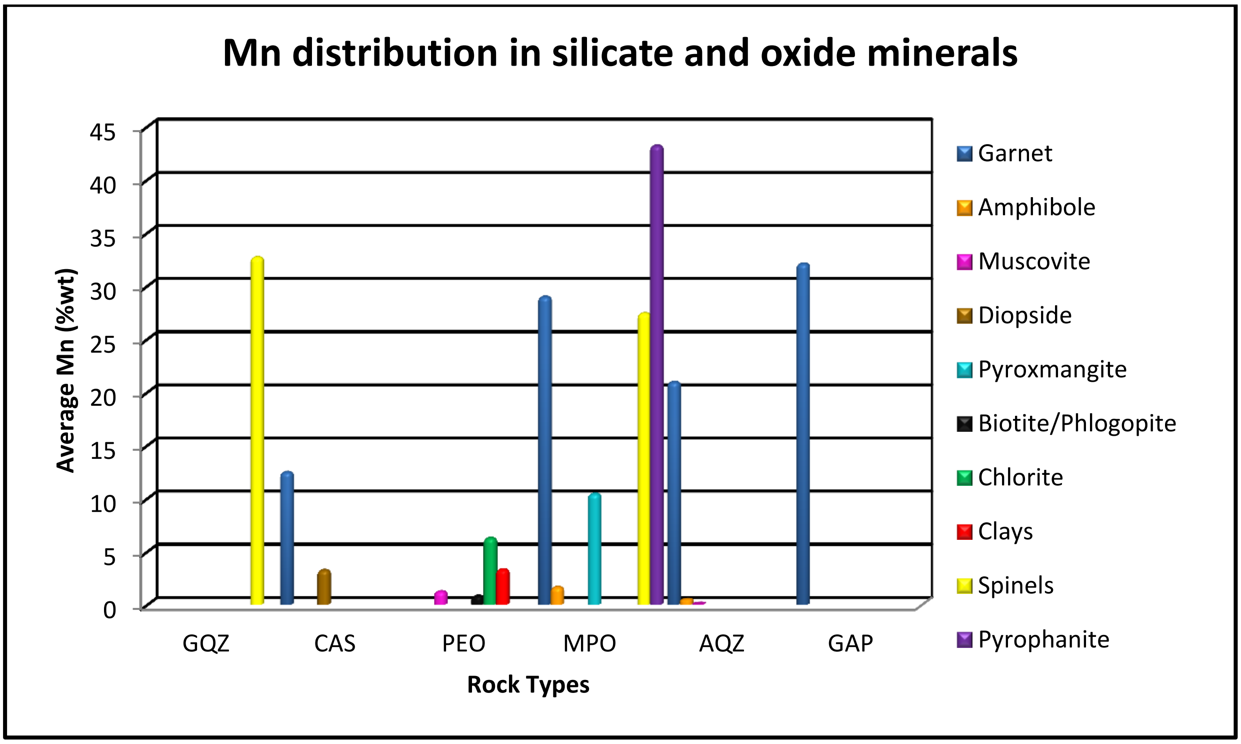

Figure 118. The distribution of manganese in silicate and oxide minerals.

Other minerals hosting significant manganese concentrations are pyroxmangite, with about 10 %wt MnO, chlorite, with about 6 %wt MnO, diopside, with about 3.5 %wt MnO, clay minerals, with about 3 %wt MnO, and amphibole (gedrite), with about 1.0 %wt MnO. Phlogopite and muscovite host MnO concentration of less than 1.5 %wt. Diopside and pyroxmangite are pyroxene and pyroxenoid end members, repectively.

Chapter 7: Discussions

Geochemistry datasets

The ICP dataset (Mn, Fe and Zn) was validated by means of comparing it with the XRF data. The ICP data, of-which is the historic dataset, was supposed to be used to generate a 3D model for the distribution of manganese, hence the need for validation. The XRF data was also generated to investigate the geochemical characterics of the Gamsberg East orebody using a subset of samples. For the purpose of consistency, similar sampling criteria/procedure as the historical dataset (eg. Sample ID, sample interval etc) was used for the generation of the XRF dataset.

The results of the compatibility tests using Spearman's correlation, showed that iron and zinc have a correlation coefficient of 0.95 and above when comparing the both the XRF and ICP datasets. Manganese, on the other hand, shows poor compatibility with the XRF and ICP techniques, with Spearman's correlation coefficient below 0.60. However, manganese in the pelitic schists and meta-pelite ores has Spearman correlation coefficient of 0.95 and above, whilst the garnet-bearing rocks continued to show poor correlation.

In addition to manganese showing poor compatibility between the XRF and ICP dataset, the element concentrations (quantities) from the ICP dataset are generally lower than those of the XRF major element analysis, and slightly higher than that of the XRF trace element analysis. Unlike manganese and iron, the zinc concentration is less variable in all rock units.

Poor compatibility and varying concentration are as a result of differences in sample preparation methodologies between the XRF, and ICP techniques. The ICP technique sample preparation methodology involves digestion of material by strong acids, whereby sulphide minerals are completely dissolved but silicate, and oxide minerals are partially dissolved. Manganese in garnet-bearing rocks dominantly occurs within silicate, and oxide minerals and these minerals are known to partially dissolve unlike sulphide minerals. Partial dissolution of Mn-bearing silicate, and oxide minerals resulted in bias in the whole-rock geochemistry dataset, especially for manganese data. The ICP dataset is therefore not a complete representation of whole-rock geochemistry at least for ICP manganese geochemistry dataset.

To further substantiate the poor compatibility between the XRF and ICP techniques, Certified Reference Materials (CRMs) data were compared. Table 29 shows the percentage difference between the XRF analysis of CRMs from the University of Pretoria and that from the Ore Research and Exploration (ORE) PTY Ltd. The average percentage difference between the XRF analysis and the ICP analysis is consistent with at least 25% and 19% higher for iron and zinc, respectively. The average percentage difference for Mn varies is 27% between the XRF and three-acid digest, and 17% between XRF and fusion method. This indicates a real fundamental bias in the Mn analysis.

Table 29. The comparison of the analysis of the CRMs and percentage differences.

Comparison of analysis of the Gamsberg Certified Reference Materials (CRMs)						
	Three-acid digest_ORE	Fusion_ORE	XRF_UP		% diff XRF vs. 3-Acid Digest	% diff. XRF vs. Fusion
Fe_LG	20.68	21.06	26.75		**23%**	**21%**
Fe_MG	23.76	23.53	31.78		**25%**	**26%**
Fe_HG	21.28	20.98	28.86		**26%**	**27%**
				Average	**25%**	**25%**
Mn_LG	1.08	1.27	1.49		**28%**	**15%**
Mn_MG	0.72	0.77	0.92		**22%**	**16%**
Mn_HG	1.37	1.57	1.99		**31%**	**21%**
				Average	**27%**	**17%**
Zn_LG	4.19	4.22	4.96		**16%**	**15%**
Zn_MG	6.26	6.3	7.86		**20%**	**20%**
Zn_HG	10.06	9.99	12.76		**21%**	**22%**
				Average	**19%**	**19%**

The results above indicate that the application of the geochemical data should always take into consideration the limitations of any analytical techniques, such as sample preparation methods, step-wise analysis as a result of upper detection limits of the ICP technique, matrix correction factors for the XRF technique, correction for inter-elemental spectral interferences, and reporting units (the ICP data is reported as elements in ppm and %, whereas the qualitative XRF analysis is reported in molecular %wt and the semi-quantitative XRF is reported in ppm).

Distribution of manganese and the geology of the Gamsberg East orebody

The distribution of manganese within the Gams Formation of the Gamsberg Zn deposit is not homogenous, and varies both laterally and vertically within the four orebodies. Laterally, the relatively thin Gamsberg East orebody hosts the highest manganese concentration compared to the other Gamsberg orebodies, as well as the highest concentration of Zn.

Vertically, a typical manganese profile of the Gams Formation shows that high concentrations of manganese are hosted by the chemogenic rocks of the A, C and transitional B2 (MPO) units, with manganese hosted specifically within the garnets and pyroxenoids. The metapelite rocks of the B1 unit host significantly lower manganese concentrations, with manganese occurring in sphalerite and occasionally within retrogressed Mn-bearing chlorite and clay minerals. In contrast to the typical manganese profile in the B1, the B1 unit in this study was found to host higher manganese concentration with a maximum of 24 %wt MnO (bulk rock geochemistry from XRF analysis), particularly within the pelitic schist. Manganese concentrations above approximately 2.0 %wt MnO in the metapelite ore are found to be associated with the presence of alabandite, particularly in the drillholes *GAMD033-2-4 and GAMD054-2-2.*

A reconstruction of the Gamsberg basin architecture shows that the basin had an uneven floor which is tentatively interpreted as basin deeeping in the half-graben structures. Basin deepening is indicated by variations in the thickness of the Gams Formation in the Gamsberg East orebody, as well as mineralogical evidence of varying redox conditions. Basin deepening played a role in controlling the redox conditions and, in turn controlling the timing of the precipitation of manganese and therefore controlling its distribution.

Figure 119 shows a cross-section through the Gamsberg South orebody with drillhole intersections and the different rock units. The interpretation of the section was prepared with the assistance of down-hole geophysical surveys. Definite undulation (pinch and swell) can be observed throughout the cross-section. This supports the idea that there is a variation in thickness of the lithological units. This variation in thickness cannot be exclusively be attributed to deformation events that affected the Gamsberg Zn deposit, as deformation also may have exaggerated the pre-existing thickness of units.

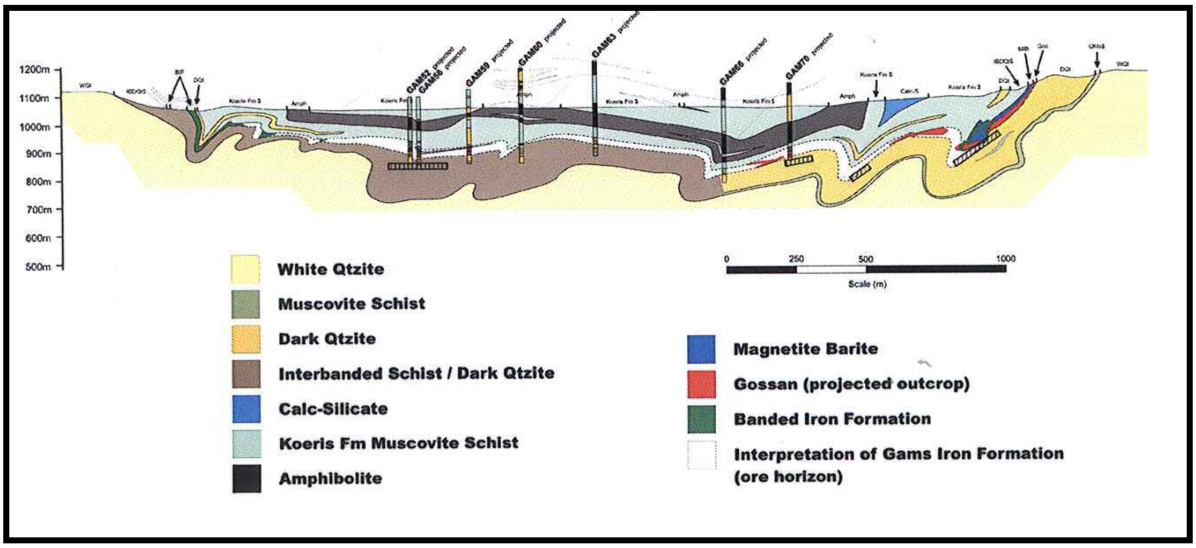

Figure 119: A map displaying a cross-section through the Gamsberg South orebody. (courtesy of Anglo Operation Division, October 2006).

“Basin deepening” is further illustrated in Figures 120 and 121. Figure 120 shows a 3D geological model of the Gamsberg East orebody with a mineralisation depth below sea level. This shows the undulation of the orebody in the N-S (left-right) direction.

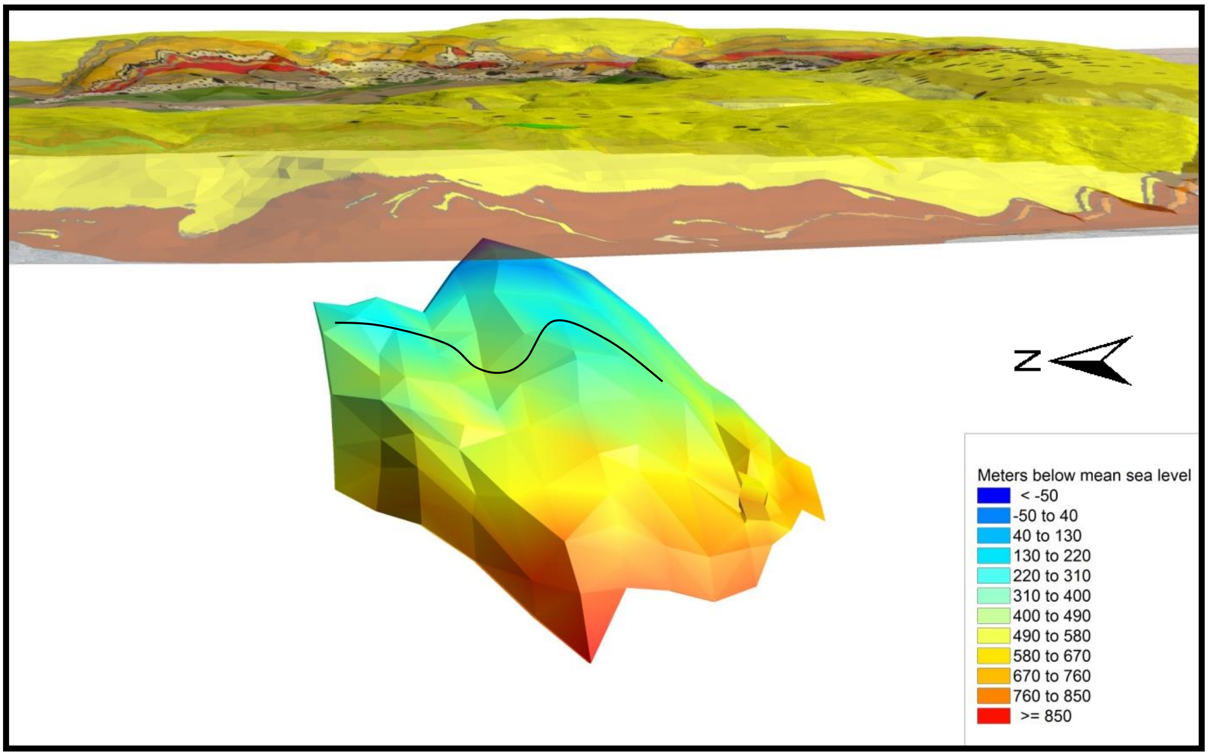

Figure 120: A 3D geological and topography model of the Gamsberg East orebody with a S-N (looking W) section view.

Figure 121 shows a map of the Gamsberg East orebody, cross-section shows a variation in thickness of the mineralised unit (Gams Formation) in the E-W direction.

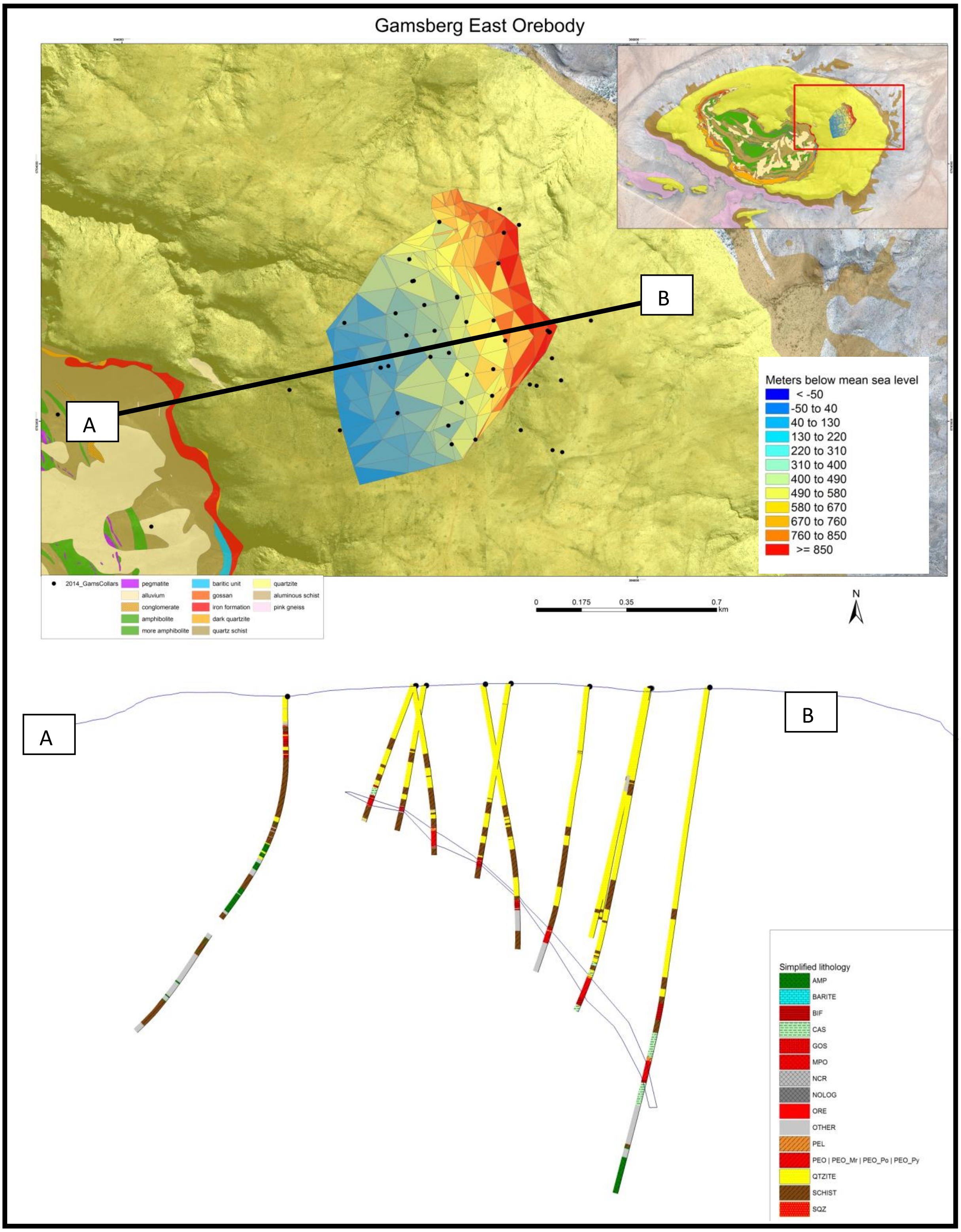

Figure 121: A geological model of the Gamsberg East orebody with a cross-section in the E-W view, which illustrate the variation in thickness of the mineralised unit.

A surface interpolation map of the manganese distribution in the Gamsberg East orebody shows NE-SW Mn-rich trends or "pockets". These trends coincide with the NE down-plunge of the Gamsberg orebody. Figure 122 is an interpretation of the distribution of manganese and alabandite, derived from drillhole information and geophysical survey information. The orientation of faults coincides with the trends of Mn-rich zones. At present, the role of these inferred faults cannot be determined.

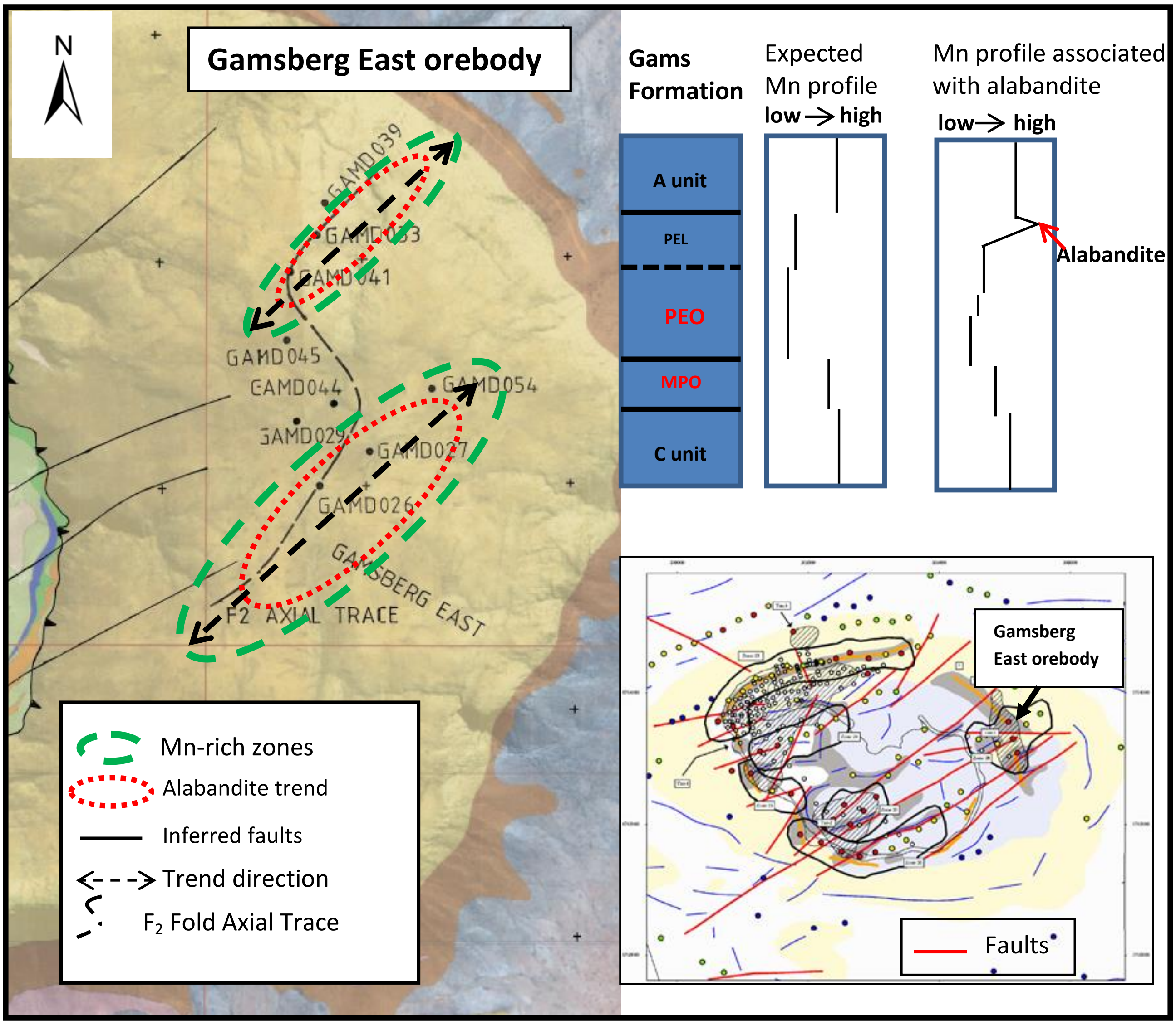

Figure 122: A map displaying a surface interpolation of the distribution of manganese and alabandite in the Gamsberg East orebody. An insert shows the distribution of the inferred faults in red.

Within the Gamsberg East orebody, the presence of the alabandite is restricted mainly to the sub-ecomomic pelitic schist (PEL) of the B1 unit, where it constitutes up to 16 %wt mineral abundance, based on quatitative XRD data. Minor occurrences of alabandite are present within the A unit, close to the contact with pelitic schist (PEL). Less than 2 %wt of alabandite is recorded within the meta-pelite ore of the B2 unit, and this concentration decreases significantly with depth. No alabandite is recorded towards the lower contact of the meta-pelite ore (PEO), or within the garnet-magnetite ore (MPO) and the C unit, despite MPO and the C unit hosting the highest Mn concentrations.

Textural relationships and mineralogy

Present-day textures of the sulphide minerals of the Gamsberg East orebody are a result of cooling after peak metamorphic conditions of upper amphibolite facies (2.8 to 4.5 kbar, 630 to 670 ˚C; Rozendaal and Stalder, 2005). Common textures associated with sphalerite, alabandite, pyrite and pyrrhotite are blebs, lamella, flame-like, cloth-like and mymerkite, to mention a few.

Typical textures associated with alabandite are: small blebs of alabandite (less than 100 microns) within sphalerite without pyrrhotite blebs; larger than 100 micron alabandite within sphalerite with pyrrhotite grains; central or enveloped alabandite grains coexisting with pyrrhotite and sphalerite; alabandite inclusions in pyrrhotite grains; and isolated alabandite grains (less than 250 microns) within silicate matrix minerals (biotite-quartz).

The variation in the grain sizes of alabandite is interpreted to be largely a result of varying diffusion speeds: larger grains coexisting with sphalerite are a result of high diffusion rates at higher temperature, while microscopic exsolution lamellae/blebs of alabandite (conforming to the cleavage of sphalerite grains), exsolved along sphalerite cleavages, are results of a slower diffusion rate at lower temprature.

Phase relationships of alabandite coexisting with other Mn-bearing minerals suggest that equilibrium cooling conditions were attained. The composition of sphalerite is homogenous and shows little variation, whether it coexist with alabandite or not. Amongst the alabandite, at least two popultations exist and the differentces are in the concentrations of sulphur and manganese.

Sulphur controls the structure of sulphide minerals in monosulphides and plays a crucial role as together with other factors such as temperature and the activities of other elements, sulphur controls the crystal structure. If there is a difference in metal sulphur ratios, then it means that the metals are fluctuation and will be reflected in the analysis. This is a well known fact for Fe-monosulphides.

To rule out the possibility of undetected elements, an SEM installed with an EDS detector was used for semi-quantitative analysis, and only iron, manganese, zinc and sulphur were reported as major elements in sphalerite and alabandite, while As and Ag were present as trace elements. No Ca and Mg were reported. Zinc occurs in alabandite only in trace concentrations.

The chemistry of alabandite

Refer to section 6.2.1 for alabandite chemistry and about the two groups of population. Group 1 alabandite is characterised by high manganese and low sulphur concentrations, whereas Group 2 is characterised by lower manganese and higher sulphur concentrations, as shown in Table 30. The separation of alabandite into two populations could not be explained using mineral assemblages and depth, except for sample Alabandite1 from a coarse-grained (vein-like) alabandite. Since no evidence for additional elements could be detected, there could a possibility of different oxidation state of manages and/or iron.

Cuda et al. (2011) investigated the magnetic properties of alabandite at low temperatures. Alabandite close to stoichiometry in Mn was reported to be inherently magnetic, with anomalous magnetic behaviour taking place at 40 K (Cuda et al., 2011). The results of Cuda et al. (2013) show that pristine alabandite is not magnetic, but the presence of an oxide layer, hausmannite (Mn_3O_4), on the surface of alabandite is the result of the anomalous magnetism detected at 40 K, and alabandite rather was nearly stoichiometric. In analogy there is a possiblilty that a sub-microscopic intergrowth between alabandite and unidentified Mn compound might be responsible the diffrerence of alabandite. In this study the differences between the two groups could not be resolved.

Table 30. The chemistry of alabandite populations.

Alabandite populations			
		Group 1	**Group 2**
S %wt	***Min***	35.02	35.94
	Ave	35.90	36.45
	Max	36.73	37.04
	Std dev.	0.38	0.22
Mn %wt	***Min***	56.48	55.03
	Ave	59.44	56.53
	Max	61.76	58.57
	Std dev.	0.84	0.80
Fe %wt	***Min***	3.32	3.79
	Ave	5.50	5.52
	Max	7.37	7.20
	Std dev.	0.79	0.78
Zn %wt	***Min***	0.00	0.00
	Ave	0.05	0.14
	Max	0.88	0.76
	Std dev.	0.13	0.23

The chemistry of sphalerite

The chemistry of sphalerite in the Gamsberg East orebody shows at least three population groups. The three groups are a result of the relationship between manganese and zinc, as manganese substitutes for zinc in sphalerite. Sphalerite with concentrations of less than 3.0 %wt Mn (refer to to section 6.2.2) is associated with remobilisation textures. This sphalerite group is honey coloured. There are trends as shown in Figures 103 to 106 (section 6.2.2) but statistically realibe separation is not possible.

Table 31 presents the chemistry of sphalerite and the colour variations. Three colour variations of sphalerite were observed in the hand specimen: reddish-black, reddish-brown and honey-coloured sphalerite. According to Wincott and Vaughan (2006), natural sphalerite is never pure and usually contains a considerable amount of transition elements like Fe^{2+}, Mn^{2+} and Cd^{2+}, substituting for Zn^{2+}, therefore resulting in colours ranging from pale yellow to dark brown, and sometimes black. This observation could explain the colour variations in the sphalerite of the Gamsberg East orebody. The honey-coloured sphalerite hosts Mn less than 2 %wt.

Table 31. The mineral chemistry and colour relationships of the sphalerite.

	Sphalerite chemistry													
	Min	**Max**	**Ave**	**Min**	**Max**	**Ave**	**Min**	**Max**	**Ave**	**Min**	**Max**	**Ave**	**Colour relationship**	
	Mn (%wt)			**Fe (%wt)**			**Zn (%wt)**			**S (%wt)**				
PEL	6.17	7.87	7.14	9.32	12.09	10.90	46.40	50.41	48.14	33.35	34.32	33.91	Reddish-black	Reddish-brown
PEO	3.21	8.75	6.60	8.07	12.46	10.43	45.49	53.91	49.10	32.50	34.85	33.65	Reddish-black	Reddish-brown
MPO	3.58	7.62	6.02	8.11	12.05	10.29	47.71	53.97	49.81	32.63	34.47	33.79		Reddish-brown
Remobilised sphalerite	1.30	3.02	2.30	8.24	10.17	9.18	53.58	55.98	54.90	32.39	34.44	33.02	Honey-coloured	

The chemistry of silicate and oxide

Manganese is also hosted in clay minerals and chlorite with an average Mn concentration of about 10 %wt and 6 %wt MnO respectively. These minerals are associated with late stage alteration processes or retrograde metamorphism. Phlogopite and muscovite also host an average Mn concentration of about 1.0 %wt MnO. The chemogenic rocks of the A, C and B2 units host Mn-bearing minerals such as spessartine, gedrite, pyroxmangite, diopside, pyrophanite, magnetite, jacobsite and franklinite.

Recalculated manganese whole-rock geochemistry from XRD and mineral chemistry data

Recalculation of manganese whole-rock geochemistry from the XRD and mineral chemistry data was undertaken to determine the contribution of Mn-bearing minerals towards Mn whole-rock geochemistry concentration. Recalculated whole-rock geochemistry of Mn is a product of the abundance (refer to Section 5.1.3 for XRD data) of Mn-bearing minerals with content of Mn within these Mn bearing minerals (refer to Chapter 6 for mineral chemistries). The equation is as follows:

Reclaculated Mn_%wt = [(n1 X a)A + (n2 X b)B + (n3 X c)C + …..]/[n1+n2+n3+…..]

n1= abundance of mineral A ***a= Mn content in mineral A***

n2= abundance of mineral B ***b= Mn content in mineral B***

n3= abundance of mineral C ***c= Mn content in mineral C***

Table 32 present the comparison between recalculated Mn geochemistry data and the Mn XRF data and also the abundances of alabandite within the ore horizon unit in of the four drillholes. The pelitic schists (PEL) from the four drillholes show a lower percentage difference, unlike the meta-pelite ore (PEO) counter-part. This could mean that the abundance of most or all Mn-bearing minerals in the pelitic schists are accounted for by XRD, and there is less variation of Mn content within Mn-bearing minerals, unlike the PEO's. Figure 123 shows a graphical presentation of the comparison.

Table 32. The comparison of Mn whole-rock geochemistry between recalculated XRD+Mineral chemistry and the XRF data. Also the abundance of alabandite and thicknesses of the rock units are presented.

BH_ID	**Rock type**	**Recalculated Mn %wt_ XRD+EMPA**	**Mn%wt_ XRF**	**Percentage difference**	**Aabandite_ %wt**	**Max. alabandite_ %wt**	**Thickness_ m**
GAMD054-2-2	PEL	14.53	14.54	0%	7.38	16.00	8.86
	PEO	5.19	3.30	-6%	0.68	2.44	20.25
	PYQ	1.55	3.49	7%			1.08
	PEO	2.18	2.93	3%			2.00
	PYQ	1.57	1.23	-1%			1.53

	PEO	1.92	1.52	-1%			2.00
GAMD033-2-4	PEL	7.39	7.98	4%	3.62	10.06	2.86
	PEO	5.25	2.82	-30%	0.23	0.71	2.97
GAMD041-1-3	PEL	2.27	3.09	15%			3.49
	PEO	5.43	1.90	-48%			3.00
GAMD045-0-0	PEL	1.70	0.45	-58%			1.76
	PEO	3.54	1.13	-52%			2.00
	MPO	5.31	9.90	30%			1.83

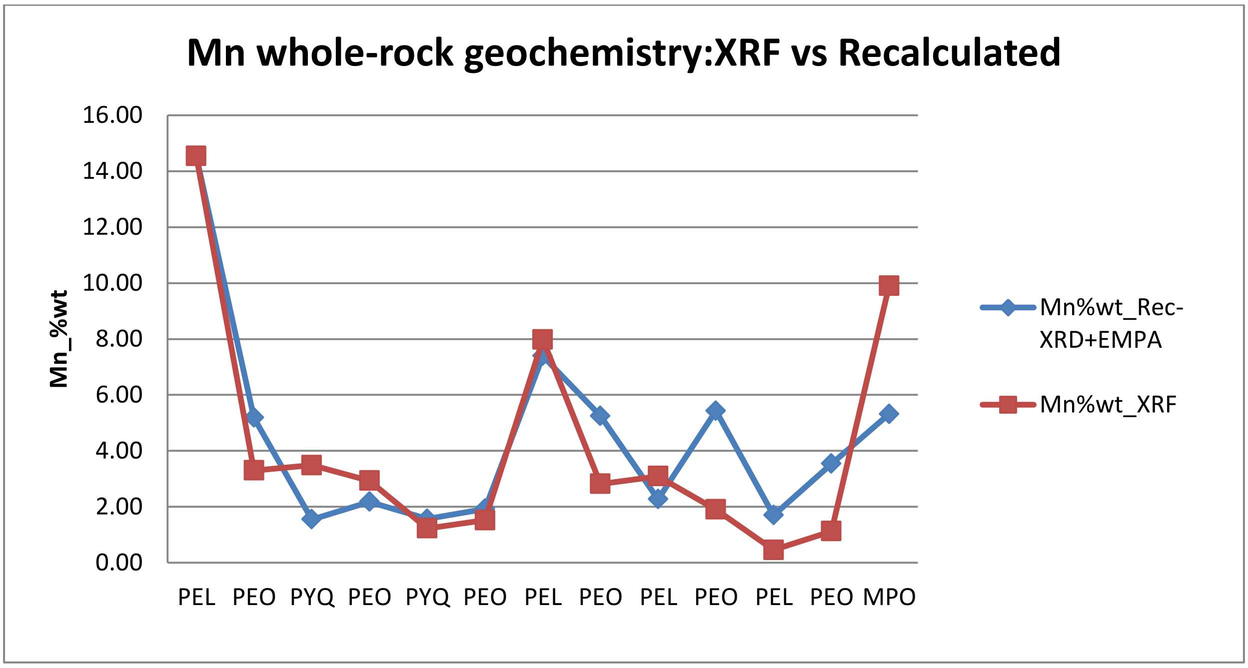

Figure 123. Comparison of Mn geochemistry data from XRF and recalculated Mn from XRD and mineral chemistry data.

There are at least two fundamental issues that arise from recalculating Mn whole-rock geochemistry for the rocks:

- The XRD data is semi-quantitative, with an error margin of 2.0 %wt

  - Some minerals such as clays and chlorite were grouped together as they share the XRD spectra and could not be refined, though thier mineral chemistries have different Mn content

- Presence of multiple population groups in a sample with unknown modal abudance of each population result in a global average being used which can be misleading

Techiques such as QEMSCAN and elemental mapping combined with point counting can be used to distinguish the modal abundances of different population groups of the minerals. There are at least two population groups of sphalerite in one sample/rock type (refer to Figure 105), but the contribution of each population group towards the total Mn content is not representative because the proportional modal abundance of the population groups is unknown and indistinguishable. QEMSCAN is an automated, quick and expensive technique whereas the elemental mapping and point counting technique, combined with XRD is a manual and a tedious process, which is prone to error. Even though such techniques are available, the representativity of the distribution is questionable as the relationship of population groups of a mineral like sphalerite is unpredictable, as demonstrated in Section 6.2.1.

Paragenesis of alabandite

The paragenesis of alabandite within the B1 unit is controlled by the interplay betweenthe bulk rock manganese concentrations approximately 2.0 %wt MnO (XRF bulk rock chemistry), the original basin architecture “basin deepening”, redox conditions, sulphur activity, and temperature.

According to Stalder and Rozendaal (2004), the B1 unit of the Gamsberg East orebody was deposited in a shallow, stratified, third-order basin, where anoxic bottom waters were overlain by an oxic water column. A positive Eu anomaly observed in the ore-bearing lithologies of the Gamsberg Zn deposit, as reported by Stalder and Rozendaal (2002; 2004; 2005c), means that the sulphide mineralisation is pre-metamorphic, indicating that relatively hot (200 to 250 ˚C) and reduced metal-rich brines were responsible for the sulphide mineralisation.

Rozendaal (2008) reported that the abundance of pyrrhotite in the Gamsberg East orebody reflects a sulphur deficiency and that some of the pyrrhotite may be primary. Pyrrhotite is known to form as a result of the breakdown of pyrite during prograde metamorphism (Craig and Vokes, 1993). During cooling or retrograde of pyrrhotite to pyrite there will be excess sulphur, which will result in sulphur movement and such effect will be supported by the presence of alteration zones rich in sulphide minerals (Craig and Vokes, 1993). This notion of sulphur movement implies sulphur stays constent, but gets re-arranged in different minerals, and no addition or depletion of sulphur is expected during pyrrhotite retrogression

Figure 124 presents a graph that illustrates the retrograde metamorphism of pyrite. The graph shows the content of pyrite in a rock mass, against pyrite content as a result of sulphur movement by pyrrhotite during cooling at various temperature ranges. This graph illustrates that, upon cooling, when pyrrhotite is expected to breakdown and form pyrite, there always will be movement of sulphur. When sulphur is moved) the proportion of pyrite and pyrrhotite will change, and this results in massive alteration textures or zones. Such textures are not observed in the Gamsberg East orebody, as pyrrhotite is more abundant than pyrite.

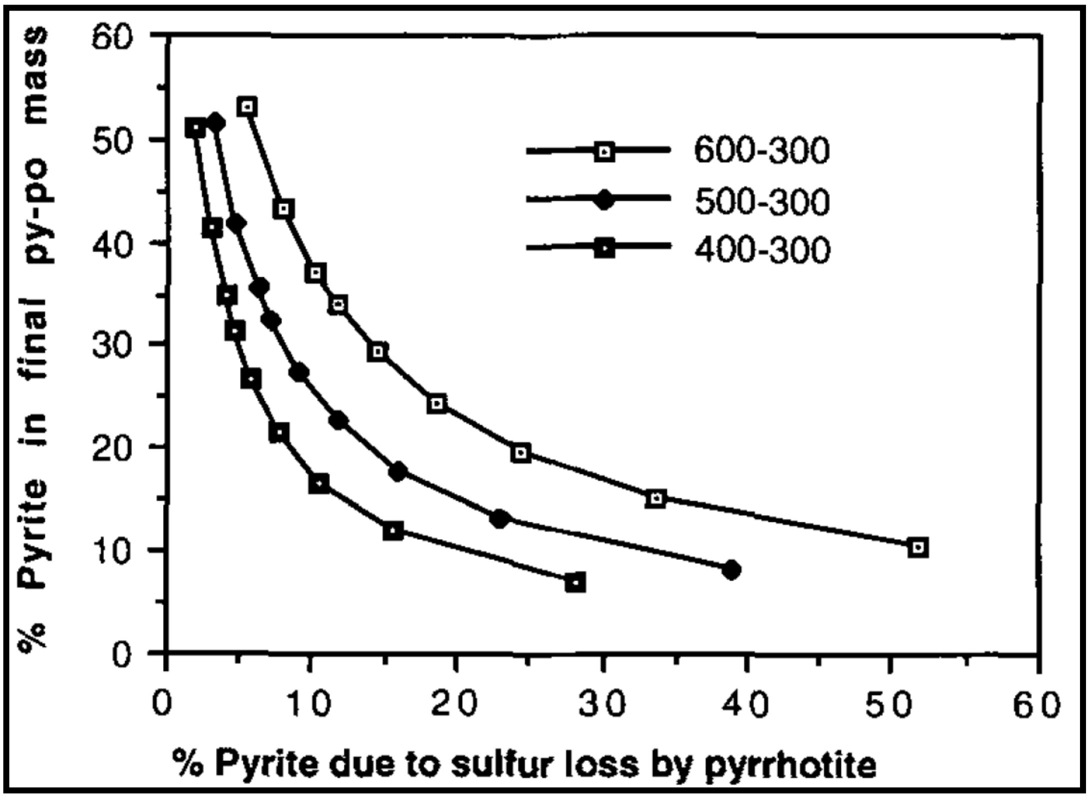

Figure 124. The % pyrite content in a rock mass vs. the % pyrite content as a result of sulphur movement by pyrrhotite during retrograde metamorphism of pyrite, at various temperatures (Craig and Vokes, 1993).

Manganese in the Gams Formation of the Gamsberg East orebody is introduced during the inception of hydrothermal pulses. These hydrothermal fluids were rich in manganese and iron, and poor in zinc. A shift from oxidising to reducing conditions took place in the water, were sub-oxic conditions existed. Alabandite occurs in high concentrations in the pelitic schist and in minor concentrations in the immediate overlaying unit (the A unit), and this defines a sub-oxic layer.

Alabandite is also known to form from the breakdown of rhodochrosite (see equation below) under reducing conditions when sulphur activity is very high (Olivo and Gibbs, 2003). The existence of alabandite depends heavily on the activity of sulphur, which should be much greater than the activity of bicarbonate species (Hem, 1963). Figure 125 shows the stability fields of different manganese species in aqueous solution and solids. Alabandite is denoted as $MnS_{(c)}$, with C standing for crystal. At high pH and under reducing conditions alabandite is stable, unless the activity of sulphur species is greater than that of bicarbonate species, as alabandite will disappear when sulphur and bicarobante species are equal to 100 ppm. As pH decreases, alabandite becomes unstable, and Mn activity exceeds 100 ppm, alabandite will be replaced by Mn-oxides. Indication for this was observed in the four drillholes of this study; where the bulk-rock manganese content was greater than 2.0 %wt MnO, alabandite was absent and Mn-bearing spinel minerals were present instead. Spinel minerals are metamorphic equivalents of original oxidized Mn species

$Mn(OH)_{2\ (c)} + SO_4^{2-} + 10H^+ = MnS_{\ (c)} + 6H_2O$ where $E° = -0.36\ v$

And at high pH

$$MnS_{\ (c)} + 2H_2O = Mn(OH)_{2\ (c)} + HS^- + H^+$$

From: Hem (1963)

Rhodochroisite Alabandite

$$2MnCO_3 + S_2 = 2MnS + 2CO_2 + O_2$$

From: Olivo and Gibbs (2003)

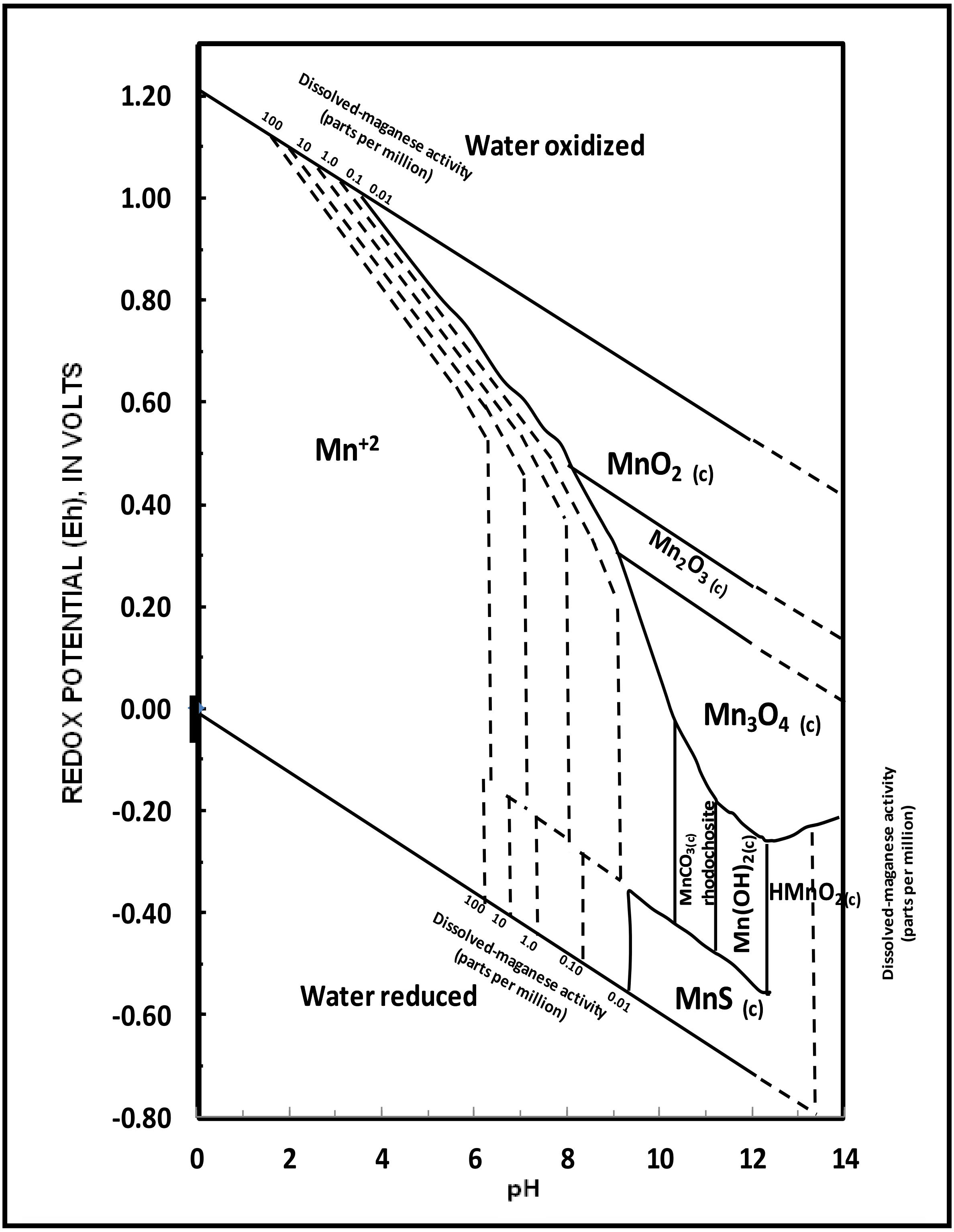

Figure 125. The stability fields of manganese species in aqueous solution. Total dissolved manganese activity is shown by the broken lines. MnS_c is alabandite (after Hem, 1963).

According to Hurai and Huraiová (2011), alabandite and mangano-ferroan sphalerite can crystallise within the pyrrhotite stability field. Figure 126 shows a phase diagram (oxygen fugacity vs. sulphur fugacity) of the Fe-S-O system, where the stability fields of Fe sulphides and Fe oxide minerals can be seen, contrained at 300 °C and atmospheric pressure. The red zone in the graphs shows the stability field where pyrrhotite can precipitate. Alabandite can also precipitate within the magnetite stability field, along with manganosite, and this is shown by the blue zone. In the Gamsberg East orebody, alabandite is strongly associated with pelitic schist, and only trace concentrations are present within the magnetite-bearing rocks of the A unit, therefore it is not likely that alabandite in the Gamsberg East orebody has precipitated within the magnetite field.

However, alabandite in the Gamsberg East orebody mostly coexists with Fe sulphide minerals (especially pyrrhotite) and sphalerite, and occurs in high concentrations within pelitic rocks. Pyrrhotite and pyrite coexist at log (-11) of sulphur fugacity (fS_2), as illustrated in Figure 127. Along log (-11), pyrite is expected to replace pyrrhotite (Hurai and Huraiová, 2011), but it already has been implied that pyrrhotite in the Gamsberg East orebody could be primary, therefore the field where pyrrhotite is stable is below log (-11). The stability field below log (-11) therefore could be the precipitation field of mangano-ferroan sphalerite and alabandite.

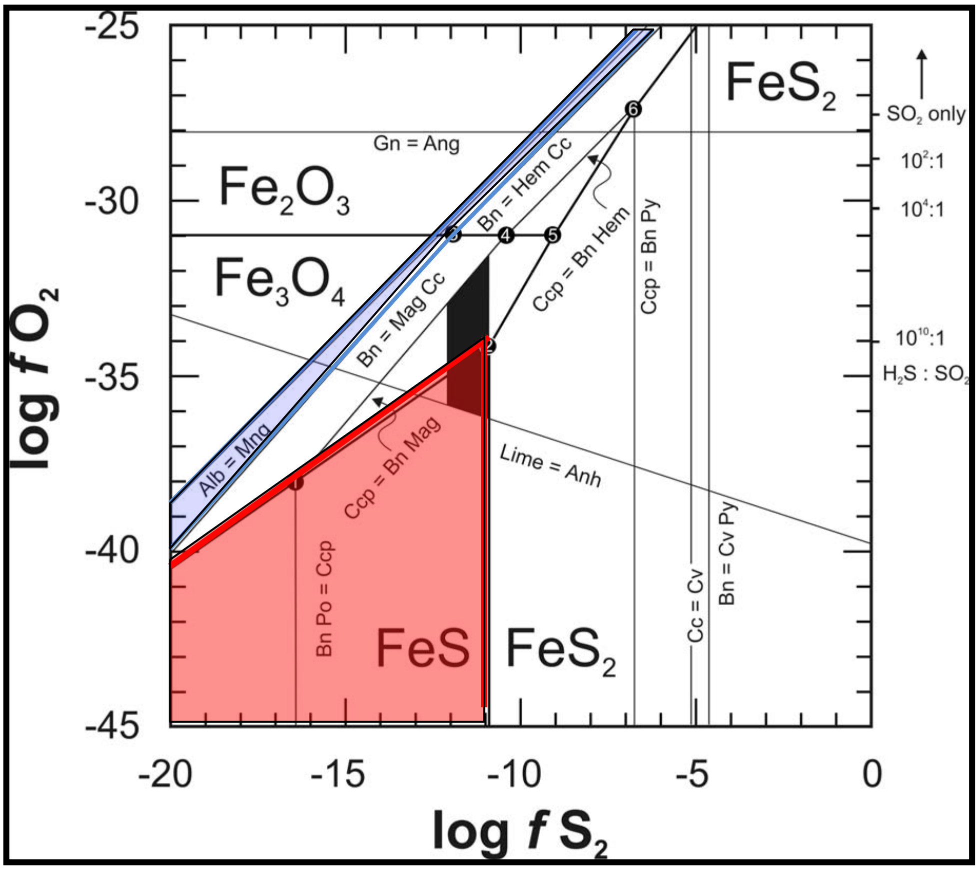

Figure 126. Phase diagram showing the sulphur and oxygen fugacities of the Fe-S-O system at 300 °C and atmospheric pressure (After Hurai and Huraiová, 2011).

With alabandite and mangano-ferroan sphalerite stable in the pyrrhotite stability field, the temperature and sulphur fugacity phase diagram is presented in Figure 127, which shows the stability field of pyrrhotite and pyrite. The broken red lines show a point where sulphur fugacity is log (-11) and pyrite coexists with pyrrhotite, as illustrated in Figure 127. When extrapolated, the temperature intersecting with the sulphur fugacity of log (-11) indicates the equilibrium temperature of alabandite-sphalerite-pyrrhotite, is just below 300 °C.

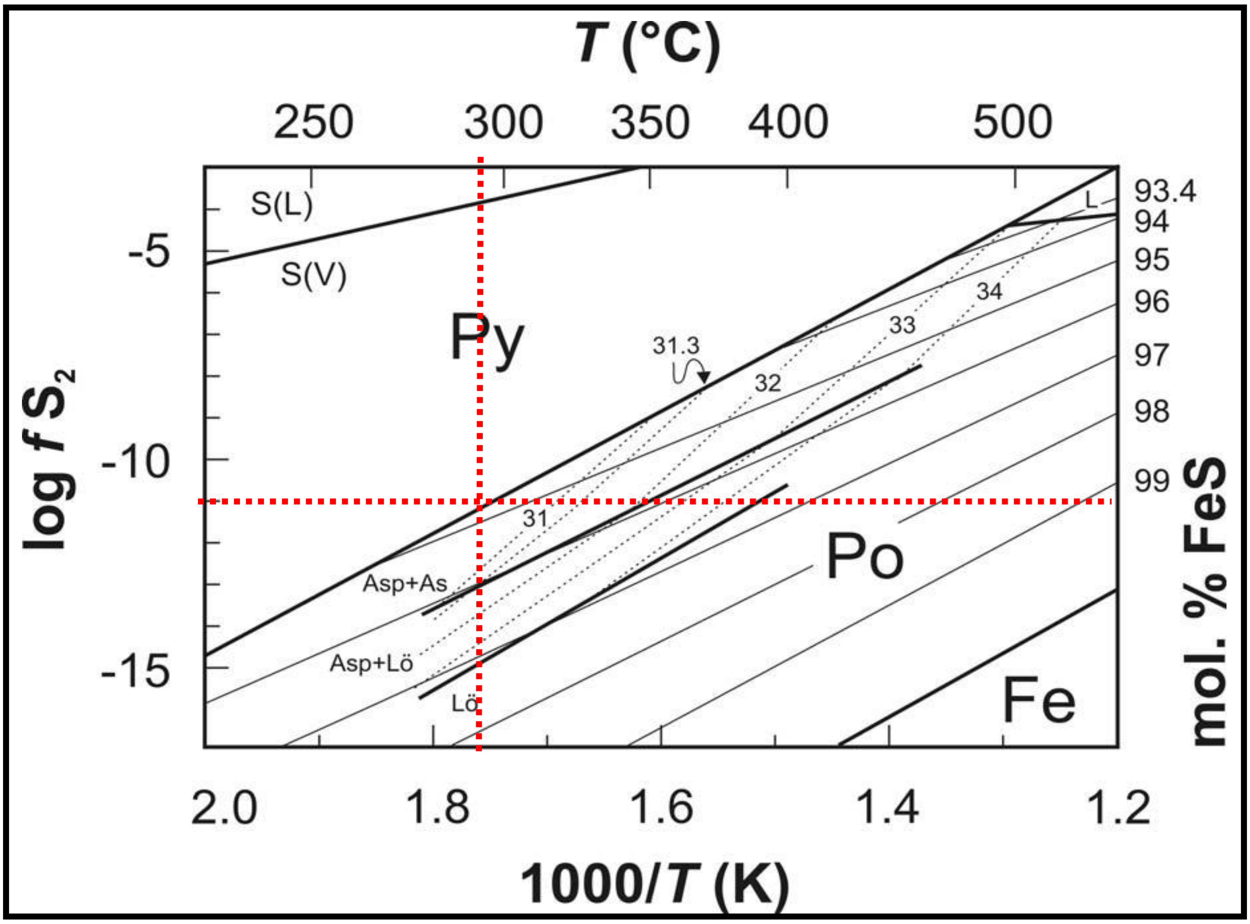

Figure 127. Phase diagram showing stability field of pyrite and pyrrhotite with sulphur fugacity and temperature. Po = pyrrhotite, Py = pyrite (Hurai and Huraiová, 2011).

Phase equilibria studies conducted by Sombuthawee et al. (1978) show that limited solubility exists between sphalerite and alabandite. The limit of sphalerite stability is approximately 7 %mol MnS at 600 °C. The extent of Zn-Mn substitution in sphalerite is temperature dependent, where a larger substitution of Mn in sphalerite can result in sphalerite inversion to wurtzite (Hurai and Horaiova, 2011). At 630 °C, about 5 %mol MnS is soluble in sphalerite, whereas 8 %mol ZnS is soluble in alabandite at 1 050 °C (Skinner and Luce, 1971). The latter temperatures are extremely high compared to the metamorphic conditions that prevailed at the Gamsberg Zn deposit, whereas the temperature of 630 °C falls within the metamorphic conditions reported by

Rozendaal (1986) (T = 630–670 ˚C, P = 2.8–4.5 kbar *inferred from silicate assemblages*).

Through experimental work, it has been shown that alabandite has a remarkable capacity to accommodate FeS in solid solution at temperatures over 400 ˚C up to the eutectic temperature of 1 162 ˚C (Skinner and Luce, 1971). Thermochemistry data from Skinner and Luce (1971) indicates that the FeS content of alabandite in equilibrium with troilite (FeS) is proportional to its minimum temperature of formation, showing a linear correlation in the ranges of 600 to 1 000 ˚C. The FeS content in alabandite indicates the last temperature at which the phases were in equilibrium, and therefore presents the minimum temperature of formation (Skinner and Luce, 1971). Temperatures above 1 000 ˚C have indicated a maximum limit of 7.5 ± 0.5 formula percentage of FeS in alabandite (Skinner and Luce, 1971). Figure 128 shows a binary phase relationship between coexisting alabandite and troilite.

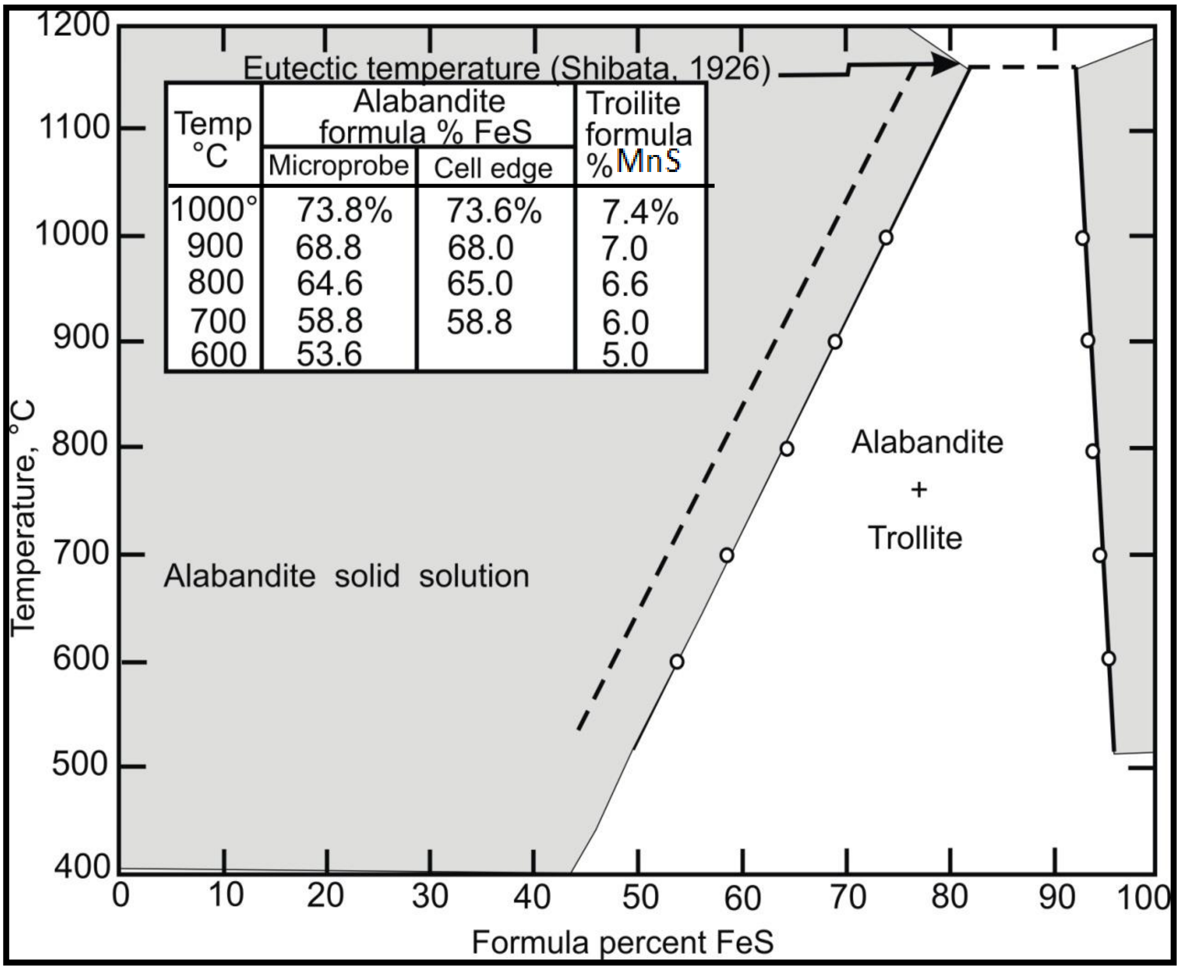

Temp °C	Alabandite formula % FeS		Troilite formula %MnS
	Microprobe	Cell edge	
1000°	73.8%	73.6%	7.4%
900	68.8	68.0	7.0
800	64.6	65.0	6.6
700	58.8	58.8	6.0
600	53.6		5.0

Figure 128. The binary diagram for coexisting alabandite and troilite with a table showing the FeS content in alabandite over ranges of temperatures (Skinner and Luce, 1971).

Skinner and Luce (1971) reported that extrapolating temperatures below 500 ˚C for the minimum formation of alabandite in solid solution with FeS can be misleading. However, temperatures of 200 ˚C and above have been reported for the formation of alabandite, and this is related to very slow cooling rates (Skinner and Luce, 1971; Dawei, 1986). The minimum temperature of formation for alabandite discussed by Skinner and Luce (1971) and Dawei (1986) coincides with the proposed temperature of the hydrothermal fluids of the Gamsberg Zn deposit, of 200 to 250 °C, proposed by Stalder and Rozendaal (2004).

Alabandite in the Gamsberg East orebody has a minimum manganese concentration of 55. %wt and a maximum manganese concentration of 62 %wt, therefore its chemistry corresponds with temperatures just above 600 °C and below 800 °C, as illustrated in Figure 128. These temperatures reflect metamorphic temperatures experienced by the Gamsberg Zn deposit.

Formation of alabandite is also associated with syndepositional model and deposition of the A unit and pelitic schist. The A unit of the Gams Formation was deposited by chemogenic processes, whereas the overlying pelitic schist of the B unit was deposited by clastic sedimentary processes. There is no hiatus associated with the deposition of the two units, but a change in water condition (pH, temperature, and oxygen and sulphur fugacities) allowed the A unit to culminate in precipitating and giving way to an uninterrupted deposition of sediments. The only reasonable explanation for the change in water conditions could be the inception of hydrothermal pulses by fluids rich in iron and manganese and poor in zinc.

Alabandite forms in the thicker portion “swells/ depression” of the orebody, and these areas are associated with a higher manganese bulk-rock concentration. This thicker portions of the orebody are associated with deeper areas within the original basin. The thinner portion “pinch” of the orebody has a lower manganese bulk-rock concentration, and no manganese-dominated minerals are present in the pelitic schist except. The transitional portions (between the pinch and swell) of the orebody have an intermediate manganese bulk-rock concentration, with spinel minerals (jacobsite and franklinite) and pyrolusite. The occurrence of alabandite is associated with slightly higher reducing conditions, in deep parts than the thinner portions or shallow area.

The change in water conditions from sub-oxic to reducing conditions, and the temperature, pH, and manganese activity associated with “basin deepening” are factors that coincide with the formation of alabandite. Alabandite is pre-metamorphic and precipitated along with Fe sulphide minerals and mangano-ferroan sphalerite. Alabandite, just like sphalerite and pyrrhotite, survived the metamorphic conditions experienced by the Gamsberg Zn deposit. The absence or presence of alabandite did not affect sphalerite crystal chemistry.

Goodfellow and Lydon (2007) reported that the lack of Cu within the Gamsberg Zn deposits suggests that the ore-forming fluid temperatures were below 300 ˚C; Stalder and Rozendaal (2004), on the other hand, reported that relatively hot (200 to 250 ˚C) and reduced metal-rich brines were responsible for the sulphide mineralisation. Alabandite, mangano-ferroan sphalerite and pyrrhotite can crystallise at temperatures of less than 300 °C, as presented in Figure 128. It therefore is reasonable to assume that less alabandite formed from fluids that were lower than 300 °C.

Figure 129 presents the proposed model of formation of alabandite in the Gamsberg East orebody. The occurrence of alabandite is related to the distribution of manganese within the pelitic rocks.These rock units has always been known to host significantly lower manganese concentration than overlaying- and underlaying-chemogenic rocks. The chemogenitic rocks are associated with oxidation state, with the presence of magnetite, as a dominant Fe-mineral, unlike the pelitic rocks which hosts pyrrhotite and pyrite as Fe-minerals. Lateral distribution of manganese is also controlled by the undulation of the basin. The “deeper parts of the basin” or “thicker portion of the orebody” has higher bulk-rock manganese concentration compared to the “shallower parts of the basin” or thinner portions of the orebody”. The deeper or shallower part of the basin also play an important role in the oxidation state in the water column, which among other factor decided where manganese species forms or precipitate as a sulphide, or as an oxide mineral and to some extent whether manganese was incorporated into the silicate minerals and sphalerite.

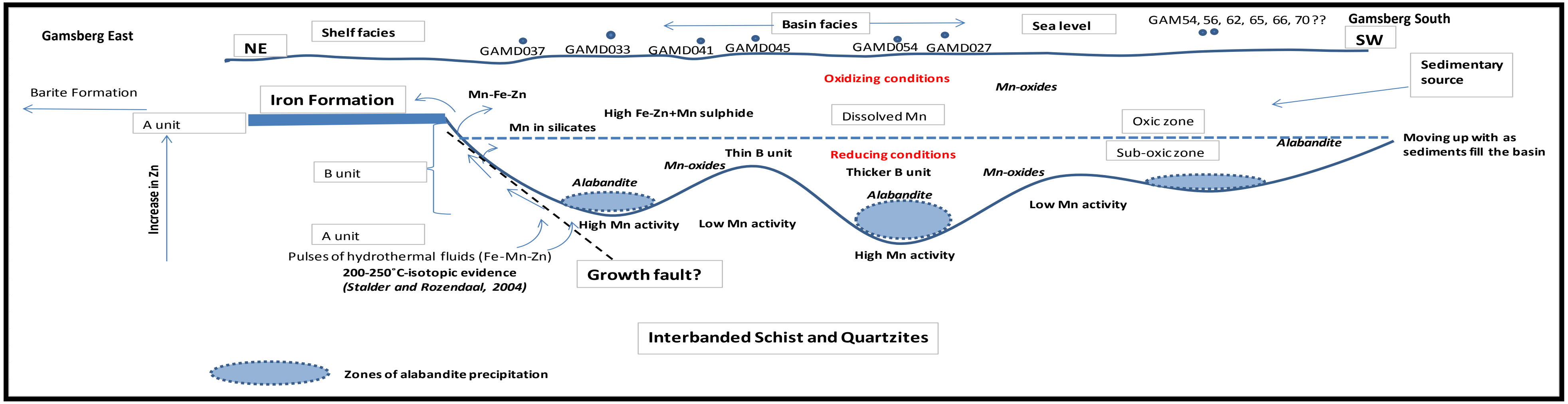

Figure 129. Proposed model of formation of alabandite in the Gamsberg East orebody.

Chapter 8: Conclusions

Discrepencies between dataset generated by the XRF and ICP technique hindered the generation of a 3D model for visual analysis of the manganese distribution of the Gamsberg East orebody. The ICP dataset was meant to be used for modelling purpose for the reason that it has larger data volume (6 000 samples from at least 50 drillholes), hence the data was validated using compatibility test between the ICP and XRF data. The difference in sample preparation methodology of the ICP and XRF techniques resulted in a bias in the manganese data of the ICP dataset, and this is as a result of mineralogical assemblages. The sample preparation method of the ICP technique requires a sample to be dissolved using strong acids, and this is not the case for some silicate- and oxide- minerals, as these minerals are known to only dissolve partially, while sulphide minerals are completely dissolved. As a result it is not known how much the silicates and oxide minerals contributed to the reported manganese concentration for whole-rock geochemistry of the ICP technique.

The selection of analytical methods is always about the objective of the investigation, and the ICP technique was chosen (for the Gamsberg sample analysis) for its ability to analyse low concentrations of elements in the sulphide minerals, especially zinc, as zinc in sphalerite is the commodity of interest. It is important to understand the logic behind a chosen analytical method, the limitations of such a method, and the meaning of the analytical results in their application for geochemical exploration.

The manganese within the Gamsberg East orebody is not homogenously distributed. The chemogenic A, C and garnet-magnetite ore (MPO) units host the highest Mn concentration relative to the pelitic schist and meta-pelite ore. The primary basin structure, “basin deepening”, which at the present-day is observed as pinch and swell orebody structures, played a major role in the precipitation and distribution of Mn-bearing minerals. Higher manganese concentrations within the pelitic schist and meta-pelite ore are associated with thicker portions/depressions of the orebody “swells”. The effects of deformation on the Gamsberg Zn deposit can not be ignored, as deformation could have accentuated the pre-existing basin structure under plastic conditions resulting to a preserved basin thickness variation structures.

Anomalous high concentrations of alabandite are found near the top contact of the pelitic schist, with a maximum concentration of 16 %wt (by quatitative XRD). The alabandite concentration in the pelitic schist decreases towards the meta-pelite ore top contact. Within the meta-pelite ore, alabandite is present almost one-third of the unit’s thickness, with a maximum concentration of 2 %wt. Up to 3 %wt alabandite is also present within the adjacent A unit rocks, which are in contact with the pelitic schist. Alabandite is hosted within the thicker portions/depressions of the orebody “swells”, associated with “basin deepening” and anomalous high manganese concentrations. No alabandite is reported in the garnet-magnetite ore (MPO) and the C unit, despite these units hosting the highest Mn concentrations.

Throughout the investigated rocks, other Mn-bearing minerals are pyrophanite, jacobsite, franklinite, magnetite, pyroxmangite, diopside, amphiboles, chlorite, micas, clays and garnet-end mebers such asspessartine, almandine and grossular. These minerals are present mainly within the A, C and MPO units, with amphiboles and minor jacobsite present within the pelitic schist and meta-pelite ore. Chlorite hosts an average of 7 %wt MnO, while phlogopite and muscovite contain an average of approximately 1 %wt MnO. Manganese concentration in clay minerals contains 3 %wt.

There are at least three colour variations of sphalerite are observed in handspeciemen, which to some extend are related to the distribution of Mn in sphalerite. Black sphalerite hosts highest Mn concentrations, whereas the light coloured (honey coloured) sphalerite hosts lowest Mn concentrations. The distribution of sphalerite grains with different Mn distribution is complex. The lack of understanding the relative proportion of sphalerite with different Mn content is part of the reason why recalculated whole-rock geochemistry is show higher diffrences when compared to the XRF data.

Coexisting phase relationships between alabandite and sphalerite show that equilibrium conditions have been attained. This is supported by the lack of reaction textures, triple junction textures, and isochemical signatures of the coexisting Mn-bearing minerals and sphalerite. This findings further supports that Mn-bearing sphalerite is primary.

Alabandite is interpretated to be pre-metamorphic and its formation is associated with the formation of Fe sulphides and sphalerite. No evidence of metamorphism and/or structural geology could be associated with the formation of alabandite; it rather is associated with original basin conditions. The temperature of hydrothermal fluids associated with the formation of alabandite was below 300 °C. The present-day textural relationships between alabandite, spahlerite and Fe sulphide minerals, particularly pyrrhotite (exsolution grains), could have result from cooling from peak metamorphic conditions.

There are two populations of alabandite that are controlled by the distributions of sulphur and manganese in the alabandite. The difference in manganese between the two population groups is 2.91 %wt and sulphur is 0.55 %wt. The distribution of iron in alabandite is homogenous and therefore factors that control the iron distribution differ from those controlling the distribution sulphur, manganese, and zinc in alabandite. Zinc concentration in alabandite is below 1 %wt and therefore considered a minor element.

Since alabandite is a mono-sulphide mineral, the sulphur distribution is expected to be homogenious, which is not the case here. An investigation to determine the cause of sulphur inhomogeneity was carried-out. This involved checking instrumental error, carbon coating procedure and possible undetected elements. For instrumental error, a pattern in sulphur analyses was plotted against the analysis entry number (order of of analyses). No pattern was obsevered that could be linked to instrumental drift. The presence of undetected element(s) was excluded, as a tedious process was undertaken to check a possibility of udetected elements using EDS techniques. Carbon coating was found to be satisfactory.

Manganese is known to have multiple oxidation states and the possibility of undetected states of Mn in alabandite shouldn't be left unquestioned. The presence of different oxidation states of manganese (Mn^{2+}, Mn^{3+}, Mn^{4+} and Mn^{6+}) in alabandite would test if alabandite from Gamsberg East orebody is stochiometric or non-stochiometric, and this could explain the 2.91 %wt Mn and 0.55 %wt S differences between the two populations of alabandite.

Metallurgical implications

The physical and mineralogical properties of the pelitic schist and meta-pelite ore are similar, but distinguished by only by the economic cut-off and visually detectable sphalerite. Pelitic schist therefore has the potential to be mined as sub-economic resources or dilution. If this is the case, higher concentrations of alabandite could contaminate the ore, therefore increasing the risk and the Mn penalty factor of the Gamsberg Zn ore. Floating sphalerite with alabandite has been proven to have undesirable results (Schouwstra et al., 2010). It is suggested that alabandite-bearing rocks (pelitic schist, garnet quartzite and calc-silicate rock) be taken in account during mine cycle (mine planning and production).

References

Ahlrichs, J.W. (1975). Investigation of manganese occurrence in three Gamsberg 3rd zinc clearner concentrates from master composite No. 6. Unpublished memorandum to Mr W. C Hellyer. Internal company report. pp 1- 4.

Alsopa, G.I. and Holdsworth, R.E. (1999). Vergence and facing patterns in large-scale sheath folds. *Journal of Structural Geology*, **21**, 1335-1349.

Anglo American Plc. (2006a). Review of the geophysics completed over Gamsberg South ending September 2006. Unpublished company report. Ockert Terblanche Exploration Division, Anglo American Operation, pp 1-8.

Anglo American Plc. (2006b). Review of the geophysics completed over Gamsberg East 2004-2006. Unpublished company report. Ockert Terblanche Exploration Division, Anglo American Operation, pp 1-8.

Bailie, R. and Reid, D.L. (2005). Ore textures and possible sulphide partial melting at Broken Hill, Aggeneys, South Africa. I: Petrography. *South African Journal of Geology*, **108**, 51-70.

Bailie, R., Armstrong, R. and Reid, D. (2007a). The Bushmanland Group supracrustal succession, Aggeneys, Bushmanland, South Africa: Provenance, age of the deposition and metamorphism. *South African Journal of Geology*, **110**, 1-59.

Bailie, R., Armstrong, R. and Reid, D. (2007b). Composition and single zircon U-Pb emplacement and metamorphic ages of the Aggeneys Granite Suite, Bushmanland, South Africa. *South African Journal of Geology*, **110**, 87-110.

Cherniak, D.J., Hervig, R., Koepke, J., Zhang, J. and Zhao, D. (2010). Analytical methods in diffusion studies. *Review in Mineralogy and Geochemistry*, **76** 107-170.

Claassen, V. (2010). Review of quality on Gamsberg East samples analyzed at ALS Chemex during the period February 2007 to September 2009. Unpublished company document, Anglo American Plc, pp 1-55.

Colliston, W.P., Praekelt, H.E. and Schoch, A.E. (1989). A broad perspective (Haramoep) of geological relations established by sequence mapping in Proterozoic Aggeneys terrane. Bushmanland, South Africa. *South African Journal of Geology*, **92**, 42-48.

Cornell, D.H. and Pettersson, A. (2007). Ion probe dating of the Achab Gneiss, a young basement to the Central Bushmanland Ore District? *Journal of African Earth Science*, **47**, 112-116.

Cornell, D.H., Pettersson, A., Whitehouse, M.J. and Schersten, A. (2009). A new chronostratigraphic paradigm for the age and tectonic history of the Mesoproterozoic Bushmanland Ore District, South Africa. *Economic Geology*, **104**, 385-404.

Cornell, D.H., Thomas, R.J., Bowring, S.A., Armstrong, R.A. and Grantham, G.H. (1996). Protolith interpretation in metamorphic terranes: a back-arc environment with Besshi-type base metal potential for the Quha Formation, Natal Province, South Africa. *Precambrian Research*, **77**, 243-271.

Craig, J.R. and Vokes, F.M. (1993). Metamorphism of pyrite and pyrite ores: An ore review. *Mineralogical Magazine*, **57**, 3-18.

Cuda, J., Kohout, T., Tucek, J., Haloda, J., Filip, J., Prucek, R. and Zboril, R. (2011). Low temperature magnetic transition in troilite: A simple marker for highly stoichiometric FeS systems. *Journal of Geophysical Research*, **116**, B11205: 1-9.

Cuda, J., Kohout, T., Tucek, J., Haloda, J., Filip, J., Prucek, R., Kosterov, A., Haloda, J., Skala, R., Santala, E., Medrik, I. and Zboril, R. (2012). Low temperature magnetism of alabandite: Crucial role of surface oxidation. *American Mineralogist*, **98**, 1550-1556.

Dawei, W. (1986). The behaviour of Fe-Mn-S system under high temperature and high pressure. *Journal CSIMM*, **4**, 17-23.

Dewey, J.F., Robb, L. and Van Schalkwyk, L. (2006). Did Bushmanland extensionally unroof Namaqualand? *Precambrian Research*, **150**, 173-182.

Eglington, B.M. (2006). Evolution of the Namaqua-Natal Belt, southern Africa – A geochronological and isotope geochemical review. *Journal of African Earth Science*, **46**, 93-111.

Eglington, B.M. and Armstrong, R.A. (2003). Geochronological and isotopic constraints on the Mesoproterozoic Namaqua-Natal Belt: Evidence from deep borehole intersection in South Africa. *Precambrian Research*, **125**, 179-189.

Gamsberg Project Manual (2010). Gamsberg Geology Overview and core logging. Unpublished company report, Anglo American Exploration Division, pp 1-88.

Gertloff, E.C. (2004) *Petrology and sulfur isotope geochemistry of the metamorphosed Cu-Pb-Zn-Ag deposits of the Aggeneys-Gamsberg district, Bushmanland, South Africa*. Diploma thesis (unpublished), Westfälische Wilhelms-Universität, Münster, 104pp.

Goodfellow, W.D. and Lydon, J.W. (2007). Sedimentary exhalative (SEDEX) deposits. In: Geological Association of Canada, Mineral Deposits of Canada Division (Editor), *Mineral deposits of Canada: A synthesis of major deposit types, district metallogeny, the evolution of geological provinces, and exploration methods. Special publication 5*. pp 163-183.

Hem, J.D. (1963). Chemical equilibria and rates of manganese oxidation. Chemistry of manganese in natural environment. *Geological survey water-supply paper*, **1667-A**, pp 1- 64.

Hurai, V. and Huraiova, M. (2011). Origin of ferroan alabandite and manganoan sphalerite from the Tisovec skarn, Slovakia**.** *N. Jb. Miner. Abh,* **188** (2), 119-134.

Joubert, P. (1986). Namaqualand – a model of Proterozoic accretion? *Transvaal Geological Society South Africa,* **89**, 79-96.

Lacassie, J.P., McClung, C.R., Bailie, R.H., Gutzmer, J. and Ruiz-Del-Solar, J. (2006). Geochemical patterns of schists from the Bushmanland Group: An artificial neural networks approach. *Journal of Geochemical Exploration*, **91**, 81-98.

Loubser, M. and Verryn, S. (2008). Combining XRF and XRD analyses and sample preparation to solve mineralogical problems. *South African Journal of Geology*, **111**, 229-238.

Malysiak, V., Hey, P. and Shackleton, N. (2009). Metallurgical and mineralogical characterisation of Gamsberg East ore types with emphasis on drill core GAMD027, GAMD035 and GAMD036. Unpublished company report, Anglo Research Metallurgical Services and Mineralogical Research, MP/01/09, pp 1-22.

McClung, C.R. (2006). *Basin analysis of the Mesoproterozoic Bushmanland Group of the Namaqua Metamorphic Province, South Africa*. Doctoral thesis, University of Johannesburg, Johannesburg, South Africa, 307pp.

McClung, C.R. and Viljoen, F. (2011). A detailed mineralogical assessment of sphalerites from the Gamsberg zinc deposit, South Africa: The manganese conundrum. *Minerals Engineering* **DOI 10.1016**, 1-9.

McClung, C.R., Gutzmer, J., Beukes, N.J., Mezger, K., Strauss, H. and Gertloff, E. (2007). Geochemistry of bedded barite of the Mesoproterozoic Aggeneys-Gamsberg Broken Hill-type district, South Africa. *Mineral Deposita*, **42**, 537-549.

Moore, J.M., Watkeys, M.K. and Reid, D.L. (1990). The regional setting of the Aggeneys/Gamsberg base metal deposits, Namaqualand, South Africa. In: P.G. Spry and L.T. Bryndzia (Editors), *Regional metamorphism of ore deposits and genetic implication: Utrecht, VSP.* Proceedings of the 28th International Geology Congress. 9-19 July 1989. pp 77-95.

Olivo, G.R. and Gibbs, K. (2003). Paragenesis and mineral chemistry of alabandite (MnS) from the Ag-rich Santo Toribio epithermal deposit, Northern Peru. *Mineralogical Magazine*, **67**, 95-102.

Prinsloo, L. (2009) (cited 2010 May 10). *Anglo sells zinc assets to Vedanta for $1.3bn* (Internet). Available from: www.miningweekly.com/article/anglo-sells-zinc-assests-to-vedanta-for-1bn-2010-05-10.

Reed, S.J.B. (1993). *Electron microprobe analysis.* 2nd edition. Cambridge University Press, London, 326pp.

Reid, S. and Harley, M. (2009). Gamsberg East preliminary mineral resource assessment, Aggeneys, Northern Cape, South Africa. Unpublished company report, Anglo American Plc. pp 1-22.

Reid, D.L., Smith, C.B., Watkeys, M.K., Welke, H.J. and Betton, P.J. (1997). Whole-rock radiometric age patterns in the Aggeneys-Gamsberg ore district, central Bushmanland, South Africa. *South African Journal of Geology*, **100** (1), 11-22.

Reid, D.L., Welke, H.J., Betton, P.J. and Erlank, A. (1987). Composition, age and tectonic setting of amphibolites in the central Bushmanland Group, western Namaqua Province, southern Africa. *Precambrian Research*, **36**, 99-126.

Robb, L.J., Armstrong, R.A. and Waters, D.J. (1990). The history of granulite-facies metamorphism and crustal growth from single Zircon U-Pb geochronology: Namaqualand, South Africa. *Journal of Petrology*, **40**, 1747-1770.

Roos, E.H. (1997). Effects of quality of concentrates on the operations of an electrolytic zinc plant. Unpublished memorandum A Bier, Anglo American Corporation of South Africa Limited, pp 1-21.

Rozendaal, A. (1978). The Gamsberg zinc deposit, Namaqualand. In: W.J. Verwoerd (Editor), *Mineralization in Metamorphic Terranes*. Van Schaik, Pretoria, pp 235-256.

Rozendaal, A. (1986). The Gamsberg zinc deposit, Namaqualand District. *Mineral Deposits of Southern Africa*, 1477-1488.

Rozendaal, A. (2008). Stratigraphy, mineralogy and ore classification of the Gams Formation in the Gamsberg East Orebody. Final Report Phase 1: Unpublished report from Anglo American Plc, pp 1-22.

Rozendaal, A. and Stumpfl, E.F. (1986). Mineral chemistry and the genesis of Gamsberg zinc deposits, South Africa. *Institution of Mining and Metallurgy (Section B: Applied Earth Science)*, **93**: B161-B175.

Ryan, P.J., Lawrence, A.L., Lipson, R.D., Moore, J.M., Paterson, A., Stedman, D.P. and Van Zyl, D. (1986). The Aggeneys Base Metal Sulphide Deposits, Namaqualand District. *Mineral Deposits of Southern Africa*, *I and II*, pp 1447-1473.

Schouwstra, R., De Vaux, D., Hey, P., Malysiak, V., Shackleton and Bramdeo, S. (2010) Understanding Gamsberg: A geometallurgical study of a large stratiform zinc deposit. *Mineral Engineering* **DOI: 10.1016**, 1-8.

SACS (South African Committee for Stratigraphy), 1980. Stratigraphy of South Afica: Geological Survey of South Africa Handbook, Geological Survy of South Africa, Pretoria, **8**, p 690.

Skinner, B.J. and Luce, F.D. (1971). Solid solutions of the type (Ca, Mg, Mn, Fe)S and their use as geothermometers for the enstatite chondrites. *American Mineralogist*, **56**, 1269-1296.

Sombuthawee, C., Bonsall, S.B. and Hummel, F.A. (1978). Phase equilibria in the systems ZnS-MnS, ZnS-$CuInS_2$, and MnS-$CuInS_2$. *Journal of Solid State Chemsitry*, **25**, 391-398.

Stalder, M. and Rozendaal, A. (2002). Graftonite in phosphatic iron formations associated with the mid-Proterozoic Gamsberg Zn-Pb deposit, Namaqua Province, South Africa. *Mineralogical Magazine*, **66** (6), 915-927.

Stalder, M. and Rozendaal, A. (2004). Apatite nodules as indicator of depositional environment and ore genesis for the Mesoproterozoic Broken Hill-type Gamsberg Zn-Pb deposit, Namaqua Province. *Mineralium Deposita*, **39**, 189-203.

Stalder, M. and Rozendaal, A. (2005a). Calderite-rich garnet and franklinite-rich spinel in amphibolite-facies hydrothermal sediments, Gamsberg Zn-Pb deposit, Namaqua Province, South Africa. *The Canadian Mineralogist*, **43**, 585-599.

Stalder, M. and Rozendaal, A. (2005b). Distribution and geochemical characteristics of barite and barium-rich rocks associated with the Broken Hill-type Gamsberg Zn-Pb deposit, Namaqua Province, South Africa. *South African Journal of Geology*, **108**, 35-50.

Stalder, M. and Rozendaal, A. (2005c). Trace and rare earth element chemistry of garnet and apatite as discriminant for Broken Hill-Type mineralization, Namaqua Province, South Africa. Mineral Deposit Research: Meeting the Global Challenge, Session 6, 699-702.

Stumpfl, E.F. (1979). Manganese haloes surrounding metamorphic stratabound base metal deposits. *Mineral Deposita*, **14**, 207-218.

Odling, N. E. (1987). Structural analysis and three-dimension modelling at Gamsberg, N.W. Cape: Department of Geology, University of Cape Town, Precambrian Research Unit Bulletin **34**, 90pp.

Thomas, R.J., Agenbacht, A.I.D., Cornell, D.H. and Moore, J.M. (1994). The Kibaran of southern Africa: Tectonic evolution and metallogeny. *Ore Geology Reviews*, **9**, 131-160.

Van Leeuwen and Ponelis (1992). Manganese removal from Gamsberg zinc electrolyte using ozone oxidation: Report on laboratory kinetics and preliminary feasibility. Unpublished company report from Van Leeuween and Ponelis Consulting Engineers. Gold Fields of South Africa LTD, pp 1-147.

Voet, H. Jerman, N. Mattthews, P.and Gushee, G. (2000). Gamsberg Zinc Mine [Bankable Feasibility Study]. Section 2 – Geology. Unpublished company report. pp 1-55.

Walters, S.J. (1996). An overview of Broken Hill type deposits. In: J. Pongratz, and G. Davidson (Editors), *New developments in Broken Hill type deposits*. CODES Special Publication 1, Hobart, University of Tasmania, pp 1-10.

Watkeys, M.K. (1986). The Achab gneiss: A 'floor' in Bushmanland or a flaw in Namaqualand? *Geological Society of South Africa,* **89** (2)*,* 103-116.

Willis, J. (2010). *Sample preparation: Glass beads by borate fusion*. PANanalytical B.V., The Netherlands, 58pp.

Wincott, P.L. and Vaughan, D.J. (2006). Spectroscopic studies of sulphides. *Reviews in Mineralogy and Geochemistry*, **61**, 505-556.

Zhang, W. and Cheng, C.Y. (2007). Manganese metallurgy review. Part III: Manganese control in zinc and copper electrolytes. *Hydrometallurgy*, **89**, 178-188.